The Pennsylvania State University

The Graduate School

Department of Materials Science and Engineering

EPITAXIAL $Pb(Mg_{1/3}Nb_{2/3})O_3$-$PbTiO_3$ THIN FILMS

A Thesis in
Ceramic Science

by
Jon-Paul Maria

Submitted in Partial Fulfillment
of the Requirements
for the Degree of

Doctor of Philosophy
August 1998

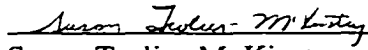We approve the thesis of Jon-Paul Maria:

Date of Signature

Susan Trolier-McKinstry
Associate Professor of Ceramic Science and Engineering
Thesis Advisor

July 6, 1998

Darrell G. Schlom
Associate Professor of Materials Science and Engineering

July 15, 1998

Clive A. Randall
Associate Professor of Materials Science and Engineering

July 1 1998

L. Eric Cross
Evan Pugh Professor of Electrical Engineering

June 18 1998

Xiaoxing Xi
Assistant Professor of Physics

July 16, 1998

John R. Hellmann
Associate Professor of Ceramic Science and Engineering
Ceramic Science Program Chairman

20 July 1998

Abstract

Pulsed laser deposition was used to deposit oxide ferroelectric heterostructures on (001) oriented $LaAlO_3$ and $SrTiO_3$ single crystal substrates. $SrRuO_3$ was used as the bottom electrode, while the ferroelectric layer was either $(Pb,La)(Mn,Ti)O_3$ (PLMT) or $Pb(Mg_{1/3}Nb_{2/3})O_3$-$PbTiO_3$ (70/30) (PMN-PT). The latter compound was the focus of this thesis given the recent discovery of anomalously large piezoelectric coefficients in single crystals of this material.

It was found that the structural, electrical, and morphological characteristics of the $SrRuO_3$ electrodes were sensitive to bombardment during growth. In general, growth conditions providing strong energetic bombardment resulted in material with lattice constants extended by as much as 4% in the out-of-plane direction. In-plane lattice parameters were enlarged to a lesser extent. Accompanying the extended lattice constants was an increased electrical resistivity and a coarsened surface microstructure.

When $SrRuO_3$ films were deposited on vicinal $SrTiO_3$ substrates, the $SrRuO_3$ *b*–axis was found to lie in the plane of the substrate with a strongly preferred orientation. To determine the mechanism behind the orthorhombic twinning, $SrRuO_3$ thin film and powder samples were analyzed using high temperature x-ray diffraction. These measurements revealed structural phase transitions at ~ 300 °C and ~ 600 °C to 700 °C corresponding to what is believed to be orthorhombic to tetragonal and tetragonal to cubic symmetry changes. Since $SrRuO_3$ is nearly cubic at growth temperatures, the preferred orthorhombic twinning cannot be dominated by a growth mechanism, as has been previously suggested. It is proposed that the preferred twinning results from anisotropic epitaxial strains arising from the substrate surface steps.

A process for depositing Pb-based perovskite films from Pb-enriched targets was developed which relies upon adsorption-controlled growth. Both La and Mn doped PbTiO$_3$ and PMN-PT were synthesized. It was found that growth conditions could be optimized using a combination of structural and electrical property analysis techniques.

The results of the PMN-PT processing study were largely analogous to those of ceramic and single-crystal investigations, i.e., great difficulty was encountered achieving phase-pure material with good electrical properties. In general, when depositing from lead-rich targets, perovskite, Pb-rich, and Pb-deficient material could be simultaneously observed in a single sample. Electrical analysis of the films revealed that the best electrical properties occurred for samples containing small amounts of second phases. either Pb-rich or deficient. For these samples, ferroelectric transitions were often shifted to lower temperature values; this activity was attributed to modification of the crystallinity via processing conditions. 2% Ba-doping was introduced into the original PMN-PT composition to improve the stability of the perovskite phase. With this small addition, the effect on phase assembly was not pronounced (i.e., pyrochlore was still difficult to avoid), however, modest improvements were seen in the electrical properties, most notably in the reduction of dielectric loss. Typically, when depositing from Pb-rich targets, the best electrical properties occurred in samples deposited at temperatures above 670 °C. The very best samples exhibited bulk transition temperatures, room temperature dielectric constants greater than 1500, remanent polarizations of 20 μC/cm^2, and x-ray line widths of 0.4°, 0.5°, and 0.8° for the 2θ, ω, and ϕ-x-ray circles respectively.

Deposition of epitaxial films was also possible from targets containing very small quantities of PbO (e.g., 3%) at temperatures below 600 °C. Under these conditions

v

phase–pure samples with high electrical resistivities could be achieved. The success of

this method was attributed to the epitaxial nucleation and stabilization of the well-lattice

matched perovskite phase. For samples deposited at these temperatures, energetic

bombardment was required to optimize the structural and electrical properties, however,

when subjected to heavy bombardment, the same lattice constant extension observed for

$SrRuO_3$ was encountered.

In-situ field dependent x-ray diffraction and the wafer-flexure method were used

to determine the longitudinal (d_{33}) and the transverse (d_{31}) piezoelectric coefficients of the

PMN-PT respectively. Values of 350 pC/N (d_{33}) and -180 pC/N (d_{31}) were determined.

From the field-dependent x-ray analysis (which enabled direct measurement of lattice

strain) no clear evidence of a field-induced phase transition was observed.

Poling and aging studies were performed on several PMN-PT thin films. In

general, all samples displayed piezoelectric properties which were characteristic of the

presence of an internal bias. For samples deposited at temperatures > 670 °C, a

polarization bias existed which resulted in a 60 % difference between the preferred and

the opposite polarization states. For samples deposited below 600 °C (under heavy

bombardment), the polarization bias was strong enough such that in the absence of an

applied electrical field, both remanent polarization states carried the same sign. When

measured in the direction of the polarization bias, the samples exhibited negligibly small

aging rates. The presence of an internal polarization bias in these samples was associated

with energetic bombardment during deposition.

Table of contents

List of figures

List of tables

Acknowledgements

In their lives, most people would consider themselves fortunate to have one person to regard as a mentor. After 8 years at Penn State (four of which were spent at the Materials Research Laboratory), I find myself having benefited from three individuals who fit this description. The foremost of whom has been my advisor, Dr. Susan Trolier-McKinstry, the others being Dr. Darrell G. Schlom, and Dr. Clive A. Randall. The education, motivation, and support which I have received from these three people can be regarded as no less than invaluable. I consider myself very lucky to have worked with them, and cannot thank them enough for the challenges and opportunities which were offered to me. As a result of their generosity (in both time and resources), I have acquired experiences available to few in my position. In addition to their professional guidance, they have become close friends, for this as well I am grateful.

My gratitude must also be extended to Brady Gibbons, Joe Shepard, Dave Cann, Atsushi Hitomi, Tom Shrout, and Eagle Park. Working (and playing) with these people has been my pleasure and privilege. Again, I find myself uncommonly lucky to be surrounded by great friends who are also acute technical peers.

It is also important to thank the MRL community. In general, the support staff members, faculty, and graduate students make working here an enjoyable experience.

Finally, and most importantly, I need to acknowledge my parents. They taught me the most important lesson of all, how to apply myself. Whenever I think that I am working hard, I need only consider their efforts to realize that I can do a little more.

Chapter 1 Introduction and Statement of Goals

1.1 Introduction

Microelectromechanical systems (MEMS) represent an area of growing

technology which has the potential to revolutionize many commercial and industrial

products. The ability to replace macroscopic mechanical devices with those constructed

from micro-sized components may allow unprecedented technological advances.

Macroscopic mechanical devices have already been replaced in ink-jet printers and air

bag deployment accelerometers. Furthermore, at present, there is tremendous research

activity concerning miniaturized analytical instrumentation, surgical tools, and micro-

combustion chambers, among others.

The incorporation of smart materials such as ferroelectrics into MEMS designs is

an attractive means of enhancing the device sensing or actuating functions.[1] While the

previous ten years have seen ferroelectric thin film technology develop to the degree

where commercial applications of ferroelectric memories are at hand, research

concerning the viability of piezoelectric thin films is much less mature.

Unfortunately, the recent research into ferroelectric thin films for piezoelectric

applications has indicated that the piezoelectric properties available to $Pb(Zr,Ti)O_3$-based

(PZT) ceramics are not (at least currently) realized in thin film form. It is the opinion of

several research groups that the cause of this observation is the inability to move non-180° domain walls in ferroelectric thin films, so that the extrinsic contributions to the piezoelectric properties cannot be realized.[2,3]

To justify the added expense and difficulty of integrating oxide materials into Si-based MEMS, significant advantages must be provided. Given the property limitations of PZT thin films, their utilization in MEMS may be hindered. A possible solution to this problem would be the use of an alternate material, specifically, one which does not require extensive domain wall motion for the development of a large piezoelectric effect.

Recently single crystals of several solid solutions between lead-based relaxor ferroelectrics and lead-titanate have been investigated. Specifically, compositions belonging to the systems $Pb(Mg_{1/3}Nb_{2/3})O_3$-$PbTiO_3$ and $Pb(Zn_{1/3}Nb_{2/3})O_3$-$PbTiO_3$, which have rhombohedral symmetry and are ferroelectric at room temperature have been investigated. When these samples were measured along the <001> directions, anomalously large piezoelectric coefficients in excess of 2500 pC/N, and ultra-large field-induced strains as high as 1.7% were recorded.[4] Beyond the magnitude of these values, these materials are interesting in that the domain states in [001]-poled samples are degenerate with respect to fields or strains applied along those directions. As a result, domain wall motion does not appear to be required for the generation of large strains. Support for this supposition is given by the low hysteresis observed for strains as large as 0.6 %.

Given the absence of extensive domain wall motion, there is a possibility that similar results can be achieved in thin films, providing that suitably oriented material can

be synthesized. If so, these materials could serve as a potential replacement for PZT films in MEMS.

Unfortunately, as has been observed in multiple processing studies, the phases in which these anomalous properties have been observed are relatively unstable, especially in the temperature range which is common for thin film deposition.[5] Strategies such as the columbite method have been developed to facilitate phase formation in powders, however, these may not be appropriate for thin film growth techniques. In the worst cases, the materials can only be processed as single crystals, where highly oxidizing and lead-rich atmospheres could be maintained.[6] A similar single crystal growth strategy may provide the best opportunity for successful thin film synthesis, since the conditions of bulk crystal growth, i.e., an oxidizing atmosphere and the presence of a Pb-rich flux may be available, at least in a transient manner.

1.2   Statement of goals

The goals of this work can be divided into the following categories:

1   Completion of previous investigations concerning $SrRuO_3$ thin films for perovskite template electrodes. Specifically, attempts will be made to determine the mechanisms behind the extended lattice constants observed in physical vapor deposition (PVD) deposited samples. Determination of the mechanisms behind extended lattice constants is important as similar effects are observed in many epitaxial perovskite films, and appear to have pronounced consequences on the electrical properties.

In addition, temperature dependent structural analysis will be attempted to determine the thermal expansion coefficients as well as the existence of high temperature structural phase transitions. This information is important in understanding $SrRuO_3$ growth mechanisms, as well as the in-plane twinning behavior of the orthorhombic unit cell, and the degree of lattice mismatch at growth temperatures with the ferroelectric film.

2   The development of an effective and reliable methodology for deposition of epitaxial Pb-based perovskites using pulsed laser deposition. In particular, the interaction between growth temperature and the required amount of excess lead in the target will be investigated.

3   The determination of the deposition conditions for synthesis of high crystalline quality relaxor-$PbTiO_3$ epitaxial thin films. Specific attention will be directed towards relationships between processing parameters, excess-lead, and the final phase assemblage. In addition, comparisons will be made to similar processing studies on single crystals and ceramics of the same composition. Following the structure analysis, the process will be optimized with respect to the pertinent electrical properties, and the resulting properties compared to measurements of bulk single crystals.

4   The piezoelectric response will be measured for the (001)-oriented epitaxial thin films to determine if the ultra-large piezoelectric response of bulk single crystals can be duplicated in epitaxial thin films. If not, the mechanisms responsible for degradation of the response will be probed. Drawing relationships between the crystal structure and the microstructure and the piezoelectric properties may provide insight into the mechanisms of ultra-large piezoelectric strains.

5   Finally, the high-field strain will be measured using four-circle x-ray

diffraction in a bulk single crystal of $Pb(Zn_{1/3}Nb_{2/3}) - 4.5\%$ $PbTiO_3$. The crystallographic

changes which occur under an electric field will be the focus of this investigation. Using

x-ray diffraction, characteristics of the crystal including symmetry and crystalline

perfection can be probed, and may provide a better understanding of ultra-large strain

generation in relaxor-PT single crystals.

Chapter 2   Literature Review

2.1   Ferroelectric materials

Ferroelectric materials may be defined as those, which under equilibrium

conditions, exhibit a stable and spontaneous dielectric polarization whose orientation may

be changed from one specifically defined crystallographic orientation to a second by the

application of an electric field.[7] In addition, normal ferroelectric materials exhibit a

maximum in the temperature dependence of the dielectric constant, below which the

ferroelectric phase occurs and above which the paraelectric phase is stable: this maxima

corresponds to the material's Curie temperature. Above the Curie temperature, the

dielectric constant, K, obeys the Curie-Weiss law:

$$K = \left(\frac{C}{T - T_0} \right) \tag{1}$$

where C is the Curie constant, which is typically on the order of 10^5 K, and T_0 is the

Curie-Weiss temperature.[7] In an ideal first order ferroelectric, $T_c > T_0$, while in a second

order ferroelectric $T_c = T_0$.

Evidence of the reorientable polarization can be observed in a trace of the

dielectric polarization plotted as a function of applied electric field. The stability of the

polarization along preferred crystallographic orientations and its resistance to

reorientation results in the hysteresis observed in a polarization/field trace. Fig. 2.1 gives

a schematic of the field dependence of the polarization typical of a ferroelectric crystal.[8]
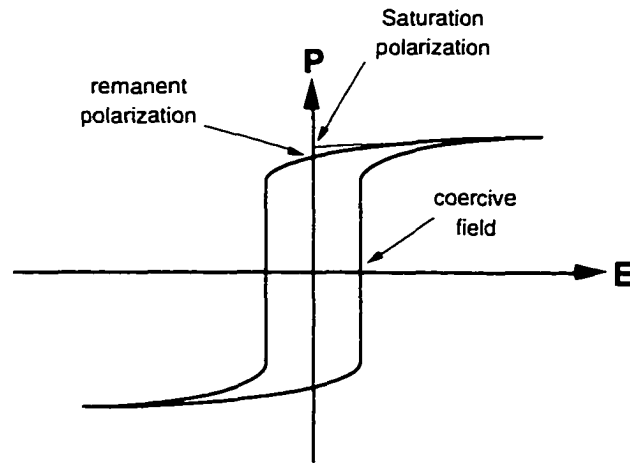
FIG. 2.1: SCHEMATIC OF POLARIZATION HYSTERESIS FOR A FERROELECTRIC

The saturation polarization (an extrapolated value from the high-field linear

portion) refers to the total polarization attributable to ferroelectric switching, the

remanent polarization, P_r, refers to the amount of polarization remaining after the

removal of the applied electric field, and the coercive field, E_c, refers to the field value

required to reverse the direction of the polarization.[8]

Microscopically, a typical ferroelectric is comprised of domains, which are

regions in the crystal where all polarization vectors are aligned along the same

crystallographic direction. These domains occur in both polycrystalline and single crystal

samples, though single domain states can be achieved in carefully prepared single

crystals. The domains typically form complicated arrangements in both large single

crystals and small ceramic grains.

Since the polarization vector is stable along more than one crystallographic direction, on cooling through the transition temperature, differently oriented domains form in each crystallite in an attempt to minimize the free energy. By application of large d.c. electric fields, the polarization vector with the largest component in the direction of the applied field will be favored, and regions of the crystal with polarization vectors lying in other directions will switch to better align with the poling field.[9] As a result of this poling operation, the $\infty\infty$ m symmetry of the random polycrystal will be changed to ∞ m, where m lies along the poling axis.[10] In a ceramic body, the theoretical limit of poling is determined by the number of allowed polarization vector orientations, and the statistical distribution of the crystallographic axes of the grains with respect to the applied electric field. Practically, poling is further limited by the residual strains which occur as a result of switching the polar vector direction. In ferroelectric perovskites, the axis along which the polar vector lies is typically longer than its non-polar equivalents, thus changing the polar orientation will result in intergranular strains. This strain effect is also largely responsible for the remanent polarization being smaller than the saturation value in ceramics; crystalline defects contribute to this effect as well. In an ideal single crystal sample, the hysteresis loop would have a rectangular central region with $P_r = P_s$.[9]

The polar vectors lie along crystallographic directions which are determined by the specific crystal structure. Table 2.1 lists several structures common to ferroelectric perovskites and their allowed polar axes.

TABLE 2.1: POLAR AXES IN SEVERAL DISTORTED PEROVSKITE SYMMETRIES

Crystal structure	Polar axes (possible orientations) (directions given in terms of the cubic prototype structure)
Tetragonal	<001> (6)
Orthorhombic	<110> (12)
Rhombohedral	<111> (8)
Morphotropic [Tetragonal and Rhombohedral]	<001> (6) & <111> (8)

2.1.1 Piezoelectricity

Materials which experience a linear dimensional change with an applied electric field are known as piezoelectrics. In the direct piezoelecric effect, the linear relationship between polarization and applied mechanical stress is given by:

$$P_i = d_{ijk}\sigma_{jk} \qquad (2)$$

where P_i is the induced polarization, d_{ijk} is the direct piezoelectric coefficient, and σ_{ij} is the applied mechanical stress. The converse effect may also be considered where the linear relationship between mechanical strain and electric field is given by:

$$\varepsilon_{jk} = d_{ijk}E_i \qquad (3)$$

where ε_{jk} is the field-induced strain, d_{ijk} is the piezoelectric coefficient, and E_i is the applied electric field. In both cases, the piezoelectric coefficients d_{ijk} are numerically identical and expressed in the units C/N and m/V for the direct and converse relationships respectively.[9] In these equations, tensor format is used to describe the coefficients, however, the reduced subscript matrix format is commonly used for the piezoelectric coefficient (i.e., they are expressed as d_{ij} where i=1,2,3 and j=1,...6).

The piezoelectric effect can occur in crystals which do not possess a center of symmetry; of the 32 crystal classes, 21 satisfy this condition. 10 of these non-

centrosymmetric crystal classes are not polar, however they possess a crystallographic direction whose respective ends are not related by a symmetry element. Thus, upon application of an electric field or applied stress, a polarization (thus piezoelectricity) can develop. An example of such a material is quartz (point group 32). Crystal class 432 is the exception to this classification: though non-centric, it possesses symmetry elements which cancel the piezoelectric effect.

The remaining 10 non-centric crystal classes are characterized by a polar structure. A polar structure is one where the positive and negative centers of charge are not coincident in the unit cell. As a result, a permanent electrical moment exists, and a stress applied in this direction of that moment will change its magnitude. This permanent polarization is also temperature dependent, which is the origin of the pyroelectric effect. ZnO (point group 6mm) is an example of such a material which contains a unique polar direction along the hexagonal axis ([001]).

Certain crystal structures which belong to the 10 polar point groups exhibit ferroelectricity. An important characteristic of a ferroelectric structure is that it contains a polar axis which can be switched between several well defined crystallographic directions by the application of an applied electric field. A consequence of this capability is that the polar axes of a polycrystalline ferroelectric ceramic can be aligned by a strong electric field. Strong piezoelectric properties however, are only observed in ferroelectric samples which have been poled. In the zero-field cooled state, ferroelectric ceramics have a random polar axis orientation, the macroscopic symmetry of which ($\infty\infty$m) is not polar. Ferroelectric ceramics are particularly useful as piezoelectrics because it is possible to achieve a "net" polar axis in any direction through the poling operation.

2.1.2 Intrinsic and extrinsic contributions to piezoelectricity

The intrinsic component to piezoelectricity is present in all piezoelectric crystals. Intrinsic refers to the response which would be observed in a single-domain single crystal, i.e, in a single domain $BaTiO_3$ or a single crystal or the appropriate average for a polycrystalline ensemble. In each case, the unit cell will elongate (or contract) along the [00ℓ] measurement direction when the field is applied along (or opposite to) the polar orientation. For ferroelectric materials, this intrinsic response can be predicted by the phenomenological treatment developed by Devonshire which is given by:

$$d_{ijk} = 2Q_{ijkl}\varepsilon_o\varepsilon_{kl}P_l \tag{4}$$

where Q_{ij} is the electrostrictive coefficient, ε_o is the permittivity of free space, ε_{ij} is the relative permittivity, and P_l is the polarization. This model has been shown to be in good agreement with experimental findings.[11] In materials such as ZnO or quartz, the entire piezoelectric response is a result of intrinsic contributions.

The extrinsic contribution to the piezoelectric properties of a ferroelectric material is due to motion of domain walls and defect contributions. This motion may be either reversible or irreversible, with respect to applied electric fields or strains. Upon switching a 180° domain, the resulting wall motion will give rise to a small extrinsic contribution. The boundary created by a 180° domain wall will provide a clamping effect in the adjacent material since applied electric fields along the polar axes will initially result in strains which are of opposite sign. As larger fields are applied, the 180° wall moves across the material as the polar vector favored by the applied electric field is stabilized. The subsequent release of this 180° domain wall clamping will result in additional strain added via an extrinsic process.

For non-180° domains, which are both ferroelectric and ferroelastic, a switch in

the polar vector orientation will be accompanied by a more substantial change in the

resultant state of the spontaneous strain. The subsequent non-180° domain wall motion is

the primary source of the extrinsic piezoelectric response. The simplest demonstration of

this concept is illustrated in Fig. 2.2, a 90° domain wall in a tetragonal crystal. In the

portion of this unclamped crystal where the polar axis is exactly perpendicular to the

applied electric field, the strain produced by a 90° switch would be equivalent to the

spontaneous strain of the structure. This "switching" process typically occurs via growth

of the favorably oriented domain, thus may be visualized as motion of the domain wall

which separates the regions of crystal with perpendicularly oriented polar axes. The

strains resulting from non-180° domain wall motion contribute appreciably to the

piezoelectric strain.
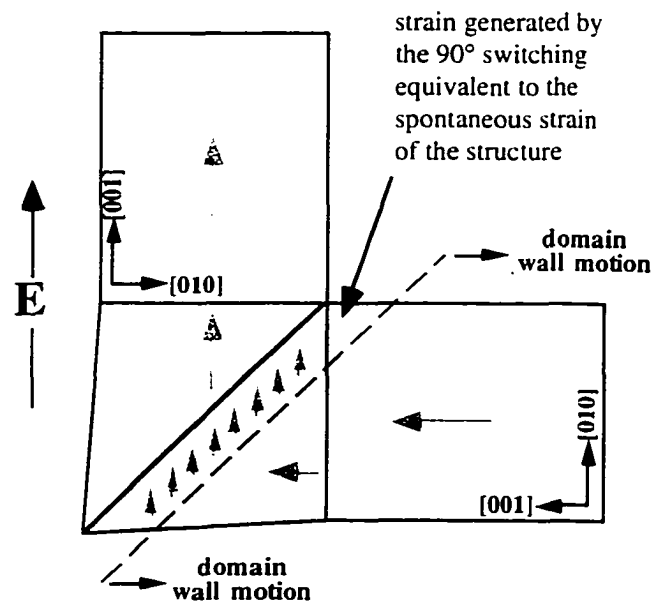
FIG. 2.2: SCHEMATIC OF 90° DOMAIN WALL MOTION IN A TETRAGONAL CRYSTAL

Since domain wall motion and defect reorientations are thermally activated, it is

possible to freeze out the extrinsic component of the polarization and dielectric response

at low enough temperatures. Thus, through measurements of the temperature dependence

of the permittivity and the longitudinal and transverse piezoelectric coefficient, Zhang *et*

al. determined the relative contributions of both the intrinsic and extrinsic components to

the piezoelectric response in several PZT compositions. In soft PZTs near to the

morphotropic phase boundary, the extrinsic contribution to the properties accounts for

> 60% of the room temperature value. [12,13] In general, materials with very large

piezoelectric coefficients depend largely on extrinsic effects. In a similar investigation,

Damjanovic *et al.* discussed the extrinsic contributions to the piezoelectric properties of

ferroelectric ceramics. In general, contributions to the piezoelectric response from

reversible sources accounted for as much as 30 % of the total response in large grained

$BaTiO_3$. Damjanovic also measured fine-grained material, finding a much weaker

extrinsic contribution. This behavior was attributed to the increased resistance to domain

wall motion with decreasing grain size. [14]

It is important to remember that non-180° domain walls are both ferroelectric and

ferroelastic. That is to say that in addition to being switchable by an electric field, these

domains can also be switched by an externally applied stress. [10] This is one source of the

significant stress dependence observed in the piezoelectric properties of many

ferroelectrics. [15,16] It is important to keep this in mind in terms of ferroelectric thin films,

which with very few exceptions, are under the influence of a significant residual stress. [17]

The importance of domain motion and the extrinsic contribution to

piezoelectricity can be further demonstrated by the compositional dependence of the

piezoelectric properties in a solid solution system with a morphotropic phase boundary

(MPB). A morphotropic boundary is a structural phase transition between closely related

symmetry groups as a function of composition. Morphotropic systems typically have end member components with complete solid solubility, and slightly dissimilar structures.[9] Such boundaries are often typified by a modest temperature dependence. PZT, the most well known morphotropic system, has the end members $PbZrO_3$ (PZ), an orthorhombic antiferroelectric, and $PbTiO_3$ (PT), a tetragonal ferroelectric. At the approximate composition 52% PZ, 48% PT, a nearly temperature independent boundary between tetragonal and rhombohedral ferroelectric structures exists, and samples processed at this particular composition show structural characteristics of both symmetries. Most importantly, the polarization vectors of both phases are viable, 8 for the case of rhombohedral symmetry (pointing along <1 1 1>) and 6 for the case of tetragonal symmetry (pointing along [001]). The possibility of 14 polarization directions allows for complicated domain structures with optimal orientational flexibility. With 14 polarization vectors available, greater than 84% of the polarization can, in principle, be oriented with an applied field in a random polycrystalline ceramic.[9] (This ability to be efficiently poled is only possible if the domains are free to reorient). Piezoelectric properties of ceramic specimens achieve a maximum value at this composition. Besides PZT, many other morphotropic systems have been investigated (including non-perovskite structures) with similar results occurring throughout.[7,9]

2.2   Relaxor ferroelectrics

In the late 1950's, Soviet researchers produced the initial reports concerning a

new class of complex perovskite ceramics which shared the generalized chemical

formula:

$$\left[(A_I^{2+})\right]\left[(B_I^{5+})_{\frac{2}{3}},(B_{II}^{2+})_{\frac{1}{3}}\right]O_3 \tag{5}$$
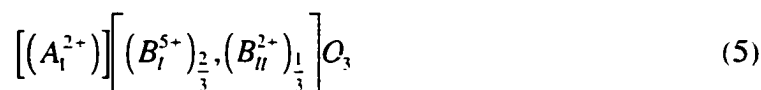
The initially-discovered compositions were $Pb(Ni_{1/3}Nb_{2/3})O_3$ (PNN) and

$Pb(Mg_{1/3}Nb_{2/3})O_3$ (PMN).[18]   Soon thereafter, many related perovskite compositions were

synthesized, which can be represented by the generalized formula:[19]

$$\left(A_1, A_2, \ldots A_k\right)\left(B_1, B_2, \ldots B_k\right)O_3$$

where

$$\left.\begin{array}{l} \displaystyle\sum_{i=1}^{k} X_{A_i} = 1, \\[2mm] \displaystyle\sum_{i=1}^{k} X_{A_i} n_{A_i} = n_A, \\[2mm] 0 \le X_{A_i} \le 1, \\[2mm] n_{A_i} = 1,2,3 \end{array}\right\} \tag{6}$$

and

$$\left.\begin{array}{l} \displaystyle\sum_{i=1}^{k} X_{B_i} = 1, \\[2mm] \displaystyle\sum_{i=1}^{k} X_{B_i} n_{B_i} = n_B, \\[2mm] 0 \le X_{B_i} \le 1, \\[2mm] n_{B_i} = 1,2,3,4,5,6 \end{array}\right\}$$

X_{A_i} and X_{Bi} are the fractions of positive ions in the elementary cell, and n_{A_i} and n_{B_i}

are the respective valencies. Such compounds are referred to as either mixed A-site or

mixed B-site unless multiple cations are on both the A and B sites, in which case the material is most often referred to as a solid solution between end members. Relaxor behavior has also been observed in materials other than perovskites, including the closely related tungsten-bronze structure, specifically in the $Ba(Nb,Ta)_2O_6$-$Sr(Nb,Ta)_2O_6$ solid solution.[20]

The most distinctive feature common to the ferroelectric compositions in this family is the pronounced frequency dependence of the dielectric constant below the Curie temperature. The specific characteristics which define relaxor behavior are as follows:[21]

(i) Anomalously large room temperature dielectric constants with a broad maximum in the permittivity at the ferroelectric transition.

(ii) A strong frequency dependence to the permittivity where the maximum value of the real component occurs at the minimum measurement frequency, and the maximum imaginary component occurs at the maximum measurement frequency.

(iii) The dielectric constant does not follow Curie-Weiss behavior above the ferroelectric transition.

(iv) No evidence of a non-centrosymmetric symmetry to long-wavelength structural probes for temperatures below the maximum in the permittivity and zero applied field. Subtle structural changes indicative of a polar structure do exist, such as the anomalous thermal expansion temperature dependence.

Fig. 2.3 gives the temperature dependence of the dielectric constant and dielectric loss for a PMN ceramic. The frequency dependence is also given between 0.4 and 4500 kHz.
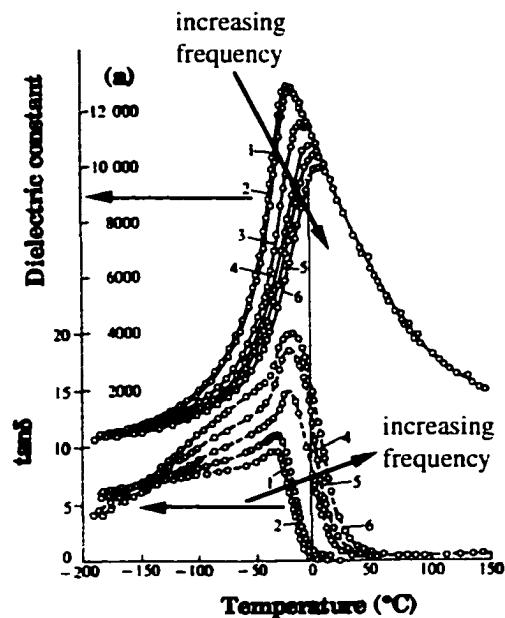
FIG. 2.3: SCHEMATIC OF THE TEMPERATURE DEPENDENCE OF THE PERMITTIVITY AND DIELECTRIC LOSS OF CERAMIC PMN, AFTER KIM *ET AL.*[22]

Many models have been proposed to explain relaxor ferroelectrics, including those based on compositional inhomogeneities, superparaelectricity, spin-glass-like behavior, and a breathing mode model.[23-26] There is still considerable controversy as to which of these ideas, if any, provides a full description of relaxor behavior. The compositional inhomogeneity model will be discussed as it provides the most intuitive description of relaxor-type behavior.

The compositional inhomogeneity model, originally proposed by Smolenskii, suggests that relaxor behavior is a consequence of disorder in the cation site occupancy. According to this model, as a result of the cation disorder, if the composition were traced across the crystal, on a nanometer scale fluctuations in the Mg:Nb ratio would be observed. Because of the potentially large fluctuations, it was proposed the Curie temperatures for the local regions could span a large temperature range. As a result, in

the vicinity of the transition temperature, the material may be considered a combination of intimately mixed polar and non-polar regions.[20]

Due to the cooperative nature of ferroelectricity, the transition point to the ferroelectric state will be influenced by the volume of the ferroelectric region. The stability of the ferroelectric phase will be reduced with decreasing volume, and at volumes approaching 1000 nm^3, the energy barrier separating the polar and non-polar structures will be on the order of kT. This concept, coupled with the assumption of nano-scopic polar regions was used to further explain the diffuseness of transition.[21] If the polar regions correspond to these sizes, the transition to a non-polar state would be expected near room temperature, and if a distribution of sizes and stoichiometries existed, a broadened transition would occur. In addition, long wavelength characterization probes (i.e., x-ray diffraction and optical birefringence) will be unable to detect the absence of a center of symmetry in these small volumes.

This reasoning can be used to explain the diffuse nature of the transition, however, it does not account for the frequency dependence of the dielectric constant below T_{max} (the temperature at which the maximum value of the dielectric constant occurs). One approach to introducing a dielectric dispersion relates to the surroundings of the polar microregions. If the adjacent material to the polar region, in the direction of a polarization vector (i.e., <1 1 1>) has a different composition from the material located in the direction of the opposite polarization vector, then the free energy associated with each orientation will be different. The orientation with the lower free energy will have a deeper associated potential well, thus at a given temperature the polarization would be expected to spend more time in that orientation. The dispersive behavior of the low-field

dielectric response may originate from the differences in the residence times of particular

polar orientations.[21]

Viehland *et al.* suggested that this disperse behavior could be modeled using the

Vogel-Fulcher relationship. The frequency dependent behavior of the small signal

dielectric constant was fit to the Vogel-Fulcher equation, and the results were interpreted

to suggest that the polar regions in PMN have an electrical moment which can reorient at

high temperatures, but becomes frozen in near 20 °C.

$$f = f_0 \exp\left(\frac{-E_a}{k(T_{max} - T_f)}\right) \tag{7}$$

The freezing temperature, T_f, corresponds to the T_0 term in the Vogel-Fulcher

equation which was added to the original Boltzman analysis to improve the experimental

fit. E_a is the activation energy for polarization reorientation. f is the measurement

frequency, and f_0 is the Debye frequency. The physical picture of this model is an array

of polar clusters with a random distribution of polar vector orientations (an analogy to the

superparamagnetic behavior of a spin-glass has been suggested). Upon cooldown, the

clusters assume a preferred polar orientation in response to the development of non-

ergodicity arising from weak polar-cluster interactions. Further development of long

range order is hindered by frustrated interactions during the "freezing" process.[24,27]

Two pieces of experimental evidence which strongly corroborate the

compositional inhomogeneity model are the investigations of Stenger *et al.*, Setter *et al.*

and Randall *et al.*[28-31] Working with the system $PbSc_{1/2}Ta_{1/2}O_3$, Setter *et al* and Stenger

et al. demonstrated that when the B-site was randomly occupied, relaxor behavior was observed. However, through annealing, (1:1) ordering of the B-site cation could be induced, and normal ferroelectric behavior resulted. Secondly, Randall *et al.* demonstrated by transmission electron microscopy direct evidence of the polar microregions in PMN and PLZT. It was found that the dimensions were on the predicted order of 50 Å.[32] Efforts to demonstrate the same type of 1:1 ordering in PMN ceramics were not successful (regardless of annealing conditions); this result was attributed for many years to the space-charge model, which suggested that the charge imbalance resulting from this ordering limits the dimension over which 1:1 ordering can occur.[33]

Recent reports by Davies *et al.* indicate that the compositional inhomogeneity model may not accurately describe relaxor behavior. Through annealing of Zr-doped $Pb(Mg_{1/3}Ta_{2/3})O_3$ ceramics, Davies demonstrated that ordering occurred over > 90% of the material without loss of the frequency dispersion in the dielectric constant and loss. The ordering was not the 1:1 B-site arrangement of Mg and Ta as proposed by the Smolenskii model, rather is was proposed to be an ordering where planes of B-site cations alternated between random occupation (with the ratio 2/3 B^{2+} and 1/3 B^{5+}) and solely B_{II}^{5+} occupation. This work presents data which are in strong contrast with the compositional inhomogeneity model. However, a complete structural and electrical evaluation of the samples has not been reported to date, so the importance of factors such as oxygen vacancies is yet unknown. As such, a comprehensive interpretation on the role of cation disorder in reference to relaxor behavior cannot currently be made.[34,35] It should be noted that the type of compositional inhomogeneity proposed by Smolenskii is

not excluded by the recent results of Davies. Given the random arrangement of B-site

cations in 50 % of the crystal, a range of local stoichiometries may still be possible.

These results certainly demonstrate that the compositional inhomogeneity model

does not completely describe all systems exhibiting diffuse and dispersive phase

transitions, and that further investigations are required to understand these phenomena.

2.2.1   Processing of lead-based relaxors

It has been found that in addition to the cation ordering in lead-based relaxors, the

electrical properties depend strongly on the initial processing conditions. In particular,

the second phases which are commonly observed may strongly influence or dominate the

electrical characteristics. The difficulty in processing high quality ceramic relaxor

ceramics certainly slowed the theoretical understanding. This section provides a brief

description of processing strategies for Pb-based relaxors, and a partial explanation for

the low stability of these phases. This section is included as the information is pertinent

to the understanding of phase relations in thin film processing.

The challenge encountered in lead-based relaxor ceramic processing arises

primarily from the appearance of Pb-based pyrochlore phases which can have a relative

stability similar to, or greater than the desired perovskite crystal.[4] Invariably, the

associated pyrochlore has dielectric properties which are deleterious to device

performance - typically, low dielectric constants and large dielectric losses.[9] Though

high quality phase-pure PMN-based relaxors have been processed using traditional

techniques, the methods involve extremely long anneals at high temperatures and do not

exhibit good reproducibility.[6]

Swartz *et al.* developed a method for synthesis of phase-pure PMN using a novel

mixed oxide approach. The technique involves pre-reacting the columbite phase

($MgNb_2O_6$), and subsequently reacting the PbO in an additional step. Insuring that the

Mg and the Nb are homogeneously reacted in the initial step allows the pyrochlore to be

avoided. Nucleating pyrochlore from columbite would require liberation of Nb, which is

known to be kinetically unfavorable.[6] This same strategy was successfully applied to

other systems including $PbNi_{1/3}Nb_{2/3}O_3$ (PNN), $PbFe_{1/3}Nb_{2/3}O_3$, (PFN), $PbMg_{1/3}Ta_{2/3}O_3$

(PMT), and $PbSc_{1/2}Ta_{1/2}O_3$ (PST), while pyrochlore still occurred in $PbZn_{1/3}Nb_{2/3}O_3$

(PZN), $PbZn_{1/3}Ta_{2/3}O_3$ (PZnT), and $PbCd_{1/3}Nb_{2/3}O_3$ (PCN). The result indicates that the

pyrochlore formation was not due to reaction kinetics (as in PMN), but rather

thermodynamic instabilities which could not be kinetically overcome.[5,6]

The tolerance factor developed by Goldschmidt can be used to understand why

Pb-based relaxors are so difficult to process. The tolerance factor is a crystal chemical

relationship which predicts a favorable crystal structure for a formula unit using the ionic

radii under the assumption that ions act as hard spheres. The tolerance factor for the

mathematically ideal perovskite is unity, and is calculated as follows [8]

$$t = \frac{r_A + r_O}{\sqrt{2}(r_B + r_O)} \tag{8}$$

where r_A, r_B, and r_O are the respective ABO_3- ionic radii. Goldschmidt determined that

the perovskite structure was favorable when $0.88 \leq t \leq 1.09$. Using the ionic radii

proposed by Shannon and Prewitt, calculations of the tolerance factors for several mixed

B-site-cation leaded perovskites were calculated and found to be on the low side of this

stability window.[36] In addition to this purely geometric instability, the electronic

structure of Pb is such that bonding with a strong covalent character is preferred. It is suspected that the covalent character of the Pb-O bond results in a tendency towards anion-deficient, covalently-bonded structures such as fluorite and pyrochlore.[36] As a result, a second correlation between crystal chemistry and phase stability can be made, specifically to the electronegativity difference between cations. Halliyal *et al.* observed that larger average electronegativity differences between the ions led to more stable perovskites, presumably due to an increased ionicity of the bonding.[5] Fig. 2.4 shows the average electronegativity difference of the cation/anion bonds in several perovskites plotted against the tolerance factor "t". It becomes apparent from this plot that stabilization of the perovskite structure can be promoted by selecting a composition which provides the appropriate ionic size ratios and electronegativity differences. This plot also provides a partial explanation for the success or failure of the columbite method for a specific composition. Those which could not be processed using the columbite method are in general characterized by a smaller electronegativity difference and a low tolerance factor.
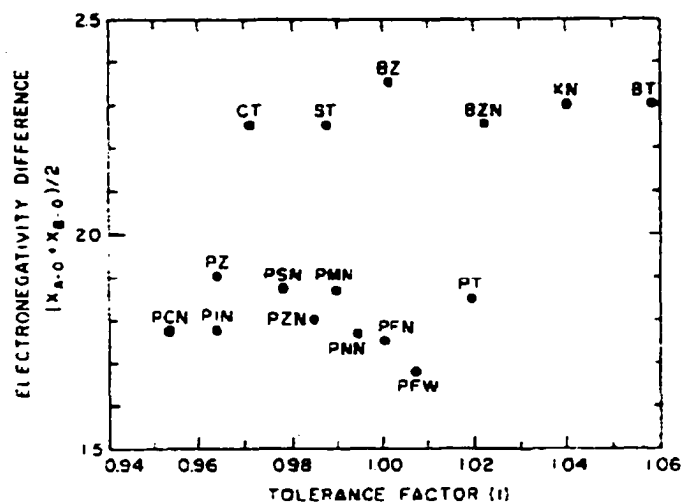
FIG. 2.4: AVERAGE ELECTRONEGATIVITY DIFFERENCE BETWEEN CATIONS AND OXYGEN PLOTTED AGAINST GOLDSCHMIDT'S TOLERANCE FACTOR[5]

With these concepts in mind it becomes clear why additions of $BaTiO_3$ or $SrTiO_3$ to PbO-based perovskites provide perovskite stabilization. $BaTiO_3$ is the most ionically bonded perovskite with a tolerance factor of approximately 1.06, thus its solid solution with less stable perovskites like PZN and PMN effectively pulls them into the region of greater stability shown in Fig. 2.4. Halliyal et al. and Belsick et al. determined that 6 to 7% of $BaTiO_3$ or 9 to 10% of $SrTiO_3$ respectively would completely stabilize perovskite PZN.[5,37] Similar results have been demonstrated by other researchers in the PMN system, however, less emphasis has been placed there, given the success of the columbite method in producing phase-pure perovskite PMN.[38]

Though these results were determined for ceramic systems produced by traditional oxide precursor powder processing, the trends are based both on thermodynamics and reaction kinetics. Thus, they are expected to provide important insight into thin film growth strategies.

2.2.2 Relaxor single-crystals

Single crystal samples of PMN and PNN were first synthesized by Bokov *et al.* in 1961 for optical and electrical investigations.[39] Their findings confirmed that to both x-ray diffraction and optical birefringence analysis, these materials exhibited cubic symmetry. Only when strong fields were applied did the material show a detectable birefringence at room temperature, which suggested that a globally polar state could be field-induced. In addition to the structural and optical investigations, maximum dielectric constants as large as 20,000 were observed; this value was nearly two times larger than previously reported for ceramic compositions.[39]

Little additional work concerning single crystals of these phases was reported until several publications from Japanese groups emerged concerning solid solutions of relaxors and $PbTiO_3$ (PT). Following the research on PZT ceramics, other morphotropic systems were investigated in hopes of finding materials with properties similar to, or better than, those observed for morphotropic PZT compositions. Ouchi *et al.* reported that a morphotropic phase boundary existed in the system PMN-PT at 35% PT, while Nomura *et al.* reported a morphotropic boundary in the PZN-PT system at approximately 9% PT. [40,41] One important difference between these systems and PZT was the ability to grow large single crystals (to date no researchers have demonstrated bulk PZT single crystal growth on a practical scale; the best examples of PZT "single crystals" have been grown in thin film form using metallorganic chemical vapor deposition by Foster *et al.* [42]).

Nomura *et al.* reported that single crystals of PZN and its solid solution with

PbTiO$_3$ could be grown easily by the flux method in 1969, and in 1981, Kuwata *et al.*

reported on the electrical and piezoelectric properties of these single crystals near the

morphotropic composition of 91% PZN-9% PT.[41,43] Because the compositions near the

morphotropic phase boundary undergo transitions from rhombohedral to tetragonal to

cubic symmetry with increasing temperature, samples oriented along the polar axes of

both phases (i.e., <111> for rhombohedral and [001] for tetragonal) were fabricated and

measured. Unusually large piezoelectric coefficients were observed when the

measurements were made along the <100> directions at room temperature. For the 0.91

PZN - 0.09 PT samples, a $d_{33[100]}$ of 1500 pC/N was found in comparison to a $d_{33[111]}$ of

600 pC/N. These large coefficients were in part attributed to contributions to the

piezoelectric response along <001> directions from shear and transverse piezoelectric

coupling modes.[43]

Shrout *et al.* demonstrated the same growth capabilities for the PMN-PT system,

again using a PbO-based flux. Dielectric and piezoelectric property measurements

revealed the same trends observed in morphotropic PZN-PT: the largest dielectric

constants and piezoelectric coefficients occurred for measurements along the <001>

directions.[44]

In 1997, Park *et al.* reported on the piezoelectric properties of both PZN-PT and

PMN-PT single crystals, with high-field strain and piezoelectric coefficient

measurements. For samples on the rhombohedral side of the morphotropic boundary,

driven along the [001] direction, ultra-large field-induced strains approaching 1.7% were

recorded. The optimal composition for high strain behavior in the PZN-PT system was

determined to contain ~8% PT (i.e., just on the rhombohedral side of the MPB). Most of the work was devoted to the PZN-PT system since the lower concentration of $PbTiO_3$ at the morphotropic composition provided for more homogeneous crystal growth. Fig. 2.5 shows a set of strain-field curves for the optimal crystal composition.[4,45]
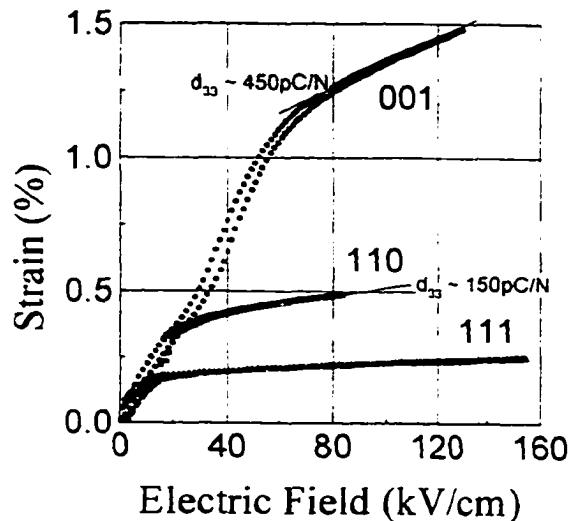
FIG. 2.5: STRAIN FIELD CURVES FOR A PZN-PT (92/8) SINGLE CRYSTAL MEASURED ALONG SEVERAL CRYSTALLOGRAPHIC ORIENTATIONS. THE INITIAL LOW-FIELD D_{33} COEFFICIENT WAS DETERMINED TO BE >2500 PC/N FOR THE (001)-ORIENTATION.[46]

In the strain-field trace for the 001 measurement direction, a discontinuity in the slope between ~ 35 kV/cm and 60 kV/cm is present. It has been proposed that this change in slope corresponds to a structural transition from the zero-field rhombohedral state, to a high-field tetragonal symmetry. A rotation of the polar axes from <1 1 1>-type directions is suggested, and this rotation is believed to be coupled with the anomalously large strains. Fig. 2.6 illustrates this proposed behavior.

• Field applied along [001]
Rotation of polar axes occurs

• Rhombohedral crystal
poled along [001], no
bias applied

(a)

(b)

• Tetragonal
symmetry at large fields
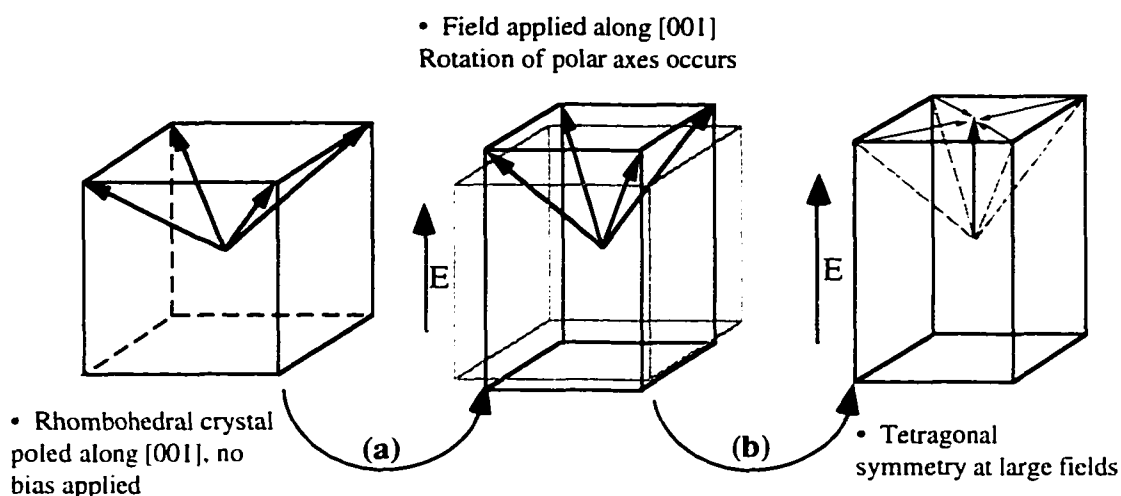
FIG. 2.6: SCHEMATIC OF PROPOSED FIELD-INDUCED PHASE TRANSITION IN (001)-ORIENTED RELAXOR-PT SINGLE CRYSTALS. (A) REPRESENTS INITIAL TRANSITION WITH APPLIED FIELD TO MONOCLINIC SYMMETRY. (B) CORRESPONDS TO SECOND TRANSITION TO TETRAGONAL SYMMETRY WHERE POLARIZATION VECTORS ROTATE INTO A [001] DIRECTION[4]

It is of technological importance that compared to other high-strain piezoelectrics, only modest amounts of mechanical hysteresis are observed. This reduced hysteresis is especially pronounced during lower-field driving conditions (i.e., at strains ≤ 0.5 % where unipolar cycling is effectively hysteresis-free[47]). Other high-strain piezoelectrics (i.e., soft PZTs) show a much higher hysteresis as well as lower mechanical quality factors (Q_m) and coupling coefficients (k_{ij}).[9] The high strains in soft PZTs are due in part to non-180° domain wall motion, which gives rise to the low mechanical quality factor. Q_m can be increased, however, always at the expense of reduced strain (i.e., hard PZT compositions). Since the relaxor-PT crystals are (001)-oriented, there is no driving force for domain wall motion (all domain states in a (001)-poled crystal are energetically degenerate with respect to the applied field). Thus, to explain these large strains and low mechanical loss values, some alternate type of domain wall activity may be occurring

(possible suggestions include mixed phases and growth or shrinkage of (001) domain wall widths).[47]

Additional measurements were made on (101) oriented crystals to determine if a second "engineered" domain state could be achieved. A similar result was observed in the high field strain curve (see Fig. 2.6), where a pronounced discontinuity indicative of a phase transition occurred. In this case, the structure was proposed to transform into orthorhombic symmetry, i.e., the polar axis was field-forced into a <101> direction.[46]

Regardless of the specific mechanism, the result is a class of materials with unusually large field-induced strains and electromechanical coupling factors (in excess of 90%). The most compelling property of these crystals is the ability to engineer the domain state to the desired crystallographic direction; even though the equilibrium orientation of the polar vector is <111>, the application of large fields along directions corresponding to polar vectors of closely related symmetries (i.e., [001] in tetragonal and [101] in orthorhombic) can apparently field-force a structural transition which is accompanied by unprecedented piezoelectric strains. Since these large strains do not appear to rely on large scale motion of non-180° domain walls, there is a possibility that similar properties can be achieved in thin films, providing that suitably oriented crystals can be grown. If so, these materials would serve as a potential replacement for PZT films in MEMS. This, in turn, would circumvent the limitations on the piezoelectric properties of PZT films due to limited extrinsic contributions to the properties.

2.3   Thin film piezoelectric measurements

Accurate characterization of piezoelectric properties in thin films is a non-trivial

matter given the small values of strain, charge, or voltage which need to be measured. In

addition, the dependence of the piezoelectric properties on both the electrical and

mechanical boundary conditions adds to the difficulty. This section presents a review of

several methods for piezoelectric measurement for both thin film and ceramic samples,

and is included as it will be pertinent for the evaluation and comparison of experimental

results with existing literature reports.

For bulk specimens, the piezoelectric coefficients d_{ij} can be accurately

characterized using the established IEEE resonance methods.[48] d_{33} is most easily

measured using a Berlincourt meter which (through application of a known force)

launches alternating elastic waves through a piezoelectric sample and collects the induced

charge. For accurate measurement, the sample must be in the shape of a fully–electroded

right circular cylinder, exhibiting only longitudinal vibrational modes at the measurement

frequency.[48] The piezoelectric coupling coefficients, which measure the

electromechanical energy conversion efficiency, may be determined from the impedance

spectrum of a plate-shaped sample. Using the frequencies at which the resonance and

antiresonance conditions occur and the sample dimensions, the longitudinal and planar

coupling factors (k_{33} and k_p) can be calculated.[48] With knowledge of the planar coupling

factor and the longitudinal piezoelectric coefficient, the transverse piezoelectric

coefficient, d_{31}, may be determined. Again, these measurements are only appropriate for

samples which are fully electroded thin plates, where the vibrational modes can be

predicted.[48,49]

A second standard method of piezoelectric characterization involves direct strain measurements as a function of applied field. The strains for standard ceramic specimens (~ 500 μm thickness) are typically on the order of 10^{-5} to 10^{-3}, thus sensitive instrumentation is required. To detect these strains two common methods exist: laser interferometry and linearly variable differential transformer (LVDT) measurements. Laser interferometry has the best resolution of all techniques (a single beam a.c. measurement can sense displacements as small as 10^{-5} Å), however, the measurement is non-trivial and the instrumentation is extremely sensitive.[50] LVDTs are significantly less expensive and easier to operate, however, the smallest detectable strains are near 10 nm.[51] The benefit of these methods over the resonance techniques described previously is the ability to perform the measurements at higher field values. Such high field measurements may give more information concerning material performance under actual operating conditions, i.e., large amplitude actuation. In addition, high-field measurements may reveal important information concerning structural transitions which can occur at high electric fields.

Of the above mentioned methods, only interferometry is appropriate for thin film measurements. Resonance techniques cannot be easily applied to thin films due to difficulties in modeling the vibration modes. Since the piezoelectric element is rigidly attached to a substrate, and the substrate is typically many times larger than the piezoelectric element size, a complex combination of longitudinal, transverse, and flexural modes will occur. These modes need to be accurately modeled in order to determine meaningful piezoelectric coefficients.[52] LVDTs do not have the sensitivity to

detect the small strains. (For a 2000 Å thick film, 0.1 % strain would amount to only 2 Å of vertical displacement.)

Laser interferometry has the resolution required to measure the induced piezoelectric displacement of thin films, however, the thin film/substrate geometry presents added difficulty. Since the film is rigidly bonded to the substrate, the top electrode is much smaller than the specimen dimension, and the thin film and substrate mechanical properties are different, piezoelectric actuation will result in wafer bending. As a result, the measured strains inducing by poling and driving the film perpendicular to the film thickness would be a combination of the true piezoelectric strain and the vertical displacement of the film surface from substrate flexure. Any displacement measuring system which relies on measurement of one sample face only will be prone to this type of error. To avoid this situation, a double-beam instrument is required which allows a subtraction of the apparent strain produced by substrate bending.[53] This measurement geometry unfortunately introduces increased expense and difficulties in sample alignment.

For measurement of the transverse piezoelectric mode, thin film structures such as suspended diaphragms or cantilevers are required. The vertical displacements measured on these structures can be used to determine d_{31} provided that the geometry of the structure, as well as the mechanical properties of all components are well known. Double-beam instrumentation is not required for this analysis, however, any uncertainties in the thin film elastic constants or sample dimensions will translate directly into error in the measured coefficient. [54]

Direct measurement techniques where a stress is applied to the material and the piezoelectrically-induced charge is integrated may also be applied to thin film specimens. Depending upon the mode of the stress applied to the material and the measurement orientation, either d_{33} or d_{31} may be determined. Several authors have reported on such measurements, their approaches are summarized below.[Jr., 1998 #237; Lefki, 1994 #230; Surowiak, 1992 #234; Xu, 1998 #164]

Xu *et al.* developed a static technique for direct measurement of the longitudinal piezoelectric coefficient where the thin film sample is sandwiched between two connected pressure cavities. Upon pressurization, a uniaxial stress state is induced. Upon release of the pressure, the induced piezoelectric charge is measured, and from this, the piezoelectric coefficient may be determined.[55] Lefki *et al.* developed a similar static uniaxial loading technique, but instead of gas pressure, a known point load was applied.[56] Finally, Surowiak *et al.* investigated an ac mechanical loading technique similar in principle to the operation of a Berlincourt meter.[57]

For measurement of the transverse coefficient, Shepard *et al.* developed the wafer flexure technique, where a sample (full circular wafer geometry) is flexed by the application of either vacuum or pressure to a single cavity to which the wafer is sealed. By mechanically cycling the cavity pressure, either tensile or compressive biaxial stress states are produced. The charge produced through the piezoelectric effect may again be collected, from which the piezoelectric constants can be calculated.[Jr., 1998 #237]

Direct methods have been demonstrated for both static or ac operation, with the latter providing superior resolution and accuracy. Sources of error in these techniques include incomplete knowledge of the material elastic constants (which may be required

for subsequent stress calculation) and the application of stresses which are not purely uniaxial or biaxial. Additional loading modes will contribute to the integrated charge and result in incorrect (usually inflated) values.[Jr., 1998 #237; Xu, 1998 #164]

It should be noted, in general, that the piezoelectric coefficient reported for a thin film is by nature an effective coefficient only. In the interpretation of such data, the fact that the piezoelectric element is rigidly bonded to a substrate which is many times thicker must be considered. In addition, attention must be given to residual stresses which act upon nearly all thin films. Direct comparison cannot be made to bulk specimens which may be regarded as mechanically "free" elements.

2.4 Microelectromechanical devices

Microelectromechanical systems (MEMS) represent an area of growing technology which appears to have the potential to revolutionize many commercial and industrial products. The ability to replace macroscopic mechanical devices with those constructed from micro-sized components is attractive for miniature instrumentation, surgical devices, and a wide variety of sensors and actuators. The incorporation of smart materials into these designs is very attractive, particularly for ferroelectric materials, which may further enhance the device utility. The following section gives a brief review of MEMS processing technology, some device designs, and some issues concerning integration of ferroelectric layers.

MEMS refer to miniaturized mechanical devices which are manufactured primarily by thin film deposition and etching technologies. Though thin film sensing and actuating devices have been proposed and protoyped for nearly 30 years, the field of

MEMS has been most active since 1987 when researchers first demonstrated thin-film fabricated movable microscopic parts. [58] For MEM devices based upon Si and its compatible materials (i.e., SiO_2, Si_3N_4, TiN, noble metals, phosphosilicate glass, etc.) remarkable capabilities have been developed for the production of micron-sized mechanical structures.[59] The processes used for fabrication may be regarded in two categories, bulk and surface micromachining.[60] Bulk micromachining techniques were developed first, and refer to processes based upon selective etching. Particular strategies take advantage of anisotropic etch rates in single crystals, or built-in etch-stop layers in multicomponent structures. This type of technology has allowed the fabrication of relatively simple structural elements such as membranes, cantilevers, or beams. Surface micromachining is regarded as a newer technology, and relies on the use of a "sacrificial layer" for constructing mechanical components. In general, this technique provides devices with greater design flexibility (more geometries of structures are possible), and feature sizes which are one order of magnitude smaller than those produced by bulk micromachining methods.[60]

A more recent improvement in micromachining technology has been the introduction of processes which allow fabrication of "deep" microstructures (i.e., surface features between 100 and 1000 µm in vertical dimension). The acronym HARM (high aspect ratio micromachining) has been applied to these methods. Since both bulk and surface micromachining depend upon lithographic techniques to pattern film devices, the ability to make high aspect ratio structures often depends upon the ability to work with thick photoresist layers.[60] (Additional techniques including laser machining and deep reactive ion etching can also be used). Lithographic patterning based upon optical

radiation exposure is limited in the allowable photoresist thickness by the penetration

depth of light. If a more energetic radiation is used, i.e., electrons or x-rays, increased

thickness would become available. The LIGA (Lithographie, Galvanoformung,

Abformung) process, which relies on soft x-rays for photoresist exposure, can be used at

thicknesses in excess of 1000 μm. Even though the thickness of the structures may be in

excess of several hundred microns, sub-micron lateral dimensions can be appreciated.[60]

Multiple device designs exist which produce actuation in MEMS; the most

common geometry is the electrostatic comb-drive which is schematically represented in

Fig. 2.7:[61]

t = vertical finger thickness
n = number of fingers
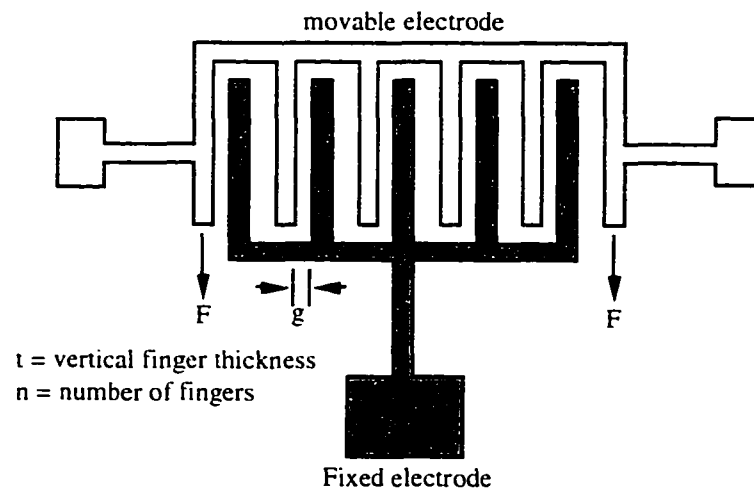
FIG. 2.7: SCHEMATIC OF ELECTROSTATIC COMB DRIVE

This comb drive consists of two sets of interdigitated electrodes elevated above a

cavity, separated by a spacing g. If a bias is applied across the electrodes, an attractive

electrostatic force is generated, the strength of which is given by:[60-62]

$$F = \frac{n\varepsilon_0 tV^2}{g}$$

(9)

Thus a static voltage could be applied for a positioning operation, while an alternating voltage induces an oscillator-type motion. For an 11-fingered comb drive of typical dimensions (t and g ~ 2-5 μm), under a 10 volt bias, a force of approximately 10 nanonewtons is produced.[60,62]

Taking advantage of this electrostatic force, actuators with a series of geometries, including rotary drives and diaphragms can be engineered.[59,63] From this equation, it is appreciated why thicker structures are desired, i.e., the electrostatic force is proportional to the electrode thickness. Additionally, increasing the device thickness does not increase the device footprint, which is the most important space consideration. Features of these types of drives are relatively large displacements (typically several microns) and relative ease of fabrication. Also, the materials required for assembly are chemically compatible with Si substrates and IC (integrated circuit) processing hardware. The most important advantage resulting from the materials compatibility is that full integration with the driving and conditioning electronics is possible (i.e., MEMS and CMOS co-fabrications have been demonstrated in the literature.)[59]

Incorporating a piezoelectric material into a MEM device may improve the utility of the system as the moving component could provide its own actuation or sensing function through either the direct or indirect piezoelectric effect. ZnO, which in bulk single crystals has a piezoelectric coefficient (d_{33}) of approximately 12 pC/N, has been used with some success, but requires a strongly c-axis oriented structure - randomly oriented polycrystalline ZnO is not piezoelectric. Advantages of ZnO include its single cation stoichiometry, which is compatible with many semiconductor processes, and its relatively low processing temperatures.[64] Growing fiber-textured films with the desired

crystallographic orientation has been demonstrated in the absence of an epitaxial template.[65]

In addition to work performed using ZnO components, ferroelectric thin films based upon PZT for similar applications have been studied. PZT ceramics offer piezoelectric coefficients more than one order of magnitude larger than those of ZnO, and the ability to pole them in the direction of interest alleviates the requirement of oriented thin film deposition.[66] Even though many successful demonstrations of high quality PZTs on Si substrates using a combination of SiO_2, Ti, and Pt buffer layers have been reported, the greatest disadvantage associated with PZT based MEMS are the processing incompatibilities with Si.[1,67,68] These intermediate layers have effectively overcome the incompatibility arising from interfacial reactions, however, the processing steps required during crystallization are problematic.[68] PZT films must be crystallized, typically at temperatures between 550 °C and 750 °C on Pt/Si substrates, either during growth or in a post deposition heat treatment. When direct integration with Si-MEMS is attempted, such heat treatments may disturb the underlying CMOS circuitry and possibly the micromachined components.

In general, Si-MEMS technology has made rapid advances in the ability to process complex shapes with high reliability, and has demonstrated elaborate micromachined devices including accelerometers, micromirror mounts, micropositioners, and gyroscopes.[59,69] Though these devices operate, the relatively low energy densities and forces which can be generated using electrostatic actuation could be improved significantly via incorporation of piezoelectric elements. Demonstrations of MEMS utilizing PZT piezoelectric layers have been reported, and include ultrasonic

micromotors, hydrophone arrays, infrared detectors, ultrasonic atomizers, micropositioning actuators, piezoelectric force sensors, and inchworm micro-steppermotors.[70-76] This list demonstrates that ferroelectric materials are suitable for MEMS applications, and that with the appropriate processing, the reaction issues with Si can be overcome.

2.5 PZT thin films

With a consideration of their use in MEMS, a brief review of PZT thin film literature is presented. Particular attention is given to the electromechanical properties, as this will be important when comparisons to relaxor-PT compositions are made.

Considerable research has been devoted to PZT thin films, driven predominantly by the non-volatile memory effort. Commonly, this research has been devoted to an understanding of polarization reversal in thin films and the stability of the written state over long time periods. Specific research topics have included investigations of fatigue, imprint, retention, and their pertinent structure-process-property relationships.[77-80] Through these studies, some understanding of the polarization reversal, and to some degree thin film defect chemistry has been developed. However, a comparatively small effort has been given to investigation of the thin film piezoelectric properties. With increasing interest in ferroelectric-based MEMS, several groups have begun programs devoted to piezoelectric characterization. However, due to the intrinsic difficulty of the measurements, and the inherent variability of electrical properties with sample characteristics (i.e., film thickness, doping, substrate choice, grain size) a consistent set of thin film reference data between research groups is not available.

In general, for well-processed randomly oriented PZT thin films, the reported

electromechanical property values are smaller than those associated with bulk ceramics

of the same composition. Piezoelectric property values of PZT thin films from several

groups are given in Table 2.2.

TABLE 2.2: PIEZOELECTRIC DATA FOR PZT (52/48) THIN FILMS COMPARED TO BULK CERAMICS

Group	d_{33}	$-d_{31}$	Film thickness	year
Bulk PZT (undoped)[9]	230 pC/N	95 pC/N	–	1972
Shepard et al.[Jr., 1998 #165]	–	50 pC/N	1 μm	1998
Polla et al.[1]	200 pC/N	–	1 μm	1996
Kholkin et al.[81]	50 pC/N	–	–	1996
Muralt et al.[76]	–	40 pC/N	22 μm	1992
Xu et al.[55]	100 pC/N	–	1 μm	1998
Chen et al.[82]	340 pC/N	–	8 μm	1996
Watanabe et al.[54]	–	90 pC/N	1 μm	1995

In contrast to the piezoelectric measurements, remanent polarization values

similar to, or larger than those of bulk ceramics have been reported in thin films.

however, these appear to be a result of epitaxial, or preferential crystallographic

orientations.[42,83] In order to explain the reduced piezoelectric coefficients, several

groups have proposed that the mobility of non-180° domain walls is reduced (and

possibly pinned) in thin films. Reducing the non-180° domain wall mobility limits the

material's ability to orientationally switch the polar vector, thus the ability to be poled,

and the ability to exhibit a strong extrinsic contribution to the electromechanical

properties. (The contribution of non-180° domain wall motion to the piezoelectric

properties was discussed in section 2.1.2.) Several experiments have been performed

which support this explanation.

Tuttle *et al.* performed in-situ x-ray diffraction analysis of 0.8 μm thick (0.2 μm grain size) PZT 40/60 capacitors deposited on Pt/Si substrates with applied electric fields. The films were *a*-domain oriented as a result of a residual tensile stress acting on the film from thermal expansion mismatch induced strain (this result is expected following the transformation stress concept developed by Tuttle *et al.*[3]). X-ray scans of the 002 and 200 reflections were collected and it was observed that the relative intensities were insensitive to electric fields in excess of the coercive field value.[3] This is in contrast to work on bulk ceramics where electrical poling significantly changes the relative intensity of these two peaks in tetragonal perovskites. This experiment gives the most direct evidence that non-180° domain walls in thin PZT films are clamped.[3]

Using a uniform pressure chuck which allows tensile or compressive biaxial stresses to be applied to thin film capacitors, Shepard *et al.* measured the pressure dependence of the dielectric constant and remanent polarization under both loading conditions. The findings indicated that for ~ ± 100 MPa of applied stress, only modest changes in the dielectric constant and loss tangent (~4%) were found, and that these changes were reversible upon unloading.[Jr., 1998 #165] Similar experiments performed on bulk ceramics indicated dielectric constants which changed by as much as 60%. These changes were accompanied by a large hysteresis (most pronounced in soft compositions) and could be explained by a stress-induced switching of the ferroelastic domains.[84] The inability to observe a strong and hysteritic stress dependence of the dielectric constant in PZT thin films suggests that either there are a limited number of non-180° domain walls in the sample, or their mobility is very low.[Jr., 1998 #165]

Aliovalent doping strongly affects the contribution of non-180° domain wall motion to the piezoelectric response in PZT ceramics. In ceramic PZTs, doping with 5⁺ cations on the B-site will produce soft behavior (i.e., reduced coercive fields, increased dielectric loss) while doping with 3⁺ cations will produce hard behavior (i.e., increased coercive fields and reduced loss). These effects are a result of enhanced or reduced domain wall mobility through the influence of defect dipoles.[9] Polycrystalline PZT thin films doped with Nb have been synthesized by several research groups. Though an appreciable amount of scatter exists between the reports, it appears that the coercive field values do not change appreciably upon Nb additions.[85,86] Problems have been observed in forming phase pure material when large amounts of Nb were incorporated, as the occurrence of a pyrochlore phase becomes difficult to avoid.[87] In general, when the effects of extra phases were excluded, the electrical property trends associated with Nb-doped PZT ceramics were not unambiguously demonstrated in thin film samples.[85] One possible explain for the lack of a clear compositional electrical property dependence is that Nb is segregated to grain boundary regions in the sample. This explanation however, is not consistent with the reports of Nb additions which result in improvements in the fatigue properties.[88] It appears to be more likely that the Nb is incorporated into the lattice, but due to non-180° domain wall pinning, the "chemical" softening effect cannot be demonstrated.

These three observations, as well as the smaller-than-expected PZT remanent polarization and piezoelectric coefficient values are a strong indication that non-180° domain wall mobility is suppressed in thin PZT layers. The possibilities which can explain this behavior include residual stresses which result from film/substrate thermal

expansion mismatch, small grain sizes (which are known to reduce the number of domain variants in fine grain ceramics[89]), and local mechanical or electric fields which may result from high structural or point defect densities (which may be 5 orders of magnitude larger thin films).[90] It is possible that a combination of these factors produce a non-180°domain wall clamping effect in thin film specimens, and limits the electromechanical response.

2.6   Relaxor and Relaxor-PT thin films

In recent years considerable attention has been devoted to the deposition and measurement of ferroelectric thin films with a primary emphasis on the $(Ba,Sr)TiO_3$ (BST), PZT, and $SrBi_2Ta_2O_9$ (SBT) systems. PZT and SBT were identified as the primary candidates for non-volatile memories, while BST was targeted for high density dynamic random access memory elements.[68] The large remanent polarizations achievable in PZT, the low fatigue in SBT and the large dielectric constants in paraelectric BST were the properties of interest for the respective applications.[68,91] Many other ferroelectric compositions were investigated during these years, however, due to the commercial interest in perovskite-based computer memories, for the most part, other compositions received diluted attention.

One such group of materials are the perovskite relaxor ferroelectrics and their solid solutions with $PbTiO_3$. The unusually large dielectric constants were well known in bulk ceramic and single crystal materials, (permittivity values in excess of 50,000 have been measured for well prepared morphotropic crystals near the ferroelectric transition

temperature.[44]) however, a strong research effort to develop thin film processing

strategies has not occurred. If such properties could be achieved in thin films, capacitors

and memory elements with enormous volumetric efficiencies would be possible.

One difficulty in processing such films is that the high processing temperatures

which are required for the perovskite phase in bulk ceramic processing can lead to

uncontrolled reactions with the substrate or excess Pb-volatization. In either case, the

pyrochlore phases common to many ferroelectric perovskites become difficult to avoid.

On the other hand, in the absence of high temperature annealing, other factors peculiar to

thin film growth, primarily the deviations from equilibrium, or epitaxial stabilization by

the substrate may be utilized to widen the processing window.

Polycrystalline PMN-PT films have been prepared by sol-gel and sputtering

routes. Several of the earliest reports on sol-gel deposited PMN indicated the desired

crystallization on a variety of substrates, however, in the temperature range of interest,

small amounts of pyrochlore were observed regardless of annealing time. [92-94] Other

reports of sol-gel derived material were published concurrently, however, none included

electrical property analysis. Jiang *et al.* reported on the sputter-deposition of randomly

oriented PMN-PT films of the compositions 50/50 and 70/30. The best results occurred

at substrate temperatures in excess of 640 °C using targets including 40 mol% excess

PbO; room temperature dielectric constants in excess of 2000 were reported. Again,

avoiding pyrochlore was extremely difficult and even the best samples contained

measurable quantities. In a follow-up article, high-field properties were measured. Non-

saturable polarization hysteresis and conduction loss were apparent. From these

measurements it appeared that some difficulties still existed concerning lead-

stoichiometry. [92-94]

Trtik *et al.* made one of the earliest attempts at deposition of epitaxial PMN thin

films. Using (110)-oriented $SrTiO_3$ substrates, PMN was pulsed laser deposited on

$YBa_2Cu_3O_{7-\delta}$ (YBCO) epitaxial bottom electrodes. The films were strongly oriented out

of the substrate plane, however complete atomic registry with the substrate was not

confirmed. The films were electrically characterized for polarization hysteresis; again,

non-saturability and conduction loss were prevalent characteristics. [95]

Takeshima *et al.* used metalorganic chemical vapor deposition (MOCVD) to

deposit PMN-PT films on Pt-coated MgO and Si substrates. A composition near the

morphotropic boundary was investigated. For the (001)-oriented films deposited on MgO

substrates, maximum dielectric constants of 1500 were recorded. In this work as well,

the associated pyrochlore was found to be very difficult to avoid. even in the case of the

strongly oriented samples, where the lattice matched perovskite phase should be

energetically preferred. [96]

Strongly oriented and random PMN-PT thin films were sol-gel deposited by Shyu

et al. onto (001)-oriented $LaNiO_3$ and Pt bottom electrodes respectively. This work is

significant in that it demonstrated the capability of achieving strongly out-of-plane

oriented films on Si substrates. The PMN-PT ratios ranged from (100/0) to (50/50).

Electrical properties including dielectric constant, loss tangent, and polarization

hysteresis were given for all compositions and orientations. The highest polarization

values of 11 $\mu C/cm^2$ were observed for the randomly oriented (50/50) composition, while

the maximum dielectric constant value occurred for the random (90/10) composition.

The hysteresis parameters for the randomly oriented material indicated saturability and low conduction loss. For the oriented PMN-PT on $LaNiO_3$ appreciable dielectric loss was shown.[97]

In all previous literature reports, several common factors are observed: achieving a film showing the perovskite phase exclusively was extremely difficult, dielectric constants were an order of magnitude or more smaller than those of the bulk counterparts, and the high field properties often showed large conduction losses. In addition, for PMN or PMN-PT compositions, a demonstration of true relaxor behavior by a loss of dispersion above T_m was not reported. It is likely that in all cases, the thin films were to some degree Pb-deficient, but the rapid kinetics of film synthesis, or the influence of the substrate on the phase development allowed this condition to be satisfied with only modest amounts of pyrochlore present.

Films demonstrating proper dielectric relaxation have been reported by Liu et al. for the system $Pb(Sc_{1/2}Ta_{1/2})O_3$, where dielectric constants at different measurement frequencies converged above the ferroelectric transition. The $Pb(Sc_{1/2}Ta_{1/2})O_3$ system is known to be more stable against Pb-loss and pyrochlore formation than PMN or PZN, which is likely why better electrical measurements were enabled.[98]

Since to date, the primary potential for usage of PMN-PT thin films has been in the field of integrated capacitors, little effort has been focused on epitaxial deposition. With the discovery of ultra-large strains in relaxor-PT single crystals however, new interest has been generated, and several groups are actively pursuing thin film single crystal growth.[99] No published reports are yet available. It is likely that improved properties will be observed in these systems as a result of the substrate stabilization of the

perovskite phase. In other perovskite systems, i.e., $Pb(Zr,Ti)O_3$ and $PbTiO_3$, reduced processing temperatures and improved electrical properties have been observed for epitaxial films.[42,83]

2.7 SrRuO$_3$

Since his investigation focuses on the deposition of single-crystal thin films, well lattice matched substrates and bottom electrodes are required. $SrRuO_3$ was chosen for the bottom electrode due to its combination of metallic conductivity and a good structural match with PMN-PT and many other perovskites.

$SrRuO_3$ shares the $GdFeO_3$ structure and belongs to the orthorhombic point group Pnma. $SrRuO_3$ may also be classified as pseudo-cubic with a 0.4° angularly distorted perovskite unit cell.[100] For most practical purposes, $SrRuO_3$ is discussed in these terms, as this structure is technologically important for use in conjunction with other lattice matched materials, including high temperature superconductors, ferroelectrics, and dielectrics.[101-103] Fig. 2.8 illustrates the structure of $SrRuO_3$, showing both the orthorhombic and simple-perovskite unit cell constructions.

——— **Orthorhombic unit cell**
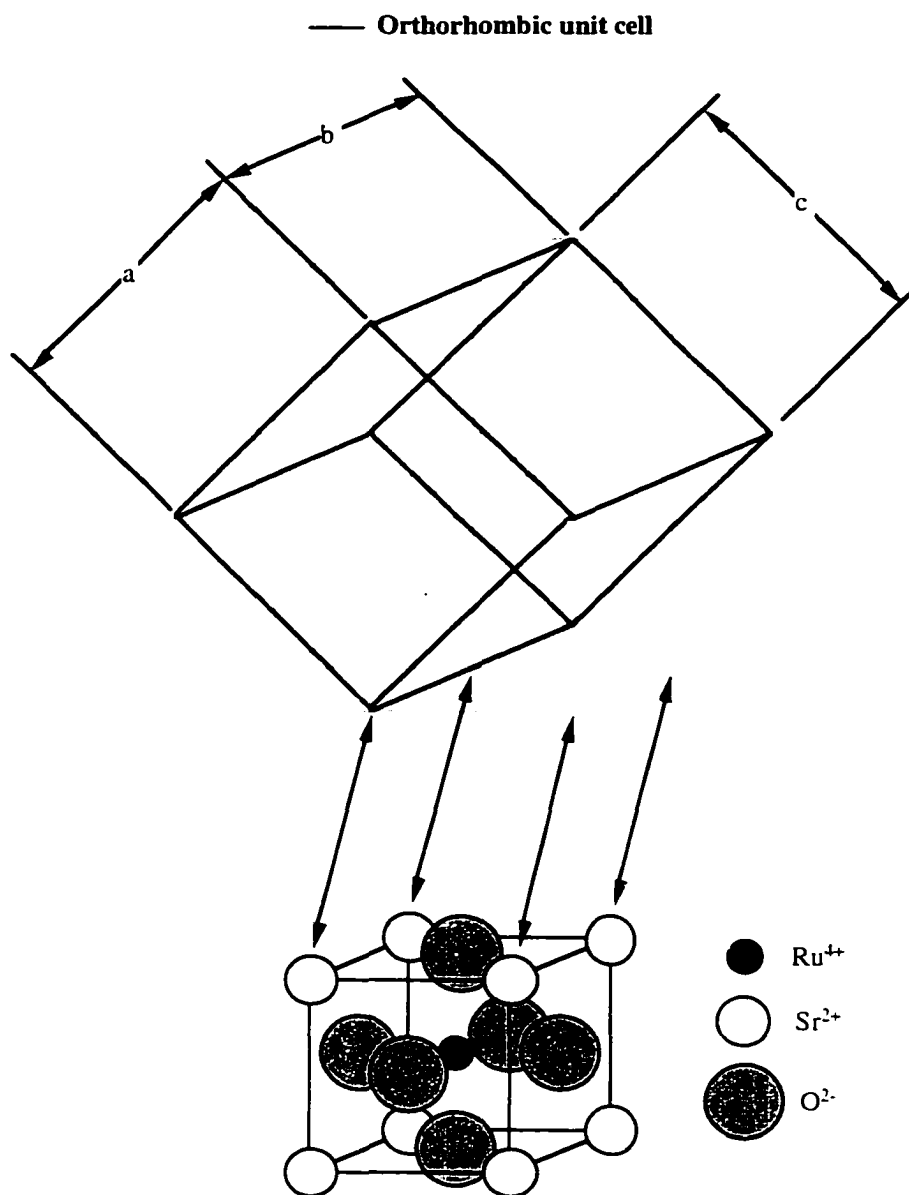
FIG. 2.8: SCHEMATIC STRUCTURE OF $SrRuO_3$, ORTHORHOMBIC AND SIMPLE-PEROVSKITE UNIT CELL CONSTRUCTIONS ARE SHOWN

The synthesis of $SrRuO_3$ was first reported by Randall *et al.* in 1959. In that work, the $SrRuO_3$ was synthesized from standard oxide precursors, and identified as orthorhombic. In addition, several of the structural homologues (belonging to the structural family sharing the formula $Sr_{n+1}Ru_nO_{3n+1}$) were observed, thus identifying

SrRuO$_3$ as a Ruddlesden-Popper phase.[100] Callaghan *et al.* studied the electrical properties of the SrRuO$_3$ phase and found it to behave as a metallic conductor down to liquid helium temperatures, having a resistivity ratio ($\rho_{room\ temp}/\rho_{liquid\ He}$) of approximately 3.2. Through measurements of the magnetization as a function of temperature, a Curie transition to the ferromagnetic state was found at ~ 160 K. This result was of interest since it was the first observation of ferromagnetism for which a single period 5 transition metal was responsible.[104]

The first investigations of single crystal properties occurred in 1972 by Bouchard *et al.* Single crystal samples were grown from SrCl$_2$ fluxes. The temperature dependence of the resistivity was again determined to be metallic, however, the observed resistivity ratio between room and liquid helium temperatures was approximately 12.[105] The increase in this value over previous reports was attributed to the absence of grain boundaries, and their contribution to electron scattering. Several other groups characterized similarly grown single crystals and found comparable results for transition temperature and resistivity ratio.[106,107]

Because of the volatility of ruthenium oxides, the stability of SrRuO$_3$ at high temperatures is compromised. Bensch *et al.* investigated the structural and thermochemical reactivity of SrRuO$_3$ in both oxidizing and reducing atmospheres. The results indicated that in oxidizing environments, SrRuO$_3$ remained stable to temperatures near 925 °C, above which small amounts of SrO and Ru metal were observed. A similar result occurred in reducing atmospheres containing hydrogen, however, in that case, the decomposition reaction began at temperatures as low as 525 °C.[108] This result is important, as it determines a practical limit for thin film processing conditions where

comparable temperatures, and reducing environments are common. Similar activity was observed by Maria *et al.* for epitaxial $SrRuO_3$ thin films which were heated in vacuum to temperatures in excess of 650 °C. Composition measurements were not taken for these samples, however, degradation of the crystallinity and conductivity were observed after heat treatment. [109]

$SrRuO_3$ and other metallic oxides are known to have transport properties which can depend strongly on externally applied mechanical stresses. For $SrRuO_3$, the hydrostatic pressure dependence of the resistivity and Curie transition temperature was investigated by Shikano *et al.* and Neumeier *et al.*[110,111] The pressure dependence of the resistivity was determined to be -8 °C/GPa and -5.7 °C/GPa respectively. These data may be important since all heteroepitaxial thin films are subject to some degree of thermal expansion induced mismatch which may potentially influence the Curie transition temperature.

A considerable effort investigating epitaxial thin films of $SrRuO_3$ has been invested, driven primarily by the small lattice constant mismatch which $SrRuO_3$ has with many perovskite-based materials. $SrRuO_3$ has been extensively used as a bottom electrode for ferroelectric and dielectric thin film devices, and has been suggested for use as the normal metal layer in superconducting/normal/superconducting (SNS) junctions.[103,112] In addition, $SrRuO_3$ was also found to display giant magnetoresistive effects, and was used as the bottom electrode in an all-oxide ferroelectric field-effect transistor.[113]

When deposited on high quality $SrTiO_3$ substrates, $SrRuO_3$ tends to grow with an ultra-smooth surface whose roughness values, in the best cases, are limited to that defined

by unit cell steps. Several groups have made this observation for MBE, PLD and magnetron sputter deposited films.[114-116] Eom et al. first demonstrated this effect in 90°-off-axis sputtered SrRuO$_3$ thin films on SrTiO$_3$. In this report, Eom also made the first observation of reduced orthorhombic twinning in SrRuO$_3$ films deposited on vicinal SrTiO$_3$ substrates.[117] This result was verified in subsequent reports.[116] Gan et al. studied the in-plane texturing as a function of the severity of the miscut angle, as well as the direction of the miscut with respect to the in-plane crystal directions. They determined that for 90° off-axis sputtered films, miscut angles (directed along [010] or [100]) $\geq 2°$ were required for single crystal films, while smaller angles, (including near-nominal cuts), resulted in films with nearly equivalent populations of orthorhombic cells along the orthogonal in-plane directions.[118] The miscut angle was also rotated in-plane towards the [110] direction, and led to a sharp increase in the degree of in-plane twinning. In this work the alignment of the orthorhombic axes was attributed to a preferential nucleation of specific orientations during film growth, with the b-axis lying along the substrate terrace direction.[118]

A final observation made on epitaxial thin-film SrRuO$_3$ by several groups is the extension of lattice constants with respect to bulk values. Eom et al. observed this effect in both SrRuO$_3$ and CaRuO$_3$, the behavior being attributed to Ru deficiency, and subsequent occupation of vacant B-sites by Sr or Ca. Accompanying the extension of the lattice constants was an increase in the resistivity, and a switch to semiconducting behavior, i.e., an induced Mott–transition near room temperature.[114] This explanation, however cannot resolve the discrepancies observed in the lattice constants of films deposited under the same conditions on different substrates. Smaller lattice constants

were found when the substrate lattice mismatch increased and the film structure became more defective. Hiratani observed a similar result in PLD-grown $SrRuO_3$ films which were studied as a function of oxygen pressure during growth. Similarly extended lattice constants and increased resistivity values were observed when films were deposited at pressures below 100 mTorr. When films were grown at pressures below 1 mTorr, a Mott-transition was induced near 50 K. These effects were attributed to oxygen deficiency during growth, and in particular, to localization of conduction electrons in the vicinity of oxygen vacancies.[119] This explanation, however, does not take into consideration the Ru-loss which was evidenced by SrO reflections in the x-ray patterns of films deposited at the lowest pressures.

2.8   Pulsed laser deposition

In this study, all samples were prepared using pulsed laser deposition (also referred to as pulsed laser ablation). Since the mechanisms of material removal, the characteristics of laser-induced plasmas, and laser technology are important for accurate interpretation of the experimental results, a review is given below of the history of laser deposition, pertinent laser technology, and some characteristics of laser-induced plasmas.

2.8.1   History

The pulsed laser deposition (PLD) technique was initially demonstrated in 1965 by University of Rochester and Bausch & Lomb researchers Smith and Turner. Using a Trion ruby laser with a pulsed output of 3 J and an operating frequency of 1/60 Hz, a variety of powders and single crystals were evaporated in vacuum, and deposited on glass, mica, and fluoride substrates. Though this was the first publication concerning

PLD, many of the important benefits and limitations of the technique were discussed: (i) *the authors immediately identified the ability to deposit films at very rapid rates,* (ii) *they observed and characterized the non-equilibrium mechanism of material removal.* (iii) *the ability to use nearly any material as a source was noted,* and (iv) *the benefits concerning cleanliness (i.e., having the evaporation power source removed from the vacuum chamber) were observed.* The negative sides of laser ablation were also demonstrated; these included: (i) *the occurrence of macroparticle ejection,* and (ii) *the non-stoichiometric nature of films deposited from multicomponent targets: a point which numerous investigators would disregard in future studies of PLD film growth.*[120]

Following this initial work, little attention was given to this technique as a result of increased interest in other emerging technologies including sputter deposition and evaporation. A factor which historically inhibited PLD was the relative youth of laser technology - at the time lasers were large, expensive, unreliable, and insufficiently powerful. In addition, the invention of the magnetron sputter source in 1971 and its rapid success took the attention of PVD researchers.[121]

In the late 1980's two occurrences led to the acceptance of PLD as a viable technique (i) marked improvements in laser technology (specifically excimer lasers fitted with magnetic Q-switches) and (ii) the discovery of high temperature superconducting oxides.[122] The magnetic Q-switch allows nanosecond-long bursts of high voltage electrical energy to be discharged. This enables very short laser pulses, ~ 30 ns (in the case of excimers, the minimum pulse length is limited by the lifetime of the excited-dimer (excimer) species). In the early investigations of laser-solid interactions, the most

favorable characteristics were observed using laser pulses which provided the highest

achievable power.[123,124]

In the past ten years, laser technology has improved further still with

technological advances including the ceramic "Nova" excimer laser tube (developed by

Lambda Physik, allowing order-of-magnitude improvements in laser gas lifetimes[125] and

the introduction of high fluence, solid state, frequency-quadrupled YAG lasers. An

important, yet unrelated application responsible for many improvements in laser

technology has been the increased usage in medicine (specifically in corrective eye

surgical procedures).

Great interest in deposition of $YBa_2Cu_3O_{7-\delta}$ (YBCO) thin films occurred in the

late 1980s when it was observed that critical current densities could be improved by

several orders of magnitude in epitaxial thin films, and that thin film processes were

particularly effective at producing exotic compositions which were thermodynamically

unstable in equilibrium conditions.[126,127] It was also quickly realized that depositing

YBCO, a three cation oxide, was non-trivial by conventional techniques. Full

oxygenation of the sample was required, along with careful control of the constituent

cation ratios. Methods such as reactive co-evaporation or molecular beam epitaxy

enabled the precise composition control, but the oxygen pressures required during

deposition are difficult to achieve.[128] Sputter deposition certainly has access to high

ambient pressures, however, negative-ion resputtering of the growing crystal becomes

problematic. 90° off-axis sputtering can be used to ameliorate the bombardment effects,

however, compared to on-axis sputtering, the stoichiometry becomes more difficult to

control.[90] At this point, it was recognized that PLD would be suitable for YBCO growth.

Deposition in atmospheres approaching 1 Torr were easily accomplished without the occurrence of substrate bombardment by reflected neutrals or oxygen anions, and reports indicated that the target stoichiometry was conserved in the deposited films.[129]

Following the research efforts in high T_c materials, interests in thin film oxides shifted towards ferroelectric, dielectric and magnetic perovskites, in pursuit of higher performance thin film devices. Given the similarities to YBCO in structure and processing conditions, these materials were also found to be amenable to the PLD process.

2.8.2 Mechanisms of ablation

The interaction of laser radiation with solid surfaces was initially studied for laser welding and machining operations, during which observations of laser plasmas under atmospheric conditions were made.[123] Researchers observing this activity soon appreciated that this plume could be used as a transport vehicle for film growth. The high energy densities available with pulsed laser technology were attractive, as they shared similarities with flash evaporation in their ability to vaporize material nearly congruently.[130] The specific mechanisms of material removal by laser-solid interaction was proposed by Foltyn et al., including the laser-plume self-regulating inverse Bremmstrahlung activity.[124] Fig. 2.9 illustrates a typical laser-induced plasma shape in the presence of a gas ambient.

two shaded regions corrspond
to different distributions of
material in the laser plasma

small spots correspond to
macroparticles ejected from surface
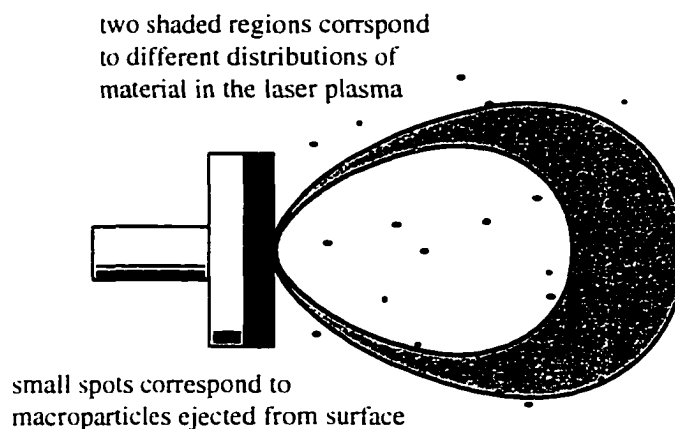
FIG. 2.9: SCHEMATIC ILLUSTRATION OF LASER INDUCED PLASMA IN THE PRESENCE OF A GAS AMBIENT

In addition to the beam-solid interaction, an important facet of ablation is the interaction of the laser-beam with the resulting vapor cloud. This interaction helps to produce the energetic species (as evidenced by the brilliant plasma plume) which can bombard the growth surface.[122] This bombardment can be either beneficial or detrimental. depending upon the material system and deposition conditions.

To understand the characteristics of laser deposited thin films. it is important to have an effective model describing the beam-solid-vapor interaction. To address issues such as stoichiometry control. energetic bombardment. and thickness uniformity. several groups have studied laser-induced plasmas.

Wiedman and Helvajian have reported on the photodecomposition of YBCO at several laser wavelengths. Particular attention was given to characterization of the species present in the plasma plume. and the influences of incident laser energy density in the range of 50 to 800 mJ/cm^2. Fig. 2.10 schematically summarizes an important result of their study.[131]

Electronic   Thermal

Photodissociation   O. O$_2$ Plasma

Cu^+
Ba^+
BaO^+

Cu^+
Y^+
BaO^+
YO^+
Ba^+

Cu.Y
Ba

Cu.Y
Ba

Cu
Cu^+
Cu_2
$Y^+.Y$
Ba
Ba^+

Increasing laser fluence
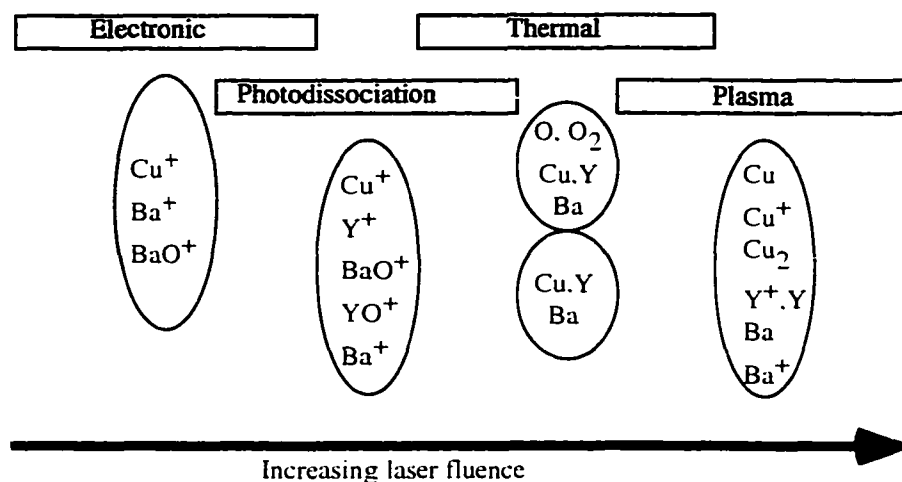
FIG. 2.10: MATERIAL REMOVAL MECHANISMS WITH INCREASING LASER FLUENCE AFTER
HELVAJIAN ET AL.[13]

It was found that there is a lower threshold below which emitted material could

not be detected. Above this threshold, but still at low laser fluences, atomic and diatomic

species comprised the majority of the ejecta. At these low incident energies, no visible

plasmas were detected, indicating that the most important mechanism of material removal

at low fluences is electronic excitation. Interestingly, the kinetic energy of all species

ejected for a given laser pulse was found to be the same within experimental error.[13]

The kinetic energies of the species will play an important role in influencing the

stoichiometry of resulting thin films.

When fluences were increased into the region where an obvious visible plasma

was excited, the neutral species product increased dramatically. This indicated that the

removal mechanism had switched to a process similar to thermal desorption. In addition,

the presence of anions revealed the high concentrations of thermionically emitted

electrons near the target surface. Kinetic energy spectra of the higher energy plasma

show a bimodal distribution where the energies between the neutral and ionic species

differed by nearly an order of magnitude. When the laser fluences were increased

further, it was found that the disparity between the neutral and ionic species velocity

increased: this indicated that the additional laser energy accelerates the ionic particles

selectively, while the thermionically emitted material velocity remains unchanged.[131]

With these results in mind, it cannot be expected that a perfectly stoichiometric growth

front will develop either in vacuum or in the presence of a gas ambient. Since the species

have different kinetic energies, atomic masses, and valence states, they will have

different scattering cross-sections. Thus the angular, as well as the temporal distributions

will be dissimilar.[90]

The arguments in the previous section indicate that a complex target

stoichiometry cannot be expected to be conserved in a PLD deposited thin film. It needs

to be mentioned, however, that the deviations from stoichiometry over modest areas (i.e.,

4 cm^2) are quite small, typically within the limits of thin film compositional

characterization. It is also important to note that other deposition techniques which rely

on single sources suffer the same (and often more severe) difficulties in achieving

perfectly stoichiometric thin films. In the case of insulating materials (especially

perovskites) it is important to consider even very small deviations from stoichiometry

(i.e., ~1%) as these may lead to defect structures which dramatically influence the

electrical properties.

2.8.3 Energetic bombardment during deposition

The effects of energetic bombardment during thin film deposition have been

appreciated in the field of sputtering for many years. Studies on the effects of

bombardment led to the development of the Structure Zone Model (SZM), which describes the microstructure of a thin film as a function of adatom mobility during deposition. In general, the model predicts that the morphology of a thin film deposited under low adatom mobility conditions will be characterized by a 2-dimensional columnar microstructure, a low density, and a rough surface. The microstructural characteristics of a thin film deposited at high adatom mobilities are a 3-dimensional grain structure, high density, and smooth surfaces.[132] These characteristics (associated with high energy depositions) are desirable for most electronic applications. In general, high adatom mobilities are achieved by supplying energy to the growing film, most commonly in the form of heat or energetic bombardment. Heat provides thermal vibration, while energetic bombardment imparts kinetic energy to deposited atoms through collisions; both mechanisms promote the deposited atoms' ability to find the most energetically favorable location available.[90]

Laser solid interactions in vacuum and gas ambients result in the production of energetic species which under the proper conditions can bombard the growth surface.[122] Since laser ablation is typically performed in the absence of electric and magnetic fields, the energy and flux of bombarding species cannot be controlled indepedently as in sputtering, i.e., during sputter deposition, the target and substrate bias can be adjusted to control the plasma energy.[132] In laser ablation, the bombarding species energy is produced as a result of rapid gas expansion, species ionization, and subsequent acceleration by the presence of a large space-charge field.[131] The laser fluence controls the initial energy of the species, while target-to-substrate distance and ambient pressure are useful for moderation of energies by collision thermalization.

Many researchers have characterized the laser plasma in both vacuum and gas

ambients using a variety of techniques. One of the greatest difficulties in laser-induced

plasma characterization is the number of species present in the plume. Laser plasmas

have been shown to contain ionic particles of both polarity, neutral species, clusters, and

charged formula units.[122] As such, a single technique may not be able to characterize the

plume entirely. In addition, the high pressures under which many depositions are

performed ($\geq$ 100 mTorr) preclude the use of such methods as mass spectroscopy which

require much lower pressure for operation.[133] For these situations, fast-photographic

optical probes have been employed. Table 2.3 shows the results of plasma

characterization from several researchers.

TABLE 2.3: CHARACTERIZATION RESULTS FOR LASER-INDUCED PLASMAS

Researcher	Characterization Technique	Conditions	Species and energy
Coccia et al. [134]	Energy dispersive mass spectroscopy	Vacuum	Pb^{*} : 30 – 100 eV
Zheng et al. [135]	Optical time of flight spectroscopy	Vacuum	Cu^{*}, Y^{*}, Ba^{*}: 40 eV Ba^{**}: 80 eV
Kurogi et al. [136]	Plasma optical emission	0.1 Torr < PO_2 < 0.4 mTorr	10 eV < Ti^{4+} < 60 eV

Though the flexible processing parameters of PLD provide for a wide range of

species energies, it is apparent from the results in Table 2.3 that under common

deposition parameters, species with sufficient energy to affect the film morphology via

bombardment are present and need to be considered during process optimization. In

general, the desired energy window for microstructure optimization is between 10 and 15

eV. Energies in excess of this range may result in subsurface damage, while energies

below this range may supply insufficient energy for surface rearrangement.[90]

For the deposition of many oxides, ambient pressures in the vicinity of, or greater than 100 mTorr, are employed. Using equilibrium calculations for mean free paths or collision frequencies, it can be shown that after travelling several cm (typical target to substrate distances) in these pressures, even the most energetic ions and neutrals would be completely thermalized. However, given that the collision scattering cross-section is energy dependent, it is appreciated that equilibrium treatments do not apply. Robinson determined that when an energetic particle travels through an atmosphere at thermal equilibrium (i.e., the energies of the gas molecules are equivalent to kT (kT = 0.025 eV), the likelihood of collision is reduced with increasing energy due to a decrease in the residence time in transit. [137] As a result, even at typical PLD gas pressures, significant amounts of energetic bombardment can occur.[136]

In many cases, the bombardment levels experienced are beneficial to film growth, however, under certain deposition parameters, the energies present can be detrimental, i.e., great enough such that subsurface crystalline damage occurs which cannot anneal out as growth continues.[90]

2.8.4   Particulate generation

As a result of the high energy density of the laser and the violent mechanism of material removal, the generation of macroparticles (or boulders) is observed in PLD.[120] To a certain extent, boulder densities may be minimized, (i.e., through the use of high density or single crystalline targets) but generation seems to be intrinsic to the technique. In general, for focused beam deposition methods, macroparticle ejection is observed, and is in most cases unavoidable.[90]

Two primary mechanisms have been proposed for macroparticle generation: spalling and splashing. Spalling refers to a mechanical mechanism where geometric irregularities produced by multiple laser incidence are fractured from the surface. One source of such surface irregularities is preferential ablation of target surfaces, i.e.. at grain boundaries. inhomogeneities. and low density regions. This preferential ablation results in a surface morphology characterized by closely packed cone-like structures directed towards the laser source (the valleys between cones corresponding to regions where material is removed more rapidly). As the aspect ratio of these structures becomes large. they become mechanically weak, break free of the surface, and are propelled towards the substrate by the pressure gradient in the plume.[122] Formation of such asperities can be minimized through the use of a dithering and rotating target holder which effectively samples the entire target surface. and changes the incident angle of the laser pulse by $90°$ between successive shots at the same site (*Neocera* Corporation). Though laser-cones are popularly believed to be a prominent source of macroparticles. careful examination of both target and film surfaces reveals that the cone tips are considerably bigger than most observed macroparticles.[122]

Spalling of solid target material can also occur as a result of thermal shock. As a result of the rapid temperature rise from laser radiation absorption at the target surface. thermal gradients can be as large as 10^4 °C/cm, and lead to surface fracture from thermal expansion-induced strains.[123] These effects are most important for brittle target materials.

The mechanism in which a thin region of liquid is produced on the surface of the target and is subsequently ejected is known as splashing. When a thin skin of liquid

phase is present on the surface. the recoil pressure from the rapidly expanding plume can cause liquid droplets to be "splashed" from the surface. This effect is intrinsic to the technique. and its severity is determined by the target material properties. The volume of material heated by the laser radiation will scale with the thermal conductivity: larger volumes result in lower overall temperatures. which will promote less sublimation and more liquid. In addition. materials with smaller ultraviolet radiation-absorption coefficients will have larger interaction volumes. lower temperatures. and again more liquid phase.[123] Reducing the laser wavelength and pulse duration will increase the power density and reduce the interaction volume. thus reducing the splashing effect.

Regardless of the mechanism. macroparticle ejection has limited the applicability of pulsed laser deposition in industrial settings. The resulting macroparticles may result in shorted insulating layers. failure of lithographic patterning, and compositional gradients in the immediate vicinity of the macroparticle.[122] As such. pulsed laser deposition has found the greatest applicability in laboratory settings where these difficulties may be tolerated. Several mechanical contrivances which make use of the fact that macroparticles travel with velocities much slower than those of the plume species have been devised to prevent macroparticle deposition. Several groups have developed such "mechanical filters". One design incorporates a spinning spoked wheel which is rotated at a speed determined by the laser frequency and macroparticle velocity such that the spokes bat the particles out of the expanding plasma while allowing the remaining plume matter to pass unhindered.[138,139] It has been suggested that spinning the laser target at very rapid rates (10.000 rpm) would also result in reduced boulder densities. In this condition. once the macroparticle is free of the target surface, the

centripetal force on it would be lost. and the particles inertia would propel it in a radial direction.[122] Application of these techniques has been reported to reduce macroparticle densities. however. complicated mechanical devices are required. and deposition rates are typically reduced.

A final method used for the reduction of boulder deposition involves growth in the 90°-off-axis geometry. i.e.. the substrate and target normals are orthogonal. Since the macroparticles travel in a line-of-sight manner. their deposition on the substrate is very unlikely.[140] Unfortunately. off-axis deposition results in reduced deposition rates. decreased thickness uniformity. and added difficulty in composition control.[109,122]

2.8.5 Composition control

Central to the deposition of any multiple component material from a single source is the maintenance of thin film stoichiometry. In PLD. since the cations are coming from one single laser target. (in the absence of strong resputtering) three parameters are crucial for stoichiometric growth: (i) *the material is removed from the target stoichiometrically*. (ii) *during transport from the target to the substrate. the constituent cation distributions are identical*. and (iii) *all cations have identical sticking coefficients*. Since the laser fluence is intense. the material removed by a laser pulse is nearly congruent.[123] However. in the case of materials like high temperature superconductors and perovskite ferroelectrics. the constituent cations typically have different valencies and different atomic masses. Cations with larger valencies will be subject to greater acceleration. while cations with larger atomic masses will have smaller velocities. In general light. highly charged cations like Ti^{++} will travel much faster than heavy cations with smaller

valence states, such as Pb^{2+}.[135] As a result, the angular distributions of the cations in the plasma can not be identical, either in vacuum or in the presence of an ambient gas. These trends are true of all energy assisted PVD methods.

In PLD, several adjustments may be made to minimize nonstoichiometry:

(i) short target to substrate distances can be used – this will minimize the distance which the plume travels, thus minimizing the angular spreading, (ii) high pressures can be used during deposition – this again confines the plume from spreading in the lateral direction, and (iii) the minimum laser energy consistent with congruent material removal should be employed – it has been shown that the initial distribution of species velocity is small at laser fluences near the threshold energy for material removal. [131]

Many claims have been made concerning the ability to conserve complex target stoichiometries in laser deposited thin films. These claims, however, are often based on characterization results from techniques such as Rutherford backscattering spectrometry (RBS) and energy dispersive x-ray spectroscopy (EDS).[129] When these methods are applied to thin film specimens, as a result of the small sampling volume and geometry, the uncertainties are limited to approximately ± 3-5%.[133]. What is more likely is that laser deposition provides film growth to within several percent of the target stoichiometry. In systems where phase-fields are small, like YBCO, the possibility of a self-correcting composition produced by second phase nucleation exists. This helps explain why excellent transport properties like T_c can be observed. In systems like $BaTiO_3$, small deviations in stoichiometry can be tolerated in the structure. Thus, in epitaxial thin films, the perovskite structure can be conserved even when the A/B ratio deviates from unity.[109] This situation is further evidenced by the large number of

publications citing phase-pure epitaxial growth with electrical properties dominated by conduction loss, and the even larger number of publications reporting no electrical properties whatsoever.[141-144]

As a result of these considerations, it is apparent that for depositions of truly stoichiometric material, a target composition must be used which compensates for the preferential deposition of one cation over another. In addition, assessments of composition need to be corroborated by material property measurements (i.e., dielectric loss and permittivity) which are far more sensitive to small stoichiometric deviations.

Several negative aspects of PLD have been elaborated upon, including macroparticle ejection, stoichiometry deviations, and poor thickness uniformity control. Though these aspects may make PLD an inappropriate tool for industrial usage, it remains an excellent method for the research scale. PLD offers several advantages over alternative techniques for new materials development. These include:

(i) The ability to use any target material; dc magnetron sputtering is limited to conductive targets, while very refractory materials such as platinum are excluded from thermal evaporation methods. In a very practical sense, the small spot-size of the laser beam (typically ~ 5 mm^2) allows penny-sized targets to be used; for researching new compositions this capability is very useful considering the expense, time, and difficulty associated with fabrication of certain ceramics (targets several inches in diameter are standard for magnetron sputtering systems).

(ii) In PLD, no limitations exist concerning the atmosphere during growth, effectively 10 decades of pressure are acceptable during deposition, from UHV conditions (i.e., 10^{-10} Torr) to pressures approaching 1 Torr. In addition, there is a

considerable flexibility in the gas composition. In MBE, low pressures are mandated to minimize scattering events, and the reaction of the crucible and its heating elements with the gas phase is potentially problematic, particularly in oxidizing ambients. In sputtering, a minimum partial pressure of Ar must be maintained to support the plasma, thus very low pressure deposition is excluded. In addition, severe negative anion resputtering (common to sputter deposition of oxides) is easily avoided during PLD growth.

(iii) PLD is a rather fast growth technique, under typical conditions, material accumulation rates range between 0.1 Å and 1 Å per laser shot. With modern lasers, repetition frequencies as high as 500 Hz are available.

(iv) Stoichiometry conservation between target and substrate is relatively good in comparison to other single-source PVD methods. Material removal is congruent, and growth conditions can be chosen which minimize cation segregation in the plasma during transport to the substrate.

Chapter 3   Experimental Procedure

3.1   Description of equipment

Epitaxial thin film samples were prepared by pulsed laser deposition (PLD). The laser was a Lambda Physik Compex 102 operated using the krypton fluorine gas mixture. The output radiation was 248 nm. which corresponds to the decomposition energy of the KrF* excimer species. Laser pulses were approximately 30 ns in duration with a pulse frequency ranging from 0 to 20 Hz. All depositions were performed with the laser in constant energy mode with an energy setpoint of 250 mJ. Using this mode. the laser internally monitors the energy output and actively modulates the voltage applied to the capacitor banks. thus providing minimal pulse-to-pulse fluctuations or long term energy drifts.[145] With each laser gas change. the output energy of the laser was measured with a Coherent laser-sure energy meter. Using this information. the internal laser energy meter (thermopile detector) calibration was checked.

The laser was focused by means of a plano-convex fused silica lens with a focal length of 0.5 m. The laser lens was positioned on a short length of optical rail to enable translation. By changing the lens position. the laser spot size at the target surface. and thus the energy density could be adjusted. The focused beam was introduced into the chamber through a fused silica window. The laser window and lens were positioned such

that the laser beam passed through the edge of the chamber port, while being aimed at the chamber center. With this geometry the laser window could be rotated between depositions such that the rate of optical damage accumulation in any one spot would be reduced by distribution over a much larger window area. Several windows were used for different depositions. For film growths which were relatively insensitive to laser fluence. i.e., top electrodes, platinum, etc., a "dirty" window was used, and rotated after each deposition. For depositions where volatile species were involved and precise reproduction of experimental conditions was required, i.e., PMN-PT growth, a second window was used. This window was also rotated regularly, but in addition, it was etched with concentrated nitric acid before every deposition. Because of the high pressures during deposition, significant amounts of vapor condense on the inside of the laser window. The interaction of the laser beam with this film results in severely accelerated optical damage. The resulting reduction in the window transmission is large enough to drastically affect the laser plume characteristics. Fig. 3.1 shows the chamber schematic.

a - Compex 102 excimer laser
(λ = laser wavelength)
b - plano-convex fused silica lens
c - K-type thermocouple
d - fused quartz laser port
e - Baratron capacitance manometer

f - power feedthrough for hot-stage
g - ionization pressure gage
h - ferrofluidic rotary feedthrough
i - laser target
j - resistively heated stage
k - diffusion pump
l - ozone generator

10% O$_3$
90% O$_2$
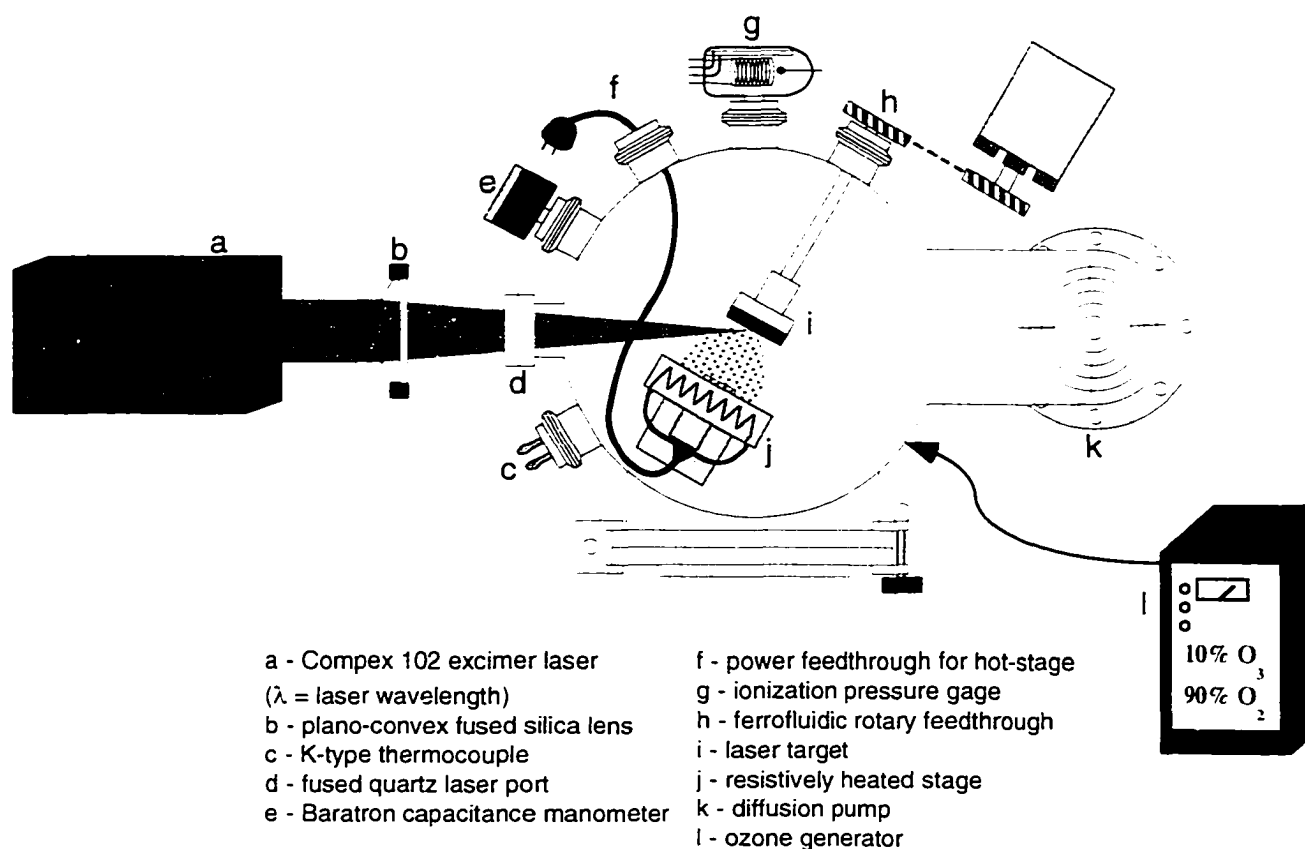
FIG. 3.1: PLD VACUUM CHAMBER SCHEMATIC

The laser was focused onto ceramic targets approximately 1" in diameter. Energy densities between 1.5 and 2.5 J/cm^2 were used. The particular energy density was determined by the composition of the laser target and the specific deposition requirements. In general, increasing the energy density insures that the material removal is stoichiometric, and increases the kinetic energy of the plume species.[13] In addition, increasing the fluence promotes deeper optical penetration and greater macroparticle fluxes. To minimize changes in the target surface stoichiometry after multiple laser shots, after each deposition the targets were resurfaced using SiC abrasive paper.

The targets were mounted on rotating stainless steel holders using silver paint. Mounting was accomplished by applying a liberal quantity of the silver paint to the steel holder, and pressing the target on the holder to squeeze out air bubbles. The freshly mounted targets were then placed in a 150 °C oven for 30 minutes. Oven-drying the targets insured complete solvent removal, thus minimizing the possibility of bond failure upon chamber evacuation.

The chamber vacuum was maintained by a Varian diffusion pump roughed with an Alcatel rotary vane pump. The diffusion pump operated with Dow-Corning type 701 silicone fluid, while the roughing pump used Krytox Fomblin oil. These two fluids were used because of their oxidation resistance. The base pressure of the laser chamber was 8 x 10^{-8} Torr, however, prior to depositions, a pumpdown to 10^{-6} Torr was standard. This pumpdown pressure corresponds to the ppm purity levels of the process gases. Prior to opening the gate valve, the chamber pressure was roughed to less than 100 mTorr. High vacuum pressures were measured with an ion gauge, while deposition pressures (typically tens to hundreds of mTorr) were measured with a Baratron capacitance manometer instrument. This type of gauge is preferable due to its absolute measurement capabilities and insensitivity to the atmosphere composition. Periodically, due to accumulation of condensed target vapor on the chamber walls, the chamber interior was cleaned with a mild nitric acid etch.

For most depositions, a mixture of 10% ozone and 90% oxygen was used as the reactive ambient. This mixture corresponds to the undistilled output of a PCI-1 ozone generator. The ozone generator was operated at a flow rate of 5 cubic feet per minute and a ozonator cell pressure of 5 psi. These settings provided the largest ratio of ozone to

oxygen. UHP-grade oxygen was supplied to the ozone generator. Ozone will decompose rapidly with increased temperatures, thus standard mass-flow control devices (which operate at > 40 °C) could not be used to introduce ozone into the chamber. Additionally, due to the powerful oxidation potential of ozone, standard metering valves which contain polymeric sealing surfaces were unacceptable. The output of the ozone generator was split; one line going to the chamber and the other to building exhaust. This arrangement allowed the high flow rates necessary for high ozone throughput. Immediately after the split to the building exhaust, a check-valve was inserted which prevented backstreaming of the building exhaust into the chamber. An all-metal welded bellows-type micrometering valve was used to control the low flow rates necessary for the chamber pressures required for deposition. The all-metal construction was required as a result of the reactivity of ozone. The metering valve was set such that with the chamber gate valve in the full open position, the chamber pressure would reach 2 mTorr. This corresponds to a flow rate of approximately 100 sccm. To achieve higher pressures, the gate valve was throttled to reduce the chamber conductance an appropriate amount. Using this procedure, stable pressures up to 200 mTorr could be maintained. At significantly higher pressures, periodic adjustment of the gate valve position was necessary to counter system fluctuations during growth. A schematic of the ozone plumbing is given in Fig.3.2.
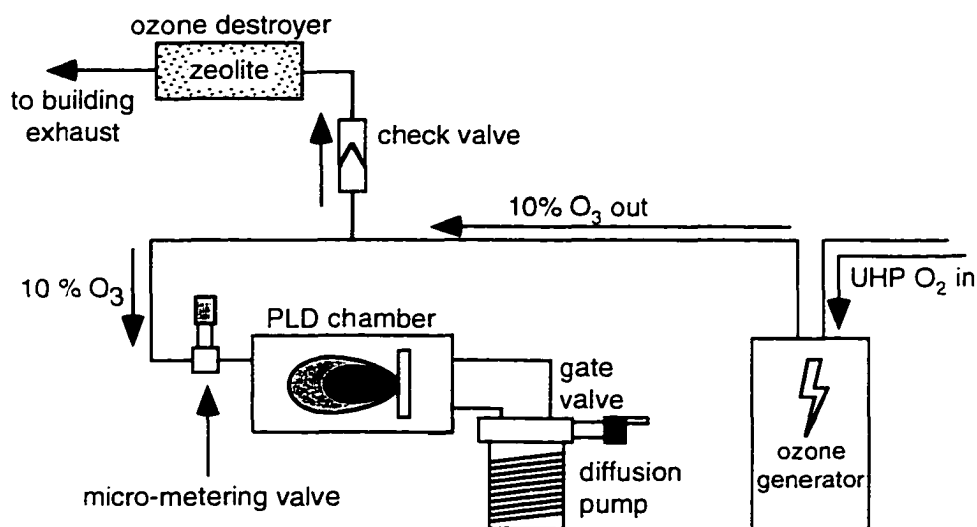
FIG. 3.2: SCHEMATIC OF THE OZONE PLUMBING SYSTEM

The largest quantity of ozone produced by the generator was passed through the building exhaust line after it was sent through a stainless steel canister filled with zeolite pellets. The high surface area of the zeolite pellets provides the catalytic action required to breakdown the unused ozone. After lengthy depositions, it was common for the zeolite canister to be warm to the touch as a result of the exothermic ozone decomposition.

The only other atmosphere needed for film growth was argon. When desired. UHP-grade argon was passed through a 200 sccm rated mass-flow controller operated at 100 sccm throughput. Chamber pressures were again achieved by throttling the gate valve.

When film growth at elevated temperatures was required. a stainless steel block-style hot stage was used. The stage consisted of a type 304 stainless block with a 1" square face and 0.5" thickness. The block was drilled. then threaded with a Thermocoax heating element. Thermocoax consists of a Kanthal resistive heating element surrounded by high purity MgO powder swaged into an inconel jacket. The diameter of the element

was 0.62". Power was fed to the thermocoax from a Hewlett Packard type 6268B dc

supply. For standard deposition temperatures (near 650 °C) the element was run at ~ 7

amps and ~ 31 volts. The heater block was surrounded by a stainless steel shield to

minimize radiative heat loss. The hot stage and its stand were not fixed to the chamber,

and thus could be translated to provide target-to-substrate distances between 2.5 cm and

10 cm, as well as on and off-axis deposition geometries. Fig. 3.3 gives a schematic of the

substrate hot stage.
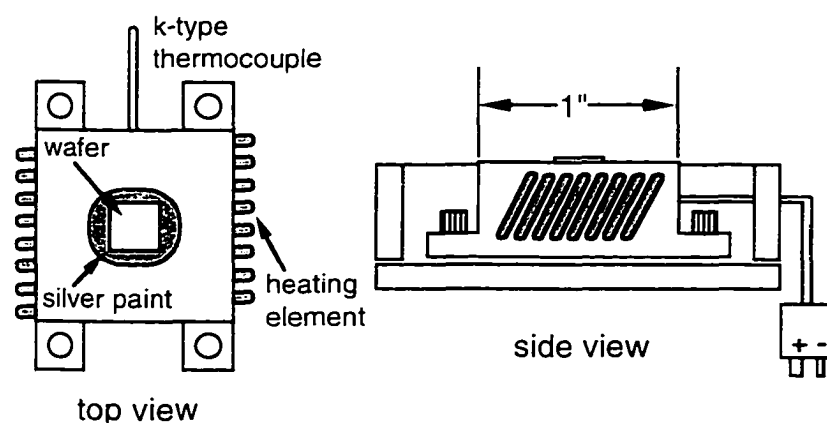
FIG. 3.3: WAFER HOT-STAGE SCHEMATIC

Substrates were fixed to the stage surface using silver paint. Before pumping

down the chamber, the stage and the freshly applied substrate were pre-heated to 100°C:

this insured that all of the silver paint solvents evaporated, and reduced the possibility

that the wafer could debond during pumpdown as a result of trapped liquid. Using this

configuration, stage temperatures approaching 800 °C could be reached. Typically, 20

minutes were allowed for the substrate stage temperature to stabilize. A k-type

thermocouple was inserted into the center of the block: all substrate deposition

temperatures refer to the value recorded at the block interior. It is likely that the wafer

surface temperature was considerably cooler than the block center. For depositions involving volatile species, block temperatures needed to be controlled to within 1 °C for accurate reproduction of results. Given the possibility of thermocouple aging, or accumulation of oxide at the thermocouple tip/heater block interface, the measured temperature needed to be corroborated by some other means. To verify the thermocouple measurements, the power consumption of the heater was carefully monitored as well. It was found that at constant thermocouple temperature readings, the hot-stage power consumption could vary considerably depending upon the wafer size, the last material ablated on the heater surface, or even the size of the silver paint spot surrounding the wafer. These effects are attributed to changes in the effective emissivity of the block face. To counter this, the surface of the heater was scraped with a razor-blade and etched with concentrated nitric acid after each deposition. In addition, while the silver paint was still tacky, any excess quantity was scraped from the stage surface. By following these precautions, the heater temperature could be reproduced between runs to within 1 °C using the identical current and voltage values. The optical properties of the target surface were also found to influence the heater temperature. When highly emissive target surfaces, such as $SrRuO_3$, were in place, the heater temperature was found to be increased as much as 10 °C compared to the case when lower emissivity materials (i.e., $BaTiO_3$) were used. The target material acts to change the amount of radiation absorbed, reflected, or re-radiated from, or back to, the hot stage.

3.2   Substrates

With the exception of the top electrodes, all samples were grown epitaxially on single crystal oxide substrates at elevated temperatures. Most frequently, $LaAlO_3$ was used due to its relatively low cost. $LaAlO_3$ wafers 3" in diameter were purchased from Lucent Technologies and subsequently machined into 1 cm^2 <100> edge-oriented squares by Commercial Crystal Laboratories. For most depositions, especially those involving process optimization, these pieces were too large, as a sample could be characterized both structurally and electrically using only a portion of the area. $LaAlO_3$ naturally cleaves along {100} type planes, thus, using a tungsten carbide scribe, the squares were commonly broken into 4 nearly equal sized pieces with approximate <100> edge orientations.

For some depositions, $SrTiO_3$ and $KTaO_3$ substrates (also (001)-oriented) served as the epitaxial templates. These materials were purchased from Commercial Crystal Laboratories. These wafers were purchased as 1 cm squares and their size was not further reduced. These substrates, as well as the $LaAlO_3$, had a surface roughness of 0.5 nm rms.

All three substrates used were either perovskite or pseudo-perovskite in structure, and thus served as excellent templates for epitaxial film growth. Table 2.1 lists the structures and relative room temperature lattice mismatches between the substrates and the epitaxial thin films. Lattice constant values are given for the simple-perovskite-based unit cells. The lattice mismatch values were calculated by dividing the difference of the film and the substrate lattice constant by the film lattice constant. The thermal expansion

coefficients (α) refer to values which have been averaged over the temperature range of

700 °C to room temperature.

TABLE 3.1: SUBSTRATE STRUCTURAL INFORMATION

Substrate	Lattice constant (Å)	Structure	Δ a$_o$ SrRuO$_3$	Δ a$_o$ PMN-PT (70/30)	α_l average ppm/°C
LaAlO$_3$	3.795 [146]	Rhombohedral pseudo-perovskite	0.135 Å 3.43 %	0.235 Å 5.83 %	11 [146]
SrTiO$_3$	3.902 [147]	perovskite	0.028 Å 0.71 %	0.128 Å 3.17 %	10 [148]
KTaO$_3$	3.988 [149]	perovskite	-0.058 Å -1.45 %	0.042 1.04 %	8 [148]

Prior to deposition, all substrates were cleaned in the same manner. A five minute

ultrasonication was performed in five liquids in the following order: Micro Laboratory

Solvent, deionized water, acetone, ethanol, and isopropanol. Using this procedure, a

particle and oil-free epi-polished surface was insured. The Micro Cleaner served as a

substitute for chlorinated solvents such as TCE (trichloroethylene) and TCA

(trichloroethane).

The SrTiO$_3$ substrates were further treated by etching with a buffered HF solution

following the procedure of Kawasaki.[150] A 10 molar concentration of a stock solution

containing 8.89 moles of NH$_4$F, 1.1 moles of HF, and enough water to arrive at 380 mL

of liquid is used. The pH of the final mixture is approximately 4.2. This acid treatment

is one of several methods which provides a smooth and TiO$_2$-terminated growth surface.

These etched substrate surfaces are characterized by a stepped appearance with the step

heights and terrace lengths determined by the miscut of the substrate from the desired

(001) orientation.[Theis, 1997 #150] Such surface preparations have been shown to be

beneficial in achieving non-cubic epitaxial thin films free of in-plane twinning.[118]

KTaO$_3$ is known to be volatile and will decompose rapidly at temperatures above 800 °C in air via K sublimation. Since reducing conditions will often promote decomposition of such phases at lower temperatures, substrates were not heated above 125 °C during pumpdown.

3.3   Deposition of SrRuO$_3$

SrRuO$_3$ thin films were deposited from a stoichiometric target purchased from Target Materials International. The specifics of the depositions are given in Chapter 4. An important consideration for SrRuO$_3$ thin films was their instability under vacuum at deposition temperatures. When exposed to these conditions, by x-ray diffraction, the SrRuO$_3$ was found to decompose. Though the thin film compositions were not directly measured in this study, previous reports indicate that Ru loss is the responsible mechanism.[108] As a result, prior to the deposition of the subsequent ferroelectric layers, the chamber was not evacuated with the heater on. Instead, the heater temperature was elevated to ~ 125 °C during pumpdown in order to remove as much adsorbed water as possible without compromising the quality of the SrRuO$_3$ electrode.

Due to the single target limitation of the PLD system, vacuum had to be broken between the deposition of the electrode and insulating layers. Given this limitation, to facilitate rapid film production, SrRuO$_3$ films were often deposited on four 1 cm^2 LaAlO$_3$ wafers at one time. The electroded wafers were then removed from the hot stage and cleaved and remounted as necessary. High quality SrRuO$_3$ films could be deposited uniformly over areas as large as 1 square inch. All SrRuO$_3$ films were cooled down immediately (T$_{sub}$ dropped below 500 °C in approximately 2 minutes) after deposition in 100 Torr of O$_3$/O$_2$.

3.4   PMN-PT target fabrication

PMN-PT (70/30) films were deposited from lead-enriched targets which were prepared in-house. The targets were processed using the following procedure. Stoichiometric PMN-PT (70/30) powder, both with and without Ba doping was processed following the columbite method.[6] Reagent grade $MgNb_2O_6$, PbO, $BaCO_3$, and TiO_2 powders were batched in stoichiometric quantities and milled for 12 hours in ethanol using 3 mm spherical stabilized zirconia media. The mixed powders were air dried, then calcined in an open crucible for 4 hours at 800 °C. The PMN-PT powder was then mixed with the desired quantity of PbO to arrive at the appropriate mass % excess, and ball milled in ethanol for 4 hours with similar media to insure homogeneous mixing. The PbO excess PMN-PT powder was again air-dried, then pressed in a 1" steel die at 20,000 pounds without binder. The resulting pellets were then placed on a Pt foil in an Al_2O_3 crucible and buried in Pb-source (a 70/30 mixture of PbO and $PbZrO_3$ powders). The crucible was loosely covered with a lid and fired at 900 °C for 1 hour. Using this procedure, less than 1 mass % was lost from the pellet during sintering. The target densities were typically around 8 g/cc, the specific value depending upon the exact amount of excess PbO.

3.5   Deposition of PMN-PT

All PMN-PT films were deposited in the oxygen/ozone mixed atmosphere using the on-axis ablation geometry. Specific processing parameters such as target to substrate distance, pressure, and temperature will be discussed in the results and discussion chapters as they pertain to experimental results.

It was necessary to cool the films as rapidly as possible to avoid a seriously Pb-depleted surface layer. In an attempt to accomplish this, the following procedure was used for each PMN-PT thin film deposition: when the appropriate deposition time had elapsed, the laser shutter was closed, the heater power supply was switched off, the gate valve was closed, and a O_2/O_2 gas line bypassing the micrometering valve used for pressure control was opened. These steps (when performed in this specific order) allowed the block temperature to be reduced to less than 500 °C in approximately 1.5 minutes. The chamber pressure was raised to 250 Torr before the gas lines were closed.

To insure that a portion of the bottom electrode was exposed for electrical property measurements, a stainless steel tab was fastened to the top radiation shield of the heater. The tab could be positioned to cover a small section of the electroded wafer before PMN-PT deposition. Because of the high pressures during growth, the tab must be in physical contact with the substrate to prevent deposition underneath.

A limited number of La and Mn doped $PbTiO_3$ samples were synthesized in the early stages of the project. Lead-enriched targets were also used for these samples: both the targets and thin films were prepared in an analogous fashion to that described above.

3.6   Top electrode deposition

Platinum top electrodes were used to complete the thin film capacitor structure. Platinum dots 0.30 mm or 0.50 mm in diameter were fabricated by room temperature deposition through a thin stainless steel shadow mask (Towne Technologies Inc.). The deposition conditions for the platinum are given in Table 3.2. The resulting films were approximately 5000 Å thick.

TABLE 3.2: PLATINUM TOP ELECTRODE DEPOSITION CONDITIONS

Target	Target to substrate distance	Pressure	Energy density	Frequency and time
Pt-metal	6 cm	vacuum	~ 10 J/cm²	20 Hz. 8 minutes

To avoid wasting costly material, the platinum target was not resurfaced after each deposition. In order to avoid a deep erosion track. the laser focusing lens and the target mounting position were varied such that the laser beam were incident on a new section of the target with each deposition. Since Pt is elemental. no danger of preferential ablation exists, thus relieving one of the major requirements for target resurfacing.

3.7 X-ray analysis

Because of the single crystal sample geometry, a four-circle instrument was required for structural analysis. The four diffractometer circles are necessary to bring the desired atomic planes into alignment with the θ-2θ circle. In addition, the four-circle geometry enables the in-plane texture of the films to be analyzed by rotation of the ϕ-circle (i.e., azimuthal scans or pole-figure analysis) at fixed θ-2θ values. The four diffractometer circles correspond to the scanning angles 2θ, θ, ϕ, and χ: a schematic illustrating the 4 x-ray circles is given in Fig. 3.4. In the figure, a sample is depicted with its surface oriented perpendicular to the θ-2θ-circle, i.e., $\chi=90°$.
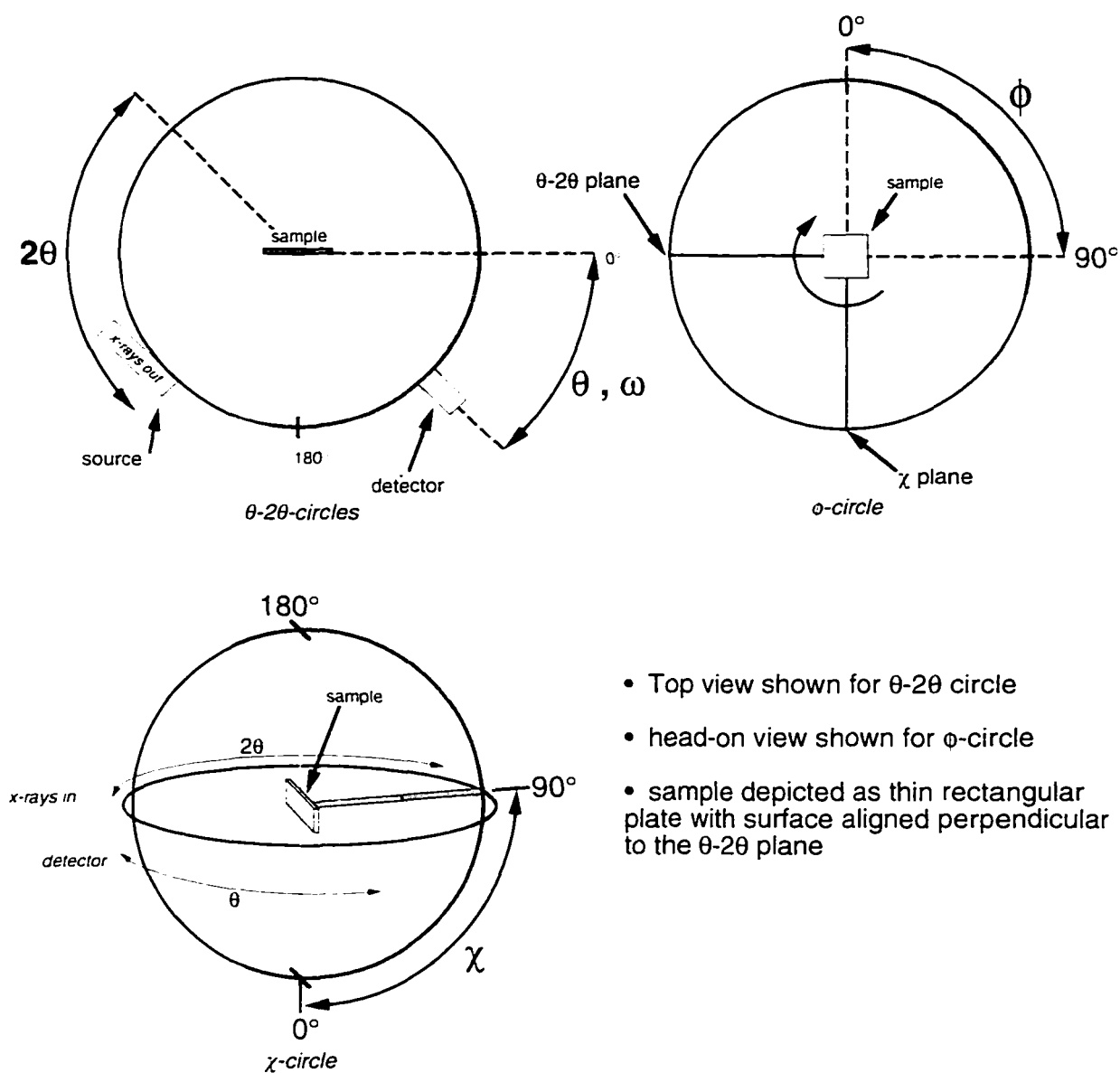
FIG. 3.4: SCHEMATIC OF 4-CIRCLE X-RAY DIFFRACTOMETER

Scans in which the θ and 2θ circles are changed simultaneously allow

measurements of interplanar spacings, thus information concerning phase identification

and out-of-plane orientation. Sweeping through values of θ-2θ satisfies the Bragg

conditions for diffraction through the relationship:

$$n\lambda = 2d\sin(\theta) \text{ [151]}$$ (8)

Typically, the Bragg conditions for d-spacings between ~0.9Å to ~ 30 Å can be satisfied by a standard (Cu anode) instrument (2θ values from 3° to 115°).

When the diffractometer is set to satisfy the Bragg conditions of a particular reflection, scans may be performed in which only the θ-circle is changed: in this case, the θ-circle may also be referred to as the ω-circle. Practically, this is accomplished by changing the angular position of the sample by rocking it about its eucentrically aligned vertical axis, the position of the detector is fixed. For this reason, the resulting diffraction pattern is often referred to as a rocking curve. The width of the rocking curve peak is indicative of the crystalline misorientation with respect to the out-of-plane crystallographic direction. The wider the rocking curve width, the greater the volume of material with an out-of-plane orientation tilted away from the substrate normal.

In order to analyze off-axis crystallographic planes, or those which are not parallel to the sample surface, the χ and ϕ-angles must be rotated from the standard positions of 90° and 0° respectively. For example, in a (001)-oriented rocksalt crystal, if the 1 1 1 diffraction line was to be satisfied, those planes would need to be brought perpendicular to the θ-2θ plane. (For reference, the crystal is assumed to be thin edge-oriented square plate with its surface perpendicular to the θ–2θ circle at χ=90°.) To observe this reflection, the ϕ and χ-circles would need to be rotated 45° and 32.7° from their original positions. These values correspond to the angles established between the plane of interest, and the reference axes. This situation is depicted in Fig. 3.5.
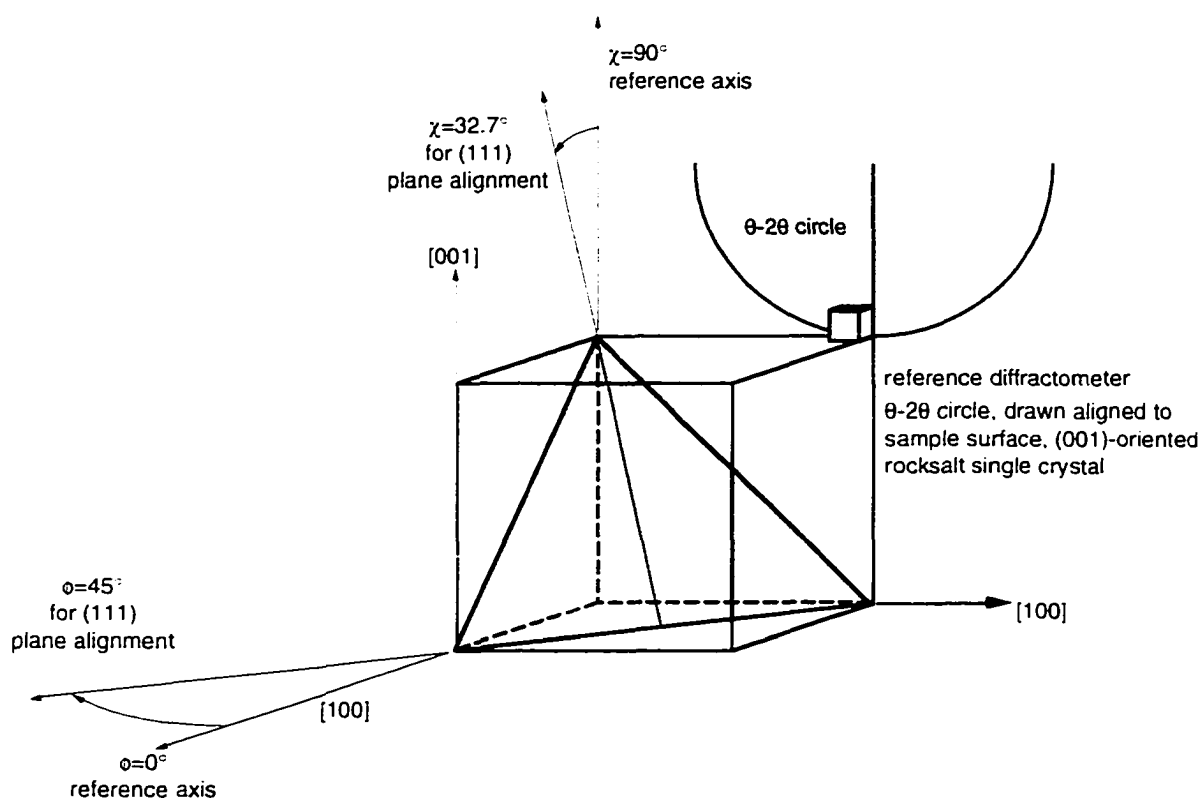
FIG. 3.5: ILLUSTRATION OF SAMPLE ORIENTATION FOR INVESTIGATION OF OFF-AXIS ATOMIC PLANES. HERE. THE SAMPLE IS ORIGINALLY ORIENTED WITH ITS SURFACE ((001)-PLANE) PERPENDICULAR TO THE θ-2θ CIRCLE. IN ADDITION. THE SAMPLE IS ORIENTED SUCH THAT THE [001] DIRECTION IS VERTICAL AT Φ=0°. IF THE INDICATED ANGULAR ROTATIONS WERE PERFORMED. THE (111)-PLANE WOULD BE BROUGHT INTO DIFFRACTING CONDITIONS. I.E.. PERPENDICULAR TO THE REFERENCE θ-2θ DIFFRACTOMETER CIRCLE

Once the appropriate angles have been established. an x-ray scan with a variable Φ angle can be performed to obtain information concerning the orientation of the crystal in the substrate plane. If the substrate is a single crystal. the Φ-scan reflections will reflect the symmetry of the particular crystallographic planes. In the case of the rocksalt material and a 111-reflection orientation, the 360° Φ-scan would show 4 peaks separated by 90°. These peaks correspond to the four positions around the pole at which the 111 planes rotate into the perpendicular orientation. If the sample has a random structure in the substrate plane. the scan would appear as a straight line of constant intensity. If the sample were twinned, then an extra set of 4 reflections would be observed. but shifted in

φ by the twinning angle. In general. the width of the phi-scan peak indicates to what

degree the sample exhibits a mosaic structure in the substrate plane. For a bulk single

crystal. the peak-width in φ and ω would be expected to be the same. however. for thin

films which have a directional growth and planar constraints established by substrate

lattice constant mismatch. these numbers are often different.

Scanning in the χ-circle at a diffraction line would give an identical result as a

rocking curve. Practically. however. this type of scan is not performed since this circle

has an inferior angular resolution in comparison to the θ-circle. The divergence of an x-

ray beam which has been monochromatized using a pyrolytic graphite is not symmetric.

That is. the divergence along the vertical beam section is much larger than that along the

horizontal section. The minimum peak width is in part determined by the beam

divergence. thus the monochromator is oriented such that the low divergence direction is

parallel to the θ-2θ plane. As a result. the angular resolution in χ is approximately 1.5°.

To perform these various x-ray scans. a Picker 4-circle x-ray diffractometer was

employed. The diffractometer was operated using $Cu_{K\alpha_1}$ radiation and was equipped with

a graphite monochromator and a scintillation detector. From measurement of the 400

reflection of single crystal silicon. instrumental resolutions of 0.15° and 0.25° in 2θ and

ω respectively. were determined. Resolution in the φ-circle was 0.4°. as measured from

the 220 reflection of the same Si sample. The x-ray tube was run at 1200 W for all scans.

For 2θ or ω scans, the diffractometer was stepped at 0.1° increments with a count time of

5 seconds. For φ–scans. the step size was increased to 0.25°. In some of the x-ray scans.

reflections labeled as "ghost-peaks" are present. These diffraction events are the result of

integer quotients (i.e., $\lambda/2$, $\lambda/4$, etc.) of the desired characteristic wavelength passing

through the monochomator. Additionally, reflections from tungsten radiation occur, and are attributed to W contamination of the Cu anode in the x-ray source.

When accurate values of the out-of-plane lattice constants were required, the Nelson-Riley method for fitting a family of x-ray reflections was used.[151] This method corrects for errors stemming from incorrect sample heights and x-ray absorption through the sample thickness.

3.8   Electrical property analysis

Electrical property measurements, including the temperature dependence of the dielectric constant and dielectric loss as well as the polarization-electric field hysteresis were performed on the PMN-PT thin films. The polarization hysteresis was measured using an RT66A standard ferroelectrics tester. For these measurements, electrical contacts were made using point probes. In addition to the RT66A instrument, an external 100x amplifier (AVC Instrumentation 790 Series Power Amplifier) was added to allow high field measurements on thicker samples. For some samples, it was necessary to measure the hysteresis below room temperature. This was accomplished by submerging the sample in a petri dish filled with liquid nitrogen; point probes were again used to electrically contact the sample.

The temperature dependence of the dielectric constant and dielectric loss was measured both above and below room temperature. To do so, a laboratory oven equipped with both heating and refrigeration capabilities was utilized. For these measurements, samples were mounted onto alumina 16 pin chip carriers with air-dry silver paint. Connections between the sample electrodes and the chip carrier bonding pads were made

by ultrasonic wire bonding. It was possible to wire bond to the PLD platinum, as well as directly to the $SrRuO_3$ surface, with 25 μm diameter aluminum wire. The chip carriers were inserted into the oven and contacted with either spring loaded probes or alligator clips. Using this equipment, temperatures between -165 °C and 210 °C could be achieved. The bridge used to make dielectric constant and loss measurements was a Hewlett Packard 4284A LCR meter. Data was collected for all samples at four frequencies: 10^1, 10^2, 10^3, and 10^4 Hz. An oscillator voltage of 0.005 V was used - this corresponds to the smallest measuring voltage possible, and a field of 0.055 kV/cm for a 1 μm thick film.

3.9   Electric field dependent x-ray analysis

With the capabilities of the Oak Ridge National Laboratory High Temperature Materials Laboratory Users Facility, an in-situ x-ray analysis of the piezoelectric strain was performed. A 4-circle x-ray diffractometer equipped with a rotating anode source and a 100 μm spot size capability was used. The interplanar spacing of epitaxial thin films was measured as a function of applied electric field. Details of the setup are given in chapter 7.

In addition to the measurements on thin film samples, in-situ field dependent x-ray analysis was also performed on (001)-oriented $Pb(Zn_{1/3}Nb_{2/3})$ - 4.5 % $PbTiO_3$ single crystals. Given the larger sizes of these samples (typically thin plates ~ 4 mm^2 area), the 4-circle Picker diffractometer provided the necessary x-ray intensity and resolution. Details of this investigation are also given in chapter 7.

3.10 d_{31} characterization by wafer flexure

A small modification to the wafer flexure method developed by Shepard *et al.* was used for d_{31} characterization of PMN-PT samples. The wafer flexure method relies on the ability to pressurize or evacuate a cavity over which a simply supported wafer is placed. With knowledge of the pressure inside of the cavity and the specific mechanical boundary conditions, small deflection plate theory may be used to predict the stress and strain values present on the wafer surface where the piezoelectric thin film resides. In the ideal case, the mode of stress is biaxial tension when the cavity is pressurized, and biaxial compression during cavity evacuation. During measurement, the cavity pressure is periodically oscillated between evacuated and pressurized states using the output of an audio speaker. During this stress oscillation, a charge integrator is connected to the sample which measures the piezoelectric current, and allows calculation of the stress-induced polarization. Prior to the modification, this technique was limited to films deposited on 3" or 4" diameter substrates.

To make measurements on epitaxial samples, small wafer chips (typically 5 mm on a side) were bonded in the center of 3" Si substrates using a cyanoacrylate based adhesive (Durabond superglue). The chips were oriented with their [001] direction coincident with that of the underlying silicon. Since unmodified plate-theory could no longer be applied to this composite assembly, strain gauges (120 Ω chrome aluminum alloy), were used to directly measure the strain during pressure oscillation. With this information, and knowledge of the PMN-PT elastic moduli, the transverse piezoelectric coefficient can be calculated. Calibration and comparison with data from the unmodified apparatus are discussed in Chapter 5.

3.11 Other characterization techniques

Other characterization techniques included high temperature x-ray diffraction. AFM analysis, STM analysis, and spectroscopic ellipsometry.

High temperature x-ray diffraction was performed using a Picker 2-circle diffractometer equipped with a radiant furnace capable of reaching 1100 °C. A detailed description of the instrument and its operating characteristics can be found by Huang.[152]

AFM images were taken using an Auto-probe instrument equipped with a Si tip in contact mode. All AFM measurements were performed with the aid of David Gundlach and Dr. Tom Jackson at the Penn State Electrical Engineering department.

STM analysis was performed with Nanoscope III STM in vacuum. The images were collected in constant current mode with a tip bias of 1.2 V. Both etched and machined PtIr tips were used. These measurements were performed at Los Alamos Nartional Laboratory.

Spectroscopic ellipsometry data was collected as a function of temperature using a rotating analyzer instrument (rotated at 50 turns/wavelength) at a 70° angle of incidence. The data was dark current corrected to account for any radiation component originating from the sample hot-stage. The wavelength range between 250 and 750 nm was used.

Chapter 4   Strontium Ruthenate Structure-Property Relationships

Previous work on $BaTiO_3/SrRuO_3/SrTiO_3$ heterostructures indicates that the structure and properties of pulsed laser deposited $SrRuO_3$ epitaxial films showed a marked dependence on the intensity of energetic bombardment during growth.[109] In general, it was found that deposition conditions which favored strong bombardment atmospheres (i.e., ambient pressures ≤ 100 mTorr) resulted in $SrRuO_3$ with anisotropically extended lattice constants and increased electrical resistivities. In particular, the out-of-plane lattice constants could be extended by as much as 4% when deposition pressures were reduced to ~ 20 mTorr, as compared to bulk lattice constants for samples deposited at pressures > 200 mTorr, all other parameters being constant. The in-plane constants were also found to expand, however, the expansion was limited to < 1%. The differences were shown to be a result of bombardment by performing a series of experiments using mixed gas atmospheres.[116] The mixed gas atmosphere was used to isolate bombardment effects from potential influences arising from incomplete oxidation. The previous work was limited to x-ray diffraction and resistivity analysis of $SrRuO_3$ films on $SrTiO_3$. This follow-up investigation considers deposition on other substrates, temperature-dependent structural properties, as well as work on the surface morphology, optical properties, and powder measurements.

4.1   Structural analysis

Films processed under both high and low bombardment conditions were grown on

etched (001)–oriented SrTiO₃ substrates. The high and low bombardment conditions

were achieved by changing the ozone/oxygen pressure during deposition. Low

bombardment films were processed at 180 mTorr, while highly bombarded films were

deposited at 20 mTorr. The films were deposited to approximately the same thickness

(~1500Å). Table 4.1 gives the other pertinent process parameters.

TABLE 4.1:   PROCESSING PARAMETERS FOR SRRUO₃ THIN FILMS

SrRuO₃ deposition conditions	
Pressure	20 – 200 mTorr
Temperature	680 °C
Target to substrate distance	8 cm
Laser power	200 mJ/pulse
Target	Stoichiometric ceramic SrRuO₃
Energy density	~ 1.5 J/cm²

The SrTiO₃ substrates used were miscut approximately 0.5° along one of the

<001> directions. The miscut along the perpendicular in-plane axis was similar less than

the diffractometer resolution (≤0.1°).

After deposition, samples were structurally analyzed by 4-circle x-ray diffraction.

Fig. 4.1 shows the θ-2θ diffraction pattern for the high pressure deposited sample.

FIG. 4.1: θ-2θ PATTERN OF SRRUO₃ ON SRTIO₃ DEPOSITED UNDER LOW BOMBARDMENT CONDITIONS. PEAKS INDEXED WITH 00ℓ INDICATE SUBSTRATE REFLECTIONS

As shown in the figure, the sample is well oriented with a peak width equivalent to that of the instrument resolution. The splitting in the SrRuO₃ 004 reflection is a result of the Cu K_{α} radiation component. The ability to observe this splitting is indicative of the high crystalline quality. For improved accuracy, the out-of-plane lattice constant was determined using the Nelson-Riley method. This analysis uses a family of reflections to determine the lattice parameters, and effectively corrects for sample height adjustment and x-ray absorption errors. In general, the interplanar spacing of the unit cell is calculated using each of the available (00ℓ) reflections. These numbers are plotted against the Nelson-Riley function, where the θ-angles correspond to values for the respective reflections:[151]

$$\left(\frac{\cos^2 \theta}{\sin \theta} + \frac{\cos^2 \theta}{\theta} \right)$$

(10)

The resulting y-intercept of the best fit straight line gives the corrected interplanar spacing. Using this treatment, a parameter of 3.94 ± 0.01 Å was calculated. This method could not be used for calculation of the in-plane value since the appropriate family of reflections are not available to our instrument (i.e., at $\phi=\omega$). The in-plane value was determined to be 3.94 ± 0.02 Å by measurement of the 222 reflection, and subsequent calculation. These numbers are equivalent to the bulk $SrRuO_3$ lattice parameters to within the instrument accuracy.

Fig. 4.2 shows a rocking curve of the $SrRuO_3$ 002 peak. A width of $0.2°$, which again corresponds to instrumental resolution was recorded. In Fig. 4.2, the sample surface is aligned with the diffractometer axes, thus, upon rocking curve analysis, the miscut of the substrate may be determined: in this case a value of $0.5°$ was measured. The wafers were <100> edge oriented, so the crystallographic direction of the miscut could be determined.
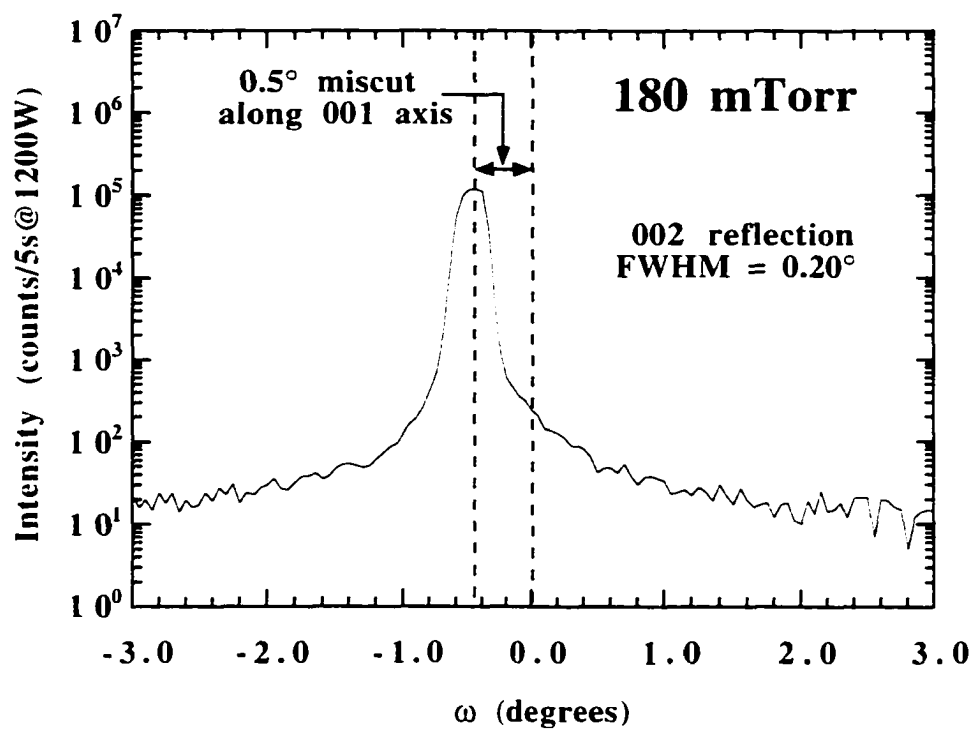
FIG. 4.2: ROCKING CURVE OF SRRUO₃ ON SRTIO₃ DEPOSITED UNDER LOW BOMBARDMENT CONDITIONS. THE SRRUO₃ 002 REFLECTION IS USED

The structural analysis of a sample deposited under the more strongly bombarding conditions (i.e.. a deposition pressure of 20 mTorr O_3/O_2) is shown in Figs. 4.3 and 4.4.
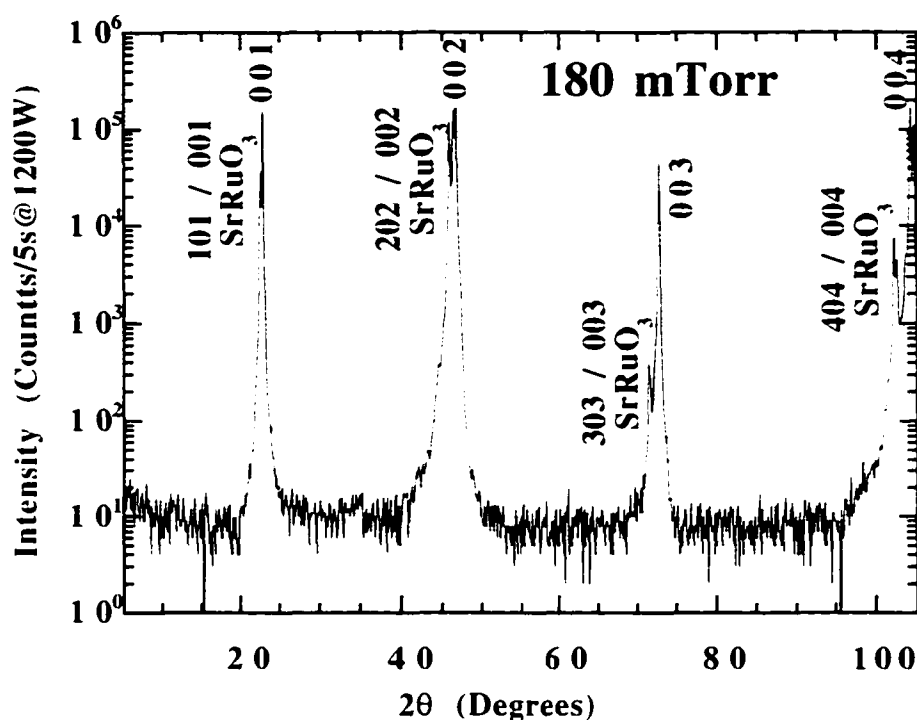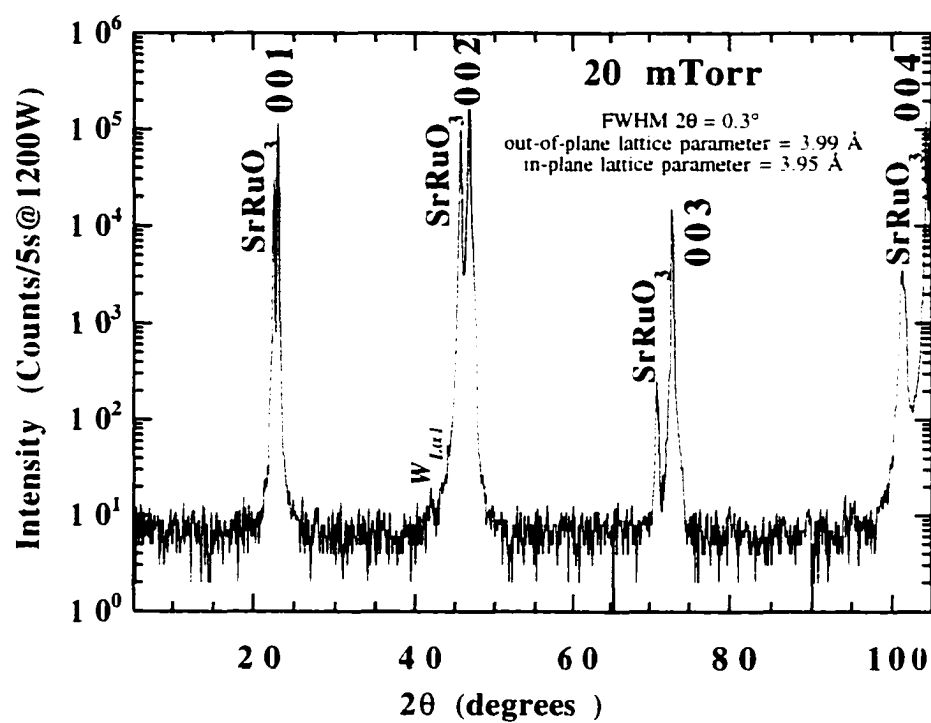
FIG. 4.3: θ-2θ PATTERN OF SrRuO₃ ON SrTiO₃ DEPOSITED UNDER STRONGLY BOMBARDING CONDITIONS. PEAKS INDEXED WITH 00ℓ INDICATE SUBSTRATE REFLECTIONS

The figure shows a rocking curve plot. The y-axis is labeled "Intensity (counts/5s @ 1200W)" with values from 10^0 to 10^7. The x-axis is labeled "ω (degrees)" ranging from -3.0 to 3.0. Annotations on the plot read: "002 reflection FWHM = 0.2°", "20 mTorr", and "0.6° miscut along 001 axis".
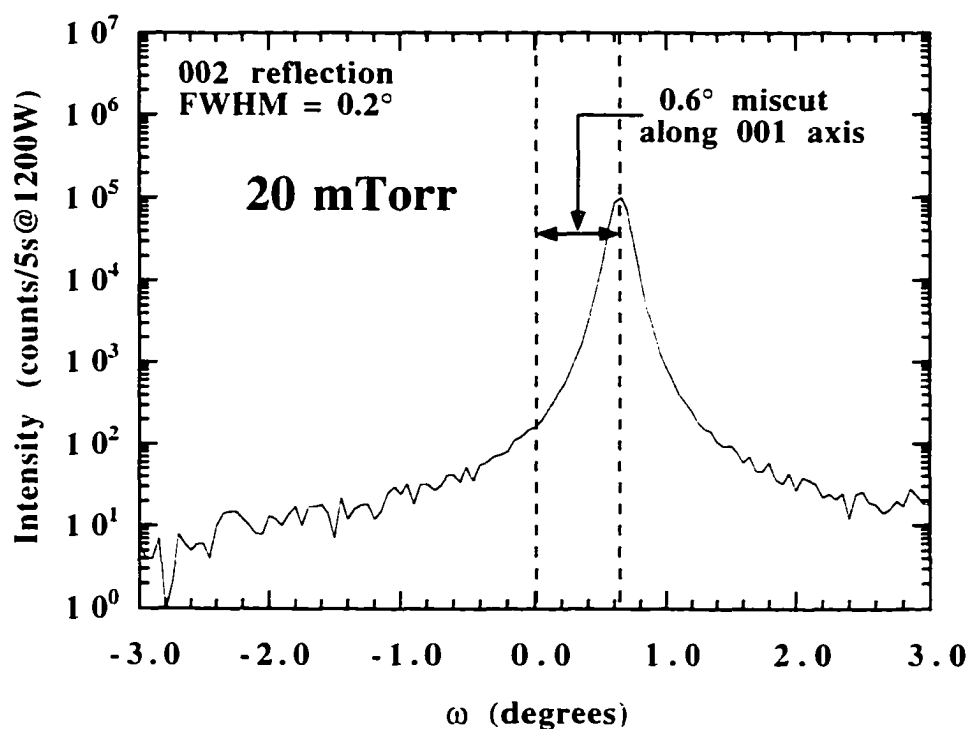
FIG. 4.4: ROCKING CURVE OF SRRUO₃ ON SRTIO₃ DEPOSITED UNDER LOW BOMBARDMENT CONDITIONS. THE SRRUO₃ 002 REFLECTION IS USED

Using the same mathematical treatment of the x-ray data. an out-of-plane lattice constant of 3.99 ± 0.01 Å was determined. From the 222 reflection. the in-plane spacing was found to be 3.95 ± 0.01 Å. Thus, decreasing the deposition pressure by 160 mTorr resulted in a 1.5 % increase in the out-of-plane lattice constant. Further decreases in the pressure or target to substrate distances resulted in extensions as large as 4 %.[116] It is also apparent from these figures that the presence of strong bombardment during growth results in a modest degradation in the crystallinity in addition to its effect of anisotropically extending the lattice constants. Though the full width half maximum values for reflections in the 2θ and ω circles do not change a significant amount. increased crystalline disorder is reflected in the inability to distinguish the $K_{\alpha2}$ radiation

component in the 004/404 reflection of the heavily bombarded film. In addition. the full width quarter maximum value in ω is appreciably larger.

The extended lattice constants in $SrRuO_3$ are believed to be a result of energetic bombardment by the ionized and neutral target species accelerated by plume expansion and a space charge field. Due to the nature of laser-solid interactions. complicated combinations of positive. negative. and neutral species exist in the plasma. This makes direct quantitative analysis difficult in comparison to sputtering plasmas where species' energies and populations may be well known.[90] Many studies of laser-induced plasmas have been reported. and indicate that at sufficiently low pressures and sufficiently small target-to-substrate separation distances. bombarding species with enough energy to damage solids impinge upon the substrate. For example. Zheng et al. reported. for the deposition of $YBa_2Cu_3O_{7-\delta}$ in vacuum, mean kinetic energies between 40 and 85eV for the ionic species at a distance of 7 cm from the target surface; time of flight mass spectrometry was used.[135] Using optical emission to study a lead zirconate titanate (PZT) plasma plume. Kurogi et al.[136] observed 60 eV titanium species 5 cm from the target under vacuum conditions. Furthermore. as pressures were increased to 200 mTorr. the energy of the titanium species were found to decrease to < 1 eV. thus indicating that as ambient pressures in PLD are increased. sufficient thermalization occurs. resulting in plasma species in the vicinity of the substrate with near kT energies.

These studies clearly indicate that the PLD process in vacuum produces species with energies large enough to damage the solid surfaces upon which they impinge. Sigmund[153] studied the effects of the Si^+ bombardment of Si surfaces both theoretically and experimentally. His findings indicated that the energy threshold for vacancy

production by atomic displacement was ~ 16 eV: energies easily achieved by laser plasma species. The penetration depth of the ions as determined by TRIM-code calculation was ~ 5 Å. In PLD, since the bombardment occurs *in-situ* with film growth. 5 Å penetration would be sufficient to produce defects or damage throughout the film thickness. Friedland investigated the argon ion implantation of MgO single crystals and determined the energy threshold for atomic displacement to be ~ 60 eV. This estimation may provide a more reasonable comparison to perovskite structures.[154]

It is clear that the extension of lattice constants is coupled with energetic bombardment during deposition. however, the mechanism responsible for the lattice constant extension is not well understood. Possibilities include collision-induced displacement of ions into non-equilibrium lattice locations, implantation of Sr. O. or Ru. resputtering of Sr or Ru. or composition differences resulting from relative cation distributions in the laser plasma which are pressure dependent.[155] Marwick *et al.*[156] observed a similar effect in the electrical properties of $YBa_2Cu_3O_{7-\delta}$ after O^+ ion bombardment: with increased amounts of exposure, a metal-insulator transition was induced. Such a transition in our samples was not observed. however previous results suggest that with sufficiently reduced pressure a sign reversal in the temperature coefficient of the resistivity at low temperatures might occur.[116] Such an observation has been reported by Hiratani *et al.*[119] at deposition pressures below 10 mTorr, although they attributed their effect to the oxidation state of the constituent cations.

4.1.1   In-plane texture analysis

Since the actual crystal structure of bulk $SrRuO_3$ is orthorhombic. with the pseudo-cubic cell [001] direction lying colinear with the orthorhombic [110] or [001]. several twinning geometries are possible given a c-axis pseudo-perovskite orientation.[147] The occurrence of these twinning arrangements can be determined by a combination of appropriate x-ray scans.

Film reflections which do not have coincident pairs need to be chosen to determine the orientation of the orthorhombic cell. In this case. "coincident pairs" refer to a set of reflections which satisfy the same. or very similar diffraction conditions in the orthorhombic and pseudo-cubic unit cell constructions. For example. a $(011)_{ortho}$ ϕ-scan of a single domain orthorhombic crystal would ideally show only two peaks separated by $180°$. However. experimentally in such a scan. the Bragg conditions for the pseudo-cubic $\{111\}$ (the specific family member depending upon the pseudo-cubic reference axes chosen) are also satisfied. and their reflections (separated by $90°$) are superimposed on the $(011)_{ortho}$ ϕ-scan.

Given the near cubic symmetry of the distorted $SrRuO_3$ perovskite. its (001)-orientation. and the perpendicular orientation of the θ-2θ circle with the (001) crystal surface. ϕ-scans of all simple perovskite reflections will reflect the m3m symmetry group. Because of this condition. only a reflection peculiar to the orthorhomic cell may be used (Fig. 2.9 illustrates the superimposed unit cell constructions). The 131_{ortho} family of reflections satisfies this requirement. as the $(131)_{ortho}$ plane actively diffracts. while the similar plane in the pseudo-cubic cell does not (in the pseudo-cubic cell. this plane is a mathematical construction only).

The first type of twinning to be discussed refers to the orientation of the b-axis with respect to the substrate normal - this will be referred to as out-of-plane twinning. Since the $(010)_{ortho}$ diffraction line is extinct, out-of-plane twinning cannot be distinguished from one θ-2θ-scan alone; multiple scans looking for different reflections must be performed. Considering a fixed set of reference axes, the χ-values necessary to satisfy the Bragg conditions for the non-coincident 131 planes of both orientations are different, thus, in order to prove the existence of either orientation, the $\bar{1}31$ reflections at the appropriate χ angles must be found. If a particular {131} reflection is found for each orientation (i.e., at different ϕ-angles), than the film is twinned, if only one orientation is observed, that orientation is predominant. Fig. 4.5 depicts this situation. In this figure, the two out-of-plane orientations for the orthorhombic cell are illustrated. Superimposed on the unit cells are the 131 planes, and the χ-angle at which the diffractometer must be set in order to bring the 131 planes into a position where the Bragg conditions for diffraction are satisfied.

b-axis orientation
χ = 33.69°
Φ = 0°, 90°, 180°, 270°

a/c-axis orientation
χ = 56.3°
Φ = 0°, 180°
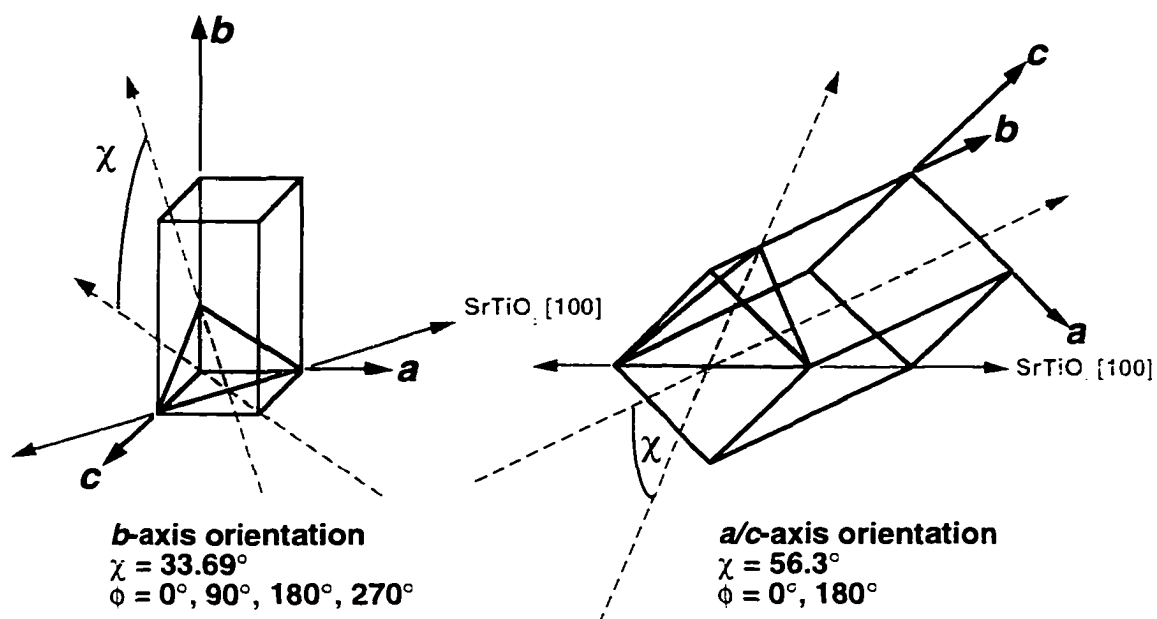
FIG. 4.5: POSSIBLE ORIENTATION OF SRRUO₃ ON SRTIO₃ SHOWING THE REQUIRED χ-VALUE TO SATISFY DIFFRACTION CONDITIONS

The second type of twinning concerns the orientations of the longer b-axes in the plane of the substrate. In order to identify this type of twinning, Φ-scans of non-coincident planes are now required; the symmetry of the resulting Φ-scans will directly reflect the sample's in-plane texture. If all b-axes are aligned in the same direction (the case for an untwinned film), then the Φ-scan will have 2-fold symmetry. If the b-axes are randomly aligned, (i.e.. 50% directed along [100] and 50% along [010]) the Φ-scan will show 4-fold symmetry. If the film has a preferred alignment, that is, greater than 50 volume % oriented in one direction, the scan will still show 4 reflections with the relative intensities reflecting the orientation distribution.

On an isotropic surface, no preference for the b-axis should exist, thus the in-plane texture would be expected to reflect a random distribution of b-axes pointing along either the substrate [100] or [010] directions. Since the (001) surface of SrTiO₃ exhibits

4-fold symmetry. no single orientation should be thermodynamically preferred.

Practically. however. a non-random twinning occurs. and appears to result from vicinal

substrate surfaces.

When a substrate is vicinal (i.e.. the substrate normal is not exactly collinear with

the desired crystallographic direction). the resulting surface morphology is characterized

by steps and terraces whose gradient runs along the miscut direction.[150] For typical

miscut angles ($\leq 0.5°$ i.e.. the standard manufacturer's orientation specification) these

steps are typically one unit cell high. and the terraces are several unit cells deep. If the

miscut is along the [100] direction. the terraces tend to align in neat rows with the step

edges following the [010] direction. This behavior is demonstrated by high resolution

AFM in Fig. 4.6.
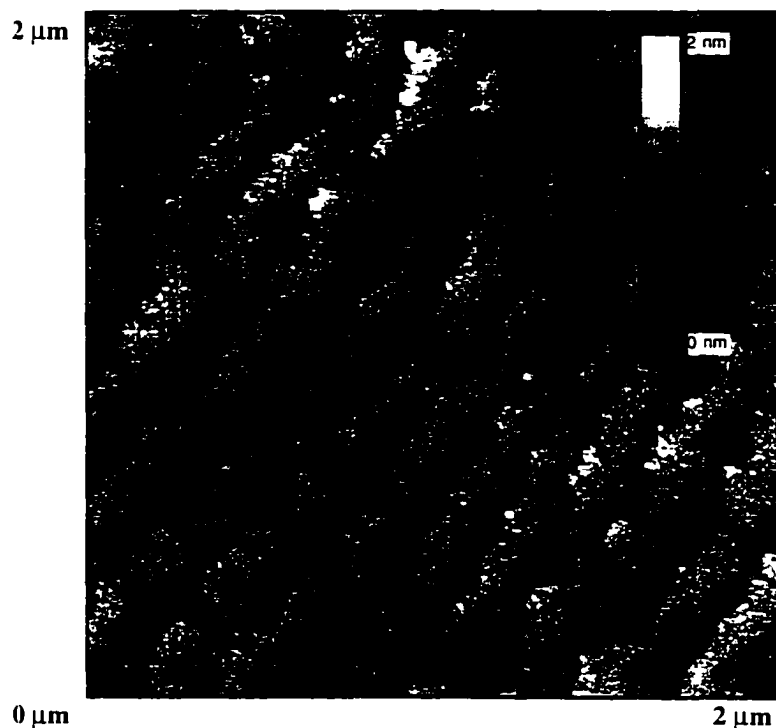
FIG. 4.6: AFM IMAGE OF KAWASAKI ETCHED (001) ORIENTED SRTiO₃ SUBSTRATE. STEP TERRACES FOLLOW A <001> DIRECTION. THE SUBSTRATE IS MISCUT PERPENDICULAR TO THE TERRACES BY ~ 0.5° (IMAGE COURTESY OF M. E. HAWLEY AT LOS ALAMOS NATIONAL LABORATORY)

When SrRuO₃ is deposited on such miscut substrates, the resulting thin films tend towards the untwinned state with nearly all of the *b*-axes aligned parallel to the step terraces or edges. Fig. 4.7 shows a phi-scan of the 131 reflection family of a lightly bombarded SrRuO₃ thin film deposited on a slightly miscut SrTiO₃ substrate. The clear two-fold symmetry of this scan suggests an untwinned microstructure.

10^3

10^2

10^1

10^0

Intensity (counts/10s@1200W)

13$\bar{1}$ 13$\bar{1}$ 13$\bar{1}$

180 mTorr

0   90   180   270   360

ϕ (degrees)
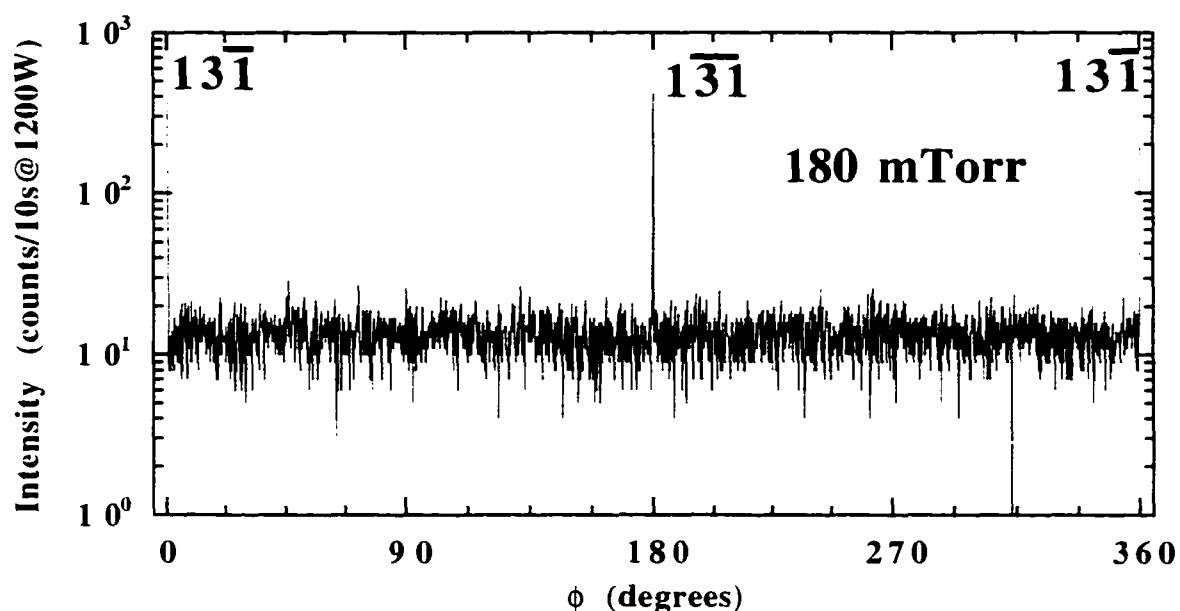
FIG. 4.7: ϕ-SCAN OF AN UNTWINNED $SrRuO_3$ THIN FILM DEPOSITED UNDER THE LOW BOMBARDMENT CONDITIONS. THE TWO-FOLD SYMMETRY OF SCAN SUGGESTS THE ABSENCE OF MULTIPLE IN-PLANE ORIENTATIONS

This ϕ-scan corresponds to the situation where the long axis lies in the plane of the substrate (c/a–axis orientation). For this and other samples, the orthogonal out-of-plane orientation, where the long axis is perpendicular to the substrate plane, was also investigated. No evidence was observed indicating its presence.

Still other similar sets of reflections can be used to look at the in-plane alignment of the $SrRuO_3$. The 131 reflections shown indicate that the film is perfectly aligned in-plane, however, the peaks are weak, which leaves the possibility that some diffracted intensity corresponding to orthogonally oriented material may exist below the noise threshold. To investigate this possibility, the ϕ-scan of the $SrRuO_3$ 212 reflections was used; these reflections are more intense, thus any twinned regions should become

apparent. Fig. 4.8 shows this data. Using these more intense reflections, approximately

1 volume % of orthogonally oriented is observed.

Φ (degrees)
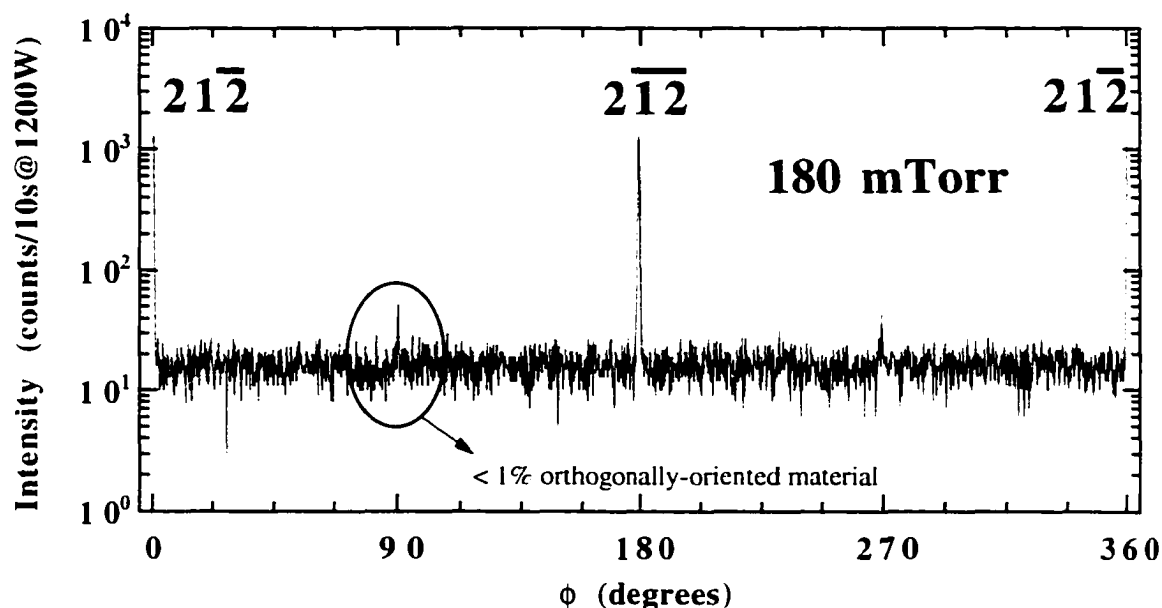
FIG. 4.8: Φ-SCAN OF AN UNTWINNED $SrRuO_3$ THIN FILM. PEAKS AT 90° AND 270° INDICATE
APPROXIMATELY 1% ORTHOGONALLY ORIENTED MATERIAL

It has been shown in previous reports that increasing the miscut angle will result

in complete in-plane alignment. In these reports it was proposed that the cause of this

preferred orientation is a preferred a or c-axis nucleation and subsequent step flow

growth.[117,118]

Though previous researchers have referred to similar $SrRuO_3$ thin films on $SrTiO_3$

substrates as single domain single crystals, the possibility of a third, and more subtle

twinning remains.[117] When a film is oriented similar to that shown in Fig. 4.8, i.e.,

nearly all b-axes lying in-plane and collinear, the crystal axis normal to the substrate can

be either [101] or $[\bar{1}0\bar{1}]$. For the high angle reflections appropriate for detection of twin-

induced peak splitting, i.e., 440 and 044, there is an angular difference of 0.45° 2θ. This corresponds to the approximate detection limits of our instrument, and thus could not be discerned. Whether these samples truly represent single domain single crystals is not known.

The same scans were attempted for the $SrRuO_3$ films deposited under the heavily bombarding conditions. In these samples, despite extensive searching, reflections corresponding to either the {212} or {131} families could not be located. Following this result, it was concluded that the true symmetry of the bombarded $SrRuO_3$ was not orthorhombic, as those reflections which occur exclusively for that symmetry are absent. The observed reflections in combination with the in and out-of-plane lattice constants suggest a tetragonal simple perovskite structure.

To further demonstrate how the oriented in-plane microstructure depends upon the substrate surface microstructure, a $SrRuO_3$ film was deposited on a nominal $LaAlO_3$ substrate under low bombardment conditions (~ 150 mTorr). A φ-scan of the 212 reflection family was performed, the results of which are shown in Fig. 4.9. The peak intensities are considerably smaller, and the peak widths significantly broader than those observed for films on $SrTiO_3$ as a result of the larger lattice mismatch (~3.5%). The four-fold symmetry of the diffraction pattern indicates the in-plane twinning microstructure.
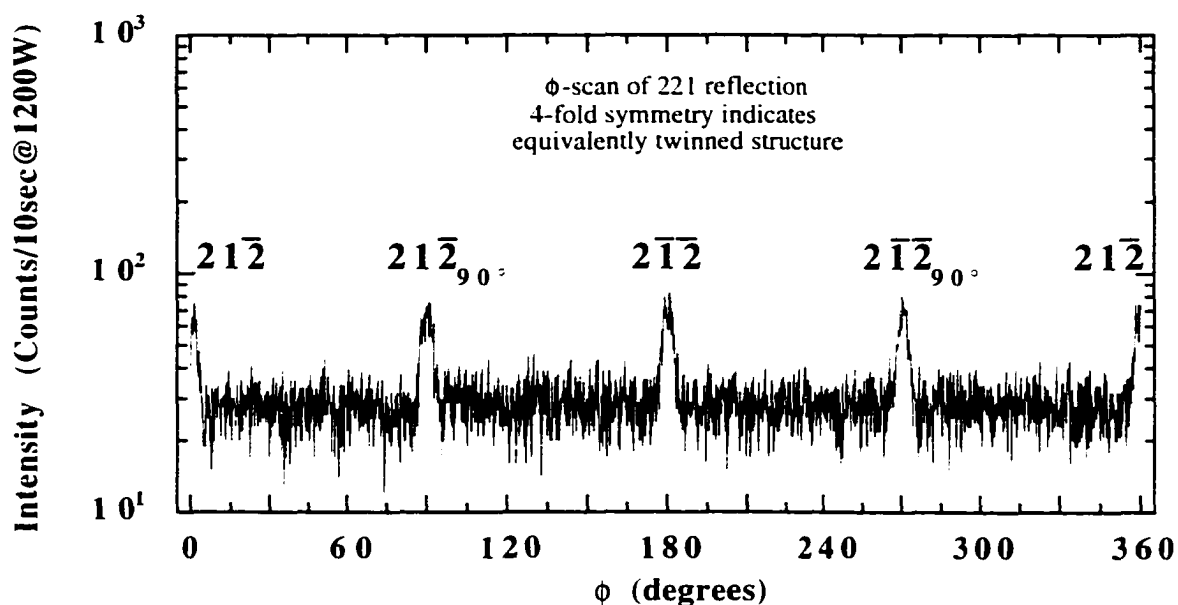
FIG. 4.9: Φ-SCAN OF A TWINNED SRRUO₃ THIN FILM DEPOSITED ON LAALO₃. PEAKS INDEXED WITH 90°
SUBSCRIPTS INDICATE RANDOM IN-PLANE TWINNING

In addition to the x-ray analysis, high resolution STM images were collected for

films deposited under both atmospheres. The surfaces of the $SrTiO_3$ substrates prior to

$SrRuO_3$ deposition were similar to the image given in Fig. 4.6. Fig. 4.10 shows a surface

image of a film deposited on $SrTiO_3$ under high pressures. This surface image

demonstrates the stepped nature of the $SrRuO_3$ thin film. Since the stepped morphology

has been conserved, edge-defined growth is the likely mechanism during deposition.

Line scans of this surface indicate a root mean square (rms) roughness value of 4.7 Å,

while linear stereology gave a terrace length of ~ 55 nm. This is quite close to the

average terrace length of 45 nm calculated assuming unit cell high $SrTiO_3$ surface steps,

and accounting for the 0.5° miscut.
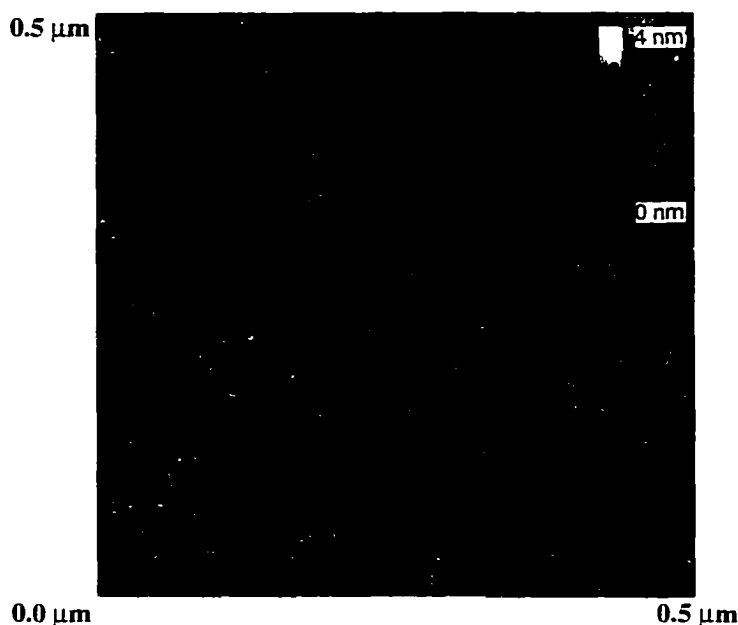
FIG. 4.10: HIGH RESOLUTION STM IMAGE OF A SRRUO₃ THIN FILM DEPOSITED UNDER A LIGHTLY BOMBARDING ATMOSPHERE – 180 MTORR OZONE/OXYGEN (IMAGE COURTESY OF M. E. HAWLEY AT LOS ALAMOS NATIONAL LABORATORY)

Fig. 4.11 shows a similar surface image of a SrTiO₃ film deposited under heavily bombarding conditions. From this image it is apparent that a more pronounced surface morphology has developed. Using the same procedure, an rms roughness of ~ 7.3 Å was determined with an average terrace length of ~ 160 nm. The increased surface roughness manifests itself in supersteps which run along the original substrate terraces. Again. the step-like features suggest edge-defined growth, however, compared to the previous surface image, the low pressure deposited surface has a coarsened appearance. This type of morphology is consistent with the increased surface adatom mobility which would be expected for a deposition accompanied by strong energetic bombardment.
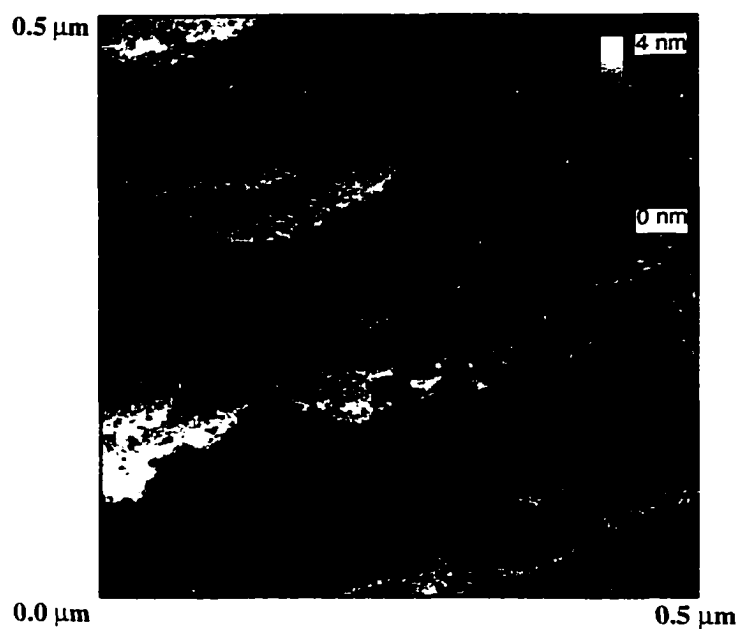
FIG. 4.11: HIGH RESOLUTION STM IMAGE OF A SRRUO₃ THIN FILM DEPOSITED UNDER AN ATMOSPHERE PROVIDING HEAVY BOMBARDMENT - 20 mTORR OZONE/OXYGEN (IMAGE COURTESY OF M. E. HAWLEY AT LOS ALAMOS NATIONAL LABORATORY)

In addition to the images collected for $SrRuO_3$ deposited on $SrTiO_3$ substrates, an AFM image respective of the $SrRuO_3$ thin film surface morphology developed when grown on $LaAlO_3$ is shown. This figure is included since all PMN-PT thin films which will be discussed in the following chapters were deposited on this type of surface. Figure 4.12 shows the AFM result. This surface morphology will be of importance upon consideration of the surface microstructures of the subsequently deposited layers. From line scans across the film surface. an rms roughness of ~ 10 nm was determined.
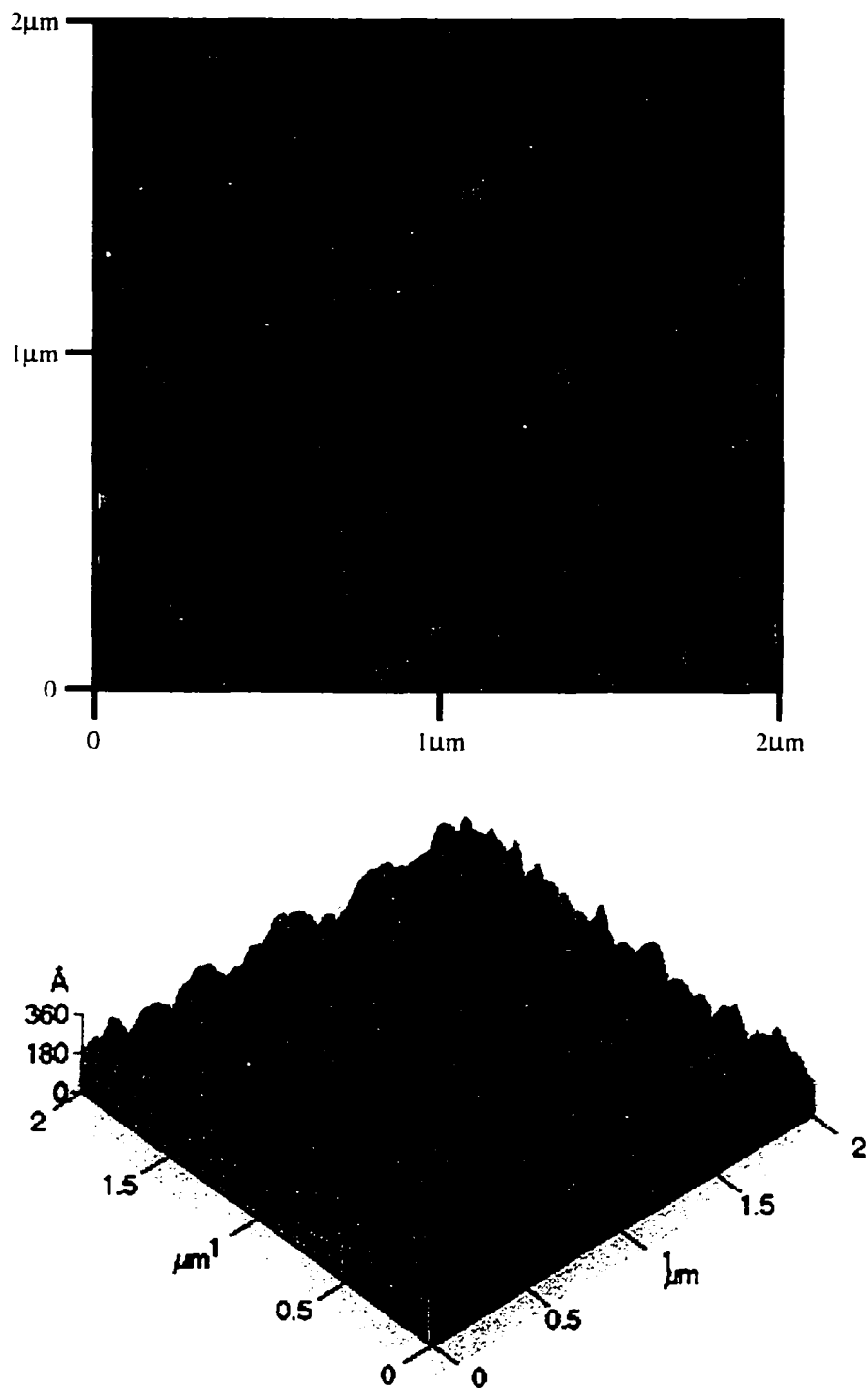
FIG. 4.12: AFM IMAGE OF SRRUO₃ DEPOSITED ON LAALO₃. TOP AND 3/4-VIEWS ARE GIVEN FOR THE SAME REGION (IMAGE COURTESY OF D. J. GUNDLACH AND T. N. JACKSON AT PENN STATE UNIVERSITY DEPARTMENT OF ELECTRICAL ENGINEERING)

4.1.2 Substrate effects

The final observation which needs to be addressed is the substrate influence on the lattice constant extension. $SrRuO_3$ films were deposited on (001)-oriented $LaAlO_3$ substrates, again changing the deposition pressure and performing x-ray analysis. A similar trend of lattice constant extension was observed, however, significantly smaller pressures (i.e., stronger bombardment) were required to produce the same lattice constant extension. In particular, during deposition in the 20 mTorr atmosphere, the lattice constant was only extended by 0.03 Å, in comparison to the film deposited on $SrTiO_3$ which had an extension of 0.06 Å. This result, and the general trend were verified in several sets of $SrRuO_3$ films on $LaAlO_3$. Assuming that the substrate has a negligible effect on the film composition, the only crystallographic difference detected between films deposited on $SrTiO_3$ and $LaAlO_3$, with the exception of lattice constant extension, is the mosaic structure as determined by x-ray diffraction line broadening. For films deposited on $LaAlO_3$, the FWHM peak breadth in all circles is at least double that measured for films on $SrTiO_3$. Knowing this, it is suggested that the lattice constant extension is influenced by the crystalline perfection of the growing film. In particular, a channeling effect which enhances the bombardment is proposed. Channeling is well documented to occur during the ion implantation of Si crystals even for large implanted species, e.g., Ge^+ and As^+. Such channeling during implantation is often difficult to avoid.[90] The higher quality $SrRuO_3$ crystals grown on $SrTiO_3$ have a narrower mosaic spread, which may provide more efficient pathways through which the shallowly implanted ablatant can travel. In contrast, the more pronounced sub-grain structure of the films deposited on $LaAlO_3$ may reduce the bombarding ion penetration depth, the

residence time in the host lattice. and the associated effects which lead to extended lattice

constants. He^{2+} channeling yields for $SrRuO_3$ on $SrTiO_3$ and $LaAlO_3$ have been reported

as 1.8% and 2.5%. respectively; thus demonstrating the improved ability of ions to

channel through structurally refined $SrRuO_3$.[117,157]

4.2 Temperature dependent structure analysis

Specific knowledge of the thermal expansion coefficient as well as possible high

temperature phase transitions of $SrRuO_3$ was desired for accurate interpretation of the

previous experimental results. With knowledge of the $SrRuO_3$ thermal expansion

coefficients. the thermal expansion mismatch induced stresses acting upon the thin films

could be quantified. This step was considered to be important given the results of

previous researchers who demonstrated the dependence of the electrical resistivity and

Curie transition upon applied hydrostatic stress. The presence of high temperature phase

transitions is also important for the establishing accurate growth mechanism and the

driving forces for preferred in-plane orientation.

Again. the epitaxial samples deposited under heavily and lightly bombarding

conditions were examined. A 2-circle x-ray diffractometer equipped with a radiant

furnace was used for lattice constant evaluation at elevated temperatures. This geometry

allowed information concerning (00ℓ) reflections only. All peak positions were

determined by a peak fitting program which allowed the Cu $K_{\alpha 2}$ peaks to be extracted.

Lattice constants were then calculated using multiple 00ℓ reflections. correcting for

sample height errors. Data for the thin films was collected between room temperature

and 800 °C. Though the instrument was equipped to achieve temperature in excess of

1000 °C. 800 °C was viewed as the practical limit. above which SrRuO₃ reaction. or

solution into the substrate was suspected. Fig. 4.13 shows the temperature dependence of

the lightly bombarded SrRuO₃ thin film out-of-plane lattice constant.
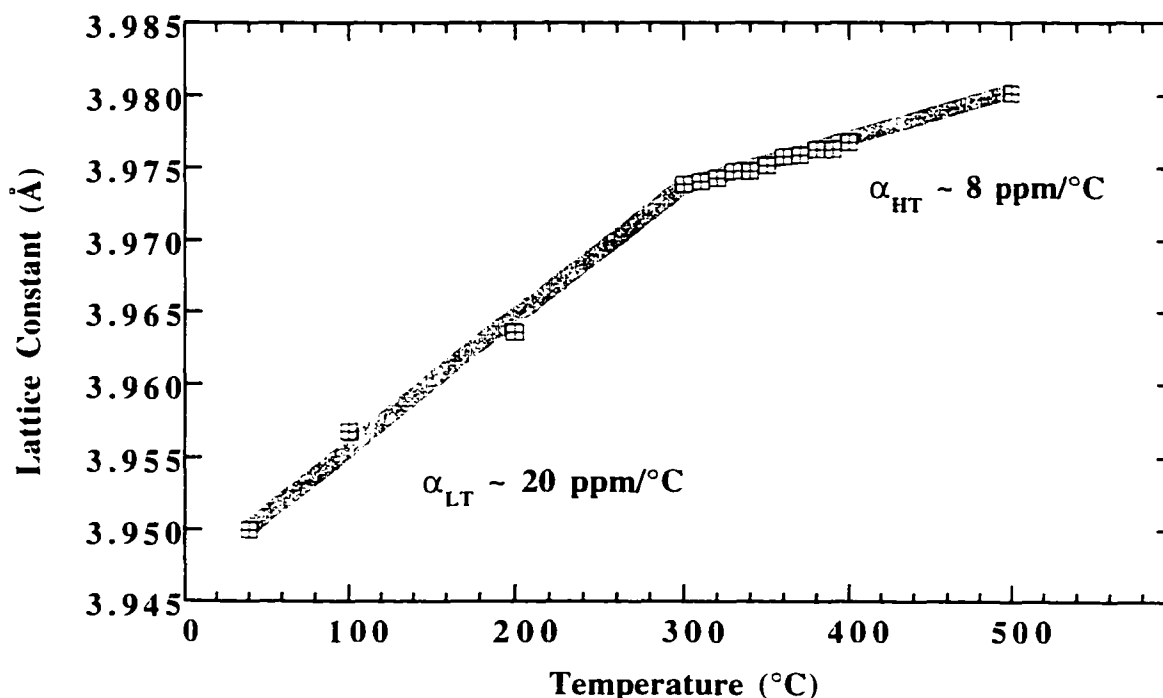
FIG. 4.13: TEMPERATURE DEPENDENCE OF THE OUT-OF-PLANE LATTICE CONSTANTS FOR A SRRUO₃ THIN FILM DEPOSITED ON SRTIO₃ UNDER THE LOW BOMBARDMENT CONDITIONS

In addition to the SrRuO₃ reflections, those of the SrTiO₃ substrate were measured

simultaneously. The thermal expansion coefficient of the substrate was calculated and

compared to reference literature to calibrate the experiment. A value of 10.7 ppm/K was

found for the SrTiO₃ substrate, which is within 1% of the accepted literature value of 10.8

ppm/K.[158] From the figure it is apparent that an abrupt change in the thermal expansion

of SrRuO₃ occurs in the vicinity of 275 °C. In this region, the thermal expansion

coefficient value drops from approximately 20 to 8 ppm/K. This discontinuity is suggestive of a structural phase transition, however, confirmation of such behavior cannot be made without information concerning other reflections. Lattice constant measurements were collected during both heating and cooling with little observed thermal hysteresis. The same measurements were performed on the heavily bombarded $SrRuO_x$, this data is shown in Fig. 4.14.
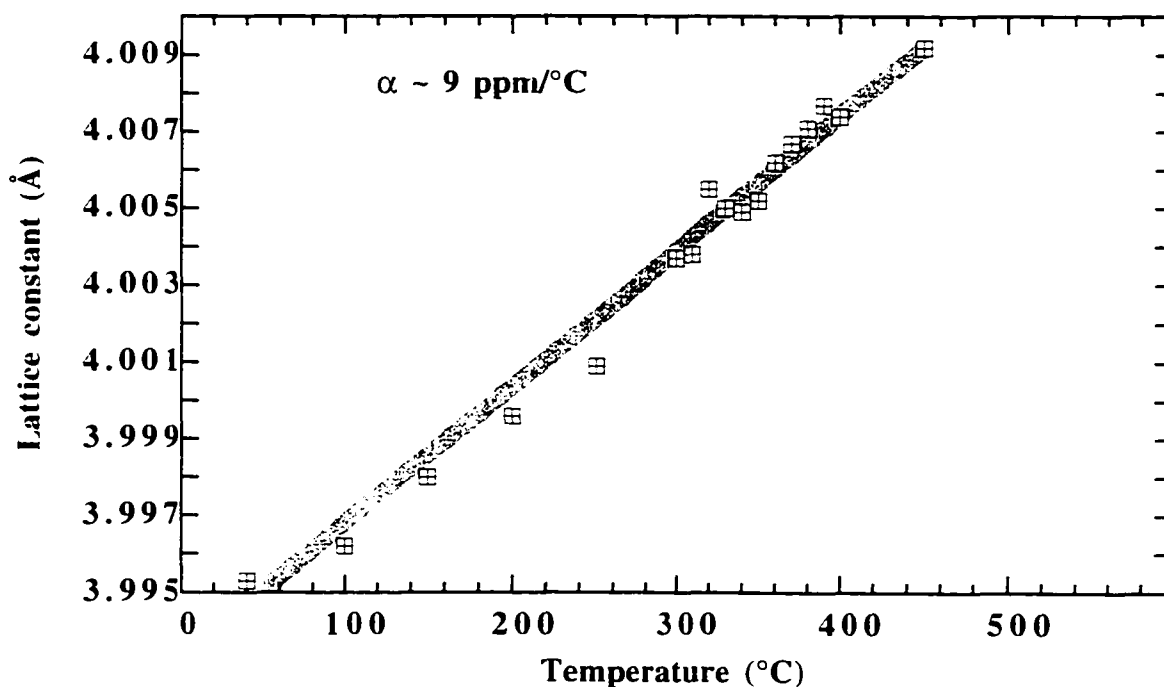
FIG. 4.14: TEMPERATURE DEPENDENCE OF THE OUT-OF-PLANE LATTICE CONSTANTS FOR A $SrRuO_x$ THIN FILM DEPOSITED ON (001)-$SrTiO_3$ UNDER THE HIGH BOMBARDMENT CONDITIONS

It is apparent from this figure that the discontinuity observed in the temperature dependence of the lattice constant of the high pressure deposited material is absent. The thermal expansion coefficient throughout the entire temperature range is similar to the value measured for the low bombardment sample above 275 °C. Again, the $SrTiO_3$

reflections were simultaneously measured in order to validate the interplanar spacing measurements; excellent agreement to literature values was also observed.

In order to determine the nature of the discontinuity in the temperature dependence of the SrRuO$_3$ thin film lattice constant. a similar measurement was performed on a powder specimen. The SrRuO$_3$ powder was fabricated using the mixed oxide method, combining RuO$_2$ and SrCO$_3$ in stoichiometric amounts. The powder was ball milled for 12 hours in ethanol and stabilized zirconia media. then calcined for 96 hours at 1000 °C. This lengthy calcination step was required for complete phase formation. Using shorter calcination times, small quantities of residual RuO$_2$ remained. Fig. 4.15 shows an x-ray pattern for the SrRuO$_3$ powder.
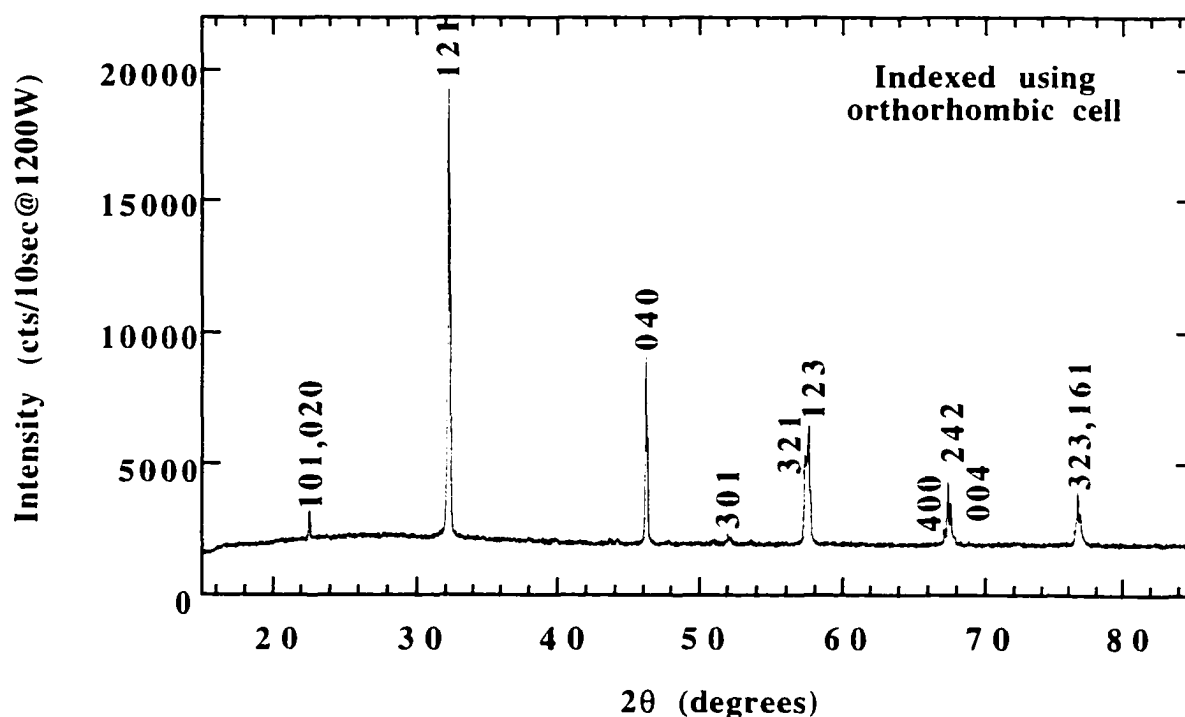
FIG. 4.15: X-RAY DIFFRACTION POWDER PATTERN OF SRRUO$_3$ PREPARED USING MIXED OXIDE METHOD

Once phase pure material was synthesized, a small pellet was pressed and bisque-fired for strength. No attempt was made at sintering to preclude any possibility of high temperature ruthenium loss. X-ray diffraction experiments were performed on the pellet between room temperature and 900 °C. After cycling at temperatures above 900 °C. changes were observed in the ruthenate room temperature powder pattern, thus any data taken at or above these conditions is regarded as unreliable. This observation is consistent with a report by Bensch et al.[108] who found that $SrRuO_3$ decomposed in air at temperatures near 1000 °C. Since the entire powder pattern could now be collected. the presence of any phase transitions could be verified, and new high temperature phases identified. Fig. 4.16 gives the temperature dependence of the $SrRuO_3$ lattice constants showing data points for both heating and cooling.
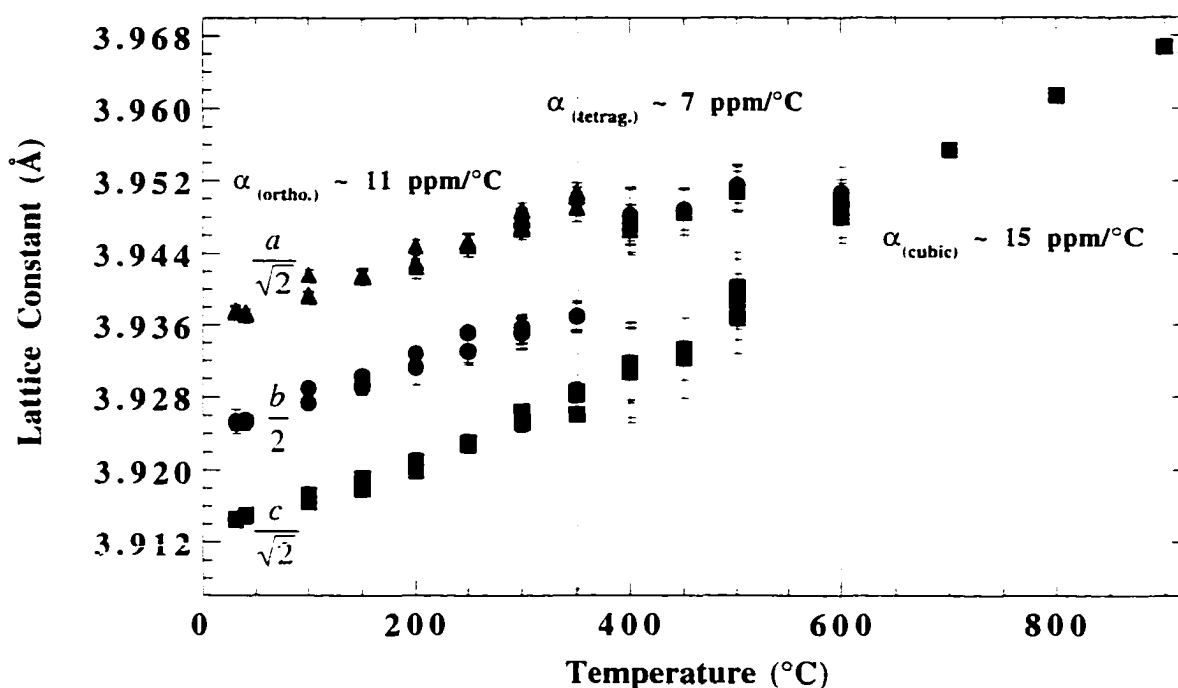
FIG. 4.16: TEMPERATURE DEPENDENCE OF THE LATTICE CONSTANTS FOR SRRUO₃ POWDER

The interplanar spacings for the orthorhombic cell were originally measured. Good agreement was obtained with reference values for lattice parameters. In the figure, the lattice constant values for the perovskite subcell are shown as they are more pertinent to epitaxial considerations with other perovskites. Typically, two lattice constants and a tilting angle are given for the pseudo-perovskite cell, in the present, however, three constants corresponding to $a_{ortho}/\sqrt{2}$, $b_{ortho}/2$, and $c_{ortho}/\sqrt{2}$ are given. These constants are used as they reflect the orthorhombic nature of the true unit cell and allow all three values to be easily viewed on the same scale. Two features are observed in the temperature dependence of the SrRuO₃ powder lattice constants (i) a transition from orthorhombic to a higher symmetry (possibly tetragonal) at 350°C, and (ii) a transition from this intermediate phase to cubic symmetry above 600°C. In the case of the tetragonally

indexed phase. the lattice constants refer to a and c, while in the cubic case, the parameter

is for the cubic simple perovskite cell. The space group for the orthorhombic phase has

been given as Pnma, and the space group for the cubic phase is proposed to be Pm3m.[147]

The space group for the intermediate phase could not be determined without additional

experiments. i.e., a Rietvelt refinement of the intermediate phase diffraction data. An

approximately 50° C difference exists between the orthorhombic to tetragonal transition

temperature measured for the thin film and powder specimens. When the thermal

expansion coefficients for the orthorhombic phase of both thin film and powder samples

are compared. their values are different by approximately a factor of two: $\alpha_{ortho/powder}$~11

ppm/°C. and $\alpha_{ortho/film}$~20 ppm/°C. The room temperature expansion coefficient

calculated for the powder sample seems more reasonable in its consistency with values

for other perovskites. however, the in-situ calibration of the film measurements with the

$SrTiO_3$ substrate preclude the possibility of large experimental errors. Possible sources of

these disparities include substrate clamping and small deviations from stoichiometry. It

is interesting to note. however. that the thermal expansion coefficients measured for both

thin film and bulk samples in the proposed tetragonal phase are in good agreement.

What is certain from this data is that $SrRuO_3$ grows near or in its cubic phase at

high deposition temperatures (typically ~ 680 °C). If it is assumed that $SrRuO_3$ is cubic

at 680 °C. in the context of thin films having either twinned or untwinned

microstructures, this data implies that the growth mechanism has little influence on the

resulting orthorhombic twinning structure. If $SrRuO_3$ grows as an isotropic crystal, a

mechanism other than a preferred nucleation site or growth direction must occur.

One possibility is that $SrRuO_3$ is ferroelastic. and interfacial strains present in the thin film at temperatures where the structural phase transitions occur influence the nucleation of rotation–domains. It is clear however, that the presence of a stepped substrate surface provides an important influence and must be included in the proposed model. Fig. 4.17 depicts the perovskite $SrRuO_3$ cell at a step edge prior to, and after the structural phase transition. It is postulated that for unit cells located at step edges. compressive stresses arise due to lattice constant mismatch. while either compressive or tensile stresses will develop from thermal expansion mismatch (the sign of the thermal expansion mismatch induced strain will depend upon the orientation of the tetragonal cell during cooldown). Regardless of the specific stress state, since these stresses will be applied at only two of the six unit cell faces (for those unit cells located at interior step corners). a large asymmetry will be present, thus providing a lower free energy for a particular orthorhombic cell orientation. With two sides of a perovskite cell under stress. the angular distortion of the cell may orient most favorably with its entire component perpendicular to the step edge. or similarly, the rotation axis of the distorted unit cell will lie parallel to the step edge. As a result of this orientation, the b-axis of the orthorhombic cell lies in-plane and perpendicular to the step-flow direction.

The effects concerning the favorability of one orientation over another with respect to lattice mismatch at the transition temperature were also considered. Upon comparison of the data, no preference for a single orthorhombic cell orientation could be elucidated.
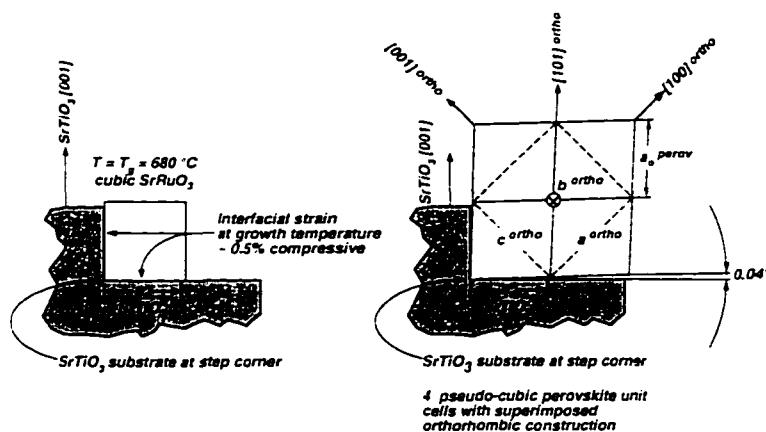
FIG. 4.17: ANISOTROPIC STRESS MODEL FOR SrRuO₃ UNIT CELL LOCATED AT A STEP EDGE DEMONSTRATING THE PROPENSITY FOR SrRuO₃ FERROELASTIC DOMAIN ALIGNMENT

This model is consistent with the observations of Gan et al., where similar orientational relationships were observed for SrRuO₃ on vicinal SrTiO₃.[118] In this work, a minimum miscut value of nearly 1° was required for the absence of any rotation-domains. In this work, only a 0.5° miscut was needed to obtain a similar result. The Kawasaki etch was not used by Gan et al., which may be the source of the larger miscut requirement. Both studies imply that a sufficient density of c or a-oriented nuclei are required to persuade the entire crystal to orient to a single domain state. Gan et al. also reported that the single domain microstructure was lost when the miscut direction was rotated away from <001>. This result is also consistent with the proposed model.

4.3   Spectroscopic ellipsometry

The real and imaginary components of the $SrRuO_3$ dielectric functions were measured as a function of temperature using a spectroscopic ellipsometer equipped with a block-style hot-stage. Films deposited under both strongly and weakly bombarding atmospheres were investigated. Primarily. the temperature dependence of the dielectric function was examined to determine if the structural transitions observed by x-ray diffraction contained an optical signature. In addition. from samples exhibiting the best structural and electrical properties. reference optical data was obtained. This reference optical data is useful for characterization of transparent thin films. i.e.. dielectrics. or thin high temperature superconducting layers, which may use $SrRuO_3$ as a metallic bottom electrode.

Due to radiation emitted from the hot stage. the practical *in situ* measurement temperature limit is approximately 500 °C. At higher temperatures. radiation from the hot stage reduces the signal to noise ratio. As a result, only the transition temperature occurring near 275°C could be investigated.

Since the $SrRuO_3$ samples are strong absorbers. when deposited to sufficient thicknesses. they may be treated as optically opaque. This approximation allows a direct inversion technique to be used to derive the high frequency dielectric function. The direct inversion was done assuming atomically flat surfaces since modelling of the SE data indicated that the surface roughness was negligible. This is also consistent with the extremely small rms surface roughnesses observed in the STM data. Films of several thicknesses were measured: in doing this, any artifacts. or contributions from the substrate dielectric function could be detected. Fig. 4.18 shows the room temperature

real and imaginary components of the $SrRuO_3$ dielectric function. Data are shown for films deposited under high and low bombardment conditions. The structure in both spectra indicate that the material deposited at higher pressures has sharper features which is consistent with the superior crystal quality of the films which experienced less bombardment during growth. In addition. the 180 mTorr deposited film has a somewhat higher extinction coefficient over the majority of the wavelength range investigated. This increased opacity is consistent with the smaller electrical resistivity of the high pressure deposited samples.[116]
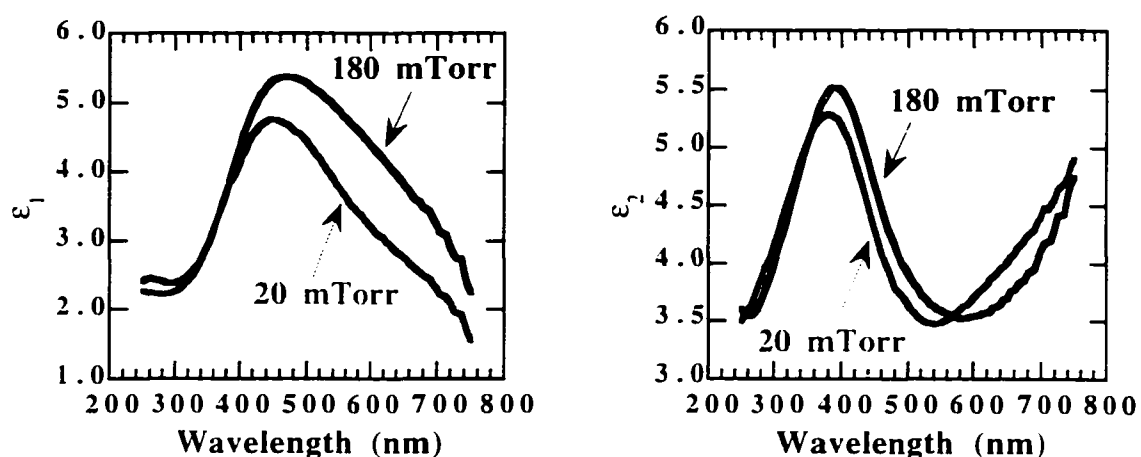
FIG. 4.18: REAL (ε_1) AND IMAGINARY (ε_2) COMPONENTS OF THE $SrRuO_3$ DIELECTRIC FUNCTION SHOWN FOR BOTH HEAVILY AND LIGHTLY BOMBARDED SAMPLES

The dielectric function of the high pressure deposited sample in which the structural phase transition was first observed was measured as a function of temperature to 300 °C. The real and imaginary components are given in Fig. 4.19. In the figures. data for four temperatures at 25 °C increments are shown.
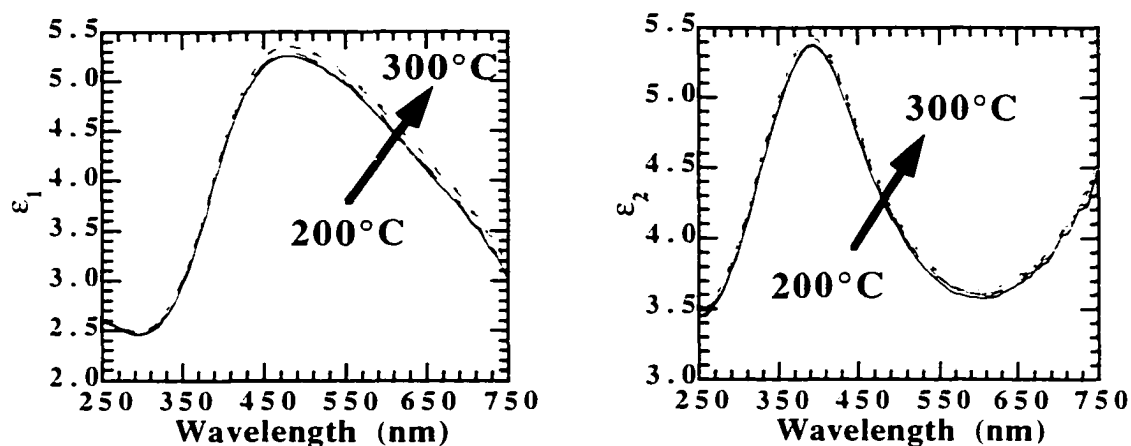
FIG. 4.19: REAL AND IMAGINARY COMPONENTS OF THE SRRUO₃ DIELECTRIC FUNCTION SHOWN AS A FUNCTION OF TEMPERATURE FOR A LIGHTLY BOMBARDED FILM

It is apparent from these measurements that there is no clear sign of the transition from orthorhombic symmetry in the high frequency dielectric properties. This result is consistent with the result of Allen *et al.* who measured the resistivity as a function of temperature on flux-grown $SrRuO_3$ single crystals. His work indicated that above the Curie temperature, the resistivity remained linear with temperature to 1000 °C.[106] Were some discontinuity or anomaly to occur in the resistivity with increasing temperature it is expected that a similar event would be manifested in the dielectric function.

4.4   Summary

Epitaxial $SrRuO_3$ thin films were grown on $SrTiO_3$ and $LaAlO_3$ substrates as a function of ambient pressure during growth. The anisotropically extended lattice constants observed in some samples were determined to be a result of energetic bombardment during growth. The ambient pressure during growth was used to control the bombardment, while experiments involving mixed atmospheres with Ar were used to

determine the influence of oxygen pressure. The mechanism behind the extended lattice constants is proposed to be implantation of energetic plasma species.

The surface quality of films showing bulk and extended lattice constants were investigated by scanning tunneling microscopy. In general, the surface topography revealed an edge-defined growth mechanism, i.e., the conservation of crystalline terraces from the substrate surfaces. Films grown under stronger energetic bombardment showed a coarsened appearance with respect to those grown at higher pressures. The surfaces were characterized by larger step heights and longer terrace lengths.

The crystallographic texturing of the $SrRuO_3$ twins was characterized using 4-circle x-ray diffraction. For films deposited under conditions with less bombardment, the in-plane texture was found to be nearly twin-free. The presence of a stepped $SrTiO_3$ substrate was required for preferred orthorhombic twinning. For films deposited under strongly bombarding conditions, the orthorhombic distortion was destroyed and the unit cell seemed to be best characterized as a tetragonal simple perovskite.

High temperature x-ray diffraction was performed on both thin film and powder samples. Discontinuities in the temperature dependence of the lattice constants indicated that structural phase transitions occur at ~ 300 °C and ≥ 600 °C which are believed to correspond to orthorhombic to tetragonal and tetragonal to cubic transitions respectively. This x-ray data suggests that $SrRuO_3$ grows in the cubic phase, thus develops a twin-structure upon cooldown through 600-700 °C. This information implies that the growth mechanism of $SrRuO_3$ may not be responsible for the oriented orthorhombic twinning. Rather, it is possible that preferred twinning results from an epitaxial interfacial strain, which is anisotropic due to the presence of substrate steps.

Chapter 5   PMN-PT Deposition and Structural Analysis

5.1   Deposition of La and Mn doped PbTiO₃

In initial work, the deposition of La and Mn doped $PbTiO_3$ epitaxial thin films was investigated. During these experiments, the methodology for film deposition using Pb-enriched targets was developed. Relationships between the required target Pb-enrichment and specific sets of deposition conditions were determined. In addition, the most efficient methods of exploring PLD processing space were investigated. The La and Mn doped $PbTiO_3$ composition was chosen for the inherent compositional range (i.e., Pb vacancy concentrations) over which insulating electrical properties can be achieved.[159]

The specific target composition was $Pb_{0.88}La_{0.10}Mn_{0.02}Ti_{0.98}O_3$ (PLMT). Powder of this composition was prepared by the standard mixed oxide method, i.e., ball milling and calcining, while Pb-enriched targets were prepared by adding the appropriate amount of PbO to the stock powder and sintering. Targets including 10 and 25 weight % excess PbO were tested. This relatively large lead excess was required to insure sufficient PbO overpressures when substrate temperatures were maintained at or above 650 °C. These temperatures have been found to be necessary for good epitaxy and crystalline structure.[109,160]

A simple iterative process based upon adsorption-controlled growth of the PbTiO$_3$ phase was used to determine the conditions which provided phase-pure material. Initially, samples were purposely deposited under conditions which resulted in a phase assemblage of epitaxial PLMT and polycrystalline PbO$_x$. Conditions were then modified to provide increased Pb volatility, until x-ray analysis exhibited only epitaxial PLMT. To achieve these conditions, several deposition parameters could be adjusted. These included laser fluence, target to substrate distance, oxygen pressure, laser frequency, and temperature. Modulations of the deposition were performed most precisely by adjustments of laser frequency and temperature. The laser frequency controls the time between pulses, during which Pb can evaporate, while changing the temperature of the substrate raises or lowers the rate of Pb volatility.

Repetition frequency and temperature are felt to be the optimal control variables, as they have minimal influence on other aspects of the deposition. Other deposition parameters such as pressure, fluence, and target-to-substrate distance are strongly coupled, thus changing only one may have ramifications on multiple aspects of the deposition. This in turn makes isolation of a single control variable difficult. For instance, if the pressure is reduced from 200 mTorr to 50 mTorr, the expected result would be an increase in the Pb volatilization rate due to the reduction of species such as PbO$_x$ (Pb has a higher vapor pressure than its oxide at deposition temperatures). However, the deposition rate is considerably larger at 50 mTorr than at 200 mTorr, thus a competing effect occurs.[109] In addition, an increased level of energetic bombardment would be expected at these lower pressures which could further influence the film structure, stoichiometry, and surface morphology. A similar effect would be observed

when changing the target to substrate distance or laser fluence. where deposition characteristics are again coupled and the effects on the deposition would be difficult to accurately predict.

For the PLMT system. Pb-rich samples were characterized by the presence of x-ray peaks attributable to PbO_x, while lead deficient samples typically contained peaks corresponding to the anion-deficient $Pb_2Ti_2O_{6-x}$ structure. Signatures indicating the presence of titanium oxide were not observed. The pyrochlore and excess lead containing phases were found to be mildly textured. but not epitaxial. Figure 5.1 shows the x-ray analysis for a structurally optimized PLMT thin film on $SrRuO_3/LaAlO_3$. In these figures. and all subsequent x-ray patterns. the same notation will be used. "P" denotes a peak to the particular perovskite ferroelectric phase. "S" denotes a reflection for $SrRuO_3$. and "*" indicates a reflection from the substrate.
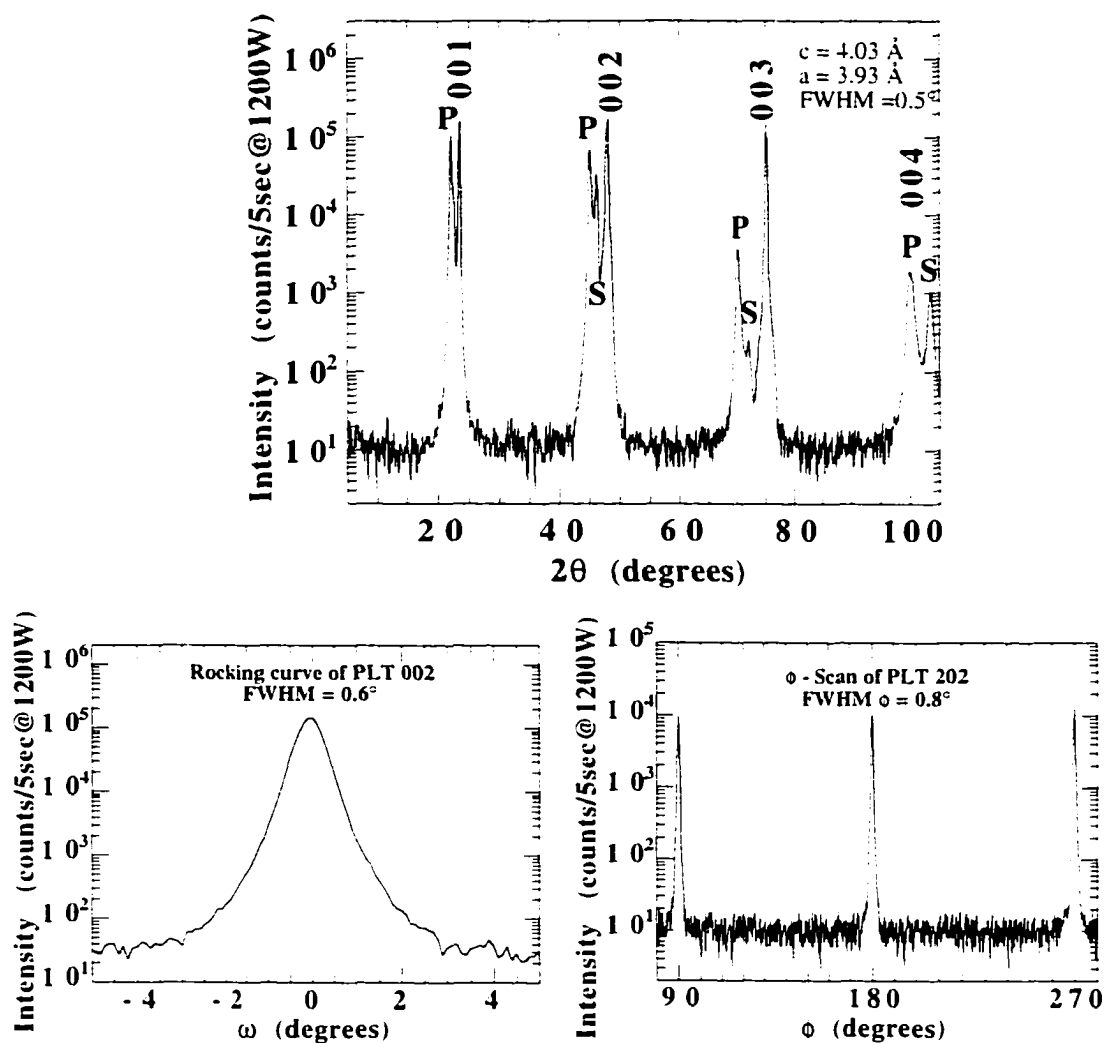
FIG. 5.1: 4-CIRCLE X-RAY ANALYSIS FOR STRUCTURALLY OPTIMIZED PLMT THIN FILM

This film was deposited from a 25 % PbO excess target at a temperature of 690 °C, a pressure of 150 mTorr, and a 10 Hz, 300 mJ laser pulse. In general, the best PLMT thin films were grown from the 25% excess target. Using the 10 % excess PbO target, phase-pure films could be grown, however, due to the rapid deposition rates required, the film surfaces were rough, and the crystallinity was inferior. In general, it was found that a reduction in the film tetragonality was observed with lead deficiency.

Thus. the relative lead stoichiometry could be determined even when Pb-deficient second phases were not present.

Fig 5.2 shows a plot of the out-of-plane c-axis lattice constant as a function of laser frequency. With the remaining parameters held constant, reducing the laser frequency results in a systematic decrease of the sample lead content. The samples deposited at laser frequencies of 8 and 10 Hz were phase-pure. while small amounts of pyrochlore were detected in the sample grown at 6 Hz. The unit cell shrinkage was accompanied by x-ray peak broadening and reduced diffracted intensity. Interestingly. going to conditions where excess lead-containing phases are present does not result in lattice constants which are detectably larger than the bulk values. The in-plane lattice constants follow a similar trend. however, the changes are smaller.
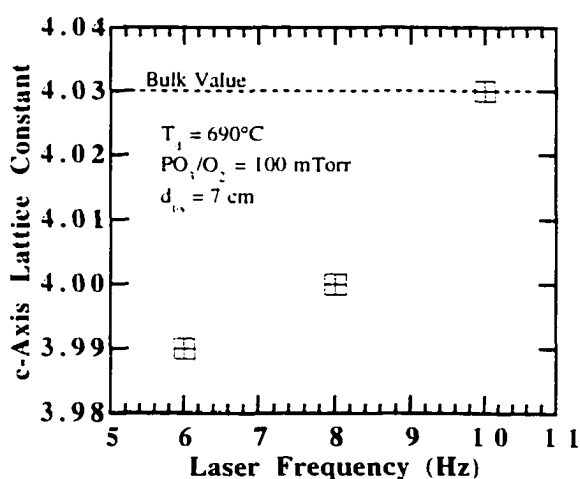
FIG. 5.2: LATTICE CONSTANT DEPENDENCE UPON LASER DEPOSITION FREQUENCY

In general. using this iterative process, phase-pure samples could be produced at several sets of deposition parameters: fast deposition rates and high Pb-volatility. or slow growth rates and reduced Pb-volatility. The films were determined to be roughly equivalent through assessment of the crystal structure, surface morphology, and electrical properties.

A final observation was made for the PLMT thin films concerning the out-of-plane arrangement of a-axis oriented domains. From the reports of several authors on epitaxial PbTiO$_3$ films. it is known that regions exist in the film where the a-axis orients nearly perpendicular to the substrate plane.[161,162] The orientation is not perfectly perpendicular. but tilted off of the substrate by a small angle. These a-oriented domains and their small angular tilts are necessitated by the large spontaneous strains. which result from the ferroelectric transition (in materials like PbTiO$_3$) and the thermal strains produced by expansion coefficient mismatch between film and substrate. These strains are relieved by the formation of ferroelastic domains. The a-oriented domains accommodate these strains in an analogous fashion to 90° domains in a tetragonal ferroelectric ceramic.

By collecting rocking curves at 2θ angles corresponding to the d-spacing of the a-axis. additional peaks could be observed which corresponded to a-oriented regions tilted away from the substrate plane. The rocking curve given in Fig. 5.3 illustrates this behavior.
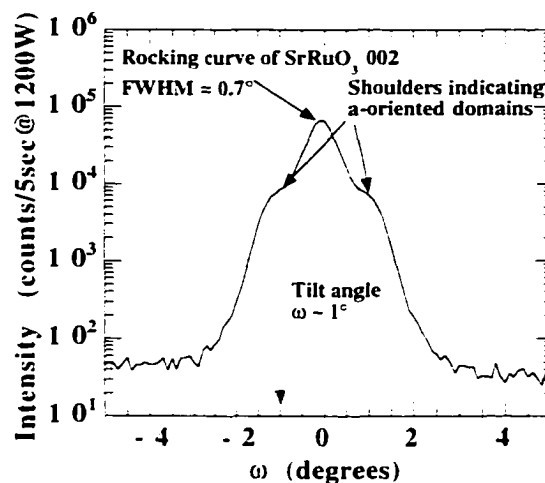
FIG. 5.3: ROCKING CURVE SHOWING A-ORIENTED DOMAINS OF PLMT. CENTER PEAK CORRESPONDS TO SRRuO$_3$ 002 WHICH OCCURS AT A SIMILAR 2θ ANGLE

The angular tilt from the substrate plane is estimated to be approximately 1°. Literature values of approximately 3° have been reported for pure PbTiO$_3$ thin films: the 2° disparity between these values can be justified by the reduced tetragonality resulting from the relatively large dopant (i.e.. La^{3+}) concentrations.[161,162] In addition, it is clear from this diffraction pattern that the distribution of a-oriented grains is symmetric about ω=0. This is the expected result given the nearly nominal cut of the LaAlO$_3$ substrate.[162]

This section of the research provided a better understanding of pulsed laser deposition. and a successful methodology for the synthesis of Pb-containing perovskites from Pb-enriched ceramic targets. These results were applied to the deposition of PMN-PT compositions for which considerable interest has recently developed.

5.2 PMN-PT deposition

Following the results obtained from the PLMT thin film investigations. PMN-PT

thin films of the specific composition 0.7 $Pb(Mg_{1/3}Nb_{2/3})O_3 - 0.3$ $PbTiO_3$ were

synthesized. The initial targets used for structural optimization included 30 weight %

excess PbO. It was assumed that more difficulty would be encountered in attempting to

grow phase-pure PMN-PT. thus a target with this larger quantity of PbO was used. Such

a target gives access to a greater range of deposition conditions. specifically the higher

temperatures which are expected to favor the perovskite phase. [6] As in the previous case.

the iterative procedure beginning with the deposition of a film rich in PbO_x was followed.

Fig. 5.4 shows a θ-2θ x-ray pattern for a PMN-PT film containing excess PbO_x.
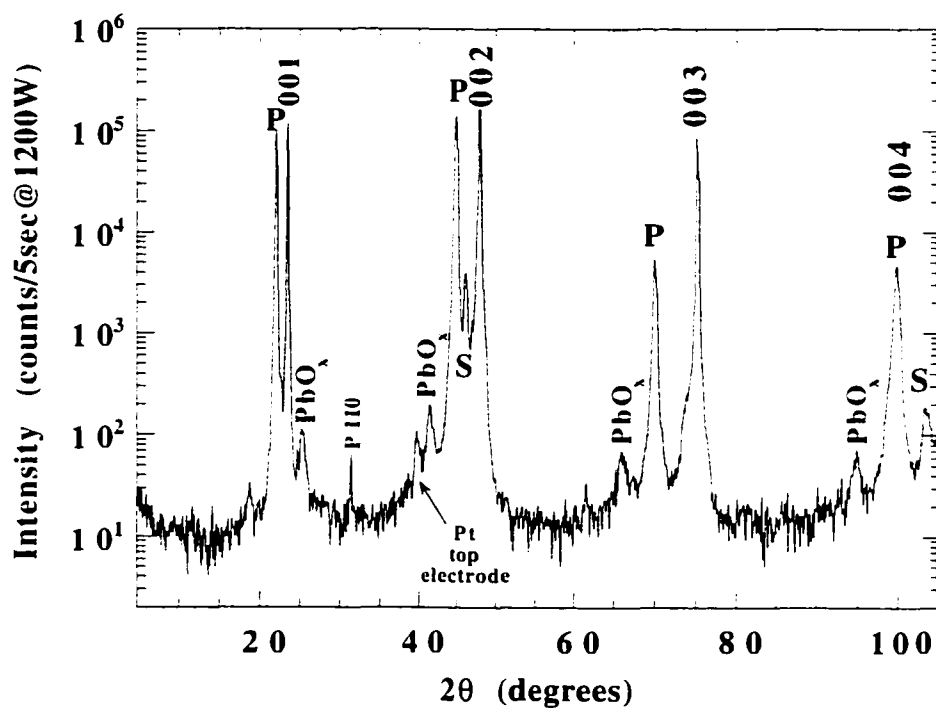
FIG. 5.4: θ -2θ X-RAY DIFFRACTION PATTERN FOR PMN-PT FILM DEPOSITED UNDER CONDITIONS WHICH RESULT IN EXCESS LEAD-CONTAINING PHASES

The next step in the iterative process was to increase the Pb-volatility and approach the deposition conditions required for phase-pure film synthesis. Fig. 5.5 shows the θ -2θ x-ray pattern for such a sample. while Table 5.1 gives the processing conditions for the samples indicated in Figs. 5.4 and 5.5.

TABLE 5.1: PROCESSING CONDITIONS FOR THIN FILMS IN FIGS. 5.4 AND 5.5

Parameters	Pb-rich film (Fig. 5.4)	Increased volatility (Fig. 5.5)
Temperature (°C)	660	660
Atmosphere	O₃/O₂	O₃/O₂
Pressure (mTorr)	200	200
Laser energy density (J/cm²)	2	2
Target to substrate distance (cm)	5.5	5.5
Laser frequency (Hz)	18	15
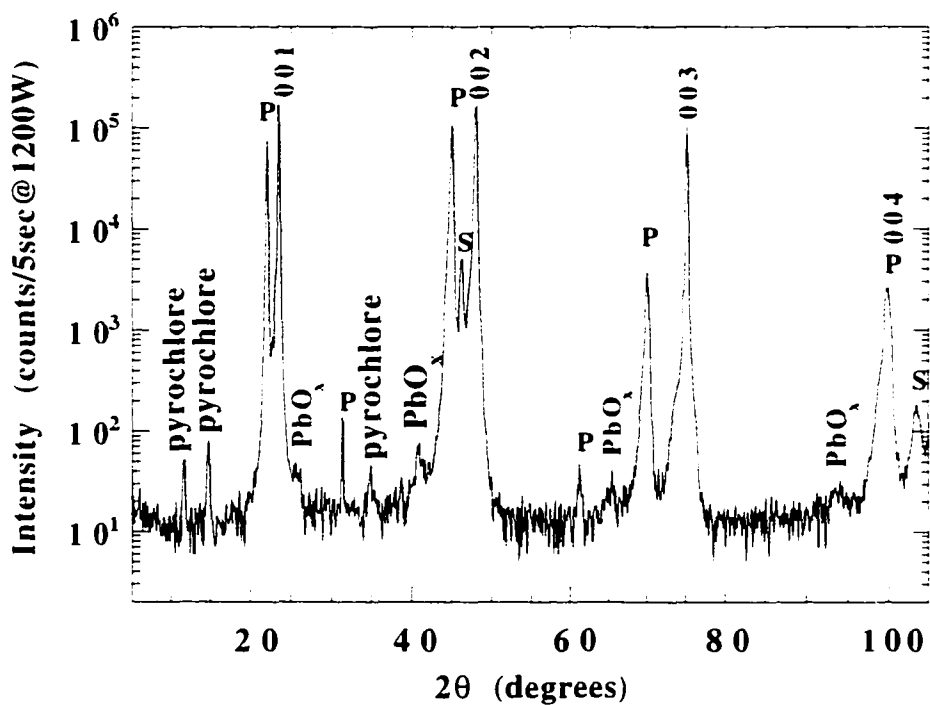
FIG. 5.5: θ -2θ X-RAY DIFFRACTION PATTERN FOR A PMN-PT FILM WHICH SHOWS THE COEXISTANCE OF PbOₓ, PEROVSKITE, AND PYROCHLORE

It is clear in this pattern that the quantity of excess PbO_x is reduced. however.

before it is completely removed, a significant amount of pyrochlore has evolved. The

observed pyrochlore phase has an x-ray pattern similar to $Pb_{1.83}Nb_{1.71}Mg_{0.29}O_{6.39}$,

however, many phases with nearly identical x-ray signatures and plausible

stoichiometries exist, thus an unambiguous assignment is not possible. This coexistence

of stoichiometric, Pb-rich, and Pb-deficient phases has been observed in bulk processing

of ceramics as well, and is attributed to the relatively similar thermodynamic stabilities of

the perovskite and pyrochlore phases in the temperature and pressure range of interest.[6.36]

From the ceramic processing and single crystal growth literature it is known that

increased temperature and oxygen partial pressures will favor the perovskite phase.[163]

Following these ideas, the deposition pressures and temperatures were raised to 710°C

and 700 mTorr respectively. Under these conditions, the film structure was again

optimized. Fig. 5.6 shows a θ-2θ pattern for a PMN-PT film deposited under these

conditions.
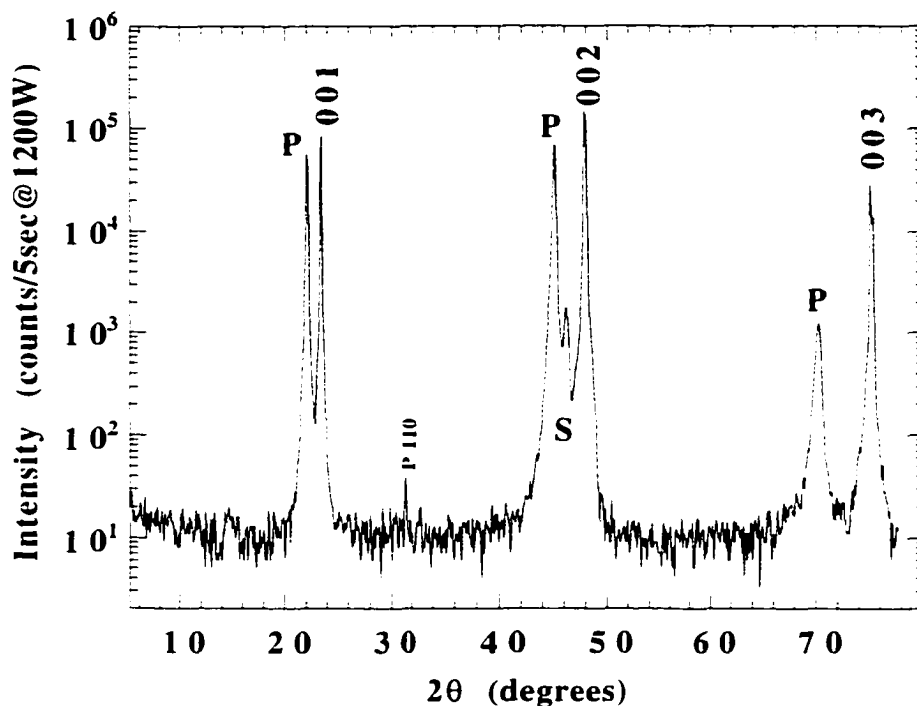
FIG. 5.6: θ-2θ X-RAY DIFFRACTION PATTERN FOR PMN-PT FILM DEPOSITED AT TEMPERATURES AND PRESSURES LARGE ENOUGH TO PROVIDE PHASE-PURE GROWTH (I.E., 710 °C & 700 mTORR). A SMALL QUANTITY OF NON-EPITAXIAL MATERIAL IS INDICATED BY THE "P 110" REFLECTION

In addition to the increased pressure and temperature, the target–to–substrate distance was reduced to 3.5 cm. This step was necessary to increase the instantaneous deposition rate and supply enough Pb to the growing film. To the detection limits of our diffractometer. no pyrochlore or Pb-rich phases are present. Intermediate oxygen pressures and temperatures were also attempted (~400 mTorr and ~ 680 °C) and improved results were observed. however, purely perovskite material was not available until temperatures and pressures were increased to even larger values.

5.2.1   Crystalline perfection and epitaxy

Quantification of the crystalline perfection and epitaxy of the samples was made by comparison of the peak widths. peak intensities, and the presence of peaks

corresponding to non-(00ℓ) orientations. For the materials system used, i.e., LaAlO$_3$

substrates, a lattice mismatch of approximately 5% exists. Given this large value, it is

expected that x-ray peak widths will be significantly broader than those of the substrate,

and that small quantities of non-epitaxial material may occur. Table 5.3 lists the

approximate range of x-ray peak widths measured for PMN-PT samples for the three x-

ray scanning circles

TABLE 5.2: TYPICAL FULL-WIDTH HALF-MAXIMUM PEAK VALUES FOR PMN-PT EPITAXIAL THIN FILMS ON LaALO$_3$ SUBSTRATES

x-ray reflection full-width-half-maximum	2θ	ω	ϕ
	0.3° - 0.6°	0.5° - 0.8°	0.8° - 1.2°

Similar peak widths have been observed for other perovskites with comparable

unit cell sizes deposited on the same substrate/electrode configuration including BaTiO$_3$,

PbTiO$_3$, and Pb(Zr,Ti)O$_3$.[83,164,165] The narrowest peak widths and the largest peak

intensities occurred for samples which were deposited at the highest substrate

temperatures and lower deposition pressures, (i.e., conditions which favored the greatest

adatom mobility). The x-ray peak intensities are also indicative of the crystalline quality.

For structurally optimized samples, even those only several thousand Å in thickness, the

peak intensities approached, and sometimes exceeded those of the substrate.

The epitaxial relationship between the film and substrate must be confirmed by

performing azimuthal (or ϕ) x-ray scans which can determine the crystal symmetry in the

substrate plane. In-plane epitaxial texture was seldom lost in the PMN-PT films (large

quantities of misoriented material were never observed), however, for samples containing

pyrochlore, small shoulders were often present on the ϕ-scan peaks. Fig. 5.7 shows a ϕ-

scan exhibiting this. It is likely that additional misoriented nuclei form on or adjacent to the pyrochlore phase and result in the peak shoulders.
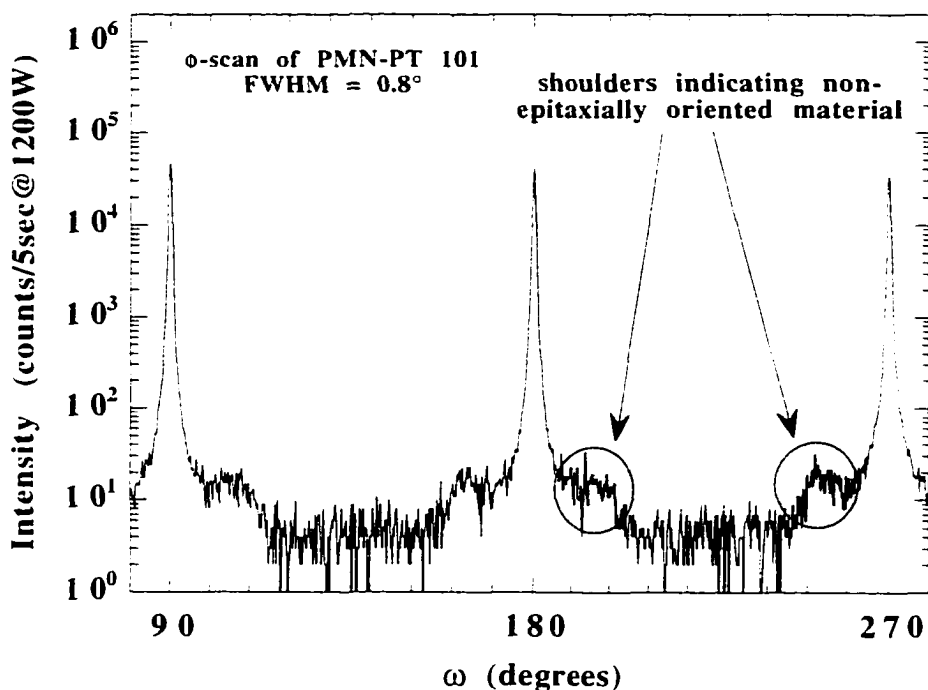
FIG. 5.7: Φ-SCAN OF PMN-PT SAMPLE (101 REFLECTION) CONTAINING PYROCHLORE. SHOULDERS ON MAJOR PEAKS ARE ASSOCIATED WITH THE OCCURRENCE OF PYROCHLORE

5.3   Low temperature deposition

An alternate strategy was applied for growth of PMN-PT thin films which relied on low temperature synthesis from targets with a very small amount of excess PbO. It is known from previous reports that during deposition of lead-containing materials such as PZT in low oxygen pressure conditions, little lead-loss occurs below 500 °C.[102] In an attempt to achieve similar results, a final group of PMN-PT films were grown at

temperatures below 600 °C using a PMN-PT target containing approximately 3 weight %

excess PbO.

Deposition under these conditions allowed for several advantages, the foremost of

which is lower ambient pressures. Low pressure deposition (i.e., pressures less than 100

mTorr) provides for improved film thickness uniformity and increased amounts of

energetic bombardment. With appreciable energetic bombardment, energy can be

supplied to the substrate by kinetic transfer rather than thermal vibration. Kinetic transfer

on the order of 10-20 eV would be preferable in this case as it should allow the growth of

very smooth and highly crystalline samples, without promoting Pb-loss, as would the

equivalent quantity of thermal energy. (Impingement on the order of 10 to 20 eV is

recognized as the level, especially during epitaxial growth, at which crystallinity and

smoothness can be enhanced without subsurface penetration and damage.[90]) Since the

rate of evaporation of a material is exponential with temperature, it is expected that a

larger processing window will exist for reduced temperatures since the inevitable

deposition parameter fluctuations during, or between growths, should cause only small

deviations in lead stoichiometry. Table 5.3 gives the processing parameters for the initial

low temperature deposited PMN-PT epitaxial thin films.

TABLE 5.3: PROCESSING PARAMETERS FOR PMN-PT DEPOSITED UNDER LOW TEMPERATURE CONDITIONS

Initial parameters for lower temperature growth	
Temperature (°C)	580
Atmosphere	O_3/O_2
Pressure (mTorr)	100
Laser energy density (J/cm^2)	2
Target-to-substrate distance (cm)	6.5
Laser frequency (Hz)	14

Films were deposited under these conditions and structurally optimized for crystalline quality and phase purity. Fig. 5.8 shows x-ray patterns for the three diffractometer circles for an optimized sample.
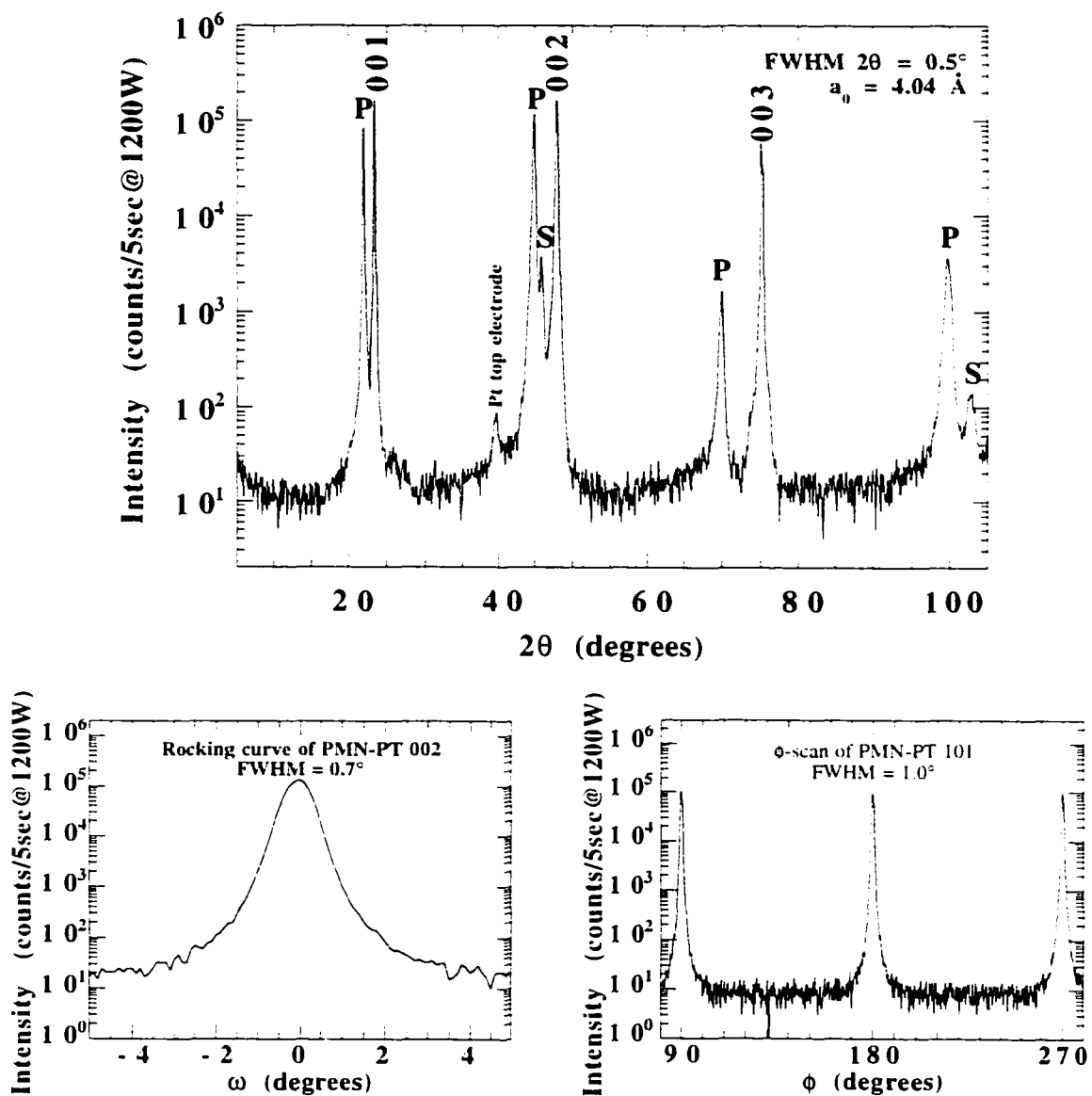
FIG. 5.8: X-RAY SCANS FOR THREE DIFFRACTOMETER CIRCLES OF A LOWER TEMPERATURE DEPOSITED PMN-PT THIN FILM ON SRRUO$_3$ ON A LAALO$_3$ SUBSTRATE (PEAK WIDTHS ARE GIVEN IN THE FIGURE LEGENDS)

The x-ray analysis indicates phase-pure epitaxial material with excellent peak intensities. Compared to the high temperature deposited material, however, the line widths (given in the figures) are slightly larger.

It was desired to further improve the crystallinity and achieve a film structure comparable to that of the higher-temperature deposited material, however, it was necessary to do so without appreciably increasing the deposition temperature. This goal was accomplished by increasing the sample temperature by 10 °C and reducing the ambient pressure to 60 mTorr. Achieving phase-pure material in this region was slightly more difficult. Fig. 5.9 is a θ-2θ x-ray pattern for a film deposited under the optimized low-temperature conditions. ϕ- and ω-scans are not given for this sample, however, the FWHM values for all circles are listed in the figure legend. These line widths, in addition to the peak intensities, indicate that material with respectable crystallinity can be synthesized at temperatures below 600 °C.
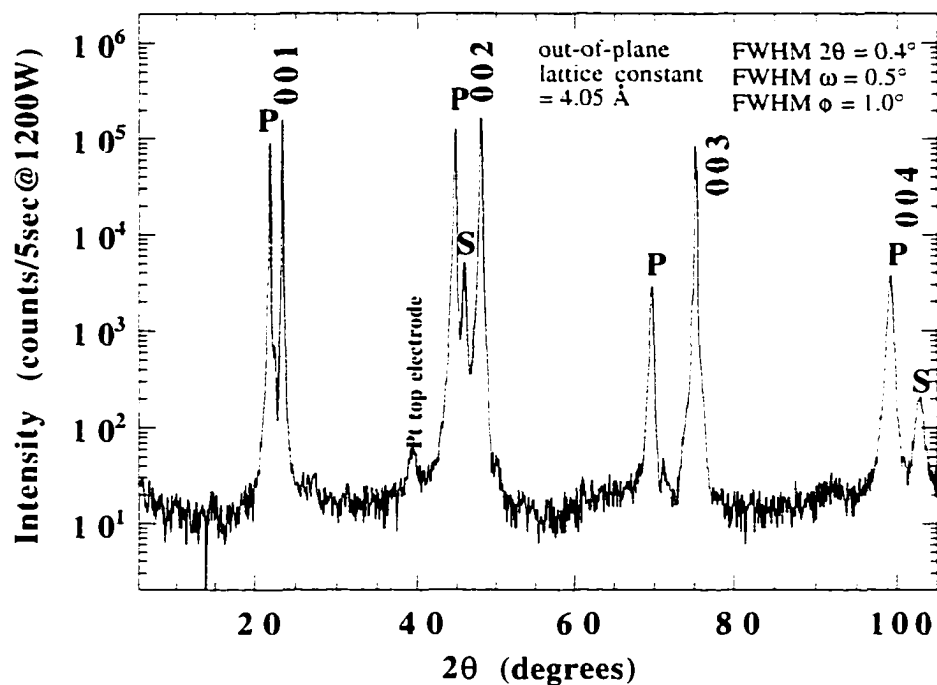
FIG. 5.9: θ-2θ SCAN FOR A PMN-PT THIN FILM DEPOSITED AT THE OPTIMIZED LOWER TEMPERATURE CONDITIONS

When the pressures were reduced to 60 mTorr. in order to achieve the desired film stoichiometry. it was necessary to increase the laser frequency by 1 Hz. This modest increase in the deposition rate indicates that even though the Pb-volatility would increase due to the reduced oxygen pressure. the final lead content remained approximately constant. This is explained by the fact that with the target-to-substrate and laser power settings used, the deposition rate is higher at 60 mTorr than at 100 mTorr (a demonstration of the coupled deposition effects). These pressure/laser energy/deposition rate dependencies were investigated and quantified in earlier work. and were briefly summarized in section 5.1.[109] Thus even though the Pb-volatility would be expected to have increased, the increase in deposition rate provided the appropriate compensation.

As expected, the surfaces of the films were considerably smoother than those deposited at higher pressures and temperatures. Fig. 5.10 shows topographical AFM images at two magnifications. The maximum light-to-dark contrast of the image corresponds to 5 nm in both cases. Analysis of the image revealed an rms roughness value of approximately 50 Å. From the 2 μm scale image, orientation of the nodule-like features is clearly evident, and appears to be directed with the long axis parallel to the <110> direction of the crystal. This type of microstructure may be consistent with island nucleation, growth and coalescence. The film thickness in this case is 4000 Å, which is approximately a factor of 4 greater than the narrow feature dimension. It is interesting to note that even though the boundaries between these nodules are coherent with respect to the PMN-PT lattice, their lateral size is similar to grain sizes commonly reported for polycrystalline sol-gel and PVD deposited perovskites. Upon examination of the SrRuO$_3$ bottom electrode (when deposited on LaAlO$_3$) features of similar size to the narrow lobe dimension of the PMN-PT, ~ 0.2 μm were found. This suggests that the surface microstructure of the SrRuO$_3$ provides some influence on the PMN-PT microstructure.

[010]

[110]

[100]

2.0 µm

1.0 µm

0.0 µm

0 µm   1.0 µm   2.0µm

1.0 µm

0.5 µm

0.0 µm

0 µm   0.5 µm   1.0 µm
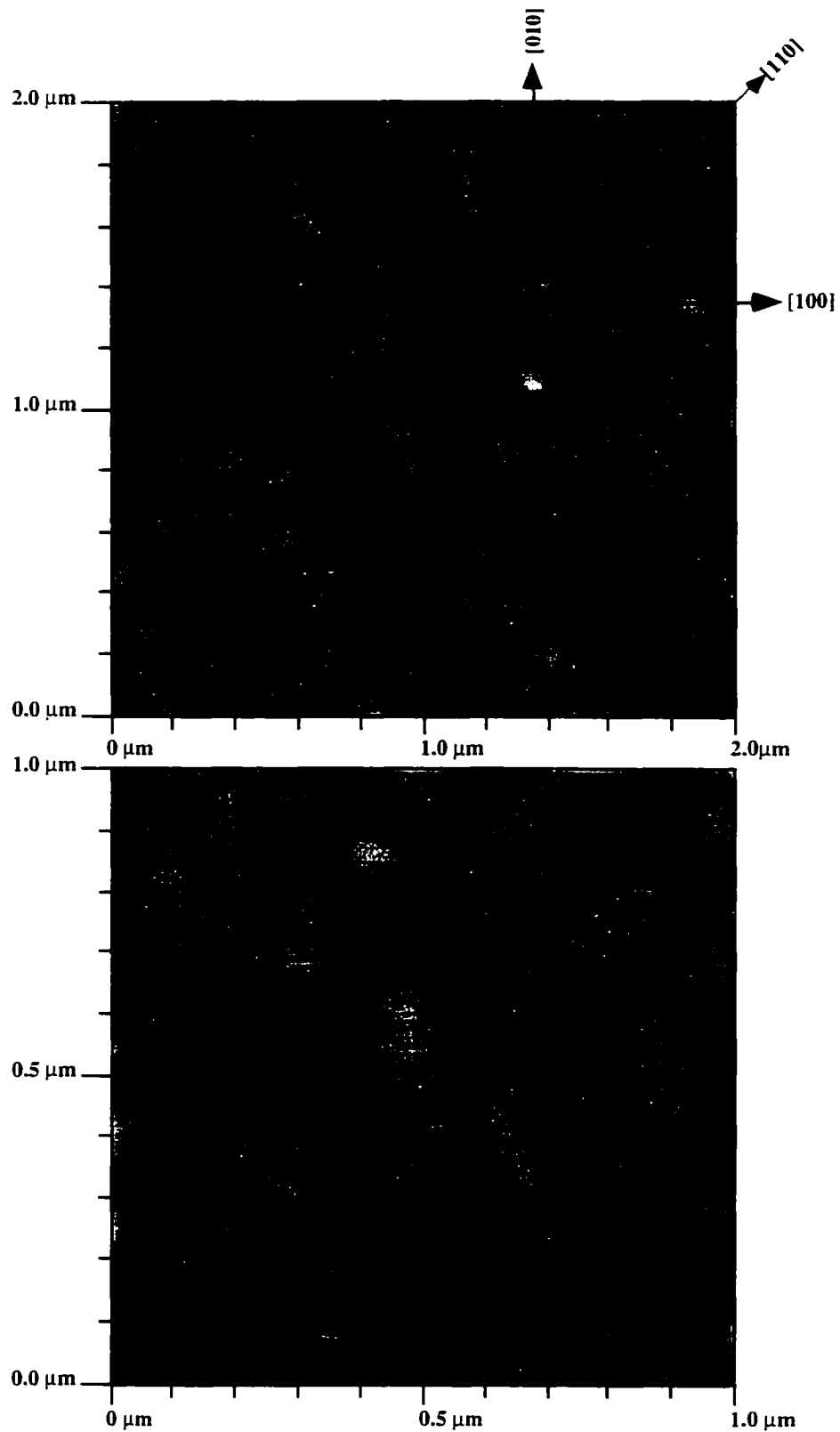
FIG. 5.10: AFM TOPOGRAPHICAL IMAGES OF PMN-PT FILM DEPOSITED AT 60 MTORR. LIGHT-TO-DARK CONTRAST CORRESPONDS TO 5 nm. (IMAGE COURTESY OF D. J. GUNDLACH AND T. N. JACKSON AT THE PENNSYLVANIA STATE UNIVERSITY DEPARTMENT OF ELECTRICAL ENGINEERING)

Using these deposition conditions. but increasing the laser frequency to 16 Hz or greater. the film composition (as judged by x-ray diffraction) could be saturated with respect to Pb-content. Films deposited under those conditions were characterized by small amounts of PbO_x second phase. If the deposition parameters were changed to provide reduced Pb-volatility, similar x-ray patterns were obtained. Second phases were also observed when samples were deposited with a Pb-deficiency. Interestingly. only one peak was observed for this additional phase, thus it could not be unambiguously identified. Only a modest out-of-plane orientation existed, so an epitaxial argument to support the absence of additional reflections is unlikely. It was possible to index the reflection as 004 PMN pyrochlore. however, this is inconsistent with the relative intensities given for the pyrochlore powder pattern. Possibly, the phase is similar to the PMN pyrochlore. however, the non-equilibrium growth conditions or deviations in the stoichiometry may result in changes in the relative x-ray scattering intensities.

X-ray analysis of these lower pressure deposited films also indicated an anomalous extension of the out-of-plane lattice constants. This is analogous to the results on $SrRuO_3$ thin films deposited at pressures below ~ 100 mTorr on $LaAlO_3$ substrates. The extension of the PMN-PT lattice is believed to be a result of the same bombardment-induced mechanism.

The ability to grow epitaxial samples at these low temperatures is of particular interest as it may allow thermodynamically unstable phases (such as PZN and its solid solution with PT) to be synthesized, as well as integration of materials which tend to react at growth temperatures in excess of 600 °C. The ability to observe phase-pure perovskite

films is undoubtedly a result of the epitaxial template. It is expected that energetic bombardment during growth provides some of the additional adatom energy necessary for crystal growth without the driving force for excessive lead volatility. To quantify the influence of the substrate template, a film was deposited on a polycrystalline platinum growth surface {111} textured Pt on Ti on SiO_2 on Si) using processing conditions identical to those which afford phase-pure epitaxial films. Structural analysis for this sample is given in Fig. 5.11.
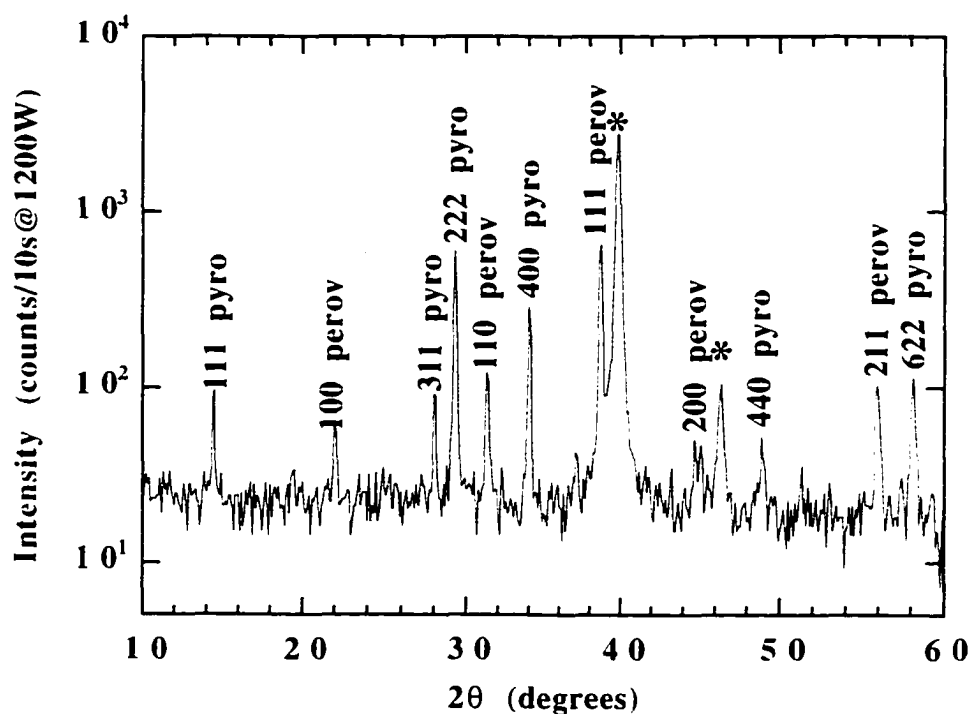
FIG. 5.11: θ-2θ SCAN FOR A PMN-PT THIN FILM DEPOSITED AT THE OPTIMIZED LOW TEMPERATURE CONDITIONS ON A PT-COATED SI SUBSTRATE

Approximately 50% of the material is pyrochlore; this effectively demonstrates the strong influence which a lattice-matched single crystal substrate can have on film growth.

5.4 Summary

Three important conclusions can be drawn from the investigation of the structural and phase development of PMN/PT (70/30) thin films: (i) It is possible to simultaneously observe Pb-deficient, Pb-rich, and stoichiometric perovskite phases in a single sample using typical PLD processing conditions. This unfortunately precludes the use of a straightforward adsorption controlled growth process for PMN-PT growth on $LaAlO_3$ substrates. (ii) Phase pure epitaxial PMN-PT films can be grown under high pressure and high temperature process conditions; specifically, temperatures in excess of 700 °C and pressures in excess of 700 mTorr. Film growth under these conditions will, however, result in very poor thickness uniformity and a relatively small coverage area. (iii) Deposition at temperatues below 600 °C and pressures which provide the appropriate amount of energetic bombardment can be used to deposit phase-pure epitaxial films. It appears that under these conditions the single crystal substrate is crucial in nucleating and maintaining the desired perovskite phases.

Chapter 6   PMN-PT Electrical Property Analysis

6.1   Electrical property measurements

Following the investigation of the structure-processing relationships, efforts were focused on characterization of the PMN-PT thin film electrical properties. Electrical property characterization included measurements of the dielectric constant, its temperature dependence, and the polarization hysteresis. Piezoelectric measurements are discussed in the following chapter.

The electrical and structural properties were separated in this manner to demonstrate that process optimization guided by either aspect exclusively may not lead to the expected (and ultimately desired) result. That is to say, that good electrical properties can be observed in samples with undesirable microstructures (i.e., as the existence of second phases and poor surface morphologies), and samples with excellent microstructures may have unacceptable electrical characteristics.

6.2   Phase-pure PMN-PT films

The phase-pure, highly-crystalline samples deposited at high temperatures and pressures (i.e., 710 °C and 700 mTorr) were initially characterized. Upon measurement, all similarly processed samples were found to exhibit insufficient resistivity for any meaningful dielectric analysis: conduction loss dominated all of the electrical properties.

Following this result. additional samples were processed with increased amounts of Pb.

however. acceptable resistivities were not observed in the absence of PbO_x in the

diffraction patterns. Since low resistivity phases such as pyrochlore or PbO_x were not

present (to the detection limits of x-ray diffraction). it was conjectured that the PMN-PT

was appreciably lead-deficient. thus electronically defective and leaky. Further analysis

of the x-ray data revealed that the lattice constants were consistently smaller than bulk

values. which reinforced the assumption of lead deficiency. Reduction in the lattice

constants of approximately 0.01 Å was systematically observed. This type of reduction

with lead deficiency has also been observed in the PLMT system. again. in the absence of

second phases. Further analysis of high temperature deposited films was limited to

samples which contained small quantities of PbO_x in their microstructure.

6.3   PMN-PT samples incorporating PbO_x second phase

Since samples with similar structures. i.e.. incorporating excess lead-containing

phases. could be synthesized over a broad processing range. lower temperature conditions

in the vicinity of 630 °C were chosen. These lower temperatures were selected since the

rate of lead volatility scales with temperature. and working in a range of the smallest

volatility rate would be expected to provide the best reproducibility. Fig. 6.1 is a θ-2θ x-

ray pattern for such a film. The pertinent processing conditions. as well as the x-ray line

widths. are listed in the figure legends. The broad shoulders adjacent to the 002 and 003

reflections correspond to the excess lead-containing phase present.
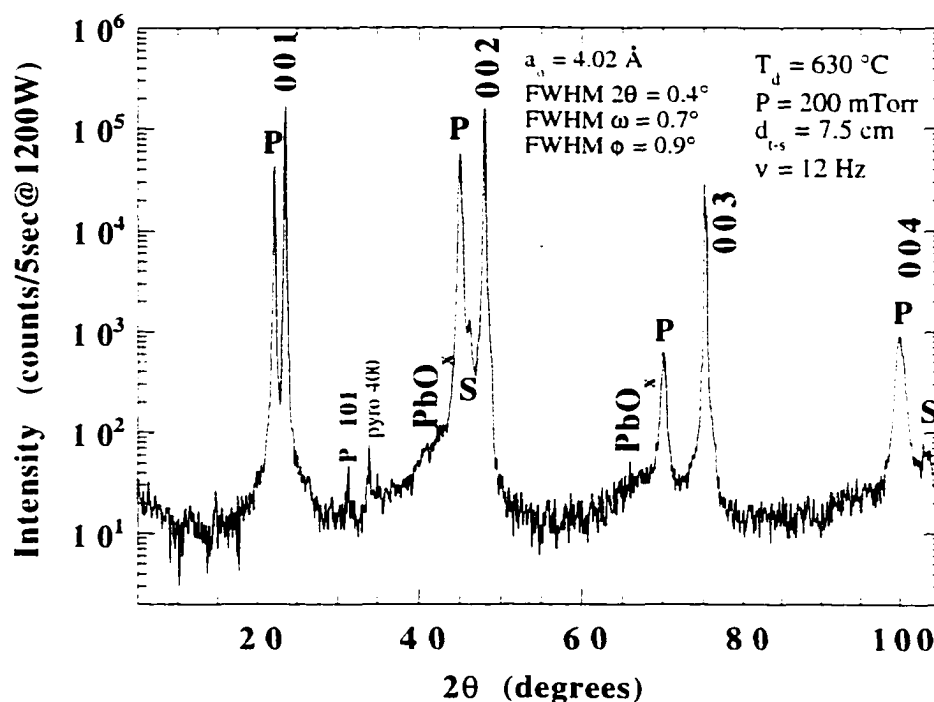
FIG. 6.1: θ-2θ X-RAY PATTERN FOR PMN-PT FILM DEPOSITED AT 630°C CONTAINING EXCESS PbO$_x$. D$_{T-s}$ CORRESPONDS TO THE TARGET-TO-SUBSTRATE SEPARATION DISTANCE AND v CORRESPONDS TO THE LASER REPETITION FREQUENCY.

A polarization hysteresis plot for the sample in Fig. 6.1 is shown in Fig. 6.2. Though the tails of the hysteresis loop indicate high resistivity, the value of remanent polarization (P$_r$) is much smaller than expected. Electrically, this sample resembles a relaxor in the vicinity of T$_m$ (the temperature at which the maxima in the dielectric constant occurs), where P$_r$ falls gradually with increasing temperature and the hysteresis loop tilts towards the positive field axis.[26] Identical behavior was observed in numerous similarly processed samples.

To verify this assumption, the sample was immersed in liquid nitrogen and again the polarization hysteresis was measured; Fig. 6.3 shows this data.
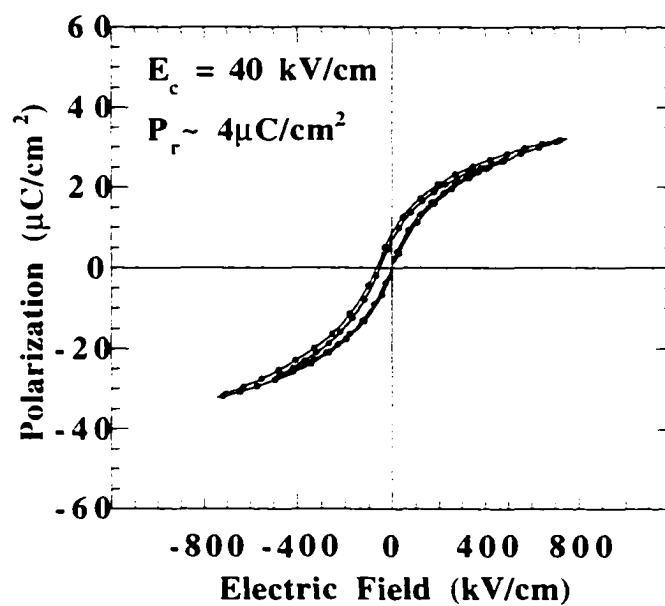
FIG. 6.2: ROOM TEMPERATURE POLARIZATION HYSTERESIS LOOP FOR PMN-PT FILM DEPOSITED AT 630°C
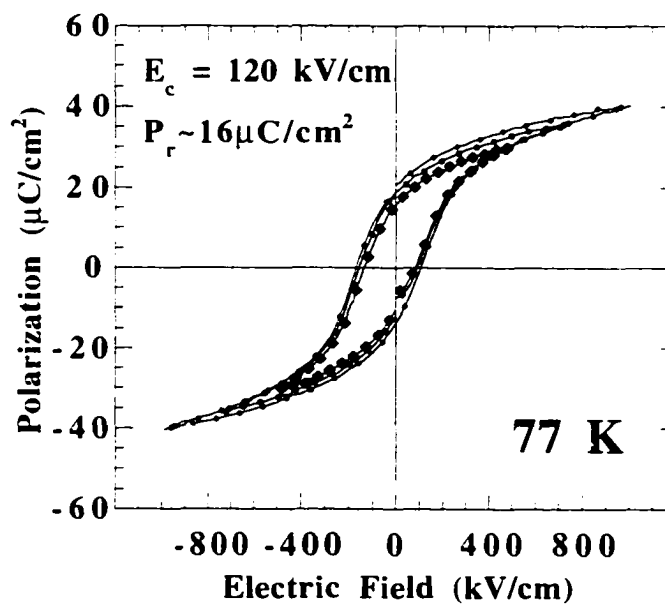
FIG. 6.3: POLARIZATION HYSTERESIS LOOP MEASURED WHILE IMMERSED IN LIQUID NITROGEN FOR PMN-PT FILM DEPOSITED AT 630°C

At this temperature a well developed hysteresis evolves with a remanent polarization of approximately 16 μC/cm^2. This low temperature result indicates that the onset of the polarization is shifted with respect to temperature, and suggests that a temperature shift also exists for the Curie transition. The temperature dependence of the dielectric constant was measured between -150 °C and 220 °C: the result is shown in Fig. 6.4.
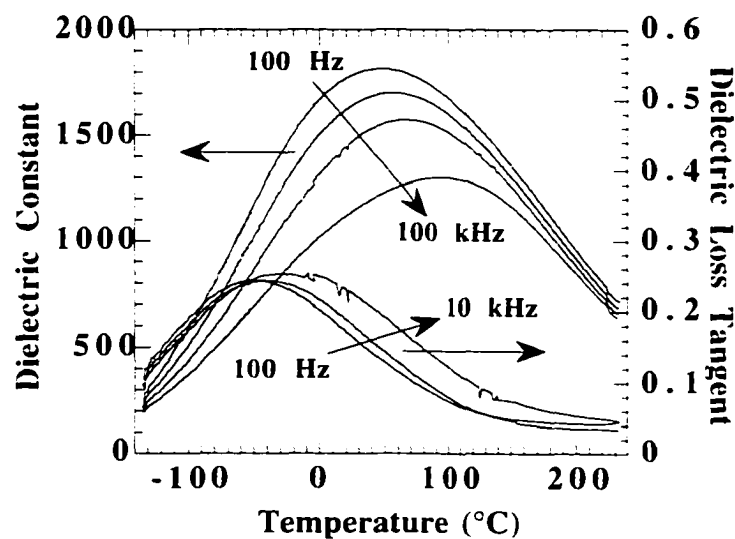
FIG. 6.4: TEMPERATURE DEPENDENCE OF THE DIELECTRIC CONSTANT AND LOSS TANGENT OF A PMN-PT FILM DEPOSITED AT 630 °C. AN OSCILLATOR VOLTAGE OF 5 mV, WHICH CORRESPONDS TO A FIELD OF APPROXIMATELY 0.5 KV/CM, WAS USED. DATA WERE TAKEN UPON COOLING

From this data a T_m of approximately 50°C at 1 kHz is evident. In contrast, a transition temperature of ~ 150 °C is expected for a bulk sample. Samples processed in conditions favoring slightly more and less Pb-volatility were synthesized, but no changes in T_m were found. Thus, the temperature shift of the ferroelectric transition cannot be solely attributed to Pb-stoichiometry.

Another interesting fact apparent on Fig. 6.4 concerns the permittivity values

above T_m. In this region, the dispersion is lost, which is consistent with the classical

behavior of relaxor materials. (For this reason, the terminology T_m is used to describe the

maxima in the dielectric constant.) It should be noted, however, that well prepared

ceramic and single crystal samples of this composition show a small amount of relaxor-

type behavior, with limited dispersion and diffuseness of transition. At the morphotropic

composition (65/35), the material behaves as a normal ferroelectric.[26,44] The thin film

permittivity data taken at 0.1 kHz was analyzed to determine if Curie-Weiss behavior was

followed. Fig. 6.5 illustrates the result. The 0.1 kHz data was used since it contains the

greatest number of data points above T_m, thus should provide the most reliable fit.
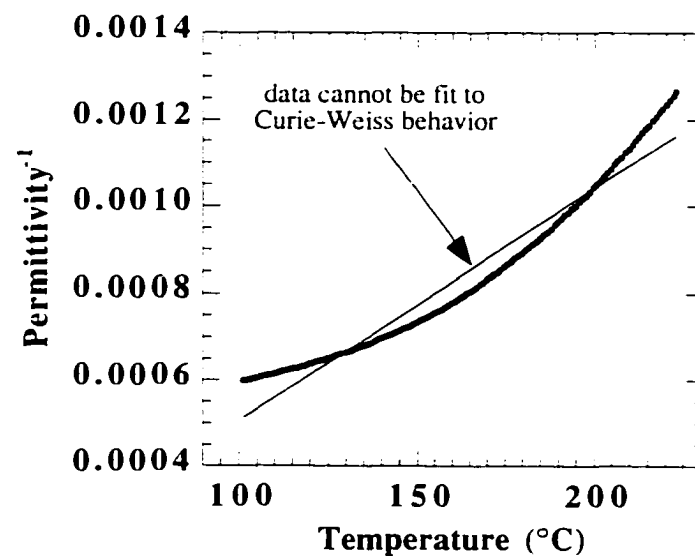
FIG. 6.5: CURIE-WEISS PLOT FOR 0.1 KHZ PERMITTIVITY DATA FROM PMN-PT FILM SHOWING
TEMPERATURE DEPRESSED ELECTRICAL PROPERTIES.

This analysis clearly demonstrates that Curie-Weiss behavior is not followed

directly above the ferroelectric transition. Again, it is noted that bulk samples of this

composition are close to the normal ferroelectric state, and thus follow the Curie-Weiss

relationship at temperatures above the ferroelectric transition.[44]

In order to determine the cause of the temperature-shifted transition, four factors

were investigated: film thickness, deposition rate, substrate thermal expansion mismatch

induced strain, and deposition temperature.

Previous investigators have reported on the influence of film thickness on

ferroelectric thin film properties.[112,166] Factors which have been identified as both

influential and dependent upon film thickness include depletion layers, film

microstructure, and residual stresses. To see if these factors were important in

determining the electrical properties of PMN-PT epitaxial layers, several 15,000 Å thick

samples were deposited and characterized (previous samples were routinely grown to a

thickness of ~2000Å). Fig. 6.6 shows the hysteresis data for a thicker film at room and

liquid nitrogen temperatures.
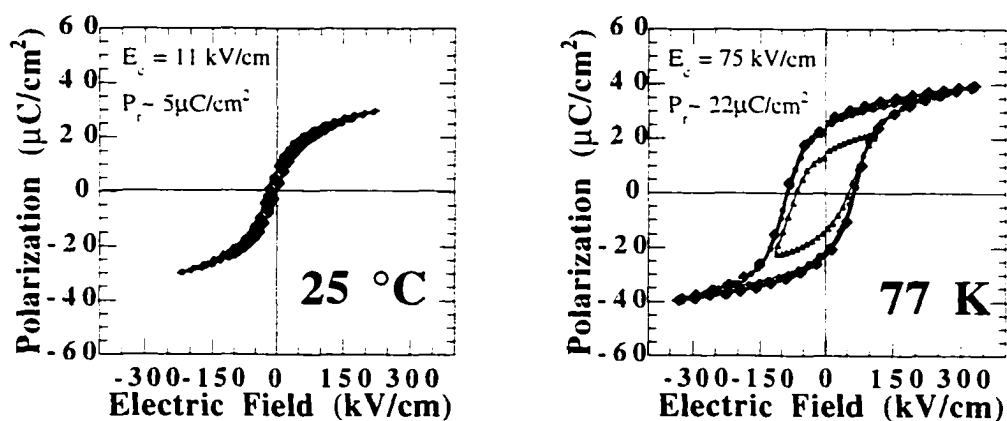
FIG. 6.6: POLARIZATION HYSTERESIS MEASUREMENTS FOR A THICK (~1.5 μM) PMN-PT SAMPLE PROCESSED AT 630 °C AT BOTH ROOM AND LIQUID NITROGEN TEMPERATURES

With the exception of a more square hysteresis loop with a lower coercive field, the electrical properties are quite similar to the thinner film. These modest changes in the low temperature hysteresis parameters are consistent with those observed by others concerning the effects of film thickness in polycrystalline PZT.[112,166] For this sample, (at 77 K) 80% of the room temperature remanent polarization observed in high quality single crystals of the same composition is realized. This result indicates that film thickness, or factors which depend solely upon it, is not responsible for the depressed T_m values.

A second factor considered was the effect of film growth rate because of its potential impact on film microstructure and morphology. An increase in the concentration of structural defects is expected for films grown at rates where material accumulates faster than rearrangement on the growth surface can occur. This may be an especially important consideration in PLD where the growth is discontinuous, and the instantaneous rate may be as large as 10^4 Å/second, i.e., 1 Å per laser pulse, where the plasma lifetime is on the order of 10^{-6} to 10^{-4} seconds.[135] This rate, however, can be controlled by the combination of laser fluence, target-to-substrate distance, and pressure. To determine whether the growth rates during deposition are too fast for sufficient structural arrangement on the surface, two additional rates were tested where the thickness deposited per pulse was reduced, but the average rate expressed in Å deposited per unit time remained constant. These reduced deposition rate situations are practically realized by reducing the plasma density at the substrate plane while increasing the laser repetition frequency. The original growth rate was 0.5 Å/pulse, and the two additional rates were 0.3 and 0.15 Å/pulse respectively. These rates were determined by measuring the film thicknesses and dividing by the total number of laser pulses used. Highly

resistive films were deposited using each of the growth rates and electrically characterized. Upon comparison of the structural and electrical properties, no appreciable differences were observed; the electrical properties indicated that T_m was in the vicinity of room temperature.

It is well known that the transition temperature of ferroelectric materials is strongly dependent upon externally applied stress.[Jr., 1954 #139; Samara, 1966 #138] To determine the importance of residual stress on the electrical properties, additional PMN-PT samples were deposited on $KTaO_3$ substrates using the same deposition conditions. $KTaO_3$ was chosen because of its small thermal expansion coefficient - approximately 6 ppm/°C over the temperature range of interest.[148] In contrast, the average thermal expansion coefficient of $LaAlO_3$ has been reported to be 11 ppm/°C between room temperature and 700 °C.[146] The average thermal expansion coefficient of PMN-PT (70/30) is approximately 8 ppm/°C; this value is a combination of the lower temperature coefficient (which is less than 1 ppm/°C) and the high temperature coefficient (which is approximately 10 ppm/°C).[167] The coefficient falls sharply from the higher temperature value at the Burn's (or depolarization) temperature (T_d) which corresponds to the onset of a stable root mean-square polarization.[168]

Stress-free films are assumed during deposition in the following arguments due to the nucleation of strain-accommodating growth dislocations. Given the assumption of relaxed growth, it is believed that the stress state of the PMN-PT films, or at least the differences between films deposited on different substrates, would be governed by the thermal expansion mismatch of the film/substrate system. The films grown on $LaAlO_3$ would be in compression, while those deposited on $KTaO_3$ would be in tension. The

polarization hysteresis was measured for films prepared on KTaO₃ substrates under

conditions identical to those used for films referred to in Fig 6.2; Fig. 6.8 shows the

result. The temperature shift in the onset of the polarization is once again observed, thus

it is concluded that the thermal expansion mismatch induced strain does not dominate the

anomalous electrical behavior.
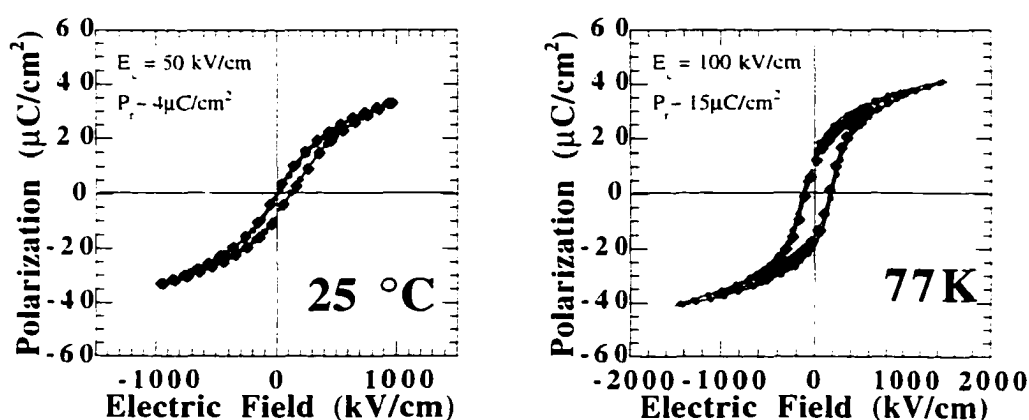
FIG. 6.7: POLARIZATION HYSTERESIS MEASUREMENTS FOR A PMN-PT SAMPLE PROCESSED AT 630 °C USING A (001)-ORIENTED KTaO₃ SUBSTRATE

Finally, the influence of crystalline quality on the electrical properties was

investigated. To improve the crystalline quality, deposition temperatures were increased

to values greater than 670 °C, which through increased vibrational energy (i.e., adatom

mobility) should improve the film-substrate crystallographic registry, and ultimately the

crystal quality. In this temperature regime, PMN-PT thin films with optimized

resistivities were deposited using a target to substrate spacing of 5.5 cm and an

atmosphere of 400 mTorr oxygen/ozone mixture. The laser repetition rate required to

achieve the desired Pb-stoichiometry was 17 Hz. This corresponded to a relatively rapid

average deposition rate of 3 μm/hour. As a result of this rapid deposition (and despite the

increased temperature), the film surface became irregular with an rms roughness of

approximately 0.05 μm. Fig. 6.8 shows an AFM topographic image for thin film samples

grown under these processing conditions.
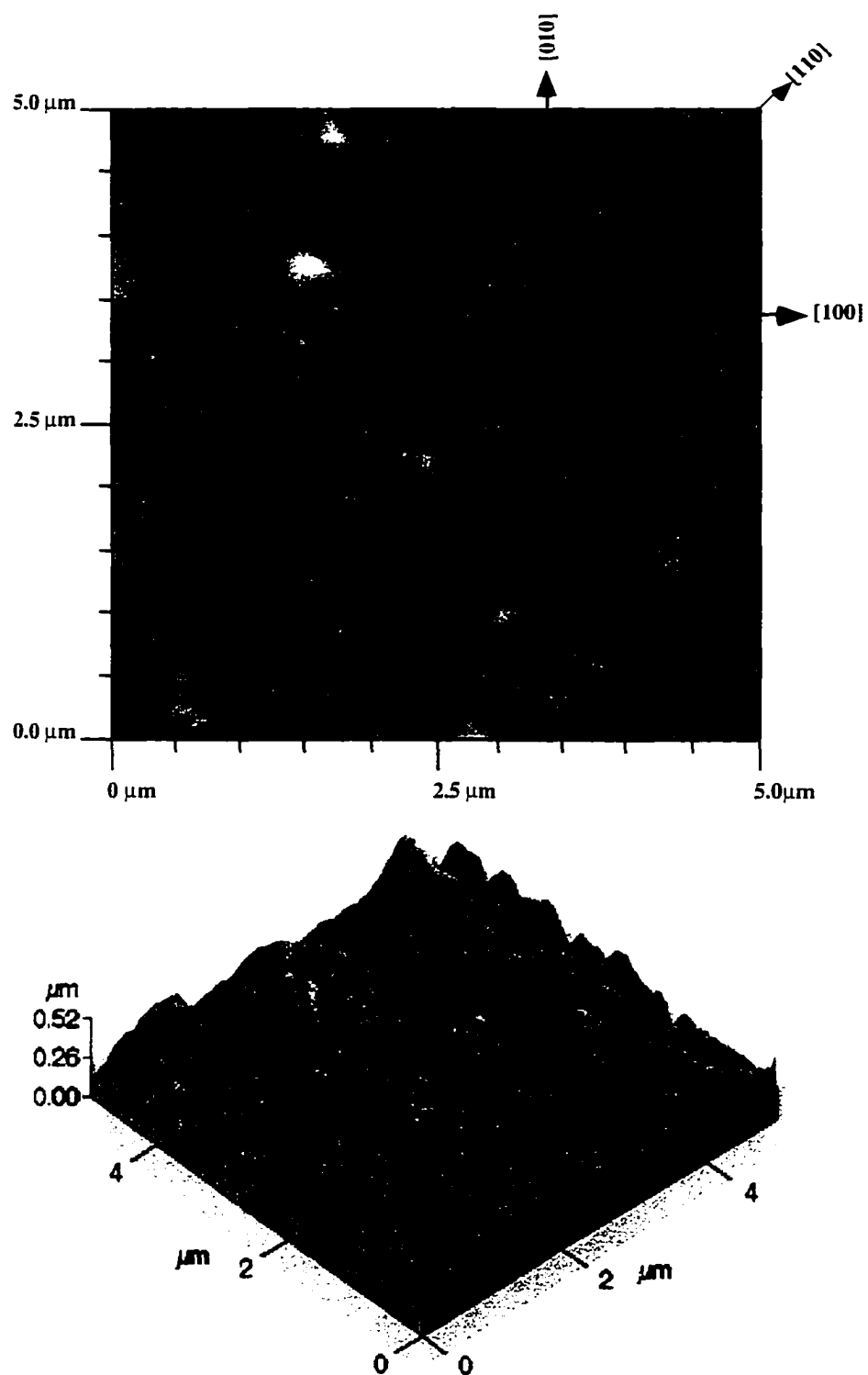
FIG. 6.8: AFM IMAGE OF HIGH TEMPERATURE DEPOSITED PMN-PT THIN FILM. TOP AND 3/4-VIEWS ARE GIVEN FOR THE SAME FILM REGION (IMAGE COURTESY OF D. J. GUNDLACH AND T. N. JACKSON AT THE PENNSYLVANIA STATE UNIVERSITY DEPARTMENT OF ELECTRICAL ENGINEERING)

In general, electrical properties closer to those measured for bulk samples were achieved. Table 6.1 lists the electrical properties for a well-prepared single crystal of PMN-PT (70/30), these values serve as a reference for comparison and sample evaluation.[47] Ceramic data cannot be used for comparison because of the strong property anisotropy between the <111> and <001> orientations.

TABLE 6.1: REFERENCE PROPERTIES FOR PMN-PT (70/30) SINGLE CRYSTALS MEASURED ALONG THE <001> CRYSTALLOGRAPHIC DIRECTION

Parameters[47]	PMN/PT (70/30)
Dielectric constant (25°C)	3000
Transition temperature	150 °C
Remanent polarization	25 μC/cm^2
Saturation polarization	27 μC/cm^2
Lattice constant	4.03 Å
Symmetry	rhombohedral

Because of the difficulty in reproducing high quality samples at elevated temperatures (a result of increased lead and lead oxide volatility), a target containing 2% Ba dopant was introduced. Ba was chosen because of its ability to stabilize the perovskite phase with respect to the associated lead-deficient pyrochlore. The addition of Ba into PMN-PT increases the tolerance factor and hence the thermodynamic stability of the perovskite structure.[36] For Ba-substitution in both PMN and PT, a decrease in T_m of approximately 20° C/mol% has been reported.[9,38] Though it has not been reported for the specific PMN-PT ratio investigated here, it is likely that the Ba addition will have a similar effect. Reports on La and Sr substitution into morphotropic PMN-PT show very similar transition shifts (i.e., approximately 20 °C/mole%).[9,22,38] Since T_m for undoped (70/30) single crystals is 150° C,[47] with 2% Ba–doping, the T_m value would be expected

to fall to approximately 110° C. Fig. 6.9 gives the temperature dependence of the

dielectric constant and loss tangent for a PMN(2%Ba)-PT film deposited under the newly

optimized deposition conditions. A transition temperature of 115 °C was recorded.

Considering the temperature measurement accuracy of the apparatus, as well as the

conservation of the exact target Ba-concentration, this value is effectively equivalent to

the expected value of 110 °C. Some dispersion and diffuseness of transition is observed

in this data and may be attributed to the crystalline disorder which is present (in

comparison to a bulk single crystal), as well as the 2% Ba-doping. Ba doping of similar

concentrations has been shown to enhance the relaxor-like characteristics in ceramic

PMN samples.[38]
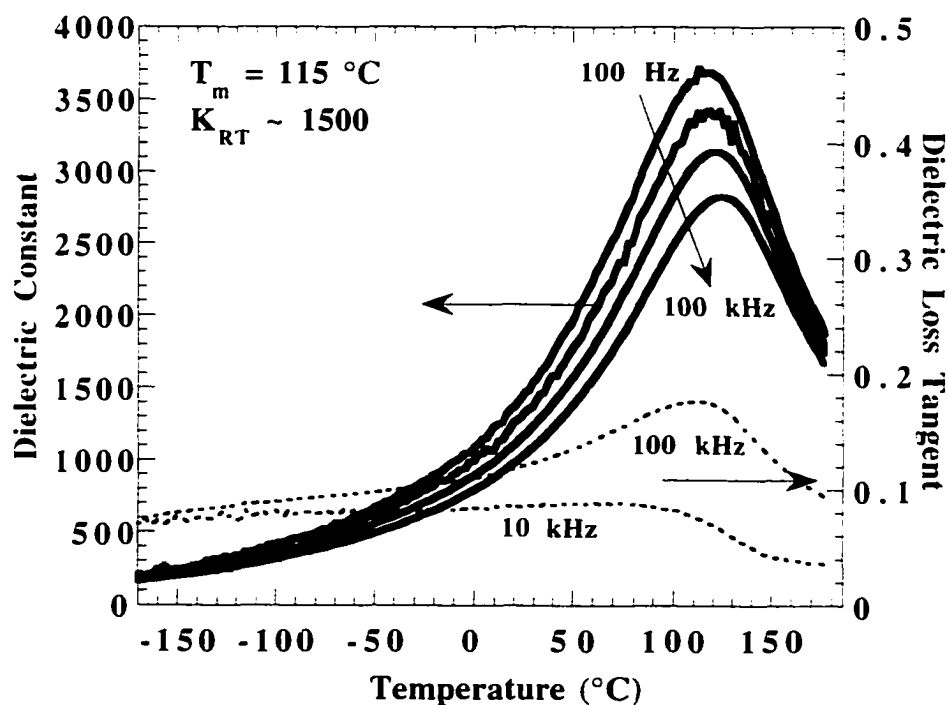
Fig. 6.9: Temperature dependence of the dielectric constant and dielectric loss for a
PMN(2% Ba)-PT thin film deposited at 670 °C

The temperature dependence of the dielectric constant in the paraelectric region was fit to Curie-Weiss behavior and a Curie-Weiss constant. C, of 1.5 x 10^5 °C was calculated. This value is on the same order as other relaxor-PT solid solutions in the vicinity of the morphotropic composition and was found to be frequency independent.[47] The Curie-Weiss plot is shown in Fig. 6.10.
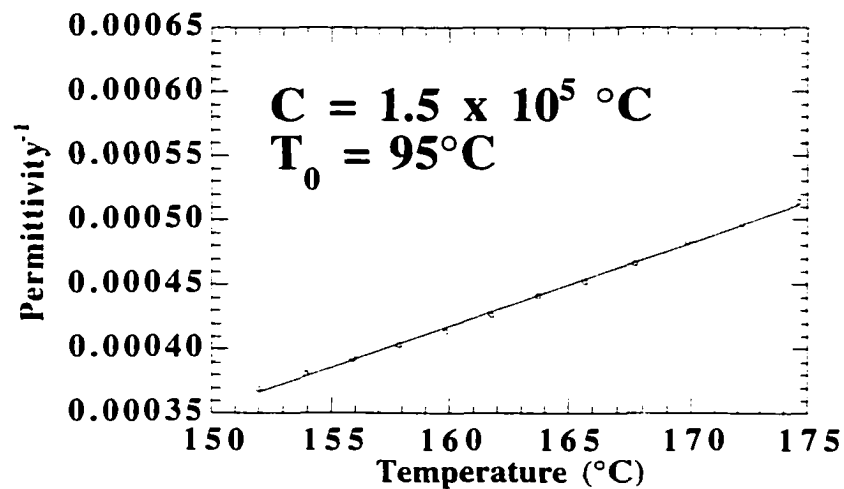
FIG. 6.10: CURIE-WEISS ANALYSIS FOR A PMN(2% BA)-PT SAMPLE DEPOSITED AT 670 °C

High field data was also collected for the higher-temperature deposited samples. Two examples of polarization hysteresis loops are given in Fig. 11. Fig. 11a gives a hysteresis loop for an optimized sample under standard driving voltages, while Fig. 11b gives a hysteresis loop driven to approximately 1 MV/cm. This figure demonstrates the large ac breakdown strengths available to PMN-PT thin films.
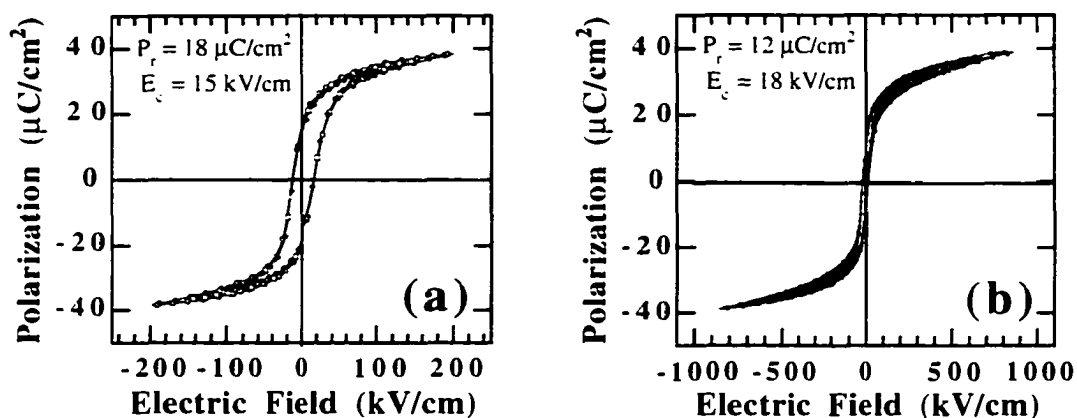
FIG. 6.11: HYSTERESIS LOOPS COLLECTED FROM PMN(2% BA)-PT SAMPLES DEPOSITED AT TEMPERATURES IN EXCESS OF 670 °C: (A) SHOWS HYSTERESIS AT NORMAL OPERATING FIELDS (B) DEMONSTRATES HIGH A.C. FIELD STRENGTHS AVAILABLE TO EPITAXIAL PMN-PT THIN FILMS

Remanent polarizations as large as 18 $\mu C/cm^2$ have been recorded for these samples. which corresponds to approximately 75% of the undoped single crystal values.[47] Extrapolations of the saturation polarization agree very closely with observations on bulk samples.

The qualitative difference between the samples deposited at 630 °C and 670 °C can be observed in the x-ray diffraction results. Fig. 6.12 contains a θ-2θ diffraction pattern typical of high temperature deposited samples showing electrical properties consistent with bulk single crystals. Again, samples processed under these conditions contained a lead-rich second phase indexed as PbO_x. In some of these samples, modest amounts of 110-oriented crystals were present. From a relative intensity argument (where the intensity of the non-epitaxial material is multiplied by 10 to account for the distribution of material in ω), the quantity of non-epitaxial material was established to account for less than 2% of the volume in the worst cases.
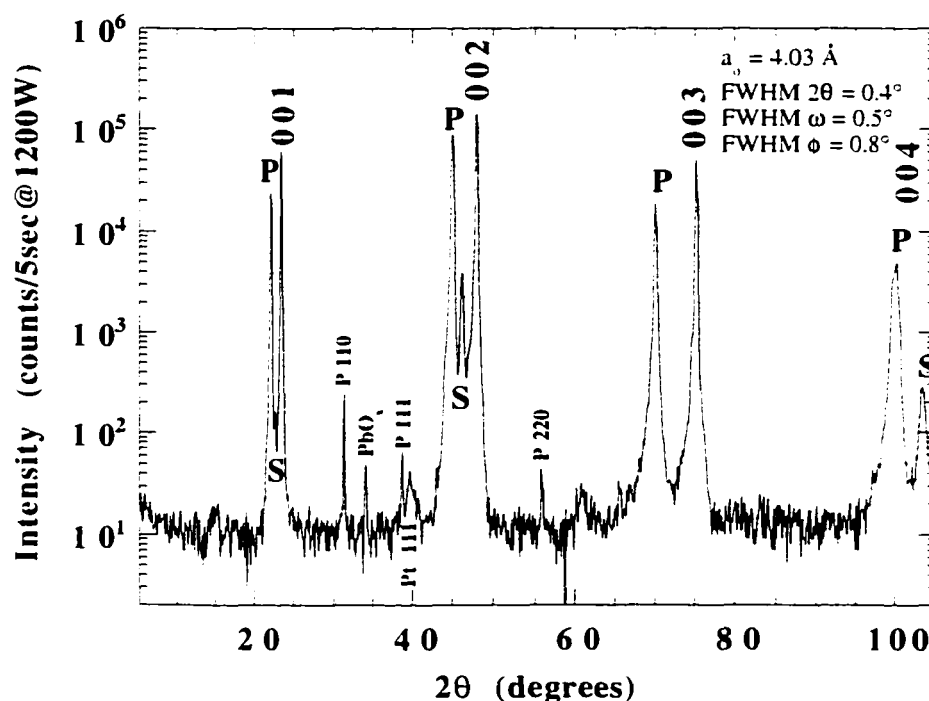
FIG. 6.12: θ-2θ X-RAY PATTERN TYPICAL OF A PMN-PT FILM DEPOSITED ABOVE 670 °C AND INCORPORATING LEAD-RICH SECOND PHASES

Upon comparison of the x-ray patterns for the low and higher temperature deposited PMN PT films, subtle differences in the structure are observed. In general, for the lower temperature deposited samples, the x-ray line-widths are slightly greater while peak intensities are between 30% and 600% smaller (depending upon the particular reflection). These factors indicate a more pronounced mosaic structure as well as a greater variation in the interplanar spacings. With this information in mind, and the results of the experiments investigating thickness, strain, and deposition rate, the temperature-shifted electrical properties observed in previously measured samples were attributed to the sample crystallinity.

To explain this behavior, it is useful to consider first a pure relaxor like PMN which is characterized by a strong frequency dispersion and a diffuse phase transition. If relaxor behavior is due, at least in part, to the interruption of long-range order, normal ferroelectricity may be expected to occur upon chemical modifications like the solid solution with $PbTiO_3$. With the appropriate amount of $PbTiO_3$, the chemical disorder is lost, and the material behaves as a normal ferroelectric. If in some way, disorder can be re-installed into this otherwise normal ferroelectric composition, a transition to relaxor behavior may be expected. As has been observed in the work of Setter *et al.* on $Pb(Sc_{1/2}Ta_{1/2})O_3$ [29,30], in addition to the occurrence of dispersion with the destruction of long range order, it is also expected that the ferroelectric transition will shift to lower temperature.[21] It is proposed that this is the case for PMN-PT epitaxial thin films which show temperature shifted electrical properties, and that the root of this disorder lies in symmetry-breaking structural defects distributed throughout the film. These defects are believed to be associated with the low-angle-tilt boundaries which are necessitated by the crystal's mosaic structure. If this mosaic structure is envisioned as regions of "perfect" crystal separated by boundaries encompassing large defect concentrations, then an analogy may be drawn between the ordered regions in a PMN ceramic and the "perfect" regions in an epitaxial film with a sizeable substrate lattice mismatch. Experimental evidence for this argument is drawn primarily from two sets of data: x-ray analysis and the temperature dependence of the permittivity for samples deposited from Pb-rich ceramic targets. In a very straightforward manner, the x-ray analysis indicates that the high temperature grown samples have a larger coherent x-ray scattering dimension.[169] Using a Williamson-Hall analysis, a dimension of ~500 Å is calculated. In comparison,

with the same treatment, the scattering size for the lower temperature deposited is found to be ~100 Å. This analysis gives a semi-quantitative picture of the sub-grain structure. Combining this data with the permittivity temperature dependence, one finds that the smaller scattering regions are accompanied by the temperature shifted transition, the broadened and more dispersive dielectric maxima, and the deviation from Curie-Weiss behavior. Interestingly, the ~100 Å dimension is consistent with the 100 Å diameter ordered regions observed in ceramic relaxors of several compositions.[21]

This explanation suggests that if samples of better crystalline quality could be processed, additional improvements to the electrical properties may be expected. The best method of accomplishing this would be to choose a more closely lattice-matched substrate/bottom electrode combination.

It should be noted that the reproducibility for samples processed at temperatures in excess of 670 °C from PbO-rich targets was marginal. Though samples with electrical properties and structures similar to those given in the figures were reproduced on multiple occasions, many samples with poor electrical properties or structures containing unacceptable quantities of second phases were grown. It is believed that the processing windows for these materials are on the scale of the natural fluctuations of the equipment, or the precision in the deposition parameter controls.

6.4   Low temperature deposited PMN-PT

The phase-pure films grown at temperatures below 600 °C were the final samples

to be characterized electrically, these samples also contained 2% Ba dopant. In general,

the trends observed for the higher-temperature deposited material concerning crystallinity

and electrical properties were duplicated. As mentioned in the structural analysis section,

two sets of samples were analyzed, those deposited at 100 mTorr and 60 mTorr. The

structures of the samples were similar, with the exception of the x-ray line-widths, which

were slightly wider for the higher pressure deposition. Polarization hysteresis

measurements were collected for both samples and are shown in Fig. 6.13.
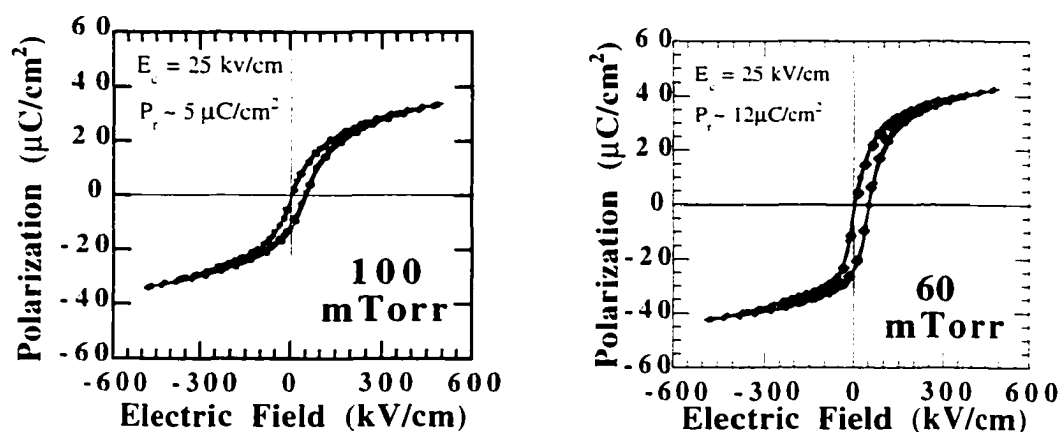
FIG. 6.13: HYSTERESIS LOOPS COLLECTED FROM PMN-PT SAMPLES DEPOSITED BELOW 600 °C. LOOPS ARE
SHOWN FOR SAMPLES GROWN AT 100 AND 60 MTORR O_3/O_2 MIXTURE. COERCIVE FIELD AND REMANENT
POLARIZATION VALUES ARE GIVEN AS MATHEMATICAL AVERAGES.

The difference between the hysteresis loops in Fig. 6.13 is reminiscent of the

differences between the electrical properties in the samples deposited from Pb-rich

targets at 630 °C and 670 °C. In this case, however, the improved crystallinity is a result

of the increased amount of energetic bombardment during deposition at 60 mTorr. The

dielectric permittivity and loss of the samples follow a similar trend as well, with the room temperature permittivity values of 1600 and 1300 for the 100 mTorr and 60 mTorr deposited samples respectively. The larger room temperature dielectric constant observed for the film deposited at 100 mTorr is explained by assuming that the ferroelectric transition has been shifted to a lower temperature and broadened.

Upon examination of these data, is becomes apparent that the hysteresis loops are shifted along the voltage axis. For samples deposited at 60 mTorr, the shift was so severe that the "negative" coercive field assumed a slightly positive value. The direction of the internal bias in these films is such that the preferred polar direction is from the film/substrate interface to the film surface. This effect is attributed to bombardment during growth, and is believed to be intimately coupled with the extended lattice constants which are observed for strongly bombarded PVD grown epitaxial films.[54,76,83,112,170,171] A more complete treatment of this effect will be given in the discussion of the piezoelectric properties.

6.5 Summary

As was mentioned in the first section, the conditions which provided the best crystalline structures were not always coincident with those conditions providing the optimal electrical properties. Indeed, with the exclusion of the samples deposited at temperatures below 600 °C, all samples with high resistivities incorporated detectable quantities of second phases. It is believed that these second phases (either Pb-rich or Pb-poor) served as locations in the crystal where precipitation of non-stoichiometric material occurred. This, in turn, may provide for the majority of the crystal having a composition

closer to the desired stoichiometry. (A loose analogy may be drawn to the zone refining process). It must be noted, however, that respectable electrical properties would only be observed if the quantity of the second phase was small and its microstructure non-contiguous. If a sample was deposited phase-pure, the possibility exists that it could be non-stoichiometric, but within the limits of the structure's solid-solubility. This situation is exacerbated by the presence of the epitaxial template and the non-equilibrium deposition conditions which may widen the solubility window. In the case of a phase-pure non-stoichiometric sample, the deviations in stoichiometry would need to be accommodated by the presence of homogeneously distributed point defects (i.e., A or B-site vacancies) which may lead to poorly insulating characteristics.

Though it was not observed, it is believed that a specific set of deposition conditions exist in the vicinity of 670 °C which would result in a phase pure crystal with excellent electrical properties. It is also believed that the acceptable deviations from these conditions are smaller than the precision of the deposition equipment. For achieving optimized electrical properties, it seems advantageous to be exactly stoichiometric or sufficiently non-stoichiometric to nucleate second phases, but not at a composition in between.

Chapter 7 Piezoelectric Measurements

7.1 Piezoelectric measurements

Piezoelectric measurements were performed using two methods. modified wafer

flexure. and *in-situ* field dependent x-ray analysis. Using these two techniques. the

transverse and longitudinal piezoelectric coefficients (d_{31} and d_{33}) were determined

respectively. In general, reasonable agreement between the methods was achieved.

Field-dependent x-ray analysis was also performed on a PZN-4%PT single crystal in

order to validate the thin film x-ray analysis. and to investigate the crystallographic

changes which accompanied the high-field response.

7.2 Modified wafer flexure

The wafer-flexure method was originally developed by Shepard *et al.* to

accommodate piezoelectric thin films deposited on circular wafers 3" to 4" in diameter

(the premise of the technique is given in the experimental section).[Jr., 1998 #237] In

order to apply this technique. a modification was necessary due to the relatively small

sizes of the PMN-PT samples (typically $\leq$ 1 cm^2). The modification of the technique

involved bonding the small single crystal substrates to Si wafers. and relying on strain

transfer through the bonding layer to achieve a biaxial stress on the PMN-PT surface.

Rather than attempting to model the silicon/glue/LaAlO$_3$ system and calculating the

surface stress. the strain was measured for reference samples using foil resistance strain gages and the system was calibrated with respect to the cavity pressure oscillation level. Fig. 7.1 shows a schematic of the wafer flexure apparatus. The small samples (hereafter referred to as chips) as well as the strain gages were bonded using a cyanoacrylate adhesive (i.e.. superglue).
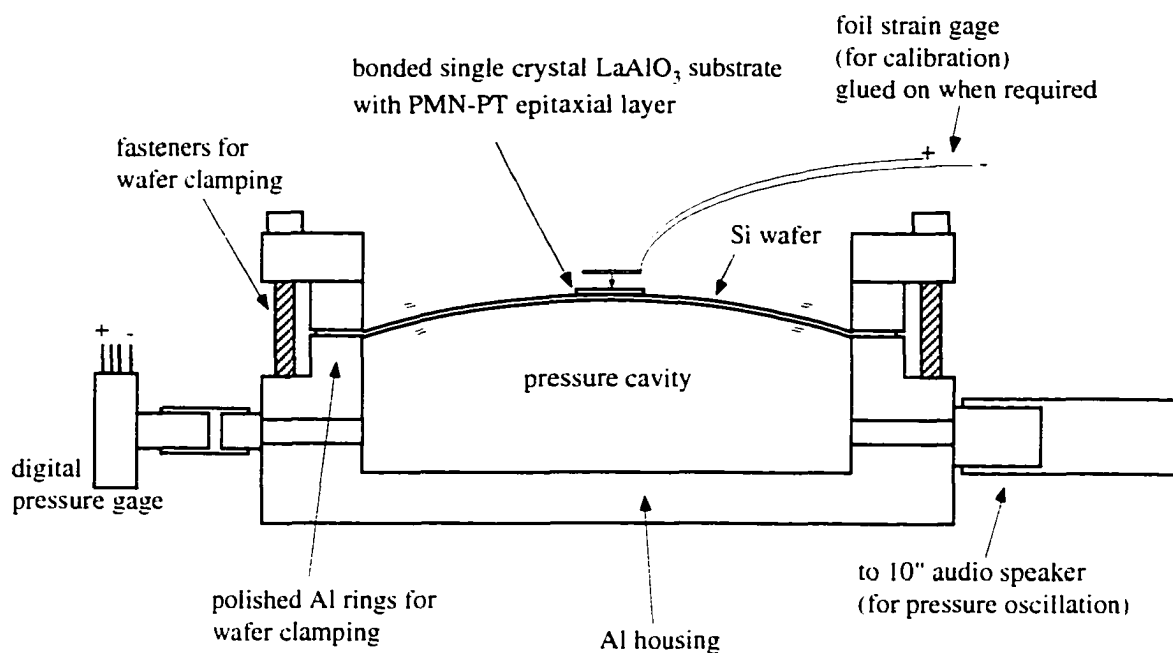
FIG. 7.1: SCHEMATIC OF THE MODIFIED WAFER FLEXURE APPARATUS

The first experiment performed to calibrate the apparatus involved bonding a PZT thin film with known piezoelectric coefficients to the center of a 3" Si wafer. A strain gage was bonded to the chip surface. and the uniaxial strain was measured for several pressure oscillation levels. In all of the bonding operations, care was taken to orient all Si and LaAlO₃ wafers and chips such that the crystallographic directions were aligned (i.e.. [100] LaAlO₃ or [100] Si // [100] Si). The strain gages were aligned such that the strain

measurement direction was directed along the [100] crystallographic axis. In addition, the crystals were all roughly square in shape and positioned in the center of the Si wafer. Using published elastic constants for PZT, the stress during oscillation on the film surface could be determined.[9] A second PZT coated chip was bonded to a Si wafer and under the same oscillation conditions used for the strain calibration, the piezoelectric charge output due to the periodic stress application was measured. With knowledge of the charge and stress oscillation, the d_{31} coefficient was determined to be approximately -40 pC/N. To within the accuracy of the technique, this value is consistent with previous measurements on full sized samples subject to the same poling treatment.[Jr., 1998 #237] This experiment effectively validated the modification and the reliability of the measurement. The calculation and measurement procedure was identical to that followed by Shepard *et al.*[Jr., 1998 #237]

The next step involved a strain calibration of $LaAlO_3$ bonded to Si. In this case a similar experiment was performed where a $LaAlO_3$ chip with a strain gage bonded to its surface was bonded to a Si wafer. Fig. 7.1 gives a plot of the strain measured on the surface of the $LaAlO_3$ chip as a function of speaker oscillation voltage. It should be noted that the strain measured by the gage is uniaxial. The linear dependence of strain with cavity pressure is indicative of the integrity of the bonding layer, as non-linearity would be expected were delamination or plastic deformation occurring. A linear relationship is also be predicted from small-deflection plate theory.[172]
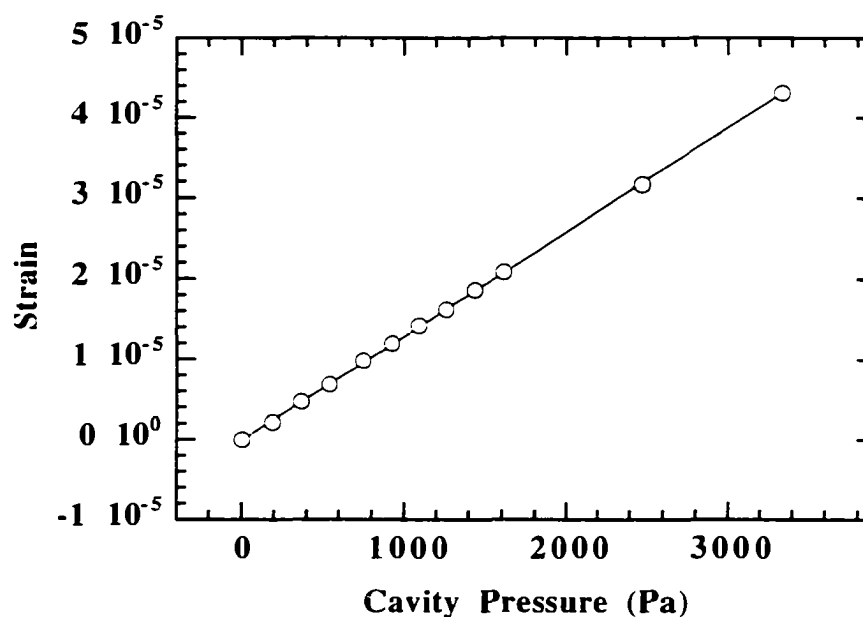
FIG. 7.2: UNIAXIAL STRAIN CALIBRATION FOR LaAlO$_3$ CHIP BONDED TO 3" DIAMETER, 380 μM THICK SILICON WAFER. [100] LaAlO$_3$ // [100] Si

The output of the strain gage conditioner was sent to a lock-in amplifier which drove the pressure oscillation. Using this arrangement, an rms strain was determined. It is important that an rms strain is used since during piezoelectric measurement, the piezoelectric charge is also measured as an rms value. For typical operating conditions, the audio speaker was driven at 0.5 V, which corresponded to an rms strain of approximately 1.5 x 10^{-5}. A second calibration experiment was performed where a LaAlO$_3$ wafer of approximately 50% smaller area was used. A similar strain calibration was undertaken and it was determined that the reduced wafer size did not result in an appreciable change in strain for the same pressure oscillation. All chips which were used for piezoelectric measurement had dimensions which were between those of the chips used for strain calibration.

A limitation in the accuracy of this analysis is that knowledge of the elastic constants are required for calculation of the piezoelectric coefficients. Elastic constants were not measured for PMN-PT thin films, however, reference data for single crystals of the same composition were available. The pertinent elastic constant c_{11} has been measured by ultrasonic techniques for a PMN-PT (70/30) single crystals, a value of 35 GPa was determined and used in all of the calculations. [47] The possibility exists that the elastic constants of the thin film samples are appreciably different than those of single crystals, especially when considering doping, residual stress, second phase, and composition effects.

Transverse piezoelectric coefficients were not measured for films showing temperature depressed electrical properties; d_{31} values are given only for the samples grown at high temperatures (~ 670 °C), and those deposited below 600 °C. For each sample type, two sets of data are presented, poling plots, where the d_{31} coefficient is given as a function of poling time, and aging plots, where the d_{31} coefficient is given as a function of time after removal of the poling field. During the aging experiments, the pressure oscillation was continuous (with the top electrode contact removed). This was done to avoid errors stemming from the instability of the pressure oscillation during the first few moments of oscillation. In contrast, during the poling experiments, the oscillation was turned off. This was done to avoid excessive wear to the top electrode surface by scratching with the metal point probe tip. To eliminate the instability of the oscillation pressure, a voltage output was recorded one minute after the oscillation began. Poling voltages of 5 V were used in all cases. The corresponding fields are approximately twice the coercive field value, larger voltages were not applied as poling

occurred too rapidly for the observation of any systematic trends with time. Figure 7.3

shows the poling curve for a PMN(2%Ba)-PT (70/30) thin film deposited at 670 °C.

Data are given in the plot for poling in both directions, i.e., top electrode positive and

negative. The d_{31} coefficients are all given as negative. Due to the oscillating method of

pressure oscillation (i.e., both compressive and tensile stresses are appplied), the absolute

sign of the d-coefficient cannot be defined. The poling directions are therefore

differentiated by the measurement phase angle.

FIG. 7.3: POLING CURVE FOR PMN(2%BA)-PT (70/30) THIN FILM DEPOSITED AT ~670 °C. DATA ARE
GIVEN FOR POLING CONDITIONS WITH THE TOP ELECTRODE HELD POSITIVE AND NEGATIVE

Error bars are included in this and all following graphs. These bars are indicative

of the ability to resolve an rms voltage on the lock-in amplifier, the measurement

accuracy of the top electrode area, and the uncertainty in the strain analysis. Potential

errors associated with knowledge of the elastic constants are not included. In addition, the phase angle. θ, is given for all curves. The phase angle corresponds to the phase of the piezoelectric response with respect to the pressure oscillation. Thus, the phase angle should have a value of either 0° or 180° depending upon the poling direction. and should switch values when the poling direction is reversed. The asymmetry in the piezoelectric properties is pronounced in the poling curves and indicative of an internal polarization bias. In the case of these samples, the direction of the preferred polarization is from the film/substrate interface to the surface, as evidenced by the larger piezoelectric coefficients available after poling with the top electrode negative. Fig. 7.4 shows the aging data for the same sample: again, evidence for a strong internal bias is observed.

FIG. 7.4: AGING CURVE FOR PMN(2%BA)-PT (70/30) THIN FILM DEPOSITED AT ~670 °C. DATA ARE GIVEN FOR POLING CONDITIONS WITH THE TOP ELECTRODE HELD POSITIVE AND NEGATIVE

For poling in the direction of the internal bias, the aging rate is effectively zero.

Films were poled in the favored direction and remeasured after more than one week with

negligible differences between the calculated piezoelectric coefficient values. When the

aging rate was measured for poling against the internal bias, rates as large as 30%/decade

were observed. Such large values are attributed to the influence of the internal bias.

The same set of experiments were performed on the samples deposited at

temperatures below 600 °C. Fig. 7.5 contains the poling information, again for top

electrode positive and top electrode negative conditions.
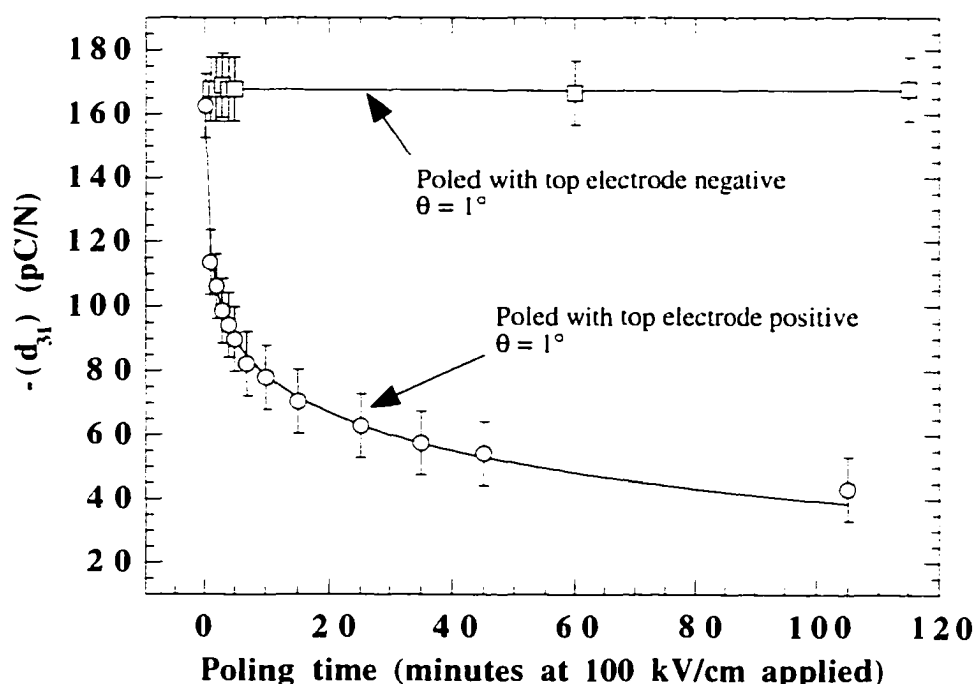
FIG. 7.5: POLING CURVE FOR PMN(2%BA)-PT (70/30) THIN FILM DEPOSITED BELOW 600 °C. DATA ARE GIVEN FOR POLING CONDITIONS WITH THE TOP ELECTRODE HELD POSITIVE AND NEGATIVE

The same type of asymmetry is observed for this film, however, the differences

between the poling conditions are even more severe. The phase angle for both poling

conditions are ~1°, which indicates that the poling direction cannot be switched using this poling treatment. Larger field values were applied for longer time periods in an attempt to achieve a zero state of poling, however, all attempts resulted in electrical breakdown. (This is in contrast to previously measured samples which could be taken through d_{31}~0 pC/N with the appropriate electric field application.)

To make sure that the inability to switch the phase angle of the measurement was not an artifact of the technique. a dc bias was applied to the film in the direction opposite to the internal bias and the piezoelectric coefficient was measured. As expected. at a field of approximately 100 kV/cm. the phase angle clearly switched to a value of 179°. thus excluding the possibility of a measurement artifact. As before. the sample was allowed to age. the results of this test are given in Fig. 7.6.
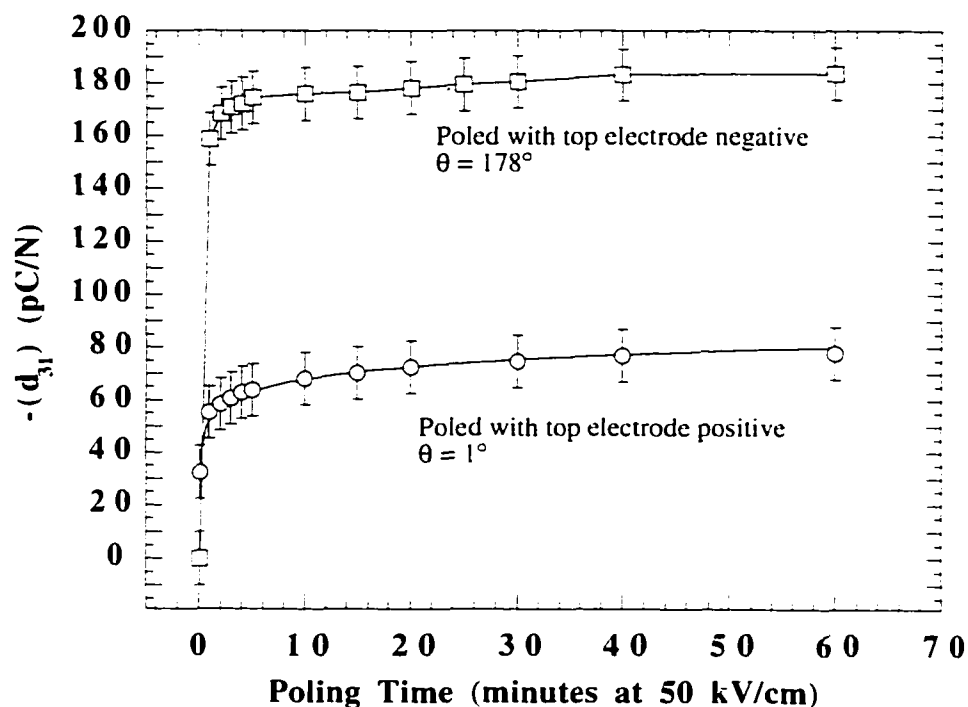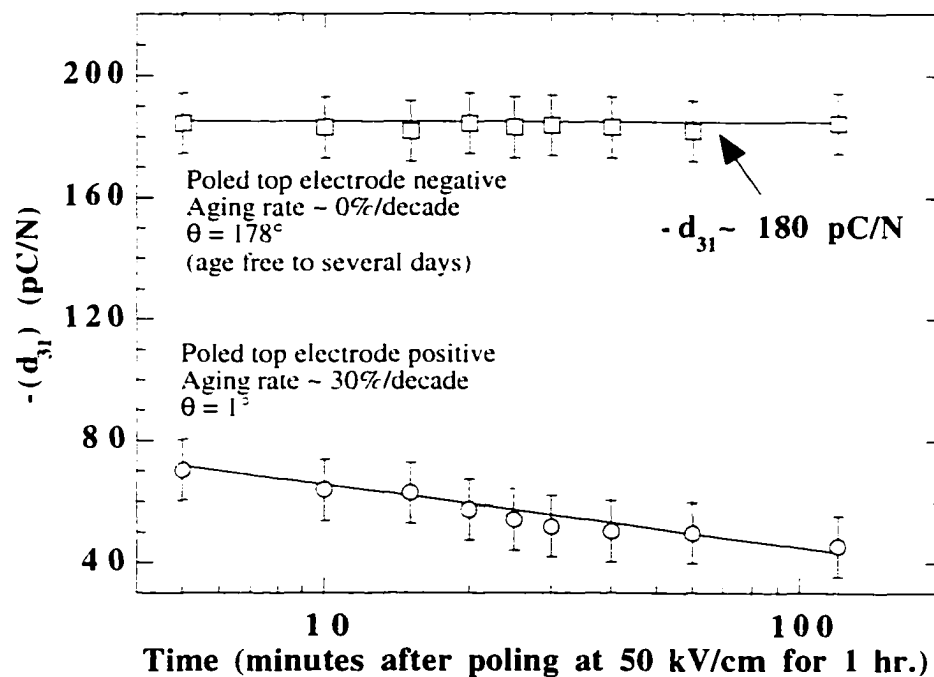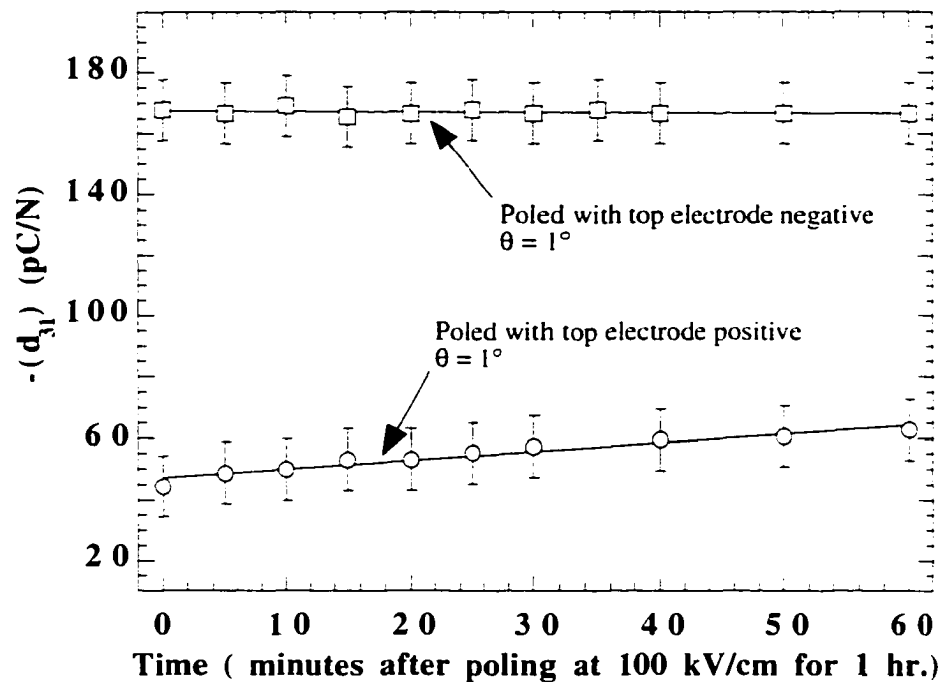
FIG. 7.6: AGING CURVE FOR PMN(2%Ba)-PT (70/30) THIN FILM DEPOSITED BELOW 600 °C. DATA ARE GIVEN FOR POLING CONDITIONS WITH THE TOP ELECTRODE HELD POSITIVE AND NEGATIVE

Again, for poling in the direction of the internal bias, a negligible aging rate was observed for times in excess of one week. When the aging measurement was performed for the poling condition opposite to the internal bias, a positive aging rate was recorded. That is, the piezoelectric coefficient increased in magnitude with respect to the as-poled situation. Asymmetric piezoelectric properties have been observed by previous researchers, however, this is believed to be the first observation of a positive aging rate in a ferroelectric thin film.[Jr., 1998 #256]

When poled in the direction of the preferred polarization orientation, the PMN-PT films exhibited transverse piezoelectric coefficients approaching –180 pC/N. These values are in excess of even the largest reported values for PZT films by nearly a factor of two.[83] In general, for well prepared PZTs of comparable thickness, reliable reports of

d_{31} typically fall in the vicinity of - 40 to - 60 pC/N. thus these materials represent an appreciable improvement in the achievable thin film piezoelectric response.[Kholkin, 1996 #66: Kholkin, 1996 #174: Jr., 1998 #237] Similar results were recorded for multiple samples. and multiple top electrodes on each sample.

After all piezoelectric experiments were performed on the samples. hysteresis loops were measured. Fig. 7.7 shows polarization hysteresis data for both samples. Multiple values are given for the coercive fields and remanent polarizations indicative of the asymmetry and internal polarization bias.
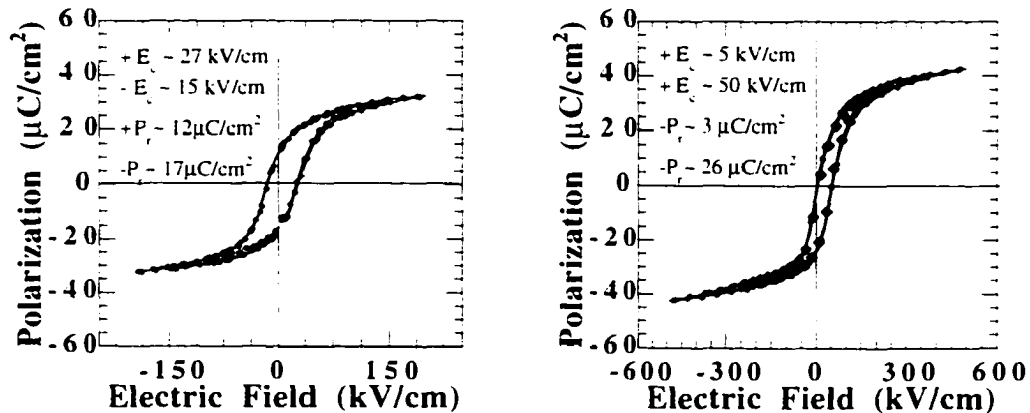
FIG. 7.7: POLARIZATIION HYSTERESIS DATA FOR PMN(2%BA)-PT (70/30) THIN FILMS DEPOSITED AT 670 °C (LEFT) AND BELOW 600 °C (RIGHT).

Evidence for the asymmetric behavior is also indicated in the hysteresis data, and is consistent with the piezoelectric measurements. For the material deposited at temperatures in excess of 670 °C, a modest shift exists on the field axis of the hysteresis loop. however, the remanent polarization states are of opposite sign. This is consistent with the piezoelectric data which indicates that a larger piezoelectric coefficient can be

achieved in one direction, and that the orientation of the remanent polarization can be switched by 180°. For the material deposited at low temperatures and pressures, a considerably larger shift is observed along the field axis such that both remanent polarization states have the same sign. This result agrees with the piezoelectric data, where in the absence of large electric fields, the phase angle for the measurement could not be switched from 0° to 180° despite changing the poling polarity.

Such shifts have been observed in previous reports, and for PVD deposited material, films with hysteresis loops free of any voltage shift seem to be the exception.[54,56,83,164,171,173] Frequently, the existence of a residual stress is suggested to explain the asymmetry, however, a systematic demonstration of this effect has not been presented.

An excellent review of voltage shifts in PZT thin films and BaTiO$_3$ ceramics has been reported by Dimos *et al.* where the field-shifted properties were associated with oriented defect dipoles. The existence of these dipoles was evidenced by ECR data, and observation of defect-dipole orientability by 2 hour anneals at temperatures of 65 °C and 120 °C. In general, Dimos *et al.* argue that $V_{Pb}'' - V_O''$ dipoles orient with time under the influence of a remanent polarization, and that electrons become trapped at potential wells associated with the positive ends of the dipoles. [77,79,80] As a result, an internal field is established across the film, providing the polarization bias.

To determine if this lead vacancy – oxygen vacancy complex was the active mechanism in PLD deposited PMN-PT, a similar experiment was performed. A sample with a fully shifted hysteresis loop was placed on a hot plate at 80° C. The sample was then subjected to a 100 kV/cm field, directed against the internal bias for two hours (a

more aggressive treatment than that used by Dimos *et al.*).[80] The polarization hysteresis

was measured for the sample taking care to duplicate the previous measurement

direction; no changes had occurred. After the hysteresis measurement, the piezoelectric

coefficient was remeasured, the same d_{31} coefficient of -170 pC/N was recorded. This

result suggests that the mechanism associated with imprint in PZT thin films does not

provide the predominant influence in pulsed laser deposited PMN-PT.

The fact that these films are partially to fully poled as deposited suggests that a

charged and oriented defect is present, and results from some aspect of the deposition. In

addition, the fact that the observations of voltage shifted hysteresis loops seem common

(and difficult to avoid) for PVD grown materials suggests that the electric fields

associated with plasmas, or some type of bombardment-related influence is responsible.

An interesting report has recently been published by Abe *et al.* concerning epitaxial

BaTiO$_3$ thin films with strongly asymmetric hysteresis loops and leakage current profiles.

Abe proposes an epitaxial interfacial stress model which results in an asymmetric free-

energy function for the ferroelectric polarization states adjacent to the substrate interface,

and a resulting energetically preferred polarization direction through the remaining film

thickness. In addition to the asymmetric electrical properties, Abe also finds that the out-

of-plane lattice constants are extended by as much as 7%. This anomalous extension is

also attributed to the epitaxial strain effect.[164] It would be unexpected that a brittle

material could withstand 7% mechanical strain, thus the interfacial stress from epitaxial

growth seems seems unable to explain both occurrences. In addition, this explanation

would predict that all epitaxial thin films would suffer from similar effects. Epitaxial

perovskite thin films with bulk lattice constants have been synthesized by multiple

researchers.[42,102,109,113,116,141,142,161,174]

As mentioned in Chapters 5 and 6, the samples which show very large voltage

shifts in the polarization hysteresis also have extended out-of-plane lattice constants.

Though the specific mechanism remains unclear, it was determined in the investigation of

$SrRuO_3$ epitaxial films that the cause of the extended lattice constants is energetic

bombardment during growth. Here, it has been demonstrated that in addition to the

extended lattice constants, moving to deposition conditions which provide increased

levels of energetic bombardment leads to samples with severely voltage-shifted hysteresis

loops. A possible link between the extended lattice constants, the asymmetric properties.

and the energetic bombardment is discussed in the following model.

In order to describe the observed effect. a plausible model must account for three

occurrences: (i) the anisotropic extension of the lattice constants, (ii) the internal

polarization bias, and (iii) the occurrence of the effect during growth, and its stability at

the deposition conditions (i.e.. temperatures in between 600 °C and 700 °C). In

consideration of these criteria, several possibilities may be excluded.

Oriented defect-dipoles can result in an internal field and a polarization bias.

however, it is difficult to explain why these dipoles would be aligned during growth.

Following the work of Dimos *et al.*, such dipoles should be very mobile during growth

(i.e., limited only by oxygen vacancy mobility), thus, in the absence of a remanent

polarization. any driving forces for alignment should be electrostatic in nature and would

be expected to produce a random array. The presence of an electric field associated with

a sputtering plasma may be able to orient defect dipoles, however, upon extinguishing the

plasma. the dipoles woud need to remain oriented through film cooldown. It is equally difficult to explain why vacancy defect-dipoles would result in a large lattice constant extensions.

A second possibility would be the implantation of charged ionic species in the lattice. It can be argued that implanted species would produce an extension in the lattice constants, however, their population would need to exist as a gradient for an internal field and a polarization bias to be established. In addition, these charged species would need to remain locally uncompensated over long time periods. Also. if such a gradient of implanted defects existed. anisotropic x-ray reflections skewed to smaller 2θ values would be expected: these were not observed.

A third explanation is the implantation of additional atoms in the lattice. (in this model, the charge on the implanted species is unimportant). If a concentration of implanted species were present in a unconstrained lattice, the expected result (for a cubic structure. i.e.. PMN-PT at 600 °C) would be isotropic expansion. If the same lattice was being "stuffed" during growth, where it could not freely expand due to in-plane substrate clamping, the lattice strain would no longer be isotropic, but suppressed in the substrate plane. and enhanced perpendicular to it. Some of the stress should be relieved by bending of the film substrate system. The resulting stress in the film could exist as a gradient, even though the implanted species were distributed homogeneously. A strain (or stress) gradient through the film thickness could stabilize one polarization state over another. (In the presence of a uniform planar stress, net polarization up, or net polarization down should be equally favorable.) The magnitude of this strain gradient would be small, but finite. Assuming that the film/substrate system can be modeled as a

beam in flexure where the neutral axis is located at the center of the substrate (the 1-D

limiting case), provided that the stresses are small enough such that linear behavior

occurs. for a 1 µm film on a 500 µm thick substrate, a strain difference between the film

surface and interface of 0.4% is predicted (this calculation simply assumes a linear

distribution of strain across a beam in flexure and an equal moduli in both film and

substrate). Even thought the relatively small film thickness results in a small strain

gradient (approximately 0.4% of total / µm), since the magnitude of stress gradient

necessary to stabilze a net [001] polarization orientation in a rhombohedral crystal is

unknown. this model cannot be completely ruled out.

A final model which may be used to explain these results is based upon research

from the 1950's involving irradiated ferroelectric crystals. Several research groups

studied the irradiation of triglycine sulfate (TGS), rochelle salt, $PbTiO_3$, and $BaTiO_3$

single crystals and ceramics from radiation sources including neutrons, x-rays, and

electron beams.[175-181] For the experiments conducted on neutron bombarded $BaTiO_3$ and

$PbTiO_3$, swelled lattice constants, depressed Curie transitions, and voltage shifted

hysteresis loops were reported. Unfortunately, in these reports, no specific mechanisms

were developed to explain these observations.[175,180,181] For reports concerning the

irradiation of TGS single crystals, similar trends were observed, and were accompanied

by a detailed discussion. In general, for x-irradiated single crystals, a voltage bias was

introduced in proportion to the exposure time, with the bias direction determined by the

direction of the remanent polarization direction or applied electric field during

bombardment (in a similar manner as demonstrated for vacancy defect dipoles on PZT

thin films). In this case. however, damage resulting from the irradiation was believed to

be responsible. The specific damage mechanism which produced these polarization-orienting defects was atomic or ionic excitation followed by chemical reaction and molecular rearrangement. In subsequent reports, the defects were identified as changes in the relative conformation of the three glycine molecules in each unit cell.[177,182] The stability of these defects after completion of the irradiation process was evidenced by the recurrence of the same domain patterns upon cycling through the ferroelectric transition.

It is postulated that a similar process is occurring in bombarded epitaxial PMN-PT thin films. In this case, the bombarding species – through collision processes – result in ionization of atoms in the lattice, which may result in chemical interactions favoring a specific polarization orientation (as opposed to distortion of a glycine molecule). Since the material is not polar at this temperature (as in the case of room temperature irradiated TGS), some external influence must provide the driving force for a commom orientation. To possibilities are given to account for this: (i) the uni-directional nature of the bombarding species, or (ii) the negative electric field which has been suggested to exist at the periphery of laser induced plasmas.[131]

Though this model involves several significant assumptions, it is consistent with the experimental observations and the deposition method. Importantly, this model is also consistent with the observation of extended lattice constants since the bombarding species which are proposed to produce the ionizing damage may still implant into the perovskite lattice, thus providing the anomalous lattice constant values.

Of the two models proposed to explain the structural and electrical properties associated with bombarded perovskite thin films, neither can be successfully validated without additional experiments. Possibilities which may elucidate the proper mechanism

include the choice of alternate substrates which will change the epitaxial interfacial strain, or depositions which include an external electrical bias which may change the orientation of the preferred polarization state.

Regardless of the mechanism behind this behavior, the results indicate the possibility of an engineered domain state, where a preferred polarization can be processed into a ferroelectric sample. In addition, this preferred polarization state appears to produce films nearly free of aging when tested in the direction of the internal bias. From this work, and the results of other researchers concerning as-processed voltage shifted samples and extended lattice constants, it appears that energetic bombardment during growth has an important influence on this behavior.

7.3   In-situ x-ray analysis

7.3.1   Thin film analysis

The wafer flexure method was effective for characterization of the transverse piezoelectric coefficient of PMN-PT samples, however, the accuracy of the numbers depends upon the value assumed for the elastic compliance. A second method was necessary which provided an independent and direct measure of the piezoelectric strain. Since the magnitudes of the strains are generally less than 1 %, few methods are appropriate for measurement when sample thicknesses are limited to ~ 1µm. One such direct measure is x-ray diffraction. X-ray diffraction presents an effective method for such an investigation in single crystals, as it involves a relatively simple relationship, and an assumptionless analysis. In general, if an x-ray beam could be confined to an electroded surface, the out-of-plane d-spacing could be easily measured as a function of

the applied electric field.

Due to the small electrode sizes of the PMN-PT heterostructure top electrodes (typically 0.3 or 0.5 mm in diameter), a particularly intense x-ray source is required, as well as the ability to use an appropriately small x-ray aperture. Sealed tube x-ray sources are typically limited to operating powers of 2 kW, however, rotating anode units may reach powers as great as 20 kW. A 4-circle rotating anode instrument was available at the Oak Ridge National Laboratory High Temperature Materials Laboratory Users Facility and was used for this measurement. The rotating anode instrument could be operated at powers in excess of 18 kW, with a 100 μm diameter collimator. In addition, a system existed enabling specific spots on the sample to be probed.

Samples processed at temperatures above 670 °C with the best electrical characteristics were used for the x-ray experiment. The diameter of the top electrodes was 500 μm. The samples were bonded to 16-pin chip-carriers, with connections between the film and chip-carrier electrodes made by aluminum wire bonding. A zip-dip socket was epoxied to the x-ray goniometer which allowed easy mounting and swapping of chip carrier packages, as well as robust electrical connection to an exterior power supply. The goniometer allowed x, y, and z translation as well as rotation in the φ-circle. Unfortunately, the capability to align the sample surface eucentrically was not available. This limitation was accomodated by a series of angular calibrations to the x-ray circles. During x-ray scans, a field was applied to the samples from a standard 50 V d.c. power supply.

The samples were positioned in the desired location using the following procedure: first, a phosphor plate with a 300 μm pitch grid was positioned on the sample

holder adjusted to the appropriate height. With the 100 μm collimator in place, the beam

was turned on. thus its position on the grid was visible from outside of the x-ray

enclosure. With a cathatometer positioned outside of the diffractometer enclosure

window, the location of the beam on the grid was determined. With the beam off. a

telescopic sight could be attached to the goniometer stage. With respect to the reticule of

the telescopic sight. the position of the grid point corresponding to the pre-determined

beam location was found. The phosphor plate was removed, and a thin film sample was

mounted. The height of the sample surface was brought into position using a micrometer

gage. The telescopic sight was placed back onto the goniometer. and with the x-y

translation controls. the desired electrode could be brought into the beam position as

defined by the optics reticule. Fig. 7.8 gives a schematic of the experimental setup.

Chip carrier fixed to PTS goniometer
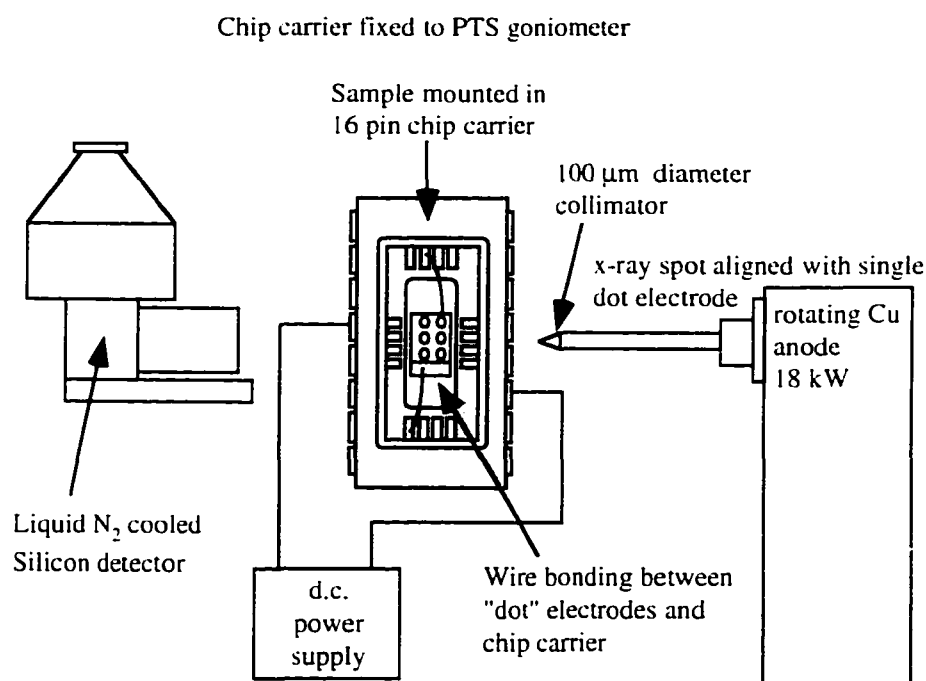
FIG. 7.8: EXPERIMENTAL SETUP OF IN-SITU FIELD-DEPENDENT X-RAY ANALYSIS

To measure the out-of-plane lattice strain with applied electric field, the 003 reflection was used. This reflection was chosen since it occurred at a high enough 2θ angle to provide sufficiently large peak shifts, while it was intense enough to provide smooth peaks at reasonable counting times. Smooth peaks were desired for the peak fitting software which was used to determine the peak position. Using the peak fitting software, the d-spacing could be calculated to three decimal places provided the appropriately good fit (the goodness of fit was determined by an error estimation routine included in the software package).

To determine the piezoelectric lattice strain under applied electric fields, a $2°$ 2θ scan was performed around the 003 reflection. Angular steps of $0.02°$ and a scan time of 10 minutes were used; these scanning parameters provided for reliable peak fits. Scans were performed at 0.5 volt increments up to 5 volts, then larger increments to 30 volts. Fig. 7.9 shows the longitudinal lattice strain as a function of applied field. The voltage was directed opposite to the preferred polarization direction.
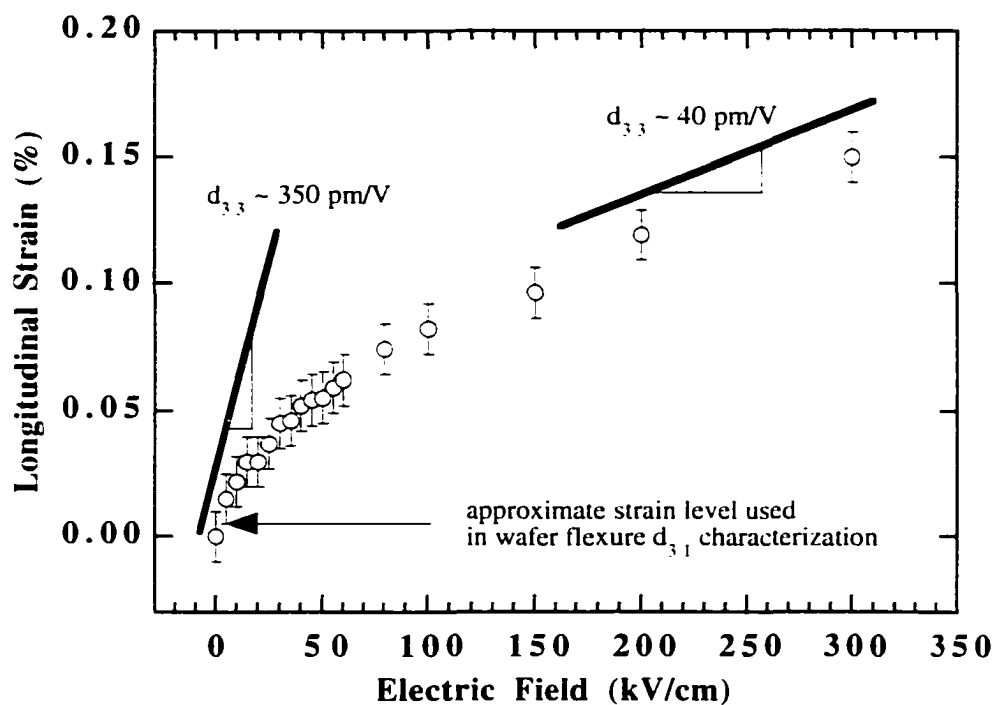
FIG. 7.9: FIELD DEPENDENCE OF THE PIEZOELECTRIC STRAIN OF AN EPITAXIAL PMN-PT FILM. THE ELECTRIC FIELD WAS APPLIED ANTIPARALLEL TO THE INTERNAL BIAS.

From the strain-field plot in Fig. 7.9, a low-field d_{33} coefficient of approximately 350 pC/N can be calculated from the initial slope. At higher fields, the coefficient becomes smaller (~40 pC/N), presumably following the polarization saturation. In single crystal samples, a saturation of strain has been observed at high fields, and was explained to result from the phase transition to the tetragonal phase.[4] Curves of this type were duplicated on several samples. Slope changes similar to those observed in single crystals indicating a crystallographic phase transition were not observed.

Larger fields were not measured due to breakdown of the samples. After reaching 300 kV/cm, the samples had been exposed to high fields for several hours, thus electrical breakdown was not unexpected. A limitation of this technique was the amount of time

that the samples needed to be held under field for reliable data to be collected. This is in contrast to interferometric techniques where strain data can be collected at fields in excess of 1 MV/cm at a.c. frequencies ~ 60 Hz (i.e.. the exposure time to high fields is limited to << 1 second).

The maximum unipolar strain values recorded for PMN-PT samples (at similar field values, ~ 300 kV/cm) are similar to the reports of other researchers on PZT compositions. An important difference however, between the strain behavior of this material and other ferroelecric films is the magnitude of piezoelectric response under low field drive conditions. At fields under 20 kV/cm, the longitudinal piezoelectric coefficient is approximately 300 pm/V, as compared to literature values for polycystalline PZT thin films which range between 50 and 100 pm/V.[53,55,183] These experiments should be repeated for an applied field of the opposite polarity to determine whether appreciable ditfferences (especially at low fields) are observed.

In Fig. 7.9. the approximate strain level corresponding to that used during the wafer flexure analysis is indicated by an arrow. As mentioned, the $-d_{31}$ coefficient measured for this strain level was approximately 170 – 180 pC/N. This value is approximately 50% smaller than the calculated d_{33} coefficient. and indicates a reasonable self-consistency and validation of both measurements. If the d_{31} coefficients are measured under large applied bias fields, the values decrease to approximately –50 pC/N at ~ 300 kV/cm.

To further examine the x-ray strain data, the piezoelectric strain was plotted against the square of the electrical polarization. If the measurements are self-consistent.

the resulting curve should be described by a linear relationship. Fig. 7.10 shows this result.
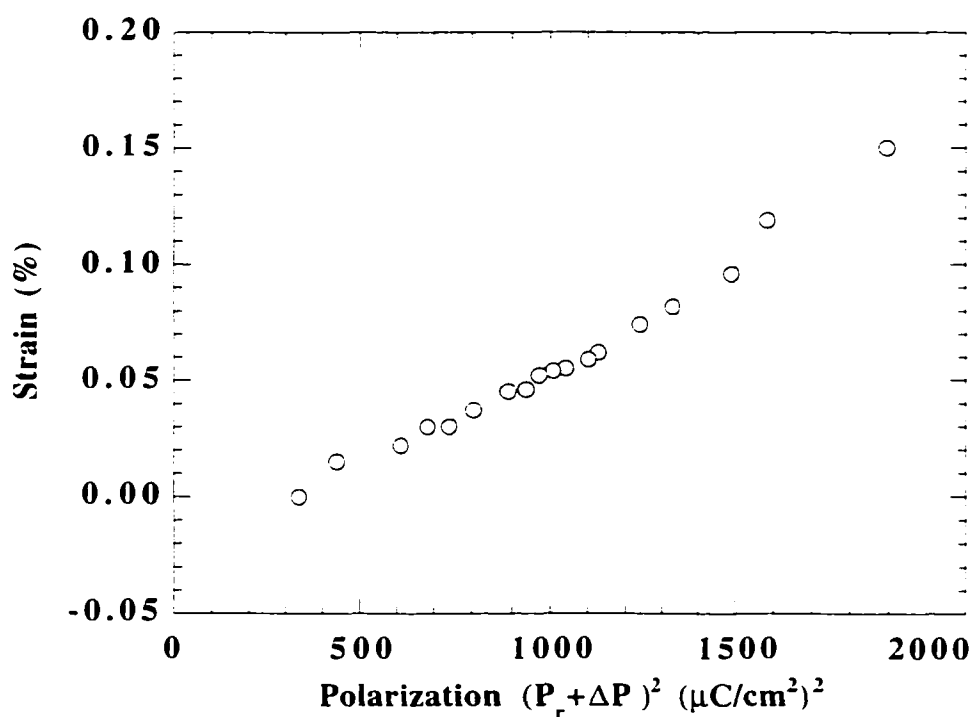
FIG. 7.10: ELECTRIC POLARIZATION VS. FIELD-INDUCED STRAIN FOR PMN(2%BA)-PT EPITAXIAL THIN FILM

The relationship between strain and the square of the polarization appears to be linear in this plot which indicates consistency between the x-ray data and the polarization hysteresis data. Unfortunately, this data shows no clear evidence that the phase transition between rhombohedral/pseudo-monoclinic and tetragonal symmetries is present. There is some indication that an anomaly exists at the highest field values, further experimentation is required for further interpretation. Fig. 7.11 gives the same data for a PZN – 4.5% PT bulk single crystal. The presence of a field-induced transition is clear in Fig. 7.11, as denoted by the shaded region. The deviation from linearity corresponds to the onset of

the phase transition, while the recovery of linearity corresponds to behavior of the new

tetragonal phase. The non-linear portion in between resulted from hysteresis associated

with the phase transition. The strain data for this measurement was collected using an

LVDT instrument.
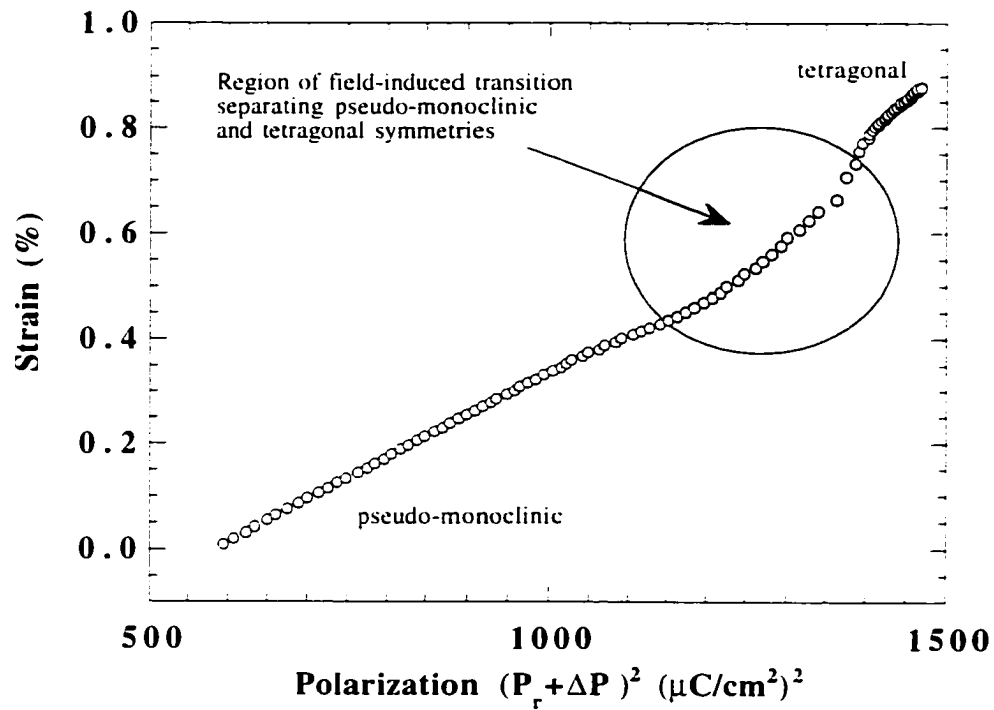
FIG. 7.11: ELECTRIC POLARIZATION VS. FIELD-INDUCED STRAIN FOR PZN – 4.5% PT SINGLE CRYSTAL

7.3.2 Single crystal analysis

In addition to the *in situ* x-ray analysis performed on PMN-PT thin films, similar experiments were performed on a (001)-oriented $Pb(Zn_{1/3}Nb_{2/3})O_3 - 4\%$ $PbTiO_3$ single crystal. The x-ray investigation was performed in order to satisfy two experimental goals: to verify the ultra-large strain and piezoelectric coefficient values on a microscopic scale, and to determine the crystallographic characteristics which accompany the anomalous piezoelectric strains. Specifically, x-ray analysis of these crystals under large electric fields is expected to verify the occurrence of a structural transition from rhombohedral to tetragonal symmetries.

A Picker 4-circle diffractometer was used for this investigation. To accommodate large electric fields, the experimental setup shown in Fig. 7.12 was used.
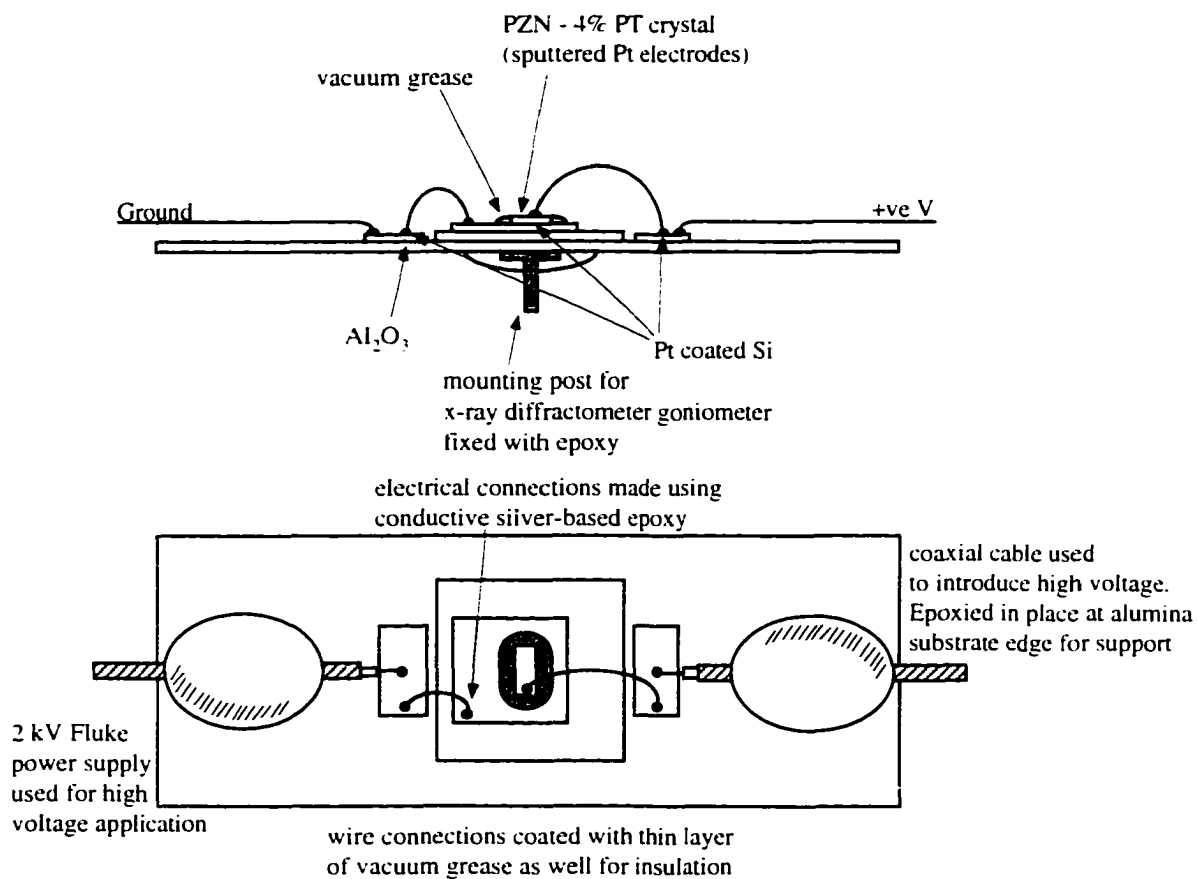
FIG. 7.12: SAMPLE HOLDER FOR BULK SINGLE CRYSTAL FIELD DEPENDENT X-RAY ANALYSIS

To allow the application of large electric fields, the single crystal as well as the

electrical leads were covered with a fluorinated vacuum grease (Krytox model #

6PL206). This system allowed electric fields as large as 30 kV/cm to be applied without

surface breakdown even when fields were maintained for times in excess of 10 minutes.

The contact to the top electrode was made using conductive silver epoxy, and was

confined to an area < 1 mm² which was well outside of the region where the diffraction

data was collected. The bottom electrode was simply a pressure contact to the Pt-coated

silicon surface. The relatively large viscosity of the grease held the crystal in position. It

was important that neither contact constrained the crystal, as this would make comparison with other data, as well as reliable interpretation more difficult.

The 004 reflection was used for measurement of interplanar spacings. This reflection was selected because it provided the largest angular shift with lattice strain. Scanning was performed using 0.02° angular increments and one second count times. These conditions provided for smooth peaks and reproducible results. For each crystal, the standard alignment procedure discussed in the experimental section was followed. In addition, for each field application, the crystal was realigned in both 2θ and ω. It was important to follow this procedure to maintain the optimal diffraction conditions. This was necessary since information concerning relative peak intensities and peak breadths could be collected in addition to the d-spacing data. Fig. 7.13 shows the field dependence of the lattice strain, while Fig. 7.14 shows the field dependence of the macroscopic strain meaured using an LVDT probe.

In Fig. 7.13 the x-ray diffraction data confirms the result measured using LVDTs for crystals of similar composition (shown in Fig. 7.14). In addition to strains as large as 0.8%, a clear strain hysteresis is observed (by x-ray diffraction) for the crystal corresponding to the proposed crystallographic phase transition from rhombohedral/pseudo-monoclinic to tetragonal symmetry. The hysteresis is shown at a field level which is smaller than observed during LVDT strain measurements.
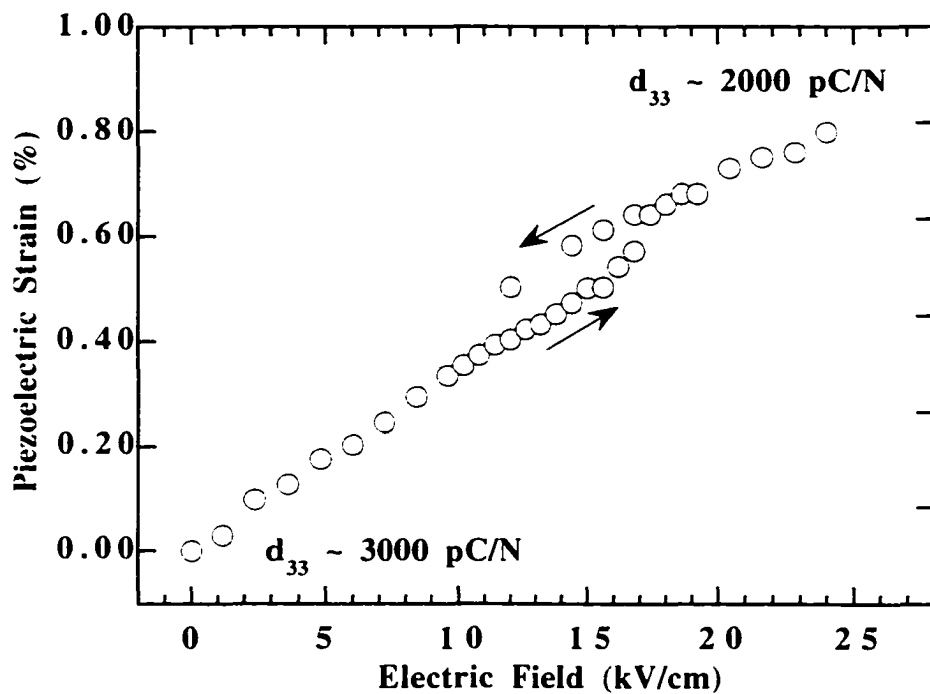
FIG. 7.13: FIELD-INDUCED STRAIN FOR A PZN-4%PT SINGLE CRYSTAL MEASURED USING 4-CIRCLE X-RAY DIFFRACTION
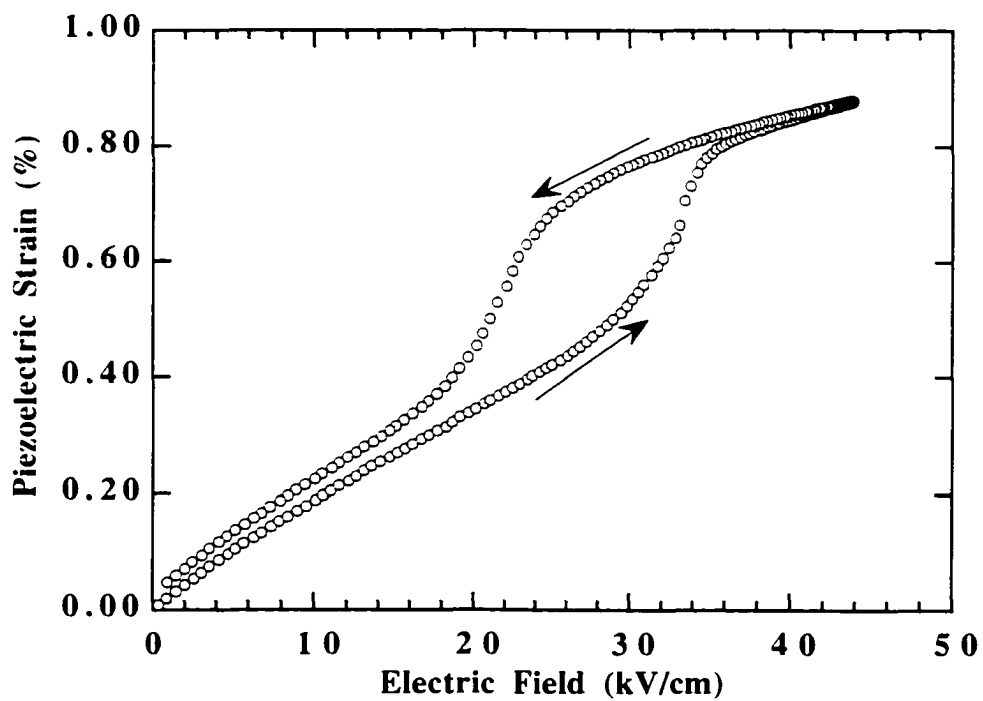
FIG. 7.14: FIELD-INDUCED STRAIN FOR A PZN-4%PT SINGLE CRYSTAL MEASURED USING AN LVDT PROBE

This may be due to the surface sensitivity of x-ray analysis. Most likely, the x-rays are limited to the top 10 to 20 μm of the sample, where the field distribution may not be representative of the entire slab. In addition, thickness effects in bulk PZN-PT crystals have been demonstrated, and are believed to be a result of regions in the crystal undergoing the tetragonal transition at different field values.[47] Both of these factors could account for the disparity in the transition field levels.

The value in the x-ray strain analysis is the ability to observed lattice strain on a microscopic level, and more importantly, to observe potential changes in the crystallinity or phase as a function of applied electric field. Attempts were made at characterizing the symmetry of the crystal at large electric field values via detection of peak splitting, however, the diffractometer rrsolution, coupled with the relatively broad peak widths in 2θ did not allow such information to be gathered. In the absence of this capability, the peak shape in 2θ was profiled as a function of electric field. Fig 7.14 shows θ-2θ scans of the 004 reflection with increasing applied electric fields.
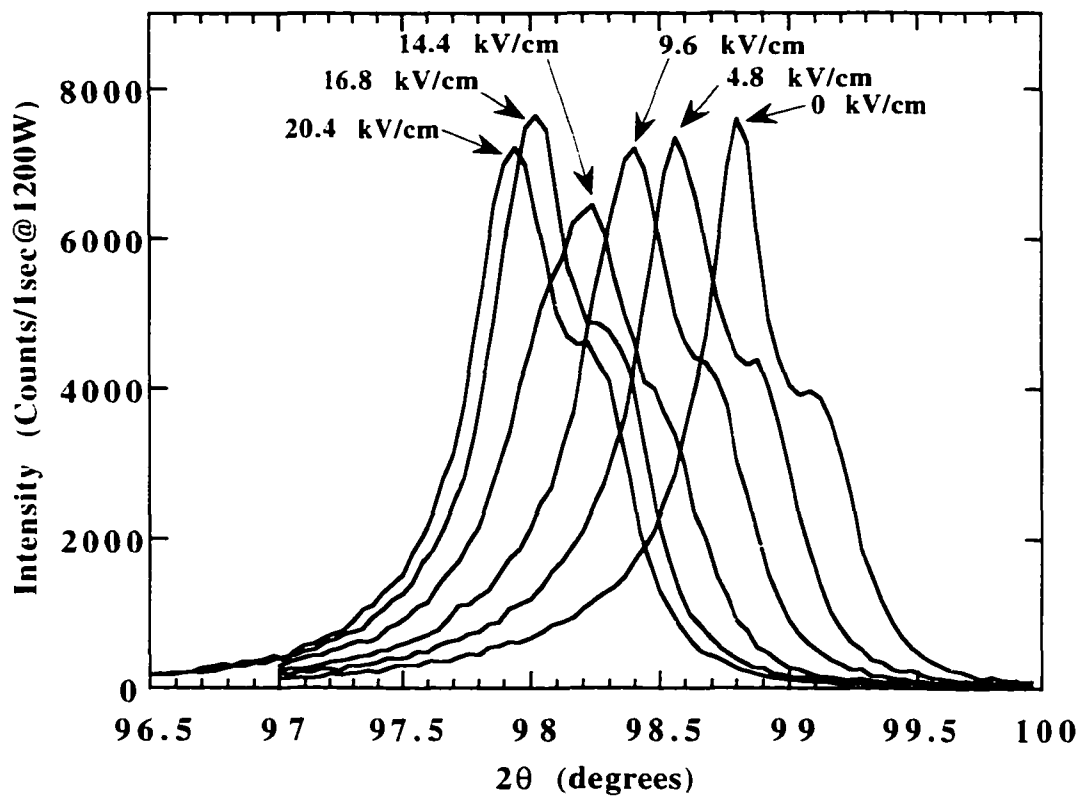
FIG. 7.14: θ-2θ PATTERNS OF THE 004 REFLECTION FOR A PZN-4%PT SINGLE CRYSTAL AS A FUNCTION OF APPLIED ELECTRIC FIELD ALONG [001]

As can be seen in Fig. 7.14. in addition to the angular shift in the 004 reflection. the maximum peak intensity as well as the peak breadth depend upon the applied field. From examination of the peak intensity it can be observed that a minimum occurs at a field value of approximately 14.4 kV/cm. This corresponds to the same level at which the hysteresis is observed in the strain-field response shown in Fig. 7.13. Moreover, the peak breadth was plotted against applied field; this result is shown in Fig. 7.15.
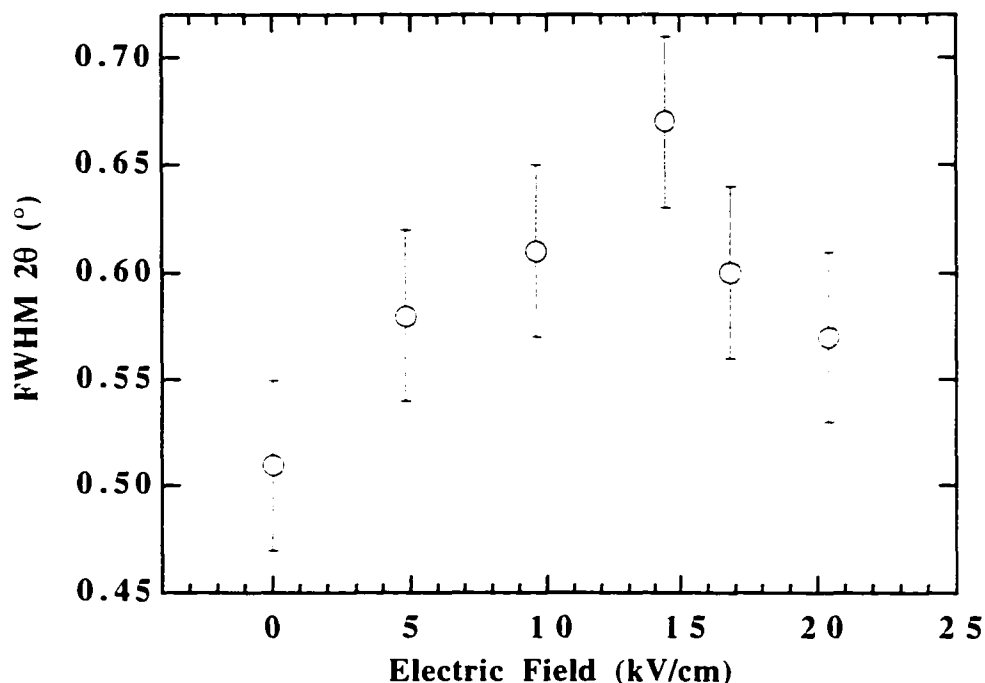
FIG. 7.15: ELECTRIC FIELD DEPENDENCE OF THE θ -2θ PEAK BREADTH FOR A PMN-4%PT SINGLE CRYSTAL MEASURED ALONG THE [001] DIRECTION

Again, in Fig. 7.15. a strong dependence of the θ-2θ full-width-half-maximum is observed as a function of applied electric field, with a maximum value occurring at the field value corresponding to the proposed phase transition to tetragonal symmetry.

From this x-ray data, three observations can be made: a discontinuous jump in field induced strain, a minimum in the x-ray peak intensity, and a maximum in the θ-2θ peak breadth all occur at the same applied electric field value, approximately 14.4 kV/cm. The trends in peak intensity and breadth indicate that the distribution of d-spacings in the crystal is broadening as some critical field level is approached, and when this field value is surpassed, the reverse process occurs.

This data can be physically interpreted as a transition to a new symmetry (and hence interplanar spacing) which occurs over a finite field range. Beginning with low

field values. a transition to pseudo-monoclinic symmetry occurs. This symmetry is assumed as a result of elongation along [001], and contraction along [100] (both observations have been made by LVDT strain measurements). With this type of strain applied to a (001)-oriented rhombohedral crystal, the 3-fold axis along <111> would be immediately lost. thus the only symmetry element remaining would be a mirror plane coincident with the (110) crystallographic plane. In the absence of an immediate transition to tetragonal symmetry, this pseudo-monoclinic structure must occur. As larger fields are applied, it is proposed that tetragonal material will begin to nucleate. The nucleation of this new symmetry will then provide for a crystal comprising an additional phase with a new interplanar spacing. This mixture of multiple phases results in the x-ray reflections with reduced maximum intensities and broadened widths. With even larger applied fields, the majority of the crystal will have switched to the tetragonal phase, and a reduction in the distribution of interplanar spacings would follow. This is consistent with the observation of a reduced peak breadth and increased maximum intensity above the electric field value at which the discontinuous jump in strain was recorded.

7.4 Summary

Both the longitudinal and transverse piezoelectric coefficients were measured for PMN(2%Ba)-PT (70/30) epitaxial thin films. Low field values for the coefficients were determined to be 350 pm/V and -170 pm/V respectively. The low-field piezoelectric response is approximately 2 to 4 times stronger than the reliable reports for both polycrystalline and oriented PZT films of similar thickness.[2,54,57,81,83,171] The results of

the techniques are within reasonable agreement, as a general relationship between the magnitude of d_{33} and d_{31} of ~ 2:1 is observed. Longitudinal strains as large as 0.15% were observed at a d.c. field of 300 kV/cm. Larger fields could not be used due to breakdown of the samples. These strains were similar in magnitude to those measured for polycrystalline PZT thin films, but much smaller than those measured for bulk relaxor-PT single crystals.[4] Unfortunately, no clear evidence for the existence of the field-induced phase transition was observed in epitaxial samples of PMN-PT deposited on $LaAlO_3$ substrates. Some of this reduction is probably associated with clamping associated with both the residual stress state and the massive substrate. In addition, the inferior crystallinity of thin films, as compared to bulk single crystals, is partially responsible. If so, films deposited on better lattice-matched substrates may exhibit more pronounced phenomena. Even in the absence of the field-induced phase transition, the low-field piezoelectric coefficients are larger than those of well-prepared and reliably measured PZTs by a factor of two to four.

From d_{31} measurements, the polarization state of the PZT thin films was found to be orientationally biased. For films deposited at temperatures in excess of 670 °C, a preferred polarization orientation existed which was similar to observations of previous investigators of ferroelectric films. For films deposited below 600 °C, the films were found to be biased to the degree that the direction of the remanent polarization could not be switched (i.e., both remanent polarization values carried the same sign). For these samples, poling in the direction of the internal bias resulted in very rapid saturation of d_{31}, and piezoelectric coefficients which had extremely low aging rates. Rapid aging was observed for samples poled against the as grown bias. To explain this behavior, two

models were proposed. The first involved implantation of energetic species into the lattice. The resulting strain would be anisotropic (preferential to the out-of-plane direction) and would exist as a gradient through the film thickness. This type of strain gradient has the potential to stabilize a preferential net polarization direction. The second model also relies on energetic bombardment. however. an analogy to results observed for bombarded TGS crystals was used. In this case further ionization was proposed to occur to species in the perovskite lattice as a result of collisions with impinging plasma particles. Interactions with these excited atoms and the surrounding lattice result in polarization stabilizing defects which are preferentially oriented by the electric field associated with the laser-induced plasma.

An in-situ field-dependent x-ray analysis was performed on a PZN – 4.5% PT single crystal in order to investigate crystallographic characteristics of the crystal under large applied fields. From these experiments. the ultra-large strains. as well as the hysteresis associated with the proposed field-induced phase transition were confirmed. In addition. by monitoring the peak intensities and breadths. further evidence was found to support the concept of a field-forced transition to tetragonal symmetry.

Chapter 8 Conclusions and Future Work

8.1 Conclusions

8.1.1 SrRuO₃

Epitaxial $SrRuO_3$ thin films were grown on $SrTiO_3$ and $LaAlO_3$ substrates as a function of ambient pressure during growth. Anisotropically extended lattice constants were observed in samples grown at deposition pressures below ~ 100 mTorr, and were determined to be a result of energetic bombardment during growth. The ambient pressure during growth was used to control the bombardment, while experiments involving mixed atmospheres with Ar were used to determine the influence of oxygen pressure. The mechanism behind the extended lattice constants is proposed to be implantation of energetic plasma species.

The surface morphology of films showing bulk and extended lattice constants was investigated by scanning tunneling microscopy. In general, the surface topography revealed an edge-defined growth mechanism, evidenced by the conservation of crystalline terraces from the substrates surfaces. Films grown under stronger energetic bombardment showed a coarsened appearance with respect to those grown at higher pressures. These bombarded surfaces were characterized by larger step heights and longer terrace lengths.

The crystallographic texturing of the $SrRuO_3$ orthorhombic twins was characterized using 4-circle x-ray diffraction. For films deposited under conditions with less strong bombardment, the in-plane texture was found to be nearly twin-free. The presence of a stepped $SrTiO_3$ substrate (miscut by ~ 0.5° along the [100] direction) was required for preferred orthorhombic twinning. For films deposited under strongly bombarding conditions, the orthorhombic distortion was destroyed and the unit cell seemed to be best characterized as a tetragonal simple perovskite.

High temperature x-ray diffraction was performed on both thin film and powder samples. Discontinuities in the temperature dependence of the lattice constants indicated structural phase transitions occur at ~ 300 °C and between 600 °C and 700 °C. To confirm the existence of transitions, the $SrRuO_3$ powder was analyzed by high temperature x-ray diffraction between room temperature and 900 °C. Structural phase transitions between what are believed to be orthorhombic / tetragonal and tetragonal / cubic symmetries were confirmed. This x-ray data suggests that $SrRuO_3$ grows in or near to the cubic phase, thus may develop a twin-structure during cooldown. With this information it is difficult to see how the growth mechanism of $SrRuO_3$ is responsible for the orthorhombic twinning, as has been suggested previously. Rather, it is proposed that preferred twinning results from an epitaxial interfacial strain, which is anisotropic due to the presence of substrate steps. This implies that the twinning in $SrRuO_3$ is accompanied by a ferroelastic component.

8.1.2 Growth of PMN-PT epitaxial thin films

Three important conclusions can be drawn from the investigation of the structural and phase development of PMN/PT (70/30) thin films: (i) It is possible to simultaneously observe Pb-deficient. Pb-rich, and stoichiometric perovskite phases in a single sample deposited from a PbO-enriched target using typical PLD processing conditions. This unfortunately precludes the use of a straightforward adsorption-controlled growth process for PMN-PT deposited on $LaAlO_3$ substrates (such a procedure proved effective in the $(Pb,La)(Mn,Ti)O_3$ system). (ii) Phase pure epitaxial PMN-PT films can be grown under high pressure and high temperature process conditions: specifically, temperatures in excess of 700 °C and pressures in excess of 700 mTorr. Film growth under these conditions will, however, result in very poor thickness uniformity and a relatively small coverage area. (iii) Deposition at temperatures below 600 °C can be used to deposit phase-pure (to x-ray diffraction) epitaxial films. Under these conditions, however, energetic bombardment appears to be crucial in achieving the desired crystallinity. In addition, an extension in the lattice constants similar to that seen in $SrRuO_3$ occurred. Under these conditions the single crystal substrate appears to be crucial in nucleating and maintaining the desired perovskite phases.

8.1.3 PMN-PT electrical property analysis

It was found that the conditions which provided the best crystalline structures were not always coincident with those conditions providing the optimal electrical properties. With the exception of the samples deposited at temperatures below 600 °C, all samples with high resistivities incorporated second phases. The electrical properties

of phase-pure samples (i.e., those deposited at ~ 700 °C and 700 mTorr) were dominated

by conduction loss. Though these samples can be deposited without pyrochlore or excess

lead, it is believed that they are slightly Pb-deficient, thus containing a large

concentration of point defects which result in poorly insulating material.

Excellent electrical properties (i.e., approaching the values for single crystals in

some cases) were observed for samples containing small amounts of second phases, both

Pb-rich and Pb-deficient. In effect, the second phase nucleation eliminates the non-

stoichiometric, but structurally stabilized perovskite phase. It is proposed that through

nucleation or precipitation of small amounts of second phases during deposition, the

composition of the remaining volume becomes closer to the desired stoichiometry. An

analogy to this process was drawn to zone refining of single crystals.

Samples could be deposited under conditions which resulted in ferroelectric

transitions which were temperature shifted by as much as -100 °C. The cause of this

temperature shift was determined to be reduced crystalline perfection. In addition to the

temperature shift, the electrical behavior became more similar to that of a relaxor, i.e.,

pure PMN, at room temperature. An increased dispersion and diffuseness of transition

was coincident with the transition temperature shift. It is suggested that the reduced

crystalline perfection interrupted the long-range ordering, and was responsible for the

relaxor-like behavior. The high temperature deposited samples also showed some

evidence of relaxor behavior, and it is felt that further improvements in the crystallinity

could reduce this behavior even further.

Samples were also deposited at temperatures below 600 °C from targets which

contained ~ 3 % excess PbO. Under these conditions, phase-pure material with excellent

electrical properties could be grown. The lower deposition temperatures appear to stabilize the perovskite phase against rapid Pb-volatilization, while the epitaxial template favors nucleation of the well lattice-matched perovskite phase. Energetic bombardment during growth was essential at these temperatures for achieving crystallinity and electrical properties similar to those of samples deposited in excess of 670 °C.

8.1.4 Piezoelectric property analysis

Both the longitudinal and transverse piezoelectric coefficients were measured for PMN(2%Ba)-PT (70/30) epitaxial thin films. Low field values for the coefficients were determined to be 350 pm/V and -170 pm/V respectively. This low-field piezoelectric response is approximately 2 to 4 times stronger than the reliable reports for both polycrystalline and oriented PZT films of similar thicknesses.[2,54,57,81,83,171] The results of the techniques are within reasonable agreement, as a general relationship between $|d_{33}|$ and $|d_{31}|$ of ~ 2:1 is observed. Longitudinal strains as large as 0.15% were observed at a dc field of 300 kV/cm. Larger fields could not be used due to breakdown of the samples during the static measurement. These strains were similar in magnitude to those measured for polycrystalline PZT thin films, but much smaller than those measured for bulk relaxor-PT single crystals.[4]

Unfortunately, no clear evidence for the existence of the field-induced phase transition was observed in epitaxial samples of PMN-PT deposited on $LaAlO_3$ subatrates. Possibly, a combination of clamping of the response by the substrate and the inferior crystallinity of thin films, as compared to bulk single crystals, is responsible. If the latter effect is important, films deposited on better lattice-matched substrates may exhibit

behavior more similar to that of bulk single crystals (support for this argument has been demonstrated for bulk single crystals, where samples having inferior crystal quality show reduced piezoelectric activity)[47]. Even in the absence of the field-induced phase transition, these films appear to represent an improvement in the existing piezoelectric thin film technology.

From d_{31} measurements, the polarization state of the PZT thin films was found to be orientationally biased. For films deposited at temperatures in excess of 670 °C, a preferred polarization orientation existed which was similar to observations of previous investigators of ferroelectric films. For films deposited below 600 °C, the films were found to biased to the degree that the direction of the remanent polarization could not be switched (i.e., both remanent polarization values carried the same sign) in the absence of an applied electric field. For these samples, poling in the direction of the internal bias resulted in rapid saturation of d_{31}, and piezoelectric coefficients which had very low aging rates. Rapid aging was observed for samples poled against the as-grown bias. To explain this behavior, two models were proposed. The first involved implantation of energetic species into the lattice. The resulting strain would be anisotropic (preferential to the out-of-plane direction) and would exist as a gradient through the film thickness. This type of strain gradient has the potential to stabilize a preferential net polarization direction. The second model also relies on energetic bombardment, however, an analogy to results observed for bombarded TGS crystals was used. In this case, further ionization was proposed to occur to species in the perovskite lattice as a result of collisions with impinging plasma particles. Interactions with these excited atoms and the surrounding lattice result in polarization stabilizing defects which may be preferentially oriented by

either the directionality of the impinging species, or the electric field associated with laser-induced plasmas.

An in-situ field-dependent x-ray analysis was performed on a PZN – 4.5% PT single crystal in order to investigate crystallographic characteristics of the crystal under large applied fields. From these experiments, the ultra-large strains, as well as the hysteresis associated with the proposed field-induced phase transition were confirmed. In addition, by monitoring the peak intensities and breadths, further evidence was found to support the concept of a field-forced transition to tetragonal symmetry.

8.2   Future work

The future work in this topic will consist of four thrusts: attempts to grow samples with greater structural perfection, elucidation of the mechanism responsible for preferred polarization directions in PVD-deposited perovskites, deposition of epitaxial material using silicon substrates, and investigation of other relaxor-PT compositions.

It is important to grow samples of improved crystallinity to determine what limitations, if any, exist concerning high strain generation in thin films. In particular, it is desired to determine if comparable limitations on the piezoelectric properties of thin film PZTs exist for relaxor-PT compositions. Growth of samples with improved crystallinity may be accomplished by choosing a more well lattice-matched substrate/bottom electrode combination. One possible selection would be $KTaO_3$ substrates and $BaRuO_3$ bottom electrodes. Determination of the factors which influence the piezoelectric response most strongly may, in turn, give insight to the mechanisms behind ultra-large strain generation in relaxor-PT crystals.

Additional experiments will be attempted to elucidate the mechanisms behind the asymmetric polarization and piezoelectric properties in PVD-grown perovskite thin films. Possible experiments include deposition on epitaxial substrates which provide a different interfacial stress, and depositions under applied electric fields which may allow the sign of the internal bias to be switched. This work is regarded as important in terms of scientific goals, since careful examination of literature data reveals that nearly all PVD-grown ferroelectric perovskite thin films display similar characteristics.

Growth of high quality epitaxial $(Ba,Sr)TiO_3$ and $BaTiO_3$ has been demonstrated using TiN coated (001)-Si substrates. This same strategy will be attempted with PMN-PT thin films in order to demonstrate the applicability of these materials with Si-technology. The additional difficulty regarding integration of relaxor-PTs for microactuator applications is the requirement of a (001)-oriented thin film. Regardless of the available material properties, if relaxor-PT compositions cannot be integrated with Si substrates, application on a commercial scale seems unlikely.

It has been suggested that for ultra-high strain generation, what is essential is the (001) measurement direction applied to a rhombohedral crystal, i.e., the specific composition may be unimportant. This being the case, it may be advantageous to choose a relaxor-PT solid solution which has an increased resistance to pyrochlore formation. One such system would be the $Pb(Sc_{1/2}Ta_{1/2})O_3-PbTiO_3$ solid solution. This system is known to be more stable, thus a wider processing window may be expected for high-quality thin film growth.[30] If this effort proves successful, further investigations of these effects may be directed into non-lead containing rhombohedral compositions, i.e.. Zr-doped $BaTiO_3$ and $KNbO_3$. In such cases, the importance of the relaxor end-member in

the solid solution and the presence of a morphotropic phase-boundary may be determined. Thin film deposition may allow compositions to be investigated which would otherwise be very difficult to synthesize as bulk single crystals.

Finally, additional work will be performed to investigate the high-field crystallography of relaxor-PT crystals measured along [001]. In particular, the field dependence of the interplanar spacings perpendicular to the applied electric field will be determined. With this information, the unit cell volume, and its field dependence can be measured. This data will further the fundamental understanding of field-forced phase transitions, allowing the order of the transition, and possibly the high-field symmetry to be determined.

Bibliography

1   D. L. Polla. "Microelectromechanical systems based on ferroelectric thin films." Micro. Eng. **29,** 51-58 (1995).

2   S. Trolier-McKinstry, J. F. S. Jr., T. Su, G. Zavala, and J. Fendler, "Piezoelectricity in ferroelectric thin films: Domain and stress issues." Ferroelectrics **206-207,** 381-392 (1997).

3   B. A. Tuttle. T. J. Garino, J. A. Voigt, T. J. Headley, D. Dimos, and M. O. Eatough. *Relationships between ferroelectric 90° domain formation and electrical properties of chemically prepared Pb(Zr,Ti)O3 thin films* (Kluwer Academic Publishers. Netherlands, 1995).

4   S. E. Park and T. R. Shrout. "Ultrahigh strain and piezoelectric behavior in relaxor-based ferroelectric single crystals," J. Appl. Phys. **82 (4)** (1997).

5   A. Halliyal, U. Kumar, R. E. Newnham, and L. E. Cross, "Stabilization of the perovskite phase and dielectric properties of ceramics in the $Pb(Zn_{1/3}Nb_{2/3})O_3$-$BaTiO_3$ system," Am. Ceram. Soc. Bull. **66 (4),** 641-676 (1987).

6   S. L. Swartz and T. R. Shrout, "Fabrication of perovskite lead magnesium niobate." Mat. Res. Bull. **17,** 1245-1250 (1982).

7   F. Jona and G. Shirane. *Ferroelectric Crystals* (Dover Publications Inc., Mineola. NY. 1962).

8   H. D. Megaw. *Ferroelectricity in Crystals* (Methuen & Co.. London. 1957).

9   B. Jaffe. W. R. Cook. and H. Jaffe. *Piezoelectric Ceramics* (R. A. N. Publishers. Marietta. OH. 1971).

10   J. F. Nye. *Physical Properties of Crystals* (Oxford University Press. New York. NY. 1957,1985).

11   M. J. Haun. Ph.D. Thesis. The Pennsylvania State University. 1988.

12   Z. Q. Zhang, H. J. Haun. S. J. Jang. and L. E. Cross. "Low temperature dielectric. piezoelectric and elastic properties of pure (undoped) PZT ceramics." Proc. IEEE, 394-397 (1986).

13   X. L. Zhang. Z. X. Chen. L. E. Cross. and W. A. Schulze. "Dielectric and piezoelectric properties of modified lead titanate zirconate ceramics from 4.2 to 300 K." J. Mat. Sci. **18**, 968-972 (1983).

14   D. Damjanovic. M. Demartin. F. Chu. and N. Setter. "Practical consequences of the extrinsic contributions to the properties of piezoelectric sensors and actators." Proc. IEEE Ultrasonics Symposium, 251-257 (1996).

15   W. R. Buessem. L. E. Cross. and A. K. Goswami. "Effect of two-dimensional pressure on the permittivity of fine- and coarse-grained barium titanate." J. Amer. Ceram. Soc. **49** (1), 36-39 (1966).

16   G. A. Samara, "Presssure and temperature dependences of the dielectric properties of the perovskites $BaTiO_3$ and $SrTiO_3$," Phys. Rev. **131** (**2**), 378-386 (1966).

17   W. D. Nix, "Mechanical properties of thin films." Mett. Trans. A **20A**, 1989-2217 (1988).

18   G. A. Smolenskii, A. I. Agranovskaya, and S. N. Popov, "On the mechanism of polarization in solid solutions of $Pb_3NiNb_2O_9$-$Pb_3MgNb_2O_6$." Sov. Phys. Sol. State **1** (1958).

19   G. A. Smolenskii and A. I. Agranovskaya, "Dielectric polarization of a number of complex compounds." Sov. Phys. Solid State **1** (**10**), 1429-1437 (1959).

20   G. A. Smolenskii, A. I. Agranovskaya, V. A. Isupov, and S. N. Popov, "Ferroelectrics with diffuse phase transitions," Sov. Phys. Solid State **2** (**11**), 2584-2594 (1961).

21   L. E. Cross, "Relaxor Ferroelectrics," Ferroelectrics **76**, 241-267 (1987).

22   N. Kim, M.S. Thesis, The Pennsylvania State Univerity, 1990.

23   D. Viehland and J. Li, "Dependence of the glasslike characteristics of relaxor ferroelectrics on chemical ordering," J. App. Phys. **75** (**3**), 1705-1709 (1994).

24   D. Viehland, S. Jang, and L. E. Cross, "The dielectric relaxation of lead magnesium niobate relaxor ferroelectrics," Phil. Mag. B **64** (**3**), 335-344 (1991).

25   A. K. Tagantsev. "Vogel-Fulcher relatioship for the dielectric permittivity of relaxor ferroelectrics." Phys. Rev. Lett. **72 (7)**, 1100-1103 (1991).

26   L. E. Cross. "Relaxor Ferroelectrics: An Overview," Ferroelectrics **151**, 305-320 (1993).

27   D. Viehland. S. J. Jang, and L. E. Cross. "Local polar configurations in lead magnesium niobate relaxors," J. Appl. Phys. **69 (1)**, 414-419 (1991).

28   C. A. Randall and A. S. Bhalla, "Nanostructural-property relatioships in complex lead perovskites," Jpn. J. Appl. Phys. **29 (2)**, 327-333 (1990).

29   N. Setter and L. E. Cross. "The role of cation disorder in diffuse phase transition behavior of perovskite ferroelectrics," J. Appl. Phys. **51 (8)**, 4356-4360 (1980).

30   N. Setter and L. E. Cross. "The contribution of structural disorder to diffuse phase transitions in ferroelectrics." J. Mat. Sci. **15**, 2478-2482 (1980).

31   C. G. F. Stenger, F. L. Scholten, and A. J. Burggraaf, "Ordering and diffuse phase transitions in $Pb(Sc_{1/2}Ta_{1/2})O_3$ ceramics." Solid State Comm. **32**, 989-992 (1979).

32   C. A. Randall, A. S. Bhalla, T. R. Shrout, and L. E. Cross. "Classification and consequences of complex lead perovskite ferroelectrics with regard to B-site cation order." J. Mat. Res. **5 (4)**, 829-834 (1989).

33   J. Chen. M. H. Chan. and M. Harmer, "Ordering structure and dielectric properties of undoped and La/Na doped $Pb(Mg_{1/3}Nb_{2/3})O_3$." J. Am. Ceram. Soc. **72 (4)**, 593-598 (1989).

34   M. A. Akbas and P. K. Davies. "Processing and Characterization of lead magnesium tantalate (PMT) ceramics." J. Mater. Res. **12 (10)**, 2617-2622 (1997).

35   M. Akbas and P. K. Davies. "Domain growth in $Pb(Mg_{1/3}Nb_{2/3})O_3$ perovskite relaxor ferroelectric oxides." J. Am. Ceram. Soc. **80 (11)** (1997).

36   T. R. Shrout and A. Halliyal. "Preparation of lead-based feroelectric relaxors for capacitors." Am. Ceram. Soc. Bull. **66 (4)**, 704-711 (1987).

37   J. R. Belsick. A. Halliyal. U. Kumar. and R. E. Newnham. "Phase relations and dielectric properties of ceramics in the system $Pb(Zn_{1/3}Nb_{2/3})O_3$-$SrTiO_3$-$PbTiO_3$." Am Ceram. Bull. **66 (4)**, 664-667 (1987).

38   S. J. Butcher and N. W. Thomas. "Ferroelectricity in the system $Pb_{1-x}Ba_x(Mg_{1/3}Nb_{2/3})O_3$." J. Phys. Chem. Soc. **52 (4)**, 595-601 (1991).

39   V. A. Bokov and I. E. Myl'niikova, "Electrical and optical properties of single crystals of ferroelectrics with a diffused phase transition." Sov. Phys. Solid State **3 (3)**, 613-623 (1961).

40   H. Ouchi, "Piezoelectric properties and phase relations of $Pb(Mg_{1/3}Nb_{2/3})O_3$-$PbTiO_3$-$PbZrO_3$ ceramics with barium or strontium substitutions." J. Amer. Ceram. Soc. **51 (3)**, 169-176 (1968).

41   S. Nomura. T. Takahashi. and Y. Yokomizo. "Ferroelectric properties in the system $Pb(Zn_{1/3}Nb_{2/3})O_3$-$PbTiO_3$." J. Phys. Soc. Japan **27**, 262 (1969).

42   C. M. Foster, G. Bai. R. Csencsits. J. Vetrone. R. Jammy, L. A. Wills. E. Carr. and J. Amano. "Single-crystal $Pb(Zr_xTi_{1-x})O_3$ thin films prepared by metal-organic chemical vapor deposition: Systematic compositional variation of electronic and optical properties." J. Appl. Phys. **81 (5)**, 2349-2357 (1997).

43   J. Kuwata. K. Uchino. and S. Nomura. "Phase transitions in the $Pb(Zn_{1/3}Nb_{2/3})O_3$-$PbTiO_3$ system." Ferroelectrics **37**, 579-582 (1981).

44   T. R. Shrout. Z. P. Chang, N. Kim, and S. Markgraf. "Dielectric behavior of single crystals near the $(1-x)Pb(Mg_{1/3}Nb_{2/3})O_3$-$(x)PbTiO_3$ morphotropic phase boundary." Ferroelectrics Letters **12**, 63-69 (1990).

45   S. Park and T. R. Shrout. "Characteristics of relaxor-based piezoelectric single crystals for ultrasonic transducers." IEEE Trans. Ultrason. Ferro. Freq. Cont. **44 (5)**, 124-132 (1997).

46   S.-E. Park and T. R. Shrout. "Relaxor based ferroelectric single crystals with high piezoelectric performance." The 8th US-Japan Seminar on Dielectric & Piezoelectric Ceramics, 235-241 (1997).

47   S. Park and T. R. Shrout. Unpublished material (1997).

48   D. Berlincourt. "Recent developements in ferroelectric transducer materials." IRE Trans. on Ultrasonic Eng. **UE-4**, 53-65 (1956).

49   W. P. Mason and H. Jaffe, "Methods for measureing piezoelectric, elastic, and dielectric coefficients of crystals and ceramics," Proc. IRE **42**, 921-930 (1954).

50   Q. M. Zhang, W. Y. Pan, and L. E. Cross, "Laser interferometer for the study of piezoelectric and electrostrictive strains," J. Appl. Phys. **63 (8)**, 2492-2496 (1988).

51   P. Moses, (1987).

52   S. Sherrit, H. D. Wiederick, B. K. Mukherjee, and M. Sayer, "Determination of the piezoelectric electromechanical coupling constant k_{33} using a frequency ratio," Ferroelectrics **193 (1-4)**, 88-94 (1997).

53   A. L. Kholkin, C. Wütchrich, D. V. Taylor, and N. Setter, "Interferometric measurements of electric field-induced displacements in piezoelectric thin films," Rev. Sci. Instrum. **67(5)**, 1935-1941 (1996).

54   S. Watanabe, T. Fujiu, and T. Fujii, "Effect of poling on piezoelectric properties of lead zirconium titanate thin films formed by sputtering," Appl. Phys. Lett. **66 (12)**, 1481-1483 (1995).

55   F. Xu, F. Chu, J. F. S. Jr., and S. Trolier-McKinstry, "The measurement of the longitudinal piezoelectric coefficient, d_{33}, in PZT thin films," Proc. Symp. Mater. Res. Soc., To be published (1998).

56   K. Lefki and G. J. M. Dormans, "Measurement of piezoelectric coefficients of ferroelectric thin films," J. Appl. Phys. **76 (3)**, 1764-1767 (1994).

57   Z. Surowiak, D. Czekaj, A. M. Margolin, E. V. Sviridov, V. A. Aleshin, and V. P. Dudkevich. "The structure and piezoelectric properties of thin $Pb(Zr_{0.53}Ti_{0.45}W_{0.01}Cd_{0.01})O_3$ films." Thin Solid Films **214**, 78-83 (1992).

58   M. Bao and W. Wang, "Future of microelectrocmechanical systems (MEMS)." Sensors and Actuators **A56**, 135-141 (1996).

59   R. T. Howe, B. E. Boser, and A. P. Pisano, "Polysilicon integrated microsystems: technologies and applications." Sensors and Actuators A **56**, 167-177 (1996).

60   R. A. Lawes, "Fabrication technology for microengineering," Sensor Review **16 (2)**, 16-22 (1996).

61   R. R. A. Syms, B. M. Hardcastle, and R. A. Lawes, "Bulk micromachined silicon comb-drive electrostatic actuators with diode isolation." Sensors and Actuators A **63**, 61-67 (1997).

62   R. Puers and Lapadatu, "Electrostatic forces and their effects on capacitive mechanical sensors." Sensors and Actuators A **56**, 203-210 (1996).

63   P. B. Chu, P. R. Nelson, M. L. Tachiki, and K. S. J. Pister, "Dynamics of polysilicon parallel-plate electrostatic actuators." Sensors and Actuators A **52**, 216-220 (1996).

64   L. Lau, K. Tanaka, and J. Lakin, "Growth of epitaxial ZnO thin films by organometallic chemical vapor deposition." J. Electrochem. Soc.: Solid State Sci. & Tech. **127 (8)**, 1843-1847 (1980).

65   J. L. Deschanvres, P. Rey, G. Delabouglise, M. Labeau, J. C. Joubert, and J. C. Peuzin, "Characterization of piezoelectric properties of zinc oxide on silicon for sensors applications," Sensors and Actuators A **33**, 43-45 (1992).

66   P. Muralt, A. Kholkin, M. Kholi, T. Maeder, K. G. Brooks, and R. Luthier, "Fabrication and characterization of PZT thin films for micromotors," Integrated Ferroelectrics **11**, 213-220 (1995).

67   D. L. Polla and P. J. Schiller, "Integrated ferroelectric microelectromechanical systems (MEMS)," Integrated Ferroelectrics **7**, 359-370 (1995).

68   S. L. Swartz and V. E. Wood, "Ferroelectric thin films," Cond. Matter. News **1** (**5**), 4-13 (1992).

69   M.-H. Kiang, O. Solgaard, R. S. Muller, and K. Y. Lau, "Micromachined polysilicon microscanners for barcode readers," IEEE Phot. Technol. Lett. **8** (**12**), 57-60 (1996).

70   J. J. Bernstein, S. L. Finberg, K. Houston, L. C. Niles, H. D. Chen, L. E. Cross, K. K. Li, and K. Udayakumar, "Micromachined high frequency ferroelectric sonar transducers," IEEE Trans. Ultrason. Ferro. Freq. Cont. **44** (**5**), 960-969 (1997).

71   W. P. Robbins, "Ferroelectric-based microactuators," Integrated Feroelectrics **11**, 179-190 (1995).

72   C. Lee, T. Itoh, and T. Suga, "Micromachined piezoelectric force sensors based on PZT thin films," Proc. IEEE Trans. Ultrason. Ferro. Freq. Cont. **43** (**4**), 533-559 (1996).

73   M. Kurosawa, T. Morita, and T. Higuchi, "A cylindrical ultrasonic micro motor based on PZT thin film." Proc. IEEE Ultrasonics Symposium, 549-552 (1994).

74   A. Lal and R. M. White, "Micromachined silicon ultrasonic atomizer." Proc. IEEE Ultrasonics Symposium, 339-342 (1996).

75   D. L. Polla, "Ferroelectric microsensors and microactuators." Proc. IEEE Ultrasonics Symposium, 127-133 (1992).

76   P. Muralt, A. Kholkin, M. Kohli, T. Maeder, and N. Setter, "Characterization of PZT thin films for microactuators," Micro. Eng. **29**, 67-70 (1995).

77   D. Dimos, W. L. Warren, M. B. Sinclair, B. A. Tuttle, and R. W. Schwartz, "Photoinduced hysteresis changes and optical storage in (Pb,La)(Zr,Ti)O3 thin films and ceramics," J. Appl. Phys. **76(7)**, 4305-4315 (1994).

78   R. Ramesh, W. K. Chan, B. Wilkens, T. Sands, J. M. Tarascon, and V. G. Keramidas, "Fatigue and aging in ferroelectric $PbZr_{0.2}Ti_{0.8}O_3/YBa_2Cu_3O_7$ heterostructures," Integrated Ferroelectrics **1**, 1-15 (1992).

79   W. L. Warren, B. A. Tuttle, D. Dimos, G. E. Pike, H.-N. Al-Shareef, R. Ramesh, and J. T. E. Jr., "Imprint in ferroelectric capacitors," Jpn. J. Appl. Phys. **35**, 1521-1524 (1996).

80   W. L. Warren, G. E. Pike, D. Dimos, K. Vanheusden, H. N. Al-Shareef, B. A. Tuttle, R. Ramesh, and J. J. T. Evans, "Voltage shifts and defect dipoles in ferroelectric capacitors," Mat. Res. Soc. Symp. Proc. **433**, 257-266 (1996).

81   A. L. Kholkin, E. L. Colla, A. K. Tagantsev, and D. V. Taylor, "Fatigue of piezoelectric properties in Pb(Zr,Ti)O$_3$ films," Appl. Phys. Lett. **68 (18)**, 2577-2579 (1996).

82   H. D. Chen, K. R. Udayakumar, C. J. Gaskey, and L. E. Cross, "Fabrication and electrical properties of lead zirconate titanate thick films," J. Am. Ceram. Soc. **79 (8)**, 2189-2192 (1996).

83   I. Kanno, S. Fujii, T. Kamada, and R. Takayama, "Pizoelectric properties of c-axis oriented Pb(Zr,Ti)O$_3$ thin films," Appl. Phys. Lett. **70 (11)**, 1378-1380 (1997).

84   R. F. Brown, "Effect of two-dimensional mechanical stress on the dielectric properties of poled ceramic barium titanate and lead zirconate titanate," Can. J. Phys. **39**, 741-753 (1961).

85   R. D. Klissurska, A. K. Tagantsev, K. G. Brooks, and N. Setter, "Use of ferroelectric hysteresis parameters for evaluation of niobium effects in lead zirconate titanate thin films," J. Am. Ceram. Soc. **80 (2)**, 336-342 (1997).

86   B. A. Tuttle, D. H. Doughty, R. W. Schwartz, T. J. Garino, S. L. Martinez, D. Goodnow, C. L. Hernandez, R. G. Tissot, and W. F. Hammetter, "Chemically prepared PZT thin films with niobium additions," Ceram. Trans. **15**, 179-191 (1990).

87   R. D. Klissurska, K. G. Brooks, I. M. Reaney, C. Pawlaczyk, M. Kosec, and N. Setter, "Effect of doping on the microstructure of sol-gel derived PZT thin films," J. Am. Ceram. Soc. **78 (6)**, 1513-1520 (1995).

88   J. Chen. M. P. Harmer, and D. M. Smyth. "Polarization fatigue in perovskite ferroelectric ceramics and thin films." Proc. IEEE 8th Int. Symp. App. Ferro., 111-115 (1992).

89   W. Cao and C. A. Randall. "TEM analysis of Domains in PZT ecramics." J. Phys. Chem. Sol. **57**, 1499-1505 (1996).

90   D. L. Smith. *Thin Film Deposition* (McGraw-Hill, Inc.. N.Y.. 1995).

91   J. F. Scott. "Ferroelectric memories." Physics World **February**, 46-50 (1995).

92   K. Okuwada, S. Nakamura, M. Imai, and K. Kakuno. "Perovskite formation of $Pb(Mg_{1/3}Nb_{2/3})O_3$ and $Pb(Fe_{1/2}Nb_{1/2})O_3$ film by sol-gel method." Jpn. J. Appl. Phys. **29 (6)**, 1153-1156 (1990).

93   K. Okuwada. M. Imai, and K. Kakuno. "Preparation of $Pb(Mg_{1/3}Nb_{2/3})O_3$ thin film by sol-gel method." Jpn. J. Appl. Phys. **28 (7)**, L1272-L1273 (1989).

94   P. Ravindranathan. S. Komarneni. A. S. Bhalla, and L. E. Cross. "Solution-sol-gel processing of lead magnesium niobate thin films." Ferroelectrics Letters **12**, 29-34 (1990).

95   V. Trtik. M. Jelfnek. and E. B. Kluenkov. "A study of laser deposited PZT, PLZT. PMN. and YBCO thin films." J. Phys. D: Appl. Phys. **27 (7)**, 1544-1547 (1994).

96   Y. Takeshima, K. Shiratsuyu, H. Takagi, and K. Tomono. "Preparation of lead magnesium niobate thin films by chemical vapor deposition." Jpn. J. Appl. Phys. **34 (9B)**, 5083-5085 (1995).

97   M. Shyu, T. Hong, and T. Wu, "Properties of highly (100)-oriented thin films of sol-gel derived [Pb(Mg$_{1/3}$Nb$_{2/3}$)$_x$Ti$_{1-x}$]O$_3$ on (100)-textured LaNiO$_3$ electrode." Mat. Lett. **23**, 221-226 (1995).

98   D. Liu and D. A. Payne. "Lower temperature crystallization and ordering in sol-gel derived Pb(Sc$_{0.5}$Ta$_{0.5}$)O$_3$ powders and thin layers." J. Appl. Phys. **77** (7), 3361-3364 (1995).

99   Y. Yamashita, H. Kanai, O. Furukawa, K. Hasegawa, S. Mukaeda, and K. Handa. "Relaxor dielectric materials for multilayer ceramic capacitor in high-temperature applications." Jpn. J. Appl. Phys. **34**, 5364-5367 (1995).

100   J. J. Randall and R. Ward. "The preparation of some ternary oxides of platinum metals." J. Electrochem. Soc. **81**, 2629-2631 (1959).

101   K. Abe, S. Komatsu, N. Yanase, K. Sano, and T. Kawakubo. "Ferroelectric properties in heteroepitaxial Ba$_{0.6}$Sr$_{0.4}$TiO$_3$ thin films on SrRuO$_3$/SrTiO$_3$ substrates." Jpn. J. Appl. Phys. **36** (9A), 5575-5579 (1997).

102   C. B. Eom, R. B. V. Dover, J. M. Phillips, D. J. Werder, J. H. Marshall, C. H. Chen, R. J. Cava, R. M. Fleming, and D. K. Fork, "Fabrication and properties of epitaxial ferroelectric heterostructures with (SrRuO$_3$) isotropic metallic oxide electrodes." Appl. Phys. Lett. **63** (18), 2570-2572 (1993).

103   L. Antognazza, K. Char, T. H. Geballe, L. L. H. King, and A. W. Sleight. "Josephson coupling of YBa$_2$Cu$_3$O$_{7-x}$ through a ferromagnetic barrier of SrRuO$_3$." Appl. Phys. Lett. **63**, 1005-1007 (1993).

104   A. Callaghan. C. W. Moeller. and R. Ward. "Magnetic interactions in ternary ruthenium oxides." Inorg. Chem. **5 (9)**, 1572-1576 (1966).

105   R. J. Bouchard and J. L. Gillson. "Electrical properties of $CaRuO_3$ and $SrRuO_3$ single crystals." Mat. Res. Bull. **7**, 873-878 (1972).

106   P. B. Allen. H. Berger, O. Chauvet, L. Forro, T. Jarlborg, A. Junod, B. Revas. and G. Santi. "Transport properties, thermodynamic properties, and electronic structure of $SrRuO_3$," Phys. Rev. B **53 (8)**, 4393-4398 (1996).

107   M. Shepard, G. Cao, S. McCall, F. Freibert, and J. E. Crow. "Magnetic and transport properties of Na doped $SrRuO_3$ and $CaRuO_3$," J. Appl. Phys. **79 (8)**, 4821-4823 (1996).

108   W. Bensch. H. W. Schmalle. and R. A, "Structure and thermochemical reactivity of $CaRuO_3$ and $SrRuO_3$." Solid State Ionics **43**, 171-177 (1990).

109   J.-P. Maria. M.S. Thesis. Penn State University, 1996.

110   M. Shikano, T. Huang. M. Itoh, and N. T, "Stress dependence of SrRuO3," Solid State Comm. **90 (2)**, 115-119 (1994).

111   J. J. Neumeier, A. L. Cornelius, and J. S. Schilling, "Influence of pressure on the ferromagnetic transition temperature of $SrRuO_3$," Physica B **198**, 324-328 (1994).

112   J. F. M. Cillessen, M. W. J. Prins, and M. R, Wolf, "Thickness dependence of the switching voltage in all oxide feroelectric thin film capacitors prepared by pulsed laser deposition," J. Appl. Phys. **81 (6)**, 2777-2783 (1997).

113   C. H. Ahn, J. M. Triscone, M. Decroux, R. H. Hammond, T. H. Geballe, O. Fischer, M. R. Beasley, L. Antognazza, and K. Char, "Ferroelectric field effect in ultrathin $SrRuO_3$ films," Appl. Phys. Lett. **70 (2)**, 206-208 (1996).

114   C. B. Eom, R. A. Rao, Q. Gan, R. J. Cava, Y. Suzuki, J. J. Krajewski, S. C. Gausepohl, and M. Lee, "Strain stabilized metal-insulator transition in epitaxial thin films of metallic oxide $CaRuO_3$," Appl. Phys. Lett. **70 (22)**, 3035-3038 (1997).

115   A. F. Marshall, L. Klein, C. H. Ahn, S. Dodge, J. Reiner, L. Antagnozza, L. Mieville, A. Kapitulnik, T. H. Geballe, and M. R. Beasley, "Magnetic and crystalline microstructure of $SrRuO_3$ thin films," Proc. Mater. Res. Soc. Symp. Epitaxial Oxide Thin Films III **477**, 223-228 (1997).

116   J.-P. Maria, D. G. Schlom, S. Trolier-McKinstry, M. E. Hawley, and G. W. Brown, "The influence of energetic bombardment on the structure and properties of epitaxial $SrRuO_3$ thin films grown by pulsed laser deposition," J. Appl. Phys. **83 (8)**, 4373-4379 (1998).

117   C. B. Eom, R. J. Cava, R. M. Flemming, J. M. Phillips, R. B. v. Dover, J. H. Marshall, J. W. P. Hsu, J. J. Krajewski, and W. F. P. Jr., "Single-crystal thin films of the isotropic metallic oxides $Sr_{1-x}Ca_xRuO_3$ ($o \leq x \leq 1$)," Science **258**, 1766-1769 (1992).

118   Q. Gan, R. A. Rao, and C. B. Eom, "Control of growth and domain structure of epitaxial $SrRuO_3$ thin films by vicinal (001) $SrTiO_3$ substrates," Appl. Phys. Lett. **70 (15)**, 1962-1964 (1997).

119   M. Hiratani, C. Okazaki, K. Imagawa, and K. Tagaki, "SrRuO$_3$ thin films grown under reduced oxygen pressure," Jpn. J. Appl. Phys. **33 (12A)**, 6212-6216 (1996).

120   H. M. Smith and A. F. Turner. "Vacuum deposited films using a ruby laser." Applied Optics **4 (1)**, 147-148 (1965).

121   P. Clarke. (U.S.A., 1971).

122   D. B. Chrisey and G. K. Hubler, *Pulsed Laser Deposition of Thin Films* (John Wiley & Sons, Inc.. New York, NY, 1994).

123   J. F. Ready, "Effects due to absorption of laser radiation." J. Appl. Phys. **36 (2)**, 462-468 (1964).

124   J. Cheung and J. Horowitz. "Pulsed laser deposition history and laser-target interactions." Mat. Res. Bull. **17 (2)**, 30-36 (1992).

125   L. P. Inc.. Compex 102 reference literature (1997).

126   D. Dijkkamp, T. Venkatesan, X. D. Wu, S. A. Shaheen, N. Jisrawi, Y. H. Min-Lee, W. L. McLean, and M. Croft, "Preparation of Y-Ba-Cu oxide superconductor thin films using pulsed laser deposition from high T$_c$ bulk material." Appl. Phys. Lett. **51 (8)**, 619-621 (1987).

127   T. Terashima, K. Shimura, and Y. Bando, "Superconductivity in one-unit-cell-thick YBa$_2$Cu$_3$O$_7$ thin films," Phys. Rev. Lett. **67 (10)**, 1362-1365 (1991).

128   V. Matiyasevic, P. Rosenthal, K. Shinohara, A. F. Marshall, R. H. Hammond, and M. R. Beasley, "Reactive coevaporation of YBaCuO superconducting films," J. Mater. Res. **6 (4)**, 682-698 (1991).

129   D. B. Geohegan, D. N. Mashburn, R. J. Culnertson, S. J. Pennycook, J. D. Budai, R. E. Valiga, B. C. Sales, D. H. Lowndes, L. A. Boatner, E. Sonder, D. Eres, D. K. Christen, and W. H. Christie, "Pulsed laser deposition of thin superconducting films of $HoBa_2Cu_3O_{7-x}$ and $YBa_2Cu_3O_{7-x}$." J. Mater. Res. **3 (6)**, 1169-1179 (1988).

130   E. K. Müller, B. J. Nicholoson, and G. L. Turner, "The epitaxial vapor deposition of perovskite materials," J. Electrochem. Soc. **110 (9)**, 969-973 (1963).

131   L. Wiedeman and H. Helvajian, "Laser photodecomposition of sintered $YBa_2Cu_3O_{6+x}$: Ejected species population distributions and initial kinetic energies for the laser ablation wavelengths 351, 248, and 193 nm." J. Appl. Phys. **70 (8)**, 4513-4523 (1991).

132   R. Messier and J. E. Yehoda, "Geometry of thin-film morphology," J. Appl. Phys. **58 (10)**, 3739-3746 (1985).

133   *ASM Handbook*, Vol. 10 Materials Characterization (ASM International, 1992).

134   L. G. Coccia, G. C. Tyrrell, and I. W. Boyd, "Analysis of pulsed excimer laser ablation of PZT, Pb, and Ti in oxygen ambient using energy dispersive mass spectroscopy," Mat. Res. Soc. Symp. Proc. **433**, 225-230 (1996).

135   J. P. Zheng, Z. Q. Huang, D. T. Shaw, and H. S. Kwok. "Generation of high-energy atomic beams in laser-superconducting target interactions." Appl. Phys. Lett. **54** (3), 280-282 (1989).

136   H. Kurogi, Y. Yamagata, T. Ikegami, K. Ebihara, B. Y. Tong, and K. Kumamoto. "Preparation of $PbZr_xTi_{1-x}O_3$ thin films by KrF excimer laser ablation technique." Mater. Res. Soc. Symp. Proc. **433**, 237-242 (1996).

137   R. S. Robinson. "Energetic binary collisions in rare gas plasmas." J. Vac. Sci. Technol. **16** (2), 185-188 (1978).

138   T. Venkatesan, X. D. Wu, R. Menchausen, and A. Pique. "Pulsed laser deposition: future directions." Mat. Res. Soc. Bull. **17** (2), 54-58 (1992).

139   D. Lubben, S. A. Barnett, K. Suzuki, S. Gorbatkin, and J. E. Greene. "Laser-induced plasmas for primary ion deposition of epitaxial Ge and Si films." J. Vac. Sci. Technol. **B 3** (4), 968-974 (1985).

140   B. Holzapfel, B. Roas, L. Schultz, P. Bauer, and G. Saemann-Ischenko. "Off-axis laser deposition of $YBa_2Cu_3O_{7-\delta}$ thin films." Appl. Phys. Lett. **61** (26), 3178-3180 (1992).

141   Y. Yoneda, H. Kasatani, H. Terauchi, Y. Yano, T. Terashima, and Y. Bando. "Ferroelectric phase transition in $BTiO_3$ films," J. Cryst. Growth **150**, 1090-1093 (1995).

142   Y. Watanabe, Y. Matsomoto, H. Kunitomo, N. Tanamura, and E. Nishimoto. "Crystallographic and electrical properties of epitaxial BaTiO3 film grown on

conductive and insulating perovskite oxides." Jpn. J. Appl. Phys. **Pt. 1, 33 (9B)**, 5183-5186 (1994).

143   T. Nose. H. Kim, and H. Uwe. "Dielectric property of epitaxial thin films of BaTiO$_3$ synthesized by laser ablation." Jpn. J. Appl. Phys. **Pt.1, 33 (9B)**, 5259-5261 (1994).

144   M. Lee. M. Kawasaki. M. Yoshimoto, and H. Koinuma. "Heteroepitaxial growth of BaTiO$_3$ films on Si using pulsed laser deposition." Appl. Phys. Lett. **66 (11)**, 1331-1333 (1995).

145   *Lambda Physik Operations Manual* (1997).

146   H. M. O'Bryan, P. K. Gallagher, G. W. Berkstresser, and C. D. Brandle. "Thermal analysis of rare earth gallates and aluminates." J. Mater. Res. **5 (1)**, 183-189 (1990).

147   JCPDS (International Centre for Diffraction Data. Swathmore. PA) for SrTiO$_3$. Card # 35-734.

148   Y. S. Touloukian, *Thermophysical Properties of Matter, The TPRC data series*. Vol. 13 (IFI/Plenum. New York.).

149   JCPDS (International Centre for Diffraction Data. Swathmore. PA) for KTaO$_3$, Card # 38-1470.

150   M. Kawasaki, K. Takahashi, T. Maeda, R. Tsuchia, M. Shinohara, O. Ishiyama, M. Yoshimoto, and H. Koinuma, "Atomic control of the SrTiO$_3$ crystal surface." Science **266**, 1540-1542 (1994).

151   B. D. Cullity, *Elements of X-ray Diffraction*, second edition ed. (Addison-Wesley, Reading, 1978).

152   C.-Y. Huang, Ph.D. Thesis, The Pennsylvania State University, 1990.

153   P. Sigmund, "On the number of atoms displaced by implanted ions or energetic recoil atoms," Appl. Phys. Lett. **14 (3)**, 114-116 (1969).

154   E. Friedland, "Study of damage structure in magnesium oxide single crystals after argon implantation," Nuc. Inst. Meth. Phys. Res. B **116**, 136-140 (1996).

155   A. Jukna, B. Vengalis, F. Anisimovis, and V. Jasutis, "Composition distributions in on and off-axis pulsed laser deposited thin films," Vacuum. Symp. Proc. 4th Euro. Vac. Conf. **46 (8-10)**, 977-978 (1995).

156   A. D. Marwick, G. J. Clark, K. N. Tu, D. S. Yee, C. Lee, U. N. Singh, J. Doyle, and J. J. Cuomo, "Annealing of ion implant damage in the high-temperature superconductor $YBa_2Cu_3O_{7-x}$," Nuc. Inst. Meth. Phys. Res. **B40/41**, 612-614 (1989).

157   X. D. Wu, S. R. Foltyn, R. C. Dye, Y. Coulter, and R. E. Muenchausen, "Properties of epitaxial $SrRuO_3$ thin films," Appl. Phys. Lett. **62 (19)**, 2434-2436 (1993).

158   *Handbook of Thermophysical Properties of Solids* .

159   D. Hennings and K. H. Hardtl, "Defect structure in La doped $PbTiO_3$," Phys. Status Solidi (a) **3**, 465-474 (1970).

160   S. Fujii, A. Tomozawa, E. Fujii, H. Torii, and R. Takayama, "Preparation of La-modified PbTiO3 thin films on the oxide buffer layers with NaCl-type structure," Appl. Phys. Lett. 65 (11), 1463-1465 (1994).

161   C. M. Foster, W. Pompe, A. C. Daykin, and J. S. Speck, "Relative coherency strain and phase transition history in epitaxial ferroelectric thin films," J. Appl. Phys. 79 (3), 1405-1415 (1996).

162   C. D. Theis and D. G. Schlom, "Domain structure of epitaxial PbTiO3 films grown on vicinal SrTiO3," J. Mater. Res. 12 (5), 1297-1305 (1997).

163   N. Wakia, A. Sakai, N. Ishizawa, K. Shinosaki, and N. Mizutani, "Crystal growth, crystal structure and chemical composition of a pyrochlore type compound in lead-magnesium-niobium-oxygen system," Mat. Res. Bull. 28 (2), 137-143 (1993).

164   K. Abe, S. Komatsu, N. Yanase, K. Sano, and T. Kawakubo, "Asymmetric ferroelectricity and anomalous current conduction in Heteroepitaxial BaTiO3 thin films," Jpn. J. Appl. Phys. 36 (9B), 5846-5853 (1997).

165   J.-P. Maria, "Electrical and structural analysis of epitaxial lanthanum modified PbTiO3 thin films exhibiting a-orientd domains," Proc. US-Japan Seminar on Dielectric and Piezoelectric Ceramics, 112-115 (1997).

166   A. K. Tagantsev, M. Landivar, E. Colla, K. G. Brooks, and N. Setter, "Depletion and depolarizing effects in ferroelectric thin films and their manifestations in switching and fatigue," Integrated Ferroelectrics 6, 309-320 (1995).

167   S.-J. Jang. Ph. D. Thesis. The Pennsylvania State University, 1979.

168   G. Burns and F. H. Dacol. "Glassy polarization behavior in ferroelectric compounds $Pb(Mg_{1/3}Nb_{2/3})O_3$ and $Pb(Zn_{1/3}Nb_{2/3})O_3$." Solid State Comm. **48 (10)**, 853-856 (1983).

169   G. K. Williamson and W. H. Hall. "X-ray line broadening from filed aluminum and wolfram." Acta. Meta. **1**, 22-31 (1953).

170   J. Li, D. Viehland, C. D. E. Lakeman, and D. A. Payne, "Frequency-dependent electromechanical properties for sol-gel deposited ferroelectric lead zirconate titanate thin layers: Thickness and processing effects." J. Mat. Res. **10 (6)**, 1435-1440 (1995).

171   M. Toyama, R. Kubo, E. Takata, K. Tanaka, and K. Ohwada, "Characterization of piezoelectric properties of PZT thin films deposited on Si by ECR sputtering," Sensors and Actuators **A 45**, 125-129 (1994).

172   A. C. Ugural. *Stresses in Plates and Shells* (McGraw Hill, New York, 1981).

173   K. Iijima, R. Takayama, Y. Tomita, and I. Ueda. "Epitaxial growth and the crystallographic, dielectric, and pyroelectric properties of Lanthanum-modified lead titanate thin films," J. Appl. Phys. **60 (8)**, 2914-2919 (1986).

174   Y. Yano, K. Iijima, Y. Daitoh, T. Terashima, Y. Bando, Y. Watanabe, H. Kasatani, and H. Terauchi, "Epitaxial growth and dielectric properties of $BaTiO3$ films on Pt electrodes by reactive evaporation." J. Appl. Phys. **76 (12)**, 7833-7838 (1994).

175   F. T. Rogers. "Effect of pile radiation on the dielectric constant of ceramic BaTiO3." J. Appl. Phys. **27 (9)**, 1066-1067 (1956).

176   A. G. Chynoweth. "Pyroelectricity, internal domains, and interface charges in triglycine sulfate." Phys. Rev. **117 (1)**, 1235-1243 (1960).

177   A. G. Chynoweth. "Radiation damage effects in ferroelectric triglycine sulfate." Phys. Rev. **113 (1)**, 159-166 (1959).

178   A. G. Chynoweth. "Surface space-charge layers in barium titanate." Phys. Rev. **102 (3)**, 705-714 (1956).

179   I. Lefkowitz. "Radiation-induced changes in the ferroelectric properties of some barium titanate-type materials." J. Phys. Chem. Solids **10**, 169-173 (1959).

180   S. P. Solov'ev, I. I. Kuzmin, and V. V. Zakurkin. "Radiation induced phase transformations in BaTiO3 and PbTiO3." Ferroelectrics **1**, 19-22 (1970).

181   M. C. Wittels and F. A. Sherrill, "Fast neutron effects in tetragonal barium titanate." J. Appl. Phys. **28 (5)**, 606-609 (1957).

182   K. L. Bye and E. T. Keve. "Structural inhibition of ferroelectric switching in triglycine sulfate. II. X-irradiation/field treatment." Ferroelectrics **4**, 87-95 (1972).

183   A. L. Kholkin, M. L. Calzada, P. Ramos, J. Mendiola, and N. Setter, "Piezoelectric properties of Ca-modified PbTiO3 thin films." Appl. Phys. Lett. **69 (23)**, 3602-3604 (1996).
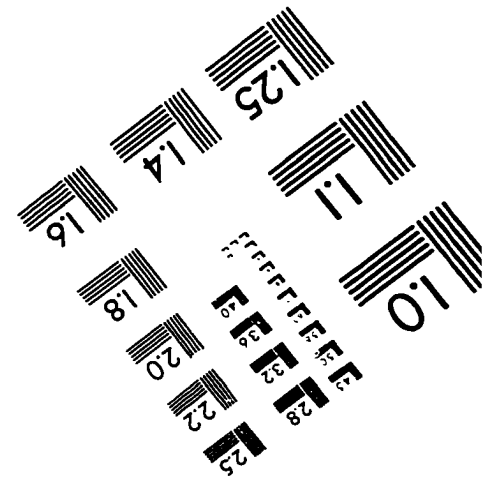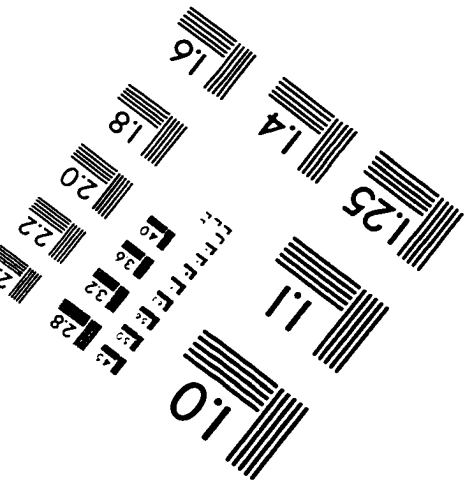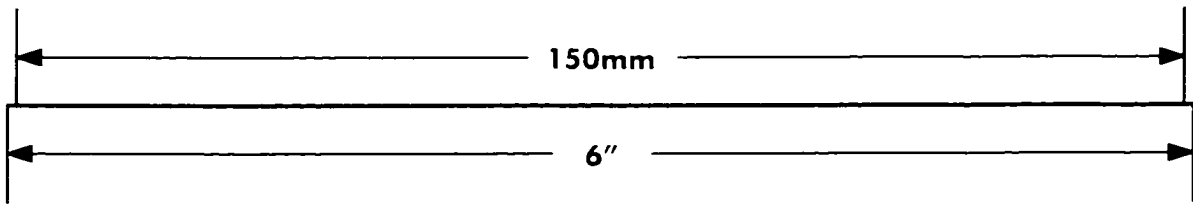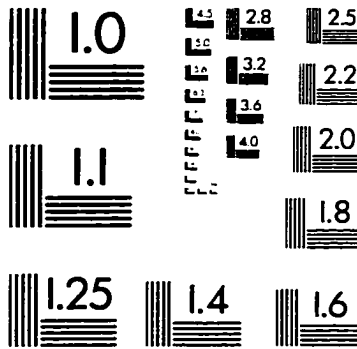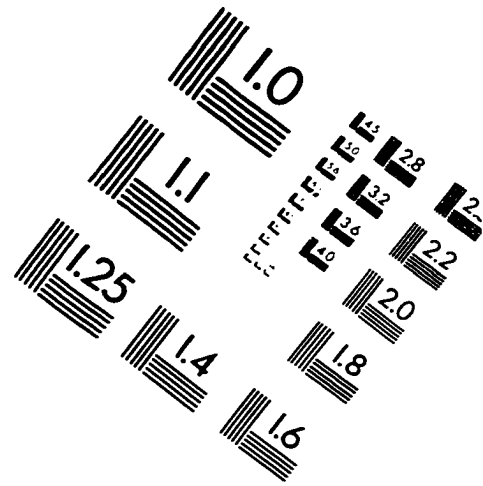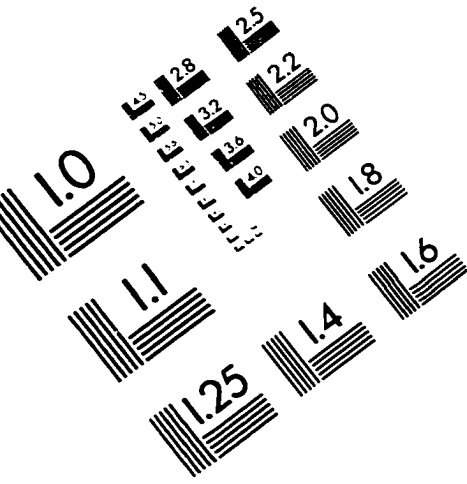
Vita

Jon-Paul Maria was born on Thanksgiving Day, November 23, 1972 in Wilkes-Barre Pennsylvania, spending the next 18 years in the Greater Wyoming Valley. After graduating from Wyoming Area High School (1990), Jon-Paul moved to Penn State where he received his B.S. in Ceramics (1994), his M.S. in Materials Science and Engineering (1996), and finally his Ph.D. in Ceramic Science (summer of 1998). In his eight years at Penn State (which went far too fast) Jon-Paul enjoyed a successful academic career, and had an unbelievably good time. After his fourth year at Penn State, Jon-Paul moved to the Materials research laboratory, where he was surrounded by top-notch scientists, and great friends. Through the good nature of his advisor and peers, Jon-Paul would go on to present at six international meetings, and publish 8 articles in international refereed journals. One of Jon-Paul's more important accomplishments during his graduate studies was his organization of tailgate parties during the 1996 and 1997 Penn State football seasons. A date of particular importance for Jon-Paul was July 21, 1997. This date signified the formation of the PSU-MRL Tailgate Consortium. The consortium involved in excess of 6 investors (7 total) who boldly fronted Jon-Paul with $350 towards the purchase of the consortium's flagship, a 1970 International Harvester Travel-All. On July 21, a group comprised of the Consortium's selectmen scoured the darkest reaches of Pennsylvania's rural district (i.e., Huntington, PA) to retrieve this treasure (this occurrence was much to the chagrin of Jon-Paul's father, Peter Maria). Under the guidance of the partners, the vehicle was named "Bud" (see figures) during a secret meeting held at McMurtry's Tavern. "Bud" made his debut appearance at the Penn State home opener against Louisville, September 6, 1997, where he received instant acclaim – the consortium proved an international success. In the subsequent Penn State games, "Bud" would provide transportation, a place to dance and be happy, as well as shelter from the elements (assuming ones constitution could withstand the fumes). Bud would become synonymous with reliable service, requiring only one custom-machined part and eight "assistance visits" from Graham's Exxon towing (AAA would become one of the Consortium's most valued investors). On a sad day in January 1998, Jon-Paul was forced to bequeath "Bud" to a local automobile recycling center where he roams to this day.

IMAGE EVALUATION
TEST TARGET (QA-3)

150mm

6"